



TRIBHUVAN UNIVERSITY
INSTITUTE OF ENGINEERING
PULCHOWK CAMPUS

Thesis No: 075/MSCCD/014

Multi- Hazard Risk Assessment of Khimti Watershed

By

Roma Thakurathi

A THESIS

SUBMITTED TO THE DEPARTMENT OF APPLIED SCIENCES AND CHEMICAL
ENGINEERING

IN PARTIAL FULFILLMENT OF THE REQUIREMENTS FOR THE
DEGREE OF MASTER OF SCIENCE IN CLIMATE CHANGE AND DEVELOPMENT
PROGRAMME

DEPARTMENT OF APPLIED SCIENCE AND CHEMICAL ENGINEERING

LALITPUR, NEPAL

SEPTEMBER 2021

Copyright©

The author has agreed that the library, Department of Applied Science and Chemical Engineering, Institute of Engineering, Central Campus, Pulchowk, may make this thesis freely available for inspection. Moreover, the author has agreed that permission for extensive copying of this thesis for scholarly purpose may be granted by professor who supervised the thesis work recorded herein or, in his absence, by the Head of Department or concerning M.Sc. Program coordinator or the Dean of the Institute wherein the thesis work was done. It is understood that the recognition will be given to the author of this thesis and to the Department of Applied Science and Chemical Engineering, Institute of Engineering, Central Campus, Pulchowk in any use of the material of thesis. Copying or publication or other use of the thesis for financial gain without approval of Department of Applied Science and Chemical Engineering, Institute of Engineering, Central Campus, Pulchowk and author's written permission is prohibited. Request for permission to copy or to make any other use of the material in this thesis in whole or in part should be addressed to:

Head

Department of Applied Science and Chemical Engineering

Institute of Engineering

Central Campus, Pulchowk

Lalitpur, Nepal

TRIBHUVAN UNIVERSITY
INSTITUTE OF ENGINEERING
PULCHOWK CAMPUS
DEPARTMENT OF APPLIED SCIENCE AND CHEMICAL ENGINEERING

Approval Page

The undersigned certify that they have read, and recommended to the Institute of Engineering for acceptance, a thesis entitled “**Multi- Hazard Risk Assessment of Khimti Watershed**” submitted by Roma Thakurathi (075/MSCCD/014) in partial fulfillment of the requirements for the degree of Master of Science in Climate Change and Development.

Supervisor:

.....
Prof. Dr. Vishnu Prasad Pandey
Department of Civil Engineering
Institute of Engineering
Pulchowk Campus

Program Coordinator:

.....
Prof. Dr. Khem Narayan Poudyal
Department of Applied Science and
Chemical Engineering
Institute of Engineering
Pulchowk Campus

Committee Chairperson:

.....
Prof. Dr. Ram Kumar Sharma
Department of Applied Science and
Chemical Engineering
Institute of Engineering
Pulchowk Campus

External Examiner:

.....
Associate Prof. Dr. Bhesh Raj Thapa
Universal College of Science and Engineering
Pokhara University

September, 2021

Abstract

Many places of Nepal are vulnerable to multiple hazards. Past and recent evidences have shown that the area near the hydropower areas is more vulnerable towards flooding and landslide. As many hydropower structures are under construction near the Khimti region, studying the vulnerability of this area is of great importance. The basin is vulnerable to flooding, landslide and seismic hazards. This study therefore aimed to assess multi-hazard risk through integration of individual hazard maps of flood, landslide and earthquake. This study utilized geographic information system (GIS) in combination with Frequency Ratio Approach for landslide hazard mapping. Flood vulnerability and risk was mapped by developing flood-inundation mapping model in HEC-RAS. Earthquake hazard map was prepared using R-CRISIS tool. The multi-hazard map was created using analytical hierarchy process for assigning weights to individual hazard map (landslide, earthquake and flood). For assessing climate change impact on flood inundation, future climate was projected using a set of five CMIP6 Global Circulation Models (GCMs) under Shared Socio-economic Pathways (SSP) scenarios.

Eleven causative factors were identified and evaluated using GIS, and a landslide susceptibility score was created based on each factor's prediction rate. Finally, a landslide susceptibility map was created with the use of the landslide susceptibility index, and it was divided into four categories (i.e., Low, Moderate, High and Very high). The areas under classified range Low, Moderate, High, and Very High susceptibility zones, respectively, are 41.0%, 28.2%, 21.0%, and 9.8%. Flood hazard map was prepared using depth grid for 100-year return period from HEC-RAS. The obtained flood hazard map was divided into three categories (i.e., Low (< 1 m), Moderate (1 – 3 m) and High (> 3 m)) based on inundation depth. The areas under classified range Low, Moderate, High zones, respectively, are 1.3 Km², 0.6 Km² and 0.3 Km². The seismic hazard maps are generated for a 500-year return period and maximum PHA in the study area are found to be 0.52g and 0.764g for rock site and soil site respectively. Finally, multi-hazard map was prepared for rock and soil using analytical hierarchy process giving certain weight to each individual hazard map. The obtained multi-hazard map was divided into five categories (i.e., Very low, Low, Moderate, High, Very high). The results show that 97.5 Km² and 97.6 Km² area fall under very low hazard category respectively for rock and soil sites, whereas for low and moderate category, 54.3 Km² and 11.4 Km² area fall in rock site and 54.6 Km² and 11.1 Km² area fall in soil sites and 49.7 Km² and 23.2 Km² area are at high and very high risk respectively, for both sites. The combination of different hazard maps (landslide

earthquake, landslide flood and earthquake flood) is prepared using analytical hierarchy process giving certain weightage to individual hazard. The obtained results show that 0.8 Km² (112.2 Km²), area lies in very low (low) hazard zone for landslide seismic hazard combination for both rock and soil sites, 86.5 Km² (65.8 Km²), 79 Km²(83.3Km²), 80.5 Km² (83.7 Km²) lies in very low (low) hazard zones respectively for landslide flood and seismic flood hazard combination for rock and soil sites, for moderate category (67.7 Km²) area for landslide and seismic hazard combination for both rock and soil sites, 45.4 Km², 37.9 Km², 37.1 Km² area lies in moderate zone for landslide flood and seismic flood hazard combination for rock and soil sites respectively. Finally, for high (very high) category, 37.2 Km² (18.3 Km²) area falls for combination of landslide seismic hazard for both rock and soil sites, 27.6 Km² (10.9 Km²), 27.5 Km² (9.3 Km²), 27.1 Km² (8.6 Km²) area falls in high (very high) zone for combination of landslide flood and seismic flood hazard for rock and soil sites respectively. The climate change projections were obtained through ensemble of five Global Circulation Models (GCMs) under Shared Socio-economic Pathways (SSP) scenarios. The annual rainfall across the Khimti watershed is projected to increase from baseline by 5.3% (1.7%), 6% (10.9%), 6.7% (22.4%) for near, mid and far futures under SSP245 (SSP585) scenarios. Annual maximum temperature is projected to increase from baseline by 0.9 °C (1.1 °C), 1.6 °C (2.2 °C), 2.1 °C (3.5 °C) for near, mid and far futures under SSP245 (SSP585) scenarios. Annual minimum temperature is projected to increase from baseline by 1.7 °C (1.8 °C), 2.7 °C (3.7 °C), 3.4 °C (5.9 °C) for near, mid and far futures under SSP245 (SSP585) scenarios.

Globally, the effects of multi-hazards have become more prominent in recent decades. Enormous lives, livelihoods, and the built environment have been lost as a result of several risks and their cascade effects. Therefore, determining hazard map is one of the first stages toward minimizing the harm they cause. Individual and multi-hazard maps developed in this study can help with integrated disaster risk planning initiatives in the Khimti watershed. Climate change projections obtained in this study can be used for assessing flood inundation mapping in the Khimti watershed.

Acknowledgements

Foremost, I would like to express my sincere gratitude to my supervisor Prof. Dr. Vishnu Prasad Pandey for his patience, motivation, enthusiasm, and immense knowledge. His guidance helped me in all time of research and writing of this thesis. I could not have imagined having a better advisor and mentor for my MSc study.

Besides my supervisors, I would like to acknowledge Surendra Maharjan, Bibid Jibi Ghimire and Arshad Ansari whose expertise was invaluable in formulating the project methodology. Their insightful feedback pushed me to sharpen my thinking and brought my work to a higher level.

I am also grateful to Prof. Dr. Khem Narayan Poudyal, MSCCD Coordinator, Prof. Dr. Ram Kumar Sharma, HOD and all faculty members for their guidance, encouragement and continuous support throughout this study.

Also, I would like to thank my parents who rendered enormous support, taught me values of dedication and hard work. I would like to share this moment of happiness with my mother, father, and brother.

Finally, thanks to all those persons who helped me directly and/or indirectly in completion of this thesis work.

Roma Thakurathi

075MSCCD014

M.Sc. in Climate Change and Development

Table of Contents

Copyright©	ii
Approval Page	iii
Abstract	iv
Acknowledgements	vi
Table of Contents	vii
List of Figures	xi
List of Tables	xiv
Abbreviations and Acronyms	xvi
1 Introduction	1
1.1 Background	1
1.2 Problem Statement	2
1.3 Objectives.....	2
1.4 Significance.....	2
1.5 Limitations of the Study.....	2
2 Literature Review	4
2.1 Landslide Hazard Mapping	4
2.2 Missing Data Estimation	6
2.3 Flood Frequency Analysis.....	7
2.4 Flood Hazard/Inundation Mapping	9
2.5 Seismic Hazard Analysis.....	11
2.5.1 Probabilistic Seismic Hazard Mapping.....	12
2.6 Multi-Hazard Mapping.....	16
2.6.1 Multi-Hazard Mapping Approaches	17
2.6.2 Analytical Hierarchy Process.....	20
2.7 Climate Change	21

2.7.1	Climate Models	22
2.7.2	Climate Scenarios	25
2.7.3	Downscaling of Climate Projections	29
2.7.4	Bias Correction	30
3	Materials and Methods	33
3.1	Study Area.....	33
3.1.1	Location	33
3.1.2	Topography	34
3.1.3	Hydro-Climate Characteristics.....	34
3.1.4	Land Use/Cover Types	35
3.2	Identification of Hazards and Indicators	36
3.3	Framework for Landslide Hazard Mapping	38
3.3.1	Landslide Inventory	41
3.3.2	Geology.....	41
3.3.3	Lineament Density	42
3.3.4	Slope Gradient	42
3.3.5	Slope Aspect	42
3.3.6	Curvature.....	43
3.3.7	Distance From Road	43
3.3.8	Distance From Stream.....	44
3.3.9	Relative Relief	44
3.3.10	Land Use/Cover	44
3.3.11	Stream Power Index (SPI)	45
3.3.12	Topographic Wetness Index (TWI)	45
3.3.13	Landslide Susceptibility Analysis	46
3.4	Framework for Flood Hazard Mapping	47
3.4.1	Average Precipitation Calculation	49

3.4.2	Catchment Area Ratio Method	49
3.4.3	Flood Frequency Analysis	50
3.4.4	Hydraulic Modelling.....	50
3.5	Framework for Seismic Hazard Assessment.....	52
3.5.1	Steps Involved in Probabilistic Seismic Hazard Analysis	53
3.5.2	Modelling and Analysis	57
3.6	Multi-Hazard Mapping.....	61
3.6.1	Possible Combination of Two Different Hazard Maps.....	62
3.7	Future Climate Projection	64
3.8	Data and Sources.....	65
4	Results and Discussion	67
4.1	Landslide Hazard Assessment.....	67
4.1.1	Landslide Inventory Map.....	67
4.1.2	Spatial Distribution of Thematic Layers.....	68
4.1.3	Frequency Ratio Model.....	71
4.1.4	Landslide Susceptibility of the Watershed	75
4.1.5	Validation of the Map	76
4.2	Flood Hazard Assessment	78
4.2.1	Floods of Different Return Periods.....	78
4.2.2	Flood Hazard Map	79
4.2.3	Flood Risk in the Watershed.....	83
4.3	Seismic Hazard Assessment.....	84
4.3.1	Completeness Test	84
4.3.2	Seismic Hazard in the Watershed	86
4.4	Multi-Hazard Mapping.....	88
4.4.1	Combination of Landslide and Seismic Hazard Maps.....	89
4.4.2	Combination of Landslide and Flood Hazard Maps	91

4.4.3	Combination of Seismic and Flood Hazard Maps	92
4.4.4	Multi-Hazard Map	94
4.5	Projected Future Climate.....	97
4.5.1	Performance Evaluation of Bias Correction	97
4.5.2	Projected Future Precipitation.....	99
4.5.3	Projected Future Temperature.....	102
4.5.4	Scope for Flood Inundation Mapping using Climate Change Projections	106
5	Conclusions and Recommendations	107
5.1	Conclusions	107
5.2	Recommendations	109
	References	110
	Annexes	126

List of Figures

Figure 2-1: SSP narratives framework (Source: O’Sullivan et al., 2018)	28
Figure 2-2: Process of downscaling (Viner, 2012)	29
Figure 3-1: Location of the study area	33
Figure 3-2: Topography, river network and location of hydro-meteorological stations in the khimti watershed.....	35
Figure 3-3: Land use/cover (LULC) in khimti watershed (source: prepared based on data from ICIMOD, 2010).....	36
Figure 3-4: Process involved in preparing landslide hazard map	40
Figure 3-5: Process involved in preparing flood risk map.....	48
Figure 3-6: Geometric data of khimti watershed	51
Figure 3-7: Steady flow boundary conditions.....	51
Figure 3-8: Khimti watershed inundation depth	52
Figure 3-9: Process involved in preparing seismic hazard map	53
Figure 3-10: Seismic source zones	55
Figure 3-11: Map of Nepal inserted in software	57
Figure 3-12: Division of area into grids of size $0.32^{\circ} \times 0.32^{\circ}$	58
Figure 3-13: Modelling the area source zones in the software	58
Figure 3-14: Providing seismicity values for each zone.....	59
Figure 3-15: Defining spectral ordinate parameters	59
Figure 3-16: Defining attenuation relationship.....	60
Figure 3-17: Defining return periods	60
Figure 3-18: Running the analysis	61
Figure 4-1 : Landslide inventory map.....	67
Figure 4-2: Thematic maps of factors used in landslide susceptibility mapping: (a) slope, (b) aspect, (c) curvature, (d) relative relief, (e) SPI, (f) TWI	70
Figure 4-3: Thematic maps of factors used in landslide susceptibility mapping: (g) distance from stream, (h) distance from road, (i) geology, (j) lineament density, (k) land use/cover...	71
Figure 4-4: Landslide susceptibility map.....	75
Figure 4-5: Landslides at khimti watershed: (a) siwalaya area (b) chyama landslide (c) pharpu dada area	77
Figure 4-6: Area under curve.....	77

Figure 4-7: Flood frequency analysis using different methods at khimti watershed.....	78
Figure 4-8: Flood hazard map.....	80
Figure 4-9: Detailed section of flood hazard map (a).....	81
Figure 4-10: Detailed section of flood hazard map (b).....	82
Figure 4-11: Flood risk map	84
Figure 4-12: Completeness analysis of earthquake data.....	85
Figure 4-13: Regional recurrence relationship	85
Figure 4-14: Seismic hazard map of source zone for PHA for rock sites (for 500 yrs. Return Period).....	86
Figure 4-15: Seismic hazard map of khimti watershed for PHA for rock sites (for 500 yrs. return period).....	87
Figure 4-16: Seismic hazard map of source zone for PHA for soil sites (for 500 yrs. return period).....	87
Figure 4-17: Seismic hazard map of khimti watershed for PHA for soil sites (for 500 yrs. return period).....	88
Figure 4-18: Combination of landslide and seismic hazard map of khimti watershed in case of rock site.....	89
Figure 4-19: Combination of landslide and seismic hazard map of khimti watershed in case of soil site	90
Figure 4-20: Combination of landslide and flood hazard map of khimti watershed	91
Figure 4-21: Combination of seismic and flood hazard map of khimti watershed in case of rock site.....	92
Figure 4-22: Combination of seismic and flood hazard map of khimti watershed in case of soil site.....	93
Figure 4-23: Multi-hazard map of khimti watershed in case of rock site.....	95
Figure 4-24: Multi-hazard map of khimti watershed in case of soil site	96
Figure 4-25: Comparison of raw and bias corrected data with observed data for precipitation of baseline period and for ACCESS- CM2 GCM used in this study for station 1103	98
Figure 4-26: Comparison of raw and bias corrected data with observed data for maximum temperature of baseline period and for ACCESS- CM2 GCM used in this study for station 1103	99
Figure 4-27: Comparison of raw and bias corrected data with observed data for minimum temperature of baseline period and for ACCESS- CM2 GCM used in this study for station 1103	99

Figure 4-28: Trends in long-term annual average total precipitation at station 1103.....	100
Figure 4-29: Range of projected change in annual total future precipitation for different futures, SSPs and GCMs at station 1103	101
Figure 4-30: Trends in long-term annual average maximum temperature at station 1103....	103
Figure 4-31: Trends in long-term annual average minimum temperature at station 1103	103
Figure 4-32: Range of projected change in future maximum temperature for different futures, SSPs and GCMs at station 1103	104
Figure 4-33: Range of projected change in future minimum temperature for different futures, SSPs and GCMs at station 1103	106

List of Tables

Table 2-1: Different types of flood forecasting models used in Nepal.....	10
Table 2-2: Random Consistency Index (RI) (Source: Saaty, 1980, 2000)	21
Table 2-3: Characteristics of RCPs (Source: van Vuuren et al., 2011)	26
Table 2-4: Type of SSPs and their short description (Source: Riahi et al., 2017).....	28
Table 2-5: Bias correction methods (Source : Chen et al., 2013)	31
Table 3-1: Details of hydrological station used in this study.....	35
Table 3-2 : Details of meteorological stations used in this study	35
Table 3-3: Land use/cover types in the study area.....	36
Table 3-4: Data layer source for different hazard assessment	37
Table 3-5: Hazard estimation approaches used in this study.....	37
Table 3-6: Selected indicators for landslide hazard mapping.....	38
Table 3-7: Selected indicators for flood hazard mapping.....	47
Table 3-8: Attenuation relation for horizontal response spectral acceleration (for rock).....	56
Table 3-9: Attenuation relation for horizontal response spectral acceleration (for soil)	56
Table 3-10: Pair-wise comparisons and weighting coefficients of each adopted factor in multi-hazard evaluation	62
Table 3-11: Pair-wise comparisons and weighting coefficients of each adopted factor in combination of landslide and seismic hazard evaluation.....	63
Table 3-12: Pair-wise comparisons and weighting coefficients of each adopted factor in combination of landslide and flood hazard evaluation	64
Table 3-13: Pair-wise comparisons and weighting coefficients of each adopted factor in combination of seismic and flood hazard evaluation.....	64
Table 3-14: List of CMIP6 GCMs used in this study	65
Table 3-15 : List of data acquired from different sources	65
Table 4-1 : Thematic layers area under different classes.....	69
Table 4-2: Frequency ratio (FR), relative frequency (RF), prediction rate (PR) of each factor for each considered class	72
Table 4-3: Landslide affected area for different hazard level.....	75
Table 4-4: Comparison of flood discharge using various methods	79
Table 4-5: Statistical parameters for best fit distributions	79
Table 4-6: Flood affected area for different hazard level	80

Table 4-7: Classification of flooded area according to land use risk.....	83
Table 4-8: Flood affected area of land use.....	83
Table 4-9: Activity rate and interval of completeness	84
Table 4-10: Combination of landslide and seismic hazard affected area for different hazard level for rock site	89
Table 4-11: Combination of landslide and seismic hazard affected area for different hazard level for soil site.....	90
Table 4-12: Combination of landslide and flood hazard affected area for different hazard level	91
Table 4-13: Combination of seismic and flood hazard affected area for different hazard level for rock site	93
Table 4-14: Combination of seismic and flood hazard affected area for different hazard level for soil site.....	94
Table 4-15: Multi-hazard affected area for different hazard level for rock site	95
Table 4-16: Multi-hazard affected area for different hazard level for soil site.....	96
Table 4-17: Projected changes in total precipitation (mm) at seasonal and annual scales at 1103 station based on ensemble of five GCMs under SSPs scenarios	102
Table 4-18: Projected future maximum temperature [°C] at station 1103 based on ensemble of five GCMs under SSPs scenarios	104
Table 4-19: Projected future minimum temperature [°C] at station 1103 based on ensemble of five GCMs under SSPs scenarios	105

Abbreviations and Acronyms

AHP	:	Analytical Hierarchy Process
ASTER	:	Advanced Spaceborne Thermal Emission and Reflection Radiometer
CC	:	Climate Change
CI	:	Consistency Index
CMIP	:	Coupled Model Inter comparison Project
CR	:	Consistency Ratio
DEM	:	Digital Elevation Model
DHM	:	Department of Hydrology and Meteorology
DJF	:	December-January-February (Winter season)
DMG	:	Department of Mines and Geology
FF	:	Far Future
FR	:	Frequency Ratio
GCM	:	Global Circulation Model
GIS	:	Geographic Information System
GLOF	:	Glacier Lake Outburst Flood
GoN	:	Government of Nepal
HDX	:	Humanitarian Data Exchange
HEC-RAS	:	Hydrological Engineering Centre – River Analysis System
IAM	:	Integrated Assessment Model
ICIMOD	:	International Centre for Integrated Mountain Development
IPCC	:	Intergovernmental Panel on Climate Change
LULC	:	Land Use Land Cover
MAM	:	March-April-May (Pre-monsoon season)
MF	:	Mid Future
MoHA	:	Ministry of Home Affairs
NF	:	Near Future
NSC	:	National Seismological Center
ON	:	October-November (Post-Monsoon season)
PBIAS	:	Percentage Bias
PR	:	Predictive Ratio
RCMs	:	Regional Climate Models

RCP	:	Representative Concentration Pathway
RI	:	Random Consistency Index
RF	:	Relative Frequency
SRES	:	Special Report on Emissions Scenarios
SRTM	:	Shuttle Radar Topography Mission
SSP	:	Shared Socioeconomic Pathways
UNDP	:	United Nations Development Programme
UNFCCC	:	United Nation Framework Convention on Climate Change
USGS	:	United State Geological Survey

1 Introduction

1.1 Background

Population, infrastructure, lifelines and agricultural land are always at threat due to natural hazards. Natural disasters have resulted in increased human and economic losses in recent decades (Guha-Sapir et al., 2004; Bouwer et al., 2011). Natural hazards are uncontrollable, but their impact can be minimized by using mitigation measures. Climate change is likely to increase people's exposure to numerous of risks that impact the magnitude, frequency, and spatial distribution of hazardous and tragic events (IPCC, 2014). Nepal is ranked 20th most susceptible countries in terms of multi-hazards, 4th most vulnerable in terms of climate change-related hazards, 11th in terms of earthquake hazards, and 30th in terms of flood-related hazards, according to the United Nations Development Program (UNDP, 2004). Over 13,000 disaster incidents were recorded in Nepal between 1900 and 2005, resulting in a total of 7,400,000 human casualties (Aryal et al., 2012). Numerous research has been conducted regarding single natural and climate related hazards. A place may be vulnerable to not only one hazard but variety of hazards including landslide, earthquake, flood, GLOF, wildfire, Tsunami and so on. So, studies related to multi-hazard risk assessment should be carried out to identify mitigation measures and better planning of such areas. Efforts to assess multi-hazard risk, however, are hampered by a number of obstacles, including a lack of a common definition for a multi-hazard risk (epistemological issues) (Marzocchi et al., 2012); developing a common approach for integrating different hazards (methodological issues) (Tate et al., 2010).

Hazard is defined as the likelihood of a potentially harmful phenomenon occurring within a particular time frame in a specific location (Varnes, 1984). The identification of risks, their chance of occurrence, and their repercussions or consequences on people and places are all part of hazard assessments (Tate et al., 2010). People, livelihoods, environmental services and resources, infrastructure, or economic, social, or cultural assets are all examples of exposure in regions that could be negatively impacted (UNISDR, 2009; IPCC, 2012). Vulnerability is a combination of characteristics and processes that arise from physical, social, economic, and environmental elements that increase a community's sensitivity to the effects of hazards (Mahendra et al., 2011). The potential loss to the exposed subject or system as a result of the

interaction of hazard and vulnerability is known as risk (Cardona, 2010). In simple form, Risk= Hazard x Vulnerability.

1.2 Problem Statement

Many places of Nepal are vulnerable to multiple hazards, and Villages lying in vicinity of Khimti basin is one of them. The basin is vulnerable to flooding, landslide and earthquake hazards. These hazards directly affect life, property of people living in villages near basin along with positioning of the Hydropower projects that are being developed in the Khimti Khola. Climate change has a large impact on river discharge, temperature and precipitation and thus, flood. Extreme precipitation events are anticipated to become more prevalent in the future as the climate warms, according to studies, and this may contribute to an increase in landslide activity in some locations. Hence, changing climate scenario will increase the intensity of the hazards. Loss of lives, economic losses, infrastructure losses are common losses occurred due to different hazards.

1.3 Objectives

The broad objective of this study is to assess multi-hazard risk through integration of individual hazard maps. The specific objectives are;

- To delineate areas with different levels of risks to individual hazards (i.e., flood, landslide, and earthquake).
- To identify areas with different levels of risk to multiple hazards.
- To understand projected change in climate and its implications.

1.4 Significance

The output of this study will help in suggesting best prescriptions for protection and management of identified sensitive areas. The identification of sensitive areas also helps policymakers and infrastructure development agencies better plan development projects so that socio-ecological impacts on the Villages near Khimti basin are minimized.

1.5 Limitations of the Study

- Landslide mapping is done using statistical approach.
- HEC-RAS is used for hydraulic modelling required for this study.

- One dimensional steady flow analysis is used for hydraulic modelling.
- Data from secondary sources are used for hazard mapping.
- Attenuation relationship is selected based on subduction zone.

2 Literature Review

2.1 Landslide Hazard Mapping

The Himalayas, formed 50 million years ago when the Indian and Tibetan plates collided, are one of the most dynamic mountain ranges on the globe. Nepal lies in the heart of the 2400-kilometer-long Himalayan arc, which stretches for around 800 kilometers (Regmi et al., 2014b). Landslides are one of the most significant land degradation processes in the Himalaya, owing to the region's tectonic instability, which includes mountainous topography, unstable geological formations, soft and weak rocks, frequent earthquakes, and heavy and prolonged rainfall during monsoon seasons. Landslides are the outward and downward movement of slope-producing materials along a determined plane of collapse under the effect of gravity (Dhakal, 2012). Slope instability causes landslides, which have an impact on people, property, and livelihood. Because of Nepal's unstable geological formations, steep and rough land surfaces, and extreme weather conditions, landslides have become more widespread in recent years. From 1971 to 2018, 5,141 people died in Nepal as a result of landslides (MoHA, 2019).

In order to prevent potential landslide damage, it is critical to analyze scientifically vulnerable locations (Lee et al., 2004). Prediction of landslides is concerned with either where or when they will occur, depending on the type of movement (i.e. slides or debris flows) and the scope of the forecasting (Carrara et al., 1999). Landslide susceptibility refers to a region's proclivity to produce landslides (Guzzetti et al., 2006). Landslide hazard assessment helps to better understand the basic characteristics of slopes and their propensity to collapse (Aksha et al., 2020).

Over the last few decades, a variety of methodologies have been employed to create landslide susceptibility index (LSI) maps in various parts of the world. These are utilized by various researchers and are divided into the following categories:

- i. Deterministic approach (Dai et al., 2002; Gökceoglu and Aksoy, 1996)
- ii. Heuristic approach (van Westen et al., 2000; Rupke et al., 1988)
- iii. Statistical method (van Westen et al., 1993; Duman et al., 2006)

Deterministic techniques are primarily concerned with the geotechnical and groundwater characteristics of unstable rock and soil, and they rely on specialized mathematical models to

calculate the factor of safety of unstable slopes (Regmi et al., 2014b). They are only employed in areas with common landslide types and consistent inherent characteristics (Yilmaz et al., 2009). The main disadvantage of these models is that they are very simplistic, and the input data required to run them efficiently is usually unavailable.

A heuristic technique makes a link between the occurrence of slope failures and the factors that cause them through a direct or semi-direct mapping procedure (Regmi et al., 2014a). The selected indicators are categorized, ranked, and weighted according to their contribution to landslide incidence, based on expert judgment. There are two sorts of heuristic approaches: geomorphological analysis, in which field researchers identify susceptibility, and qualitative analysis, wherein expert knowledge assigns weight to indicator maps. For landslide susceptibility mapping, Analytical hierarchy Process (Khatakho et al., 2021; Akgun et al., 2010) and weighted linear combination model have recently been employed (Guzzetti et al., 1999; Ayalew et al., 2004). The subjective assignment of weight and rating to factors, as well as a lack of information about the specific study topic, are both limitations of this method.

The most common methods for Landslide Susceptibility Mapping are statistical methods, which involve statistical analysis of landslide distribution and the conditioning factors that influence landslide occurrence in order to determine the relationship between topographical condition and landslide occurrence (Lee et al., 2004). In statistical methods, bivariate and multivariate approaches are often utilized. In a bivariate technique, the landslide inventory map is compared to factor maps to provide weights, and the factor maps are then overlaid to create a landslide susceptibility map. Bivariate statistical methods include frequency ratio, weight of evidence, and certainty factor (Devkota et al., 2013; Javier et al., 2019; Sujatha et al., 2014; Khan et al., 2019). In multivariate analysis, slope failure is assessed as the result of the interplay of numerous interlinked environmental factors that can vary in time and location (Baeza et al., 2001). Logical regression, discriminant analysis, and decision trees are examples of multivariate approaches (Kavzoglu et al., 2015; Carrara et al., 1991; Yilmaz et al., 2009).

Artificial neural networks (ANNs), fuzzy logic, support vector machines, and neuro-fuzzy models are some of the additional landslide susceptibility mapping methods available (Yilmaz et al., 2009; Pistocchi et al., 2002; Pradhan, 2013; Kavzoglu et al., 2015).

2.2 Missing Data Estimation

Before using a station's weather records, it is required to evaluate the data for consistency and continuity. Many stations' records contain short gaps due to a variety of factors such as the lack of an observer, instrument malfunction, and so on. Normal precipitation is utilized as a comparative standard to estimate these missing records and fill in the gaps. The average precipitation over a 30-year period is known as normal precipitation.

There are some methods for filling missing data which are described below:

i. Arithmetic Average Method

If the normal annual precipitation at several stations is within 10% of the normal annual precipitation at the station under evaluation, the missing data can be calculated as a simple arithmetic average value of the rainfall at neighboring stations. It is represented by following equation.

$$P_x = \frac{1}{M} (P_1 + P_2 + \dots + P_m)$$

Where,

P_x = Missing annual precipitation at station X

P_1, P_2, \dots, P_m = Annual precipitations at neighboring station 1,2, ..., m respectively

M = Number of neighboring stations

ii. Normal Ratio Method

The missing data is calculated using the Normal Ratio Method if the normal annual precipitation at various stations exceeds 10% of the normal annual precipitation at the station under consideration. The rainfall measurements at nearby stations are weighed by the ratio of normal annual rainfall in this method. It is represented by following equation.

$$P_x = \frac{N_x}{M} \left[\frac{P_1}{N_1} + \frac{P_2}{N_2} + \dots + \frac{P_m}{N_m} \right]$$

Where,

P_x = Missing annual precipitation at station X

P_1, P_2, \dots, P_m = Annual precipitations at neighboring station 1,2, ..., m respectively

M = Number of neighboring stations

N_x = Normal rainfall at station X

N_1, N_2, \dots, N_m = Normal rainfall at neighboring stations 1,2, ..., m

2.3 Flood Frequency Analysis

Floods, are extremely complex hydrologic processes. Floods in a watershed are governed by the features of the catchment, rainfall, and antecedent circumstances, all of which are dependent on a variety of constituent parameters.

The annual series is a hydrologic data series made up of the values of annual maximum flood from a certain catchment region over a long period of time. The data is then sorted in decreasing order of magnitude, and the plotting-position formula is used to compute the probability P of each event being equal to or exceeded (plotting position).

$$P = \frac{m}{N+1}$$

Where,

m = number of events in order

N= total number of events in the data

The return period/frequency is computed as

$$T = \frac{1}{P}$$

Flood flows are estimated using frequency analysis for various storm events using hydrologic data series and rainfall events using rainfall data series. Chow (1951) demonstrated that the general equation of hydrologic frequency analysis can be used to express most frequency distribution functions used in hydrologic studies:

$$x_T = \bar{x} + K\sigma$$

Where,

x_T = Value of the variate X of a random hydrologic series with a return period T

\bar{x} = Mean of the variate

σ = Standard deviation of the variate

K = Frequency factor which depends upon the return period T, and assumed frequency distribution

The following are some of the most often utilized frequency distribution functions for predicting extreme flood values (Subramanya, 2008):

1. Gumbel Distribution

In hydrology, the Gumbel distribution is used to assess variables like monthly and annual maximum daily rainfall and discharge volumes, as well as to explain droughts. Flood discharge is calculated using the equation below for various return periods.

Variate (X_T) for return interval T:

$$x_t = \bar{x} + K\sigma_{n-1}$$

Where,

For sample size N, Standard Deviation (σ_{n-1}) = $\sqrt{\frac{\sum(x-\bar{x})^2}{N-1}}$

$$\text{Mean, } \bar{x} = \frac{x_1+x_2+\dots+x_n}{N}$$

$$\text{Frequency Factor (K)} = \frac{y_T - \bar{y}_n}{S_n}$$

$$\text{Reduced Variate (Y}_T) = -\ln \left[\ln \left(\frac{T}{T-1} \right) \right]$$

The reduced mean (y_n) and reduced standard deviation (S_n) are obtained from Gumbel's extreme value distribution table.

2. Log-Pearson Type-III Distribution

It is applicable to almost all-natural flood series. It accounts for skew, mean and standard deviation. The flood discharge was calculated using following equation.

$$X_T = \text{Antilog } Z_T$$

Where,

$$Z_T = \bar{Z} + K_z \sigma_z$$

$$Z = \log x$$

$$\text{Mean of variate, } \bar{Z} = \frac{Z_1 + Z_2 + \dots + Z_n}{N}$$

$$\text{Standard deviation of the variate, } \sigma_z = \sqrt{\frac{\sum(x-\bar{x})^2}{N-1}}$$

$$\text{Coefficient of skew of variate, } C_s = \frac{N\sum(Z-\bar{Z})^3}{(N-1)(N-2)(\sigma_z)^3}$$

$K_z = F(C_s, T)$, obtained from Log-Pearson Type-III distribution table.

3. Log Normal Distribution

A logarithmic modification of the data can be used to apply normal distribution principles using log normal distribution when a data series is left bounded and positively skewed. The log normal distribution approach is represented by the equation below.

$$X_T = \text{Antilog } Z_T$$

Where,

$$Z_T = \bar{Z} + K_z \sigma_z$$

$$Z = \log x$$

$$\text{Mean of variate, } \bar{Z} = \frac{Z_1 + Z_2 + \dots + Z_n}{N}$$

$$\text{Standard deviation of the variate, } \sigma_z = \sqrt{\frac{\sum(x - \bar{x})^2}{N-1}}$$

$$\text{Coefficient of skew of variate, } C_s = 0$$

K_z is obtained from Log-Pearson Type-III distribution table.

2.4 Flood Hazard/Inundation Mapping

Flooding, or the overflow of water beyond a river's channel, is a major natural hazard that causes enormous loss of lives and properties each year around the world (Thapa et al., 2020). Due to a combination of highly concentrated monsoon precipitation, high relief, steep mountain topography, and deep and narrow river basins with frequent mass-wasting occurrences, Nepal is vulnerable to floods and disasters (Khanal et al., 2007). Every year, flooding occurs in Nepal, resulting in the deaths of many people, property damage, and loss of livelihood. The ultimate purpose of flood hazard, risk, and vulnerability mapping is to reduce flood damage by enhancing local people's reaction and resilience to disasters of this nature (Khanal et al., 2007). Geographic Information System (GIS) has been successfully utilized to display the extent of flooding as well as to evaluate flood maps in order to develop flood damage assessment maps and flood risk maps (Wiles et al., 2002; Aryal et al., 2020). To estimate flood profiles with a given return period, the GIS must be utilized in conjunction with a hydraulic approach (Demir and Kisi, 2016).

Various types of model used for flood forecasting in Nepal are mentioned in Table 2-1.

Table 2-1: Different types of flood forecasting models used in Nepal

Model	Model Characteristics	River/Basin
GIS and HEC-RAS	One dimensional hydrodynamic model, 1D steady flow analysis	Khando River, Karnali river, Bishnumati river (Thapa et al., 2020; Aryal et al., 2020; Dangol and Bormudoi, 2015)
Nays 2DH	Two-dimensional hydrodynamic model	Koshi River (Kafle and Shakya, 2018)
MIKE NAM, MIKE 11 and HEC-RAS	Semi distributed hydrologic model, one dimensional hydrodynamic model	West Rapti River (Talchabhadel et al., 2015)
HEC-RAS and MIKE 11	One dimensional hydrodynamic model	Bagmati River (Rastogi et al., 2018)

A hydraulic model is a mathematical representation of a fluid flow system, such as a water, sewer, or storm system, that is used to examine the hydraulic behavior of the system. Hydraulic modeling is a technological method that involves simulating free surface flow dynamics using physical and/or mathematical models.

Flood mapping is a two-step process in which flood frequency analysis is performed using either a hydrological model or observed discharge. The flood values derived from this analysis are then fed into a steady-flow hydraulic model, such as the HEC-RAS model developed by the US Army Corps of Engineers, to calculate the equivalent flood levels that would be expected along river reaches that run through inhabited areas (Hicks & Peacock, 2005). This approach has a number of difficulties, including the need for a steady-flow hydraulic evaluation to convert peak flow into water depth.

HEC-RAS is a computer program that simulates water flow in natural rivers and other waterways. The Hydrologic Engineering Center (HEC) in Davis, California, developed the River Analysis System (RAS) to aid hydraulic engineers in channel flow analysis and floodplain assessment. It can perform one-dimensional and two-dimensional hydraulic computations for a whole network of natural and artificial channels, overbank/floodplain areas, and levee protected areas, among other features (HEC-RAS, 2016). HEC-RAS has been enhanced to include an unsteady flow modeling component that, while still not capable of handling highly dynamic flows like dam breaks and ice jam release events, is more than sufficient for open water flood predictions (Hicks & Peacock, 2005). The main computational approach for natural channels is based on solving the one-dimensional energy equation (Saint Venant Equation) (HEC-RAS, 2016).

$$\frac{\partial A}{\partial t} + \frac{\partial Q}{\partial t} = q_t$$

$$\frac{\partial Q}{\partial t} + \frac{\partial(\frac{Q^2}{A})}{\partial x} + gA \frac{\partial H}{\partial x} + gAS_f = 0$$

Where,

A = cross-sectional area perpendicular to the flow

Q = discharge

q_t = lateral inflow to tributary

g = acceleration due to gravity

H = elevation of the water surface above a specified datum

S_f = longitudinal boundary friction slope

t = temporal co-ordinate

x = longitudinal co-ordinate

The four-point implicit box finite difference scheme is used to solve the equations. Friction (Manning's equation) and contraction and (Coefficient multiplied by the change in velocity head) expansion are used to calculate energy losses. In situations where the water surface profile is rapidly changing, the momentum equation is used. Mixed flow regime calculations, bridge hydraulics, and evaluating profiles at river confluences are examples of these circumstances. The model's results have been used in flood management and insurance studies across the United States (Ogras & Onen, 2020) and the rest of the world.

2.5 Seismic Hazard Analysis

Seismic hazard is a term used to describe the severity of ground motion at a structure's location. It is determined using all available databases on seismicity, tectonics, geology, and attenuation characteristics of seismic waves in the area of interest to assess the site-specific design ground motion (Bhusal et al., 2019). In the context of engineering design, seismic hazard is commonly defined as the expected amount of ground acceleration that would be surpassed with a 10% probability at the site under consideration in the next 50 years due to the occurrence of an earthquake anywhere in the region (Chaulagain et al., 2015).

Earthquakes and other natural disasters have had a long-term negative influence on human livelihoods and have caused massive socioeconomic and environmental devastation around the world (Nyimbili et al., 2018). The Himalayas have been steadily thrusting upwards since their

origin millions of years ago due to the subduction of the Indian tectonic plate into the Eurasian (Tibetan) plate, placing Nepal at seismic risk (MoHA, 2019). Due to Nepal's huge annual population growth, rapid urbanization, and infrastructure expansion, the number of fatalities and injured by earthquakes is predicted to increase in the next years (Thapa and Guoxin, 2013).

The hazard related to earthquakes can be reduced through seismic hazard mapping. The assessment of potentially hazardous earthquake-related phenomena to which a facility may be exposed during its useful lifetime is known as seismic hazard analysis (SHA) (Parashar et al., 2012). Seismic hazard can be studied deterministically, which assumes a certain earthquake scenario, or probabilistically, which takes into account uncertainties in earthquake size, location, and time of occurrence. Since the 1990s, PSHA has received attention in Nepal (Pradhan et al., 2020).

2.5.1 Probabilistic Seismic Hazard Mapping

Probabilistic hazard analysis (PSHA) considers uncertainties in the magnitude, location, rate of occurrence of earthquakes, and the predictive relationship to determine the probability of a certain level of ground shaking occurring at a site (Parajuli, 2015).

For the study of earthquake behavior, hypothesis testing, earthquake resistant design, and understanding geodynamic processes involved with earthquakes, an accurate, complete, and comprehensive earthquake catalog is required (Talukdar, 2014). Earthquake records from multiple published sources, such as the National Seismological Centre (NSC), the United States Geological Survey (USGS), and the International Seismological Centre (ISC), are collected into a single catalog for the area of interest. The composite earthquake catalogue includes earthquakes of various magnitudes (e.g., moment magnitude (M_w), body wave magnitude (M_b), surface wave magnitude (M_s), and local magnitude (M_l)) reported from various sources. The moment magnitude is chosen in the study of seismic activity, seismotectonics, and seismic hazard because it does not saturate even at large earthquakes (Kanamori, 1977; Hanks and Kanamori, 1979), is regarded as the best overall assessment of an earthquake size.

Declustering is a technique for filtering overlapping or related occurrences in a catalog. Because the presence of such occurrences can lead to an overestimation of earthquake rates, they must be removed. This study utilizes Gardner and Knopoff's 1974 algorithm in the form of self-written python language to remove the dependent events.

Due to the difficulty in obtaining historical data, non-uniformity in the recorded earthquakes data can be seen. As a result, a completeness analysis is required for the optimum fit of the frequency formula, which can be done according to Stepp, 1972 (Ghimire, 2019). Pandey et al., (2002) determined the annual rate of exceedance, b value, for the Gutenberg and Richter's laws in the range of 0.75–0.95, for magnitudes of 2.0 –5.5. Parajuli, (2009) in his study determined value of b to be 0.76. In their study, Thapa and Guoxin, (2013) calculated b value of 0.85.

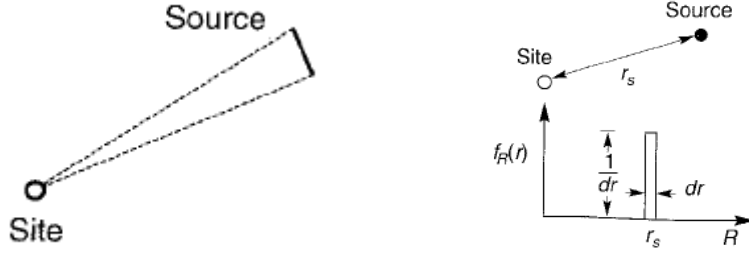
Models of ground motion attenuation have a significant impact on seismic hazard and risk (Crowley et al., 2005). Maskey et al., (2004) has concluded that among the different attenuation relationships prepared for different regions their suitability depends not only on one law but also in magnitude range and source to site distance. For example, where attenuation relationship cannot be developed because there isn't a complete collection of earthquake catalogs for Nepal it is accepted to use attenuation relationships proposed by Young's et al., 1997, Donovan, 1973 and Cornell et al., 1979 which give way the PGA values nearer to the values equivalent to the recorded intensities during the past earthquakes of 1833, 1934 and 1988.

Pandey et al for Government of Nepal generated an enhanced seismic hazard map for Nepal using the software CRISIS99 developed by the Institute de Ingenieria, UNAM, Mexico. They identified a total of 12 areal seismic source zones across Nepal and conducted the PSHA using Young's et al., (1997) attenuation relation. The final result is a seismic hazard map for peak horizontal acceleration (PHA) at bedrock with a 10% probability of being exceeded in the next 50 years.

Following steps were followed for the calculation of PSHA.

Step I: Identification and Characterization of Earthquake Sources

Earthquake sources within a given region containing the site are taken into account while calculating the PSHA of a site. Within a given source zone, earthquakes are considered to be evenly dispersed (i.e., Earthquake are considered equally likely to occur at any location). Since the distance between any point along its length and the site is almost constant, the relatively short fault can be represented as a point source. The distance (R) for the point source is known as r_s , accordingly the probability that $R = r_s$ is assumed to be 1 and probability $R \neq r_s$ is zero.



A maximum potential magnitude $M_{\max,i}$ of earthquake is assigned to each source. The geological and seismological information of the region/area around the site, as well as past earthquake data, are used to compute the total number of such sources (N) to be evaluated in the PSHA study, as well as their geometry and $M_{\max,i}$ values. From practical analysis of the harmful effect of a minimum earthquake that can affect the facility under consideration, one value of minimum earthquake magnitude, M_0 is commonly assigned to all sources.

Step II: Characterization of Seismicity or Temporal Distribution of Earthquake Recurrence

To characterize the seismicity of each source zone, a recurrence relationship is utilized, which specifies the average rate at which an earthquake of a certain size will be exceeded. The magnitude ranges are divided into N_m sections.

For each source,

M_{\max} = maximum magnitude of earthquake for that source,

M_u^j = upper limit of j^{th} interval of that source = $M_0 + \Delta M * j$,

M_l^j = lower limit of j^{th} interval of that source = M_u^{j-1} , $j > 1$
 $= M_0$, $j=1$

$\Delta M = (M_{\max} - M_0) / N_m$,

Mean Magnitude of j^{th} interval (M^j) = $(M_u^j + M_l^j) / 2$

Probability density function for Gutenberg-Richter Recurrence law with upper and lower bound can be expressed as

$$P(M = M^j | m_0 < M^j < M_{\max}) = \frac{\beta * \exp(-\beta * (M^j - M_0))}{1 - \exp(-\beta * (M_{\max} - M_0))}$$

Where $\beta = 2.303 * b$,

The relative likelihood of large and small earthquakes is described by the value of b . As the value of b increases, the number of larger magnitude earthquakes reduces in comparison to smaller magnitude earthquakes.

Step III: Use of Predictive Relationship

Predictive relationships must be used to determine the ground motion produced at a site by an earthquake of any size, occurring at any position in each source zone.

The parameters of ground motion are typically assumed to be log normally distributed. The probability of an earthquake of magnitude m originating in a source at a distance 'r' exceeding acceleration, $P(Z > z^*/M^j, r)$, is obtained from the distribution function of Z , which has the form of a log-normal distribution. The attenuation relation is used to calculate the mean value $\mu(\ln Z)$ and standard deviation $\sigma(\ln Z)$.

$$Z = \frac{x - \mu}{\sigma};$$

Where, x = natural logarithm of [peak horizontal acceleration (0.01 g to 0.6g)]

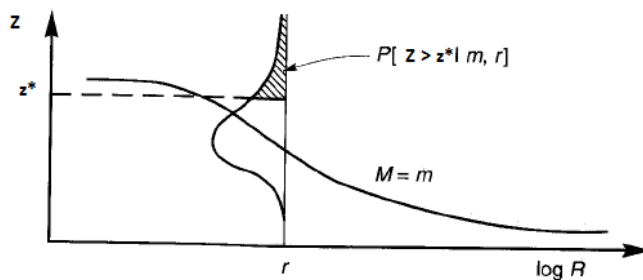
μ = natural logarithm of peak horizontal acceleration from attenuation relationship.

σ = natural logarithm of standard deviation

Z = standard normal variate

Probability of exceedance of an acceleration $P(Z > z^*/M^j, r) = 1 - F_z(z^*)$

Where $F_z(z^*)$ = Cumulative distribution function of Z at M^j



Step IV: Seismic Hazard Curves

For individual source zone seismic hazard curves can be obtained and blended to express the aggregate hazard at a certain location.

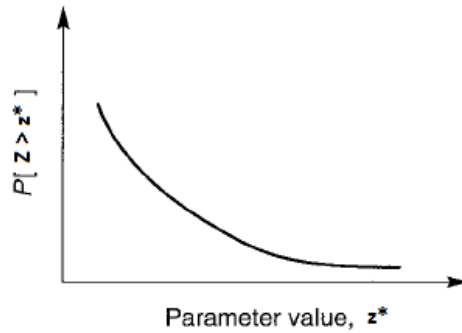
For one conceivable earthquake at one possible source location, the likelihood of exceeding a given value z^* of ground motion parameter Z is calculated and then multiplied by the probability that that particular magnitude earthquake would occur at that particular place. After that, the process is repeated for all potential magnitudes and locations, with probability for each added. The region's total average rate of exceedance is represented by

$$\lambda_{z^*} = \sum_{i=1}^{N_s} \sum_{j=1}^{N_m} \sum_{k=1}^{N_r} v_i * P(Z > z^* | m_j, r) * P(M = m_j) * P[R = r_k]$$

Where, $v_i = \exp[\alpha_i - \beta_i * M_o]$,

All sources are simulated as point sources for simplicity, and the average rate of exceedance for the region can then be determined by

$$\lambda_{z^*} = \sum_{i=1}^{N_s} \sum_{j=1}^{N_m} v_i * P(Z > z^* | m_j) * P(M = m_j)$$



Step V: Determination of Temporal Distribution

The distribution of earthquake occurrence with respect to time must be addressed when calculating the numerous hazards that may occur in a given time period. Poisson's Model is the most often used model to describe the temporal occurrence of earthquakes. To evaluate the probability of exceedance in finite time intervals, the seismic hazard curve can be integrated with Poisson's model. In the time period T, the probability of exceedance z^* is

$$P [Z_T > z^*] = 1 - \exp [- \lambda_{z^*} * T]$$

2.6 Multi-Hazard Mapping

Nepal has a land area of 147,181 square kilometers, which includes both the high Himalayas to the north and the plains to the south. Because of its diversified terrain and climatic conditions, geological position, rough mountains, and steep scenery, Nepal is very vulnerable to multiple hazards (MoHA, 2019).

It is essential to conduct a multi-hazard risk analysis to mitigate the effects of natural/anthropogenic hazards (Kaur et al., 2018). RISK-GIS (Granger et al., 1999), HAZUS (Schneider and Schauer et al., 2006), CAPRA (Cardona et al., 2010), Riskscape (Schmidt et al., 2011), and SWARA-ANFIS-GWO (Pourghasemi et al., 2019) have all been used to predict multi-hazard risk.

2.6.1 Multi-Hazard Mapping Approaches

Several studies related to multi-hazard mapping are described in following section.

Lamichhane et al., (2021) assessed prospects of transboundary multi-hazard dynamics in Bhotekoshi-Sunkoshi watershed in the Sino-Nepal Border Region since this watershed is considered as multi-hazard hotspot of Nepal. Five aspects namely topographical, geological, hydro-meteorological, glacial lakes and socio-economy were considered in this study to discover the several components of watershed characteristics that induce multiple natural hazards and contribute to related watershed vulnerabilities. Hazards were selected based on the elements and historical cases, and their repercussions were associated with the built environment in the study area. The study determined the habitable and non-habitable regions of the entire watershed, which will lead to policy changes for infrastructure development and subsequent measures.

Aksha et al., (2020) conducted a geospatial analysis of multi-hazard risk for the data limited city of Dharan, Nepal with the goal of producing a procedural model for generating a composite risk map. Statistical approaches and the Analytic Hierarchy Process (AHP) were used to analyze integrated hazard assessment for landslides, floods, and earthquakes. They used the Social Vulnerability Index (SoVI) to construct a vulnerability map of the research area, which was then coupled with a developed integrated hazard map to generate a total risk map. Dynamic modeling was not possible due to a lack of data availability and spatial resolution. This study's findings revealed the geographic extent of low- to high-risk zones, which can help with future disaster management.

Kaur et al., (2018) used geospatial technology to create a multi-hazard risk map in the Arithang ward of Gangtok City. The study used an analytical hierarchy process to create landslide and seismic hazard maps for Gangtok, as well as vulnerability maps and a semi quantitative and semi qualitative risk analysis. Leading to a shortage of funds, the investigation was limited to one ward, although the methodology can be implemented at a local to regional level. The study's findings are useful documentation for future planning and readiness in the city of Gangtok.

Pourghasemi et al., (2019) developed a multi-hazard probability map for three hazards: landslides, floods, and earthquakes for hazard-prone region management in Iran. The eleven contributing parameters employed for multi-hazard map preparation in this study include

altitude, slope aspect, plan curvature, slope degree, distance to river, profile curvature, distance to faults, lithology, distance to roads, rainfall, and land use. Landslide and flood hazard maps were created using SWARA-ANFIS-GWO ensemble models, and earthquake hazard maps were created using probabilistic seismic hazard analysis (PSHA). Finally, in ArcGIS, the multi-hazard probability map was created by combining the three natural hazard maps. The study's findings allow for the delineation of multi-hazard zones.

Skilodimou et al., (2019) used multi-criteria analysis and GIS to analyze and specify the suitable sites for urban development in the Peneus River basin, taking into account landslide, flood, and earthquake hazards. Topographic maps, geology maps, precipitation data, and information on previous landslides and flood events were among the datasets used in the study. The factors were identified based on previous research. To create landslide, flood, and seismic hazard maps, the analytical hierarchy process (AHP) provided the final weights of considered factors lithology, distance from active faults, slope, precipitation, land use, distance from roads, and distance from streams, elevation, hydro-lithology, arias intensity, and magnitude. AHP was used to assess the relative importance of the three geo-hazard maps, as well as a sensitivity analysis to account for uncertainties. As a result, a multi-hazard map was created, and the study area's existing urban areas and infrastructure were layered to create a basic suitability map. Engineers, planners, and local governments will find the suitability map beneficial in spatial planning and natural hazard management, according to the study's findings.

Tate et al., (2010) performed integrated multi-hazard mapping in Charleston, South Carolina, which is located in the United States. The primary purpose of the US Disaster Mitigation Act of 2000 was to reduce the increase in disaster losses by emphasizing a proactive approach focusing on pre-disaster hazard mitigation rather than post-disaster relief. The study's approach included data collecting and preprocessing of input data, as well as hazard impact measurement utilizing historical SHELDUS data and social vulnerability measurement for social vulnerability maps. GIS was used to create the multi-hazard vulnerability map. The study's output serve as a tool for hazard mitigation planning as well as improving the implementation of focused effect reduction techniques.

Hasalanka et al., (2019) developed a methodology for generating a multi-hazard map in order to recognize natural risks that threaten the safety of Sri Lankan hospitals. This study developed detailed and regional hazard maps based on historical data using ArcGIS. Exposure maps were developed by overlaying hospital layers on developed hazard maps (landslide, Tsunami and

flood hazard maps). The developed maps will be useful in improving the structural stability of the buildings, hazard mitigation planning, etc.

Ristya et al., (2020) applied GIS for multi-hazard mapping in Cisolok Village, Indonesia to identify hazard prone areas as Cisolok Village has potential of hazards. Based on previous research, distance from river, slope, altitude was selected as variables for flood, landslide and Tsunami hazard mapping. A multi-hazard map was created by overlapping these individual hazard maps and spatial analysis was implemented to describe the distribution of flood, landslide, and tsunami hazard and prone areas. The result of the study will help in developing hazard mitigation plans.

Mahendra et al., (2011) assessed and managed coastal multi-hazard vulnerability along the Cuddalore-Villupuram, east coast of India using geospatial approaches. Shoreline change rate, sea level rise rate, historical storm surges, and high resolution topography were used in this study with the help of Remote Sensing and GIS tools. The multi-hazard zone was created by combining all of these factors, and a multi-hazard vulnerability map (MHVM) was created by overlaying the multi-hazard areas on the base maps, and risk maps were created by intersecting land use, transportation, and structural information with the MHVM. The maps obtained will be useful in providing important information for the evacuation process and developing a management strategy during a disaster. They can also be utilized in the planning of a new facility and for insurance purposes.

van Westen et al., (2002) performed multi-hazard risk assessment using GIS in Turrialba, Costa Rica with an aim to local emergency commission and the municipality. In this study, seismic, flood and landslide hazards were analyzed. Orth photo-map, Digital Elevation Model (DEM), a slope steepness map, pseudo anaglyph image, lithological map, fault map, earthquake catalog and soil type map were data generated and collected for this study. Also, historical information on hazards was given emphasis. Based on historical information and data generated, flood, seismic and landslide hazard maps were generated for different return periods. Combining the cadastral database of the city and prepared hazard maps, vulnerability map was obtained, and combination of vulnerability and cost map was used to generate risk map. The resulting maps can be used as tools to determine the effect of certain mitigation measures.

2.6.2 Analytical Hierarchy Process

The Analytical Hierarchy Process (AHP) is a semi-quantitative decision-making procedure in which weights are employed to do pairwise relative comparisons with no inconsistencies (Saaty, 1980). There are five steps in the AHP:

- i. dividing a decision making problem into component factors;
- ii. ranking these factors;
- iii. assigning numerical values based on the relative importance of each factor (pairwise comparison);
- iv. constructing a comparison matrix; and
- v. computing the normalized principal eigenvector, which provides the weight of each factor (Saaty and Vargas, 2001).

To summarize, (a) breakdown, (b) comparison judgment, and (c) normalized weight assignment are the three main principles of AHP (Malczewski, 1999). The pair-wise comparison is used in AHP analysis to determine the priority within factors of the individual matrix by comparing the relative relevance, preference, or likelihood of two factors with respect to another factor (Saaty, 1994). A scale from 1 to 9 is used to compare the factors, with 1, 3, 5, 7, and 9 indicating equal, moderate, strong, very strong, extreme relevance, and intermediate values were assigned to 2, 4, 6, and 8, while less relevant variables were assigned to values ranging from 1 to 1/9 as illustrated in Table 2-2. The AHP's main feature is that it allows you to rate inconsistencies using the consistency index (CI), as seen below:

$$CI = \frac{(\lambda_{max} - n)}{(n - 1)}$$

Where, λ_{max} is the matrix's largest Eigen value of order n.

Saaty, 1980 suggested a consistency ratio (CR) to analyze and eliminate any inconsistencies in the judgment matrix and for various matrix ordering, developed an average random consistency index (RI). The following is done to assess CR:

$$CR = \frac{CI}{RI}$$

When CR is less than 0.1, weighting factors are acceptable; however, when CR is greater than 0.1, the matrix is inconsistent, and judgment should be modified to validate realistic results, according to Saaty, (1990).

Table 2-2: Random Consistency Index (RI) (Source: Saaty, 1980, 2000)

n	1	2	3	4	5	6	7	8	9	10	11	12	13	14	15
RI	0	0	0.58	0.9	1.12	1.24	1.32	1.41	1.45	1.49	1.51	1.53	1.56	1.57	1.59

2.7 Climate Change

Climate change is defined as the changes in climatic conditions that may be discovered (for example, using statistical tests) by variations in the mean and/or variability of its attributes over time, usually decades or more, according to the IPCC 2007 Synthesis Climate Change Report. Climate change includes both global warming induced by human-generated greenhouse gas emissions and the consequent large-scale weather pattern adjustments.

Global warming is primarily caused by the production of greenhouse gases, the majority of which are carbon dioxide (CO₂) accounting for more than 90% and methane. Fossil fuel burning (coal, oil, and natural gas) for energy consumption is the dominant source of these emissions, with contributions from agriculture, deforestation, and manufacturing. Humans are the cause of climate change, according to any scientific organization of national or international status. Climate feedbacks such as the loss of sunlight-reflecting snow and ice cover, rising water vapor (a greenhouse gas), and changes to land and ocean carbon sinks all contribute to the acceleration or slowed rate of temperature rise.

According to the Intergovernmental Panel on Climate Change's fourth Assessment Report (IPCC, 2007), carbon dioxide concentrations in the atmosphere rising from 278 parts per million before the pre-industrial level to 379 parts per million in 2005, and world temperature increased by 0.74°C over the last century. Climate change will have far-reaching consequences for the environment, as well as the socioeconomic and linked sectors, including water resources, agriculture and food security, human health, terrestrial ecosystems and biodiversity, and coastal zones (UNFCCC, 2007). The global averaged paired land and ocean surface temperature data, as computed by a linear trend, reveal a rise of 0.85 [0.65 to 1.06] °C from 1880 to 2012, according to the IPCC's Fifth Assessment Report. On a worldwide basis, ocean warming is greatest at the surface, with the upper 75 meters increasing by 0.11 [0.09 to 0.13] degrees Celsius every decade from 1971 to 2010.

Climate change impacts and adaptation Climate change (CC) has been labeled a "wicked problem" since it is defined by plenty of unforeseen problems (Dixit, 2009). Because of the

small number of scientific research undertaken in this region, including Nepal, the IPCC's Fourth Assessment Report identified this region as a "white spot" (IPCC, 2007). Droughts, storms, floods, inundation, landslides, debris flow, soil erosion, and avalanches are all common water-induced disasters and hydro-meteorological extreme events in Nepal, which is one of the most vulnerable country to climate change (MoHA, 2017). Climate-related disasters accounted for about 25% of deaths, 84% of individuals adversely impacted, and 76% of financial losses according to data over the last three decades (MoHA, 2009).

From 1971 to 2005, the average temperature in Nepal rose at a regular and continuous pace of 0.05°C per year, according to the Department of Hydrology and Meteorology (DHM). Between 1975 and 2005, the maximum temperature rose by 0.06°C each year, while the lowest temperature increased by 0.03°C per year (Marahatta et al., 2009). According to Nepal's second communication report (MoSTE, 2014), the country's overall seasonal maximum temperature is discovered to have the largest rise of 3.4°C in spring and smallest increase of 3.3°C in summer, whereas the minimum temperature in the country is found to have the largest increase of 5.4°C in winter and smallest increase of 3.4°C in summer by the end of the 21st century. Nepal receives nearly 80% of its annual rainfall during the months of June-September (Manandhar et al., 2011). Nepal's annual average rainfall is increasing by 13mm, although the number of wet days is falling by 0.8 days every year. A study of monsoon rainfall from 1971 to 2005 found a linear increasing trend of roughly 2.08mm/year with significant inter-annual variance (Baidya et al., 2008).

2.7.1 Climate Models

Climate models are mathematical representations of the climate system that are based on physical, biological, and chemical concepts. Climate models are used to forecast future climate. The climate model is composed of the following components.

- i. Atmosphere: The physical and chemical processes occurring in the atmosphere are explained with their overall systematic transport of mass and energy.
- ii. Ocean: The key features of ocean models are explored and their connection with the atmosphere is also highlighted.
- iii. Sea ice: The effect of sea ice on the climatic variations and climatic processes are explained.

- iv. Land surface: The land surface processes including the anthropogenic influences are presented.
- v. Marine biogeochemistry: Its implication for the ocean dynamics is explored with climate change in focus.
- vi. Ice sheets: Their importance in climate processes are taught.
- vii. With an emphasis on the system dynamics, the linkage between the constituents of the Earth system models is explained.

Various types of climate models that are in practice are briefly described hereunder.

i. Energy Balance Models (EBMs):

Energy balance models, as its name implies, estimate changes in the climate system based on an examination of the Earth's energy budget. They don't have any explicit spatial dimension in their most basic form, offering simply globally averaged values for the computed variables. As a result, they are termed to as zero-dimensional models.

ii. Radiative Convective (RC) Models:

Under the assumption of radiative–convective equilibrium, a form of climate model that simulates the vertical profile of atmospheric temperature. These models are capable of advanced radiative transfer treatments, making them useful for theoretical studies of climate sensitivity. They frequently overlook the impacts of horizontal transportation.

iii. Statistical Dynamical (SD) Models:

These are two-dimensional models with a vertically resolved atmosphere that explicitly deal with surface processes and dynamics in a zonally averaged framework. The chemistry of the stratosphere and mesosphere is simulated using SD models.

iv. Global Climate Models (GCMs):

It makes use of a mathematical model of a planet's atmosphere or ocean's overall circulation. It uses the Navier–Stokes equations with thermodynamic terms for various energy sources on a spinning sphere (radiation, latent heat). Computer programs that model the Earth's atmosphere or oceans are based on these equations. The model includes both atmospheric and oceanic GCMs (AGCM and OGCM), respectively.

v. Regional Climate Models (RCMs):

A regional climate model (abbreviated RCM) is a numerical climate forecast model that accounts for high-resolution topographical data, land-sea contrasts, surface features, and other Earth system components while simulating atmospheric and land surface processes. Specific lateral and ocean conditions from a general circulation model (GCM) or observation-based dataset are used to drive it. Because RCMs only cover a limited domain, the values at their limits, referred to as boundary conditions, must be clearly indicated by the findings of a coarser GCM or reanalysis.

The main disadvantage of RCMs is that they are equally as computationally demanding as GCMs, and the boundary conditions used to start trials (such as soil moisture) have an impact on the scenarios created by RCMs. RCMs have the advantage of being able to resolve smaller-scale atmospheric characteristics such as relief precipitation and low-level jets better than the host GCM. RCMs can also be used to assess the relative importance of different external forcing's; such as changes in terrestrial-ecosystem or atmospheric chemistry.

vi. Earth System Models (ESMs):

Earth system models (ESM) try to replicate all key aspects of the Earth system that are important. They are significantly more comprehensive than their predecessors, global climate models (GCMs), which solely represented physical atmospheric and oceanic processes as they incorporate physical, chemical and biological processes. In reality, variables other than the physical processes that have traditionally been examined have an impact on the climate system (such as winds, clouds, land surface, oceans and ice). Because they are involved in physical reactions and interactions with biological components of the Earth system, which are closely linked to climate change, man-made emissions have an impact on greenhouse gas and aerosol concentrations.

vii. Integrated Assessment Models (IAMs):

IAMs are mathematical computer models that are built on explicit assumptions about the behavior of the represented system. An IAM's strength is its capacity to calculate the consequences of various assumptions and to interrelate multiple parameters at the same time. Integrated assessment models (IAM) try to provide policy-relevant insights into global environmental change and sustainable development concerns by providing a quantitative description of fundamental processes in the human and earth systems, as well as their interactions.

2.7.2 Climate Scenarios

Scenarios are plausible combinations of variables consistent with what we know about human-induced climate change. Climate change scenarios with varying rates and magnitudes provide a foundation for assessing the risk of crossing identified thresholds in both physical change and biological and human system impacts. They depict the disparity between today's climate and the climate of the future. Each scenario starts with a certain radiative forcing forecast and then makes assumptions about future population, GDP, energy demand, and so on. Working with scenarios isn't about predicting the future; it's about better understanding uncertainties and alternate futures so you can think about how resilient various actions or solutions might be in a variety of scenarios. Climate scenarios are generally grouped into following classes (Chaumont, 2014):

- a. To generate probable futures, synthetic scenarios are created by altering a certain climate variable by a realistic but arbitrary amount.
- b. Analogue scenarios are created by identifying recorded climatic regimes that are similar to a region's projected climate.
- c. Climate model scenarios are created utilizing climate data generated by climate models that simulate the climate's future response to rising greenhouse gas concentrations.

The Intergovernmental Panel on Climate Change (IPCC) has created a set of scenarios based on greenhouse gas emissions extent, taking into account a coherent and internally consistent set of assumptions about the driving forces (such as technological change, demographic and socioeconomic development) and their key relationships (IPCC, 2007). Future emissions levels are ambiguous; therefore, scenarios offer different perspectives on how the future might turn out. Their range represents our current understanding and knowledge of underlying uncertainties, and as a result, it is liable to change when new data on the factors that drive them becomes available, and governments and the global population make decisions that affect emissions. The details regarding different types of scenarios is discussed in following section.

i. Special Report on Emission Scenarios (SRES):

The Intergovernmental Panel on Climate Change (IPCC) published its Special Report on Emissions Scenarios (SRES) in 2000, which described four different scenario families. The four families of alternative futures have been developed, each of which contains 40 SRES scenarios that cover a wide variety of possibilities. Each scenario was based on an integrated relationship between the socioeconomic forces driving greenhouse gas and aerosol emissions

and the levels to which those emissions would increase during the 21st century, and was referred to by letter-number combinations such as A1, A2, B1, and B2. The SRES scenarios cover a wide range of emissions of all significant greenhouse gas (GHG) and sulfur species, as well as their driving forces.

ii. Representative Concentration Pathways (RCPs):

These are the new driving emission scenarios that will be used as input to climate models in Coupled Model Inter-comparison Project Phase 5 (CMIP5), which will serve as the foundation for the IPCC's Fifth Assessment Report. RCPs are time- and space-dependent trajectories of greenhouse gas and pollutant concentrations resulting from human activities such as land use changes. RCPs provide a quantitative depiction of climate change pollutants' atmospheric concentrations through time, as well as their radiative forcing in 2100. The concept is that a wide range of socioeconomic and technological development scenarios can result in any particular radiative forcing pathway. RCP8.5, RCP 6.0, RCP4.5, and RCP2.6 are the four pathways. Table 2-3 shows the details of these four RCPs.

Table 2-3: Characteristics of RCPs (Source: van Vuuren et al., 2011)

Name	Radiative forcing	CO₂ equiv (p.p.m.)	Temp anomaly (°C)	Pathway	Description of RCP
RCP 8.5	8.5 W/m ² in 2100	≥1370	4.9	Rising	This RCP is characterized by a gradual increase in greenhouse gas emissions
RCP 6.0	6 W/m ² post 2100	~850	3.0	Stabilization without overshoot	It's a stabilization scenario in which total radiative forcing is stabilized shortly after 2100, with no overshoot, using a variety of technologies and tactics to reduce greenhouse gas emissions.
RCP 4.5	4.5 W/m ² post 2100	~650	2.4	Stabilization without overshoot	Stabilization scenario: Total radiative forcing stabilizes shortly after 2100, without overshooting the long-run radiative forcing target level.

Name	Radiative forcing	CO ₂ equiv (p.p.m.)	Temp anomaly (°C)	Pathway	Description of RCP
RCP 2.6 (RCP3PD)	3 W/m ² before 2100, declining to 2.6 W/m ² by 2100	~490	1.5	Peak and decline	By mid-century, its radiative forcing level had risen to roughly 3 W/m ² , before falling to 2.6 W/m ² by 2100 reducing greenhouse gas emissions substantially over time

iii. Shared Socioeconomic Pathways (SSP):

SSPs are societal change scenarios established by members of several research communities, such as futures studies, integrated assessment modeling (IAM), and Impacts, Adaptation, and Vulnerability (IAV). The SSPs (Riahi et al., 2017) depicted in Figure 2-1 and defined in Table 2-4 explain sustainable development, regional competitiveness, inequality, fossil-fueled development, and middle-of-the-road development..

The new SSPs provide five possible paths for the world. Their main purpose is to offer an internally consistent logic of the fundamental causal links, as well as a description of trends that are difficult to explain using models. In this regard, the SSP tales are a valuable addition to the quantitative model projections. The narratives provide significant context for a broad user group to better understand the foundation and meaning of the quantitative SSP projections by highlighting major socioeconomic, demographic, technological, lifestyle, policy, institutional, and other trend (Riahi et al., 2017).

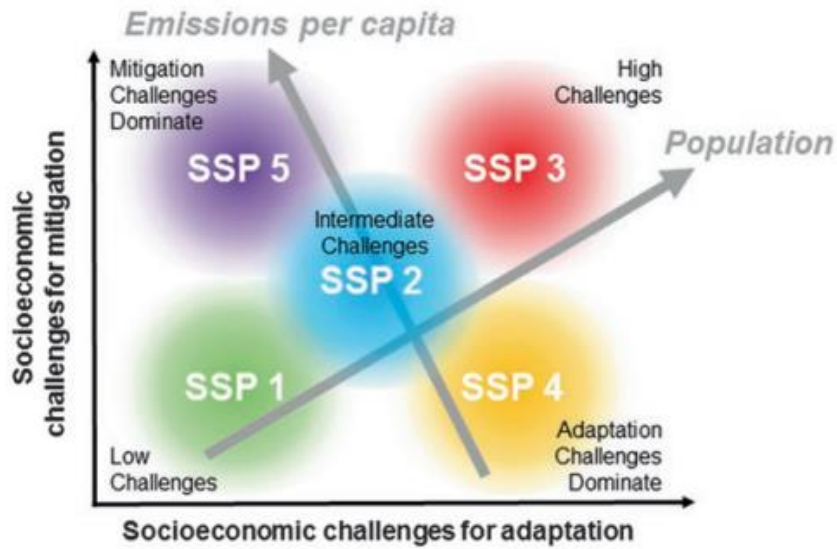


Figure 2-1: SSP narratives framework (Source: O’Sullivan et al., 2018)

Table 2-4: Type of SSPs and their short description (Source: Riahi et al., 2017)

SSP Type	Challenges	Description
SSP1	Low for mitigation and adaptation	Respecting environmental boundaries, managing health and educational investments, reducing inequality, focusing human well-being and economic progress, and employing lower energy intensity are all examples of sustainable development.
SSP2	Medium to Mitigation and adaptation	Vulnerability to societal and environmental challenges, difficulty in achieving sustainable development goal, environment degradation, energy intensity uses declines.
SSP3	High for mitigation and adaptation	Unmitigated emissions are high due to medium economic growth, a fast growing population, and gradual technology advancement in the energy industry, making mitigation difficult. Human capital investment is low, inequality is high, a regionalized globe leads to weaker trade flows, and institutional development is unfavorable, leaving millions of people vulnerable to climate change and many parts of the world with limited adaptation capacity.
SSP4	High for adaptation, low for mitigation	A composite world, with relatively rapid advances in technology in low-carbon sources of energy in major emitting countries, leading to relatively high mitigation capability in places where global emissions were most significant. Other regions, on the other hand, are still developing slowly, have high levels of

SSP Type	Challenges	Description
		inequality, and are economically isolated, rendering them particularly vulnerable to climate change and with limited adaptive potential.
SSP5	High for mitigation, low for adaptation	In the absence of climate policies, energy demand is high, and carbon-based fuels meet the majority of this demand. Alternative energy technology expenditures are limited, and mitigation options are far and few. Nonetheless, economic growth is rapid, and it is fueled by huge human capital investments. Improved human capital results in more equal resource distribution, stronger institutions, and slower population growth, resulting in a world that is less sensitive to climate change and better prepared to react.

2.7.3 Downscaling of Climate Projections

Climate change scenarios derived directly from GCM development are insufficient in terms of spatial and temporal resolution for many climate change research. Because of the spatial resolution of GCMs, the depiction of orography and land surface characteristics, for example, is much simpler than in reality, resulting in the loss of some of the characteristics that may have significant influences on regional climate. RCMs that employ the GCM as boundary conditions for the simulated regions can be used to downscale to the catchment scale.

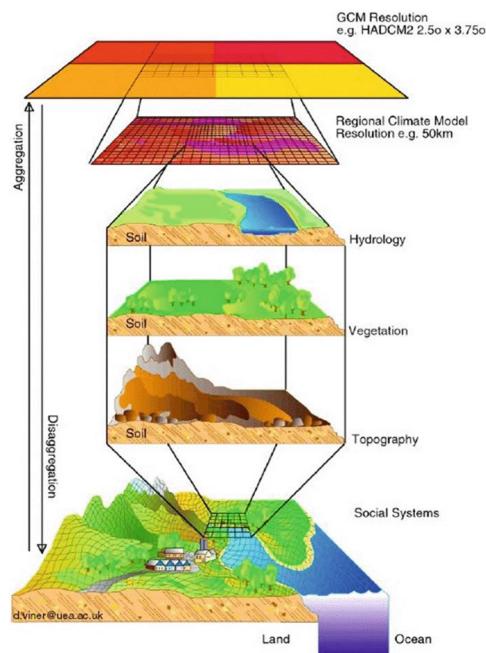


Figure 2-2: Process of downscaling (Viner, 2012)

Several techniques for producing regional GCM-based scenarios at the sub-grid scale, known as "regionalization" or "downscaling," have been used.

i. Dynamic (nested model) downscaling

A higher resolution Regional Climate Model (RCM) is nested within a coarser resolution Global Climate Model in the process of dynamical downscaling (GCM). The RCM use the GCM to generate time-varying atmospheric boundary conditions around a bounded domain, where the physical dynamics of the atmosphere are modeled using horizontal grid spacing's of 20–50 km. Despite recovering significant regional-scale features that are underrated by coarse-resolution GCMs, RCM outputs are however prone to systematic errors, necessitating bias correction and subsequent downscaling to a higher resolution.

ii. Statistical downscaling

In statistical downscaling, a statistical relationship is constructed between historic observed climate data and the output of the climate model for the same historical era. The relationship is being used to create future climate data. It can generate site-specific climate projections, whereas RCMs cannot because they are computationally constrained to a spatial resolution of 20-50 kilometers (Cafferey & Farmer, 2014).

2.7.4 Bias Correction

Climate model estimates of precipitation and temperature in the control period rarely fit exactly those of observations in the same period, such inaccuracies may have an impact on future simulated flow outcomes (Soriano et al., 2019). To eliminate biases from the obtained projected data, bias correction approach is used (Salzmann et al., 2007). Bias correction is the process of adjusting modeled values to match the observed distribution and statistics. It uses differences in the mean and variability between GCM and observations in a reference period to correct the projected raw daily GCM output.

Some of the methods of bias correction with its advantage and disadvantage are tabulated in Table 2-5.

Table 2-5: Bias correction methods (Source : Chen et al., 2013)

S.N.	Methods	Advantage	Disadvantage
1.	Linear Scaling (LS)	Mean-based The RCM simulated monthly rainfall is corrected using a mean monthly correction factor. It is the most basic way of bias correction	<ul style="list-style-type: none"> • The RCM simulated data is same as that of daily rainfall sequence (usually too many wet days compared to the observation). • It does not take into consideration the various changes in rainfall frequency distribution. • There is no change to the daily rainfall occurrence's temporal pattern..
2.	Local intensity scaling (LOCI)	Mean-based The frequency of wet days has been corrected. The RCM-simulated daily rainfall in a month is corrected using a mean monthly correction factor.	<ul style="list-style-type: none"> • It does not take into consideration the various changes in rainfall frequency distribution • There is no change to the daily rainfall occurrence's temporal pattern.
3.	Daily translation (DT)	Distribution method The frequency distribution of RCM simulated daily rainfall is corrected using various correction factors (differences in percentiles between observed and RCM simulated data at the calibration period).	<ul style="list-style-type: none"> • The RCM simulated data is same as that of daily rainfall sequence (usually too many wet days compared to the observation). • There is no change to the daily rainfall occurrence's temporal pattern.
4.	Daily bias correction (DBC)	Distribution method Combines the DT and LOCI techniques to account for the various changes in daily rainfall frequency distributions and corrects the wet-day frequency of rainfall.	<ul style="list-style-type: none"> • There is no change to the daily rainfall occurrence's temporal pattern.
5.	Quantile mapping based on an empirical distribution (QME)	Distribution method Corrects RCM rainfall simulations using point-by-point daily generated empirical cumulative distribution functions (ecdfs). At the same time, the frequency of rainfall occurrence is corrected.	<ul style="list-style-type: none"> • There is no change to the daily rainfall occurrence's temporal pattern.
6.	Quantile mapping based	Distribution method	<ul style="list-style-type: none"> • The performance is determined by whether the

S.N.	Methods	Advantage	Disadvantage
	on a gamma distribution (QMG)	Based on a gamma distribution, corrects the RCM-simulated rainfall. The LOCI method is used to correct the frequency of rainfall occurrence.	rainfall observed and simulated by the RCM follows the gamma distribution (or not). <ul style="list-style-type: none"> • There is no change to the daily rainfall occurrence's temporal pattern.

3 Materials and Methods

3.1 Study Area

3.1.1 Location

The watershed of Khimti Khola is taken as study area and it is located in Ramechhap and Dolakha district of Nepal. It is bounded by latitudes 27°33'39" N to 27°45'51" N and longitudes 86°14'53" E to 86°25'03" E and extends for 237.00 km². Out of total catchment area about 40.9% of the area comes under Ramechhap district and the remaining 59.1% comes under Dolakha district.

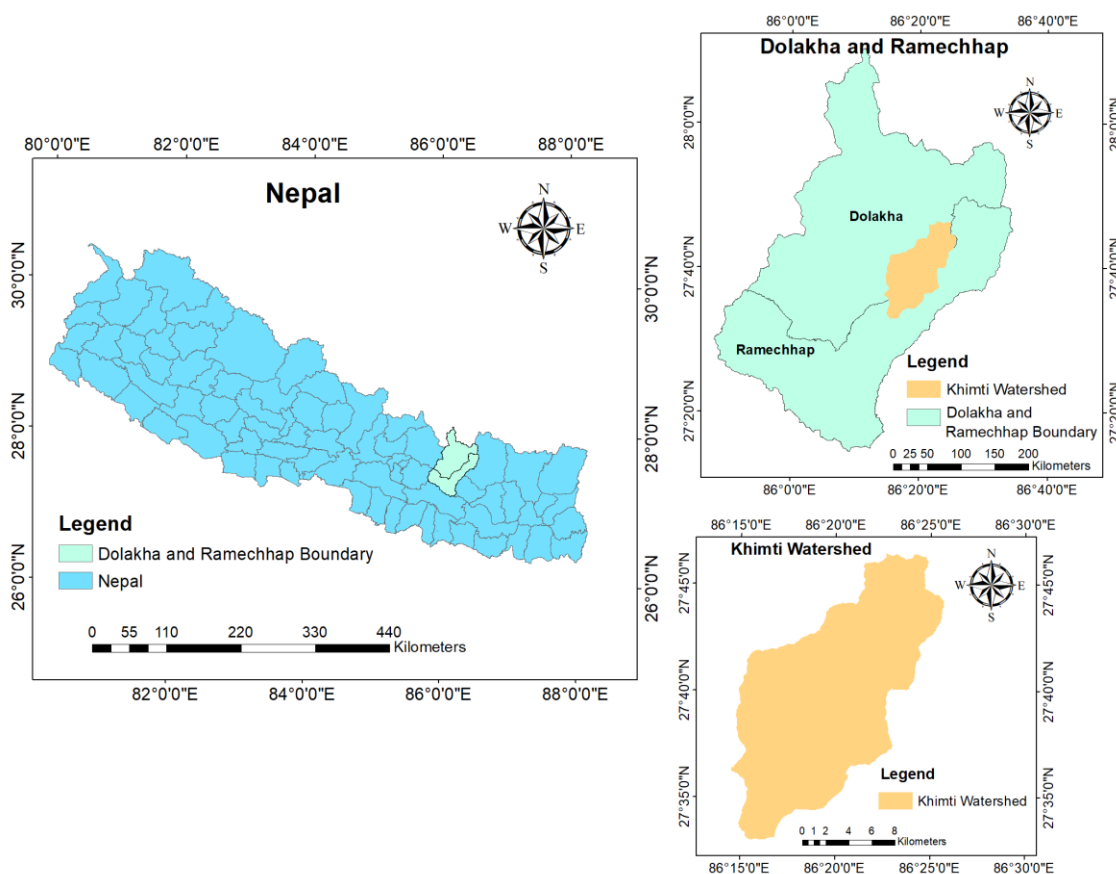


Figure 3-1: Location of the study area

3.1.2 Topography

The Khimti river watershed lies in Mid-hills of Eastern Nepal. The study area's elevation varies from 1698 to 5449 meters above mean sea level (masl). Khimti Khola is a perennial river and is partly fed by snow. It is one of the tributaries of Tamakoshi River which is the major river in the Koshi Basin. Khimti Khola after originating from an elevation of about 5230 masl flows in south-west direction and mixes with Tamakoshi River. Khimti Khola basin is confined by Rolwalin Khola to the North, Likhu Khola to the east and Tamakoshi River to the west. A 30 x 30m resolution Shuttle Radar Topography Mission (SRTM) Digital Elevation Model (DEM) was derived from the USGS (United States Geological Survey, <https://earthexplorer.usgs.gov/>). The Digital Elevation Map of the basin is presented as Figure 3-2. A Digital Elevation Model (DEM) is a digital model or three-dimensional depiction of a terrain's surface created using elevation data. The elevations of the earth's surface, as well as the location of natural and associated features, are determined using DEM data.

SRTM and Advanced Space-borne Thermal Emission and Reflection Radiometer (ASTER) DEMs with a resolution of 30m are widely available in Nepal. The use of ASTER 30m DEM in this study was accompanied by series of error while processing in ArcMap which made selection of SRTM DEM more reliable.

3.1.3 Hydro-Climate Characteristics

Data at one hydrological station (Table 3-1) and two meteorological stations (Table 3-2) were collected from Department of Hydrology and Meteorology (DHM) for hydro-meteorological characterization. Details about the Khimti watershed's hydrological and meteorological stations is presented in Table 3-1 and Table 3-2 and their location is shown in Figure 3-2. Missing data for precipitation was estimated using Normal ratio method while missing data for other variables such as temperature, was done using mean substitute method (long term average of that particular day).

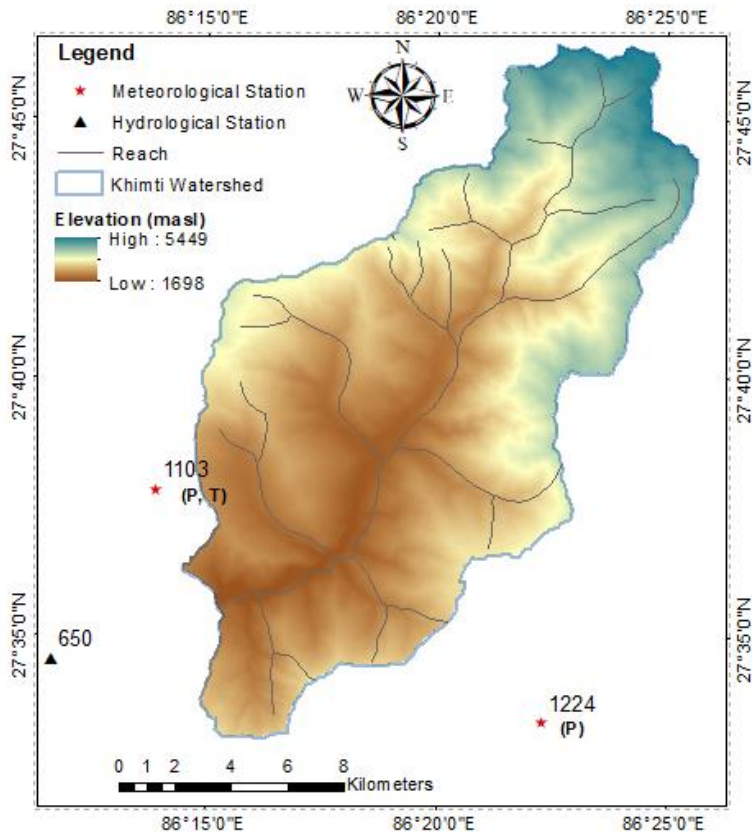


Figure 3-2: Topography, river network and location of hydro-meteorological stations in the khimti watershed

Table 3-1: Details of hydrological station used in this study

Station No.	Location	Co-ordinate		Elevation (m)	Area (Km ²)	Record	
		Latitude	Longitude			Length	Period
650	Rasnal	27° 34' 30"	86° 11'	1120	325.46	27	1980-2006

Table 3-2 : Details of meteorological stations used in this study

Station No	Name	District	Measuring type	Latitude	Longitude	Elevation (m)
1103	Jiri	Dolakha	Agro meteorology	27.63	86.23211	1877
1224	Sirwa	Solukhumbu	Precipitation	27.55	86.38	1662

3.1.4 Land Use/Cover Types

The 30 m resolution land use/cover (LULC) data required for this study was derived from ICIMOD's regional database and clipped for Khimti watershed. The Khimti watershed has seven generic LULC types listed in Table 3-3. A map with spatial distribution of LULC types in the Khimti is shown in Figure 3-3. Forest is the most prevalent LULC type in the Khimti watershed, accounting for 65.8% of the total watershed area.

Table 3-3: Land use/cover types in the study area

S.N.	Land use	Area (km ²)	Area (%)
1.	Snow/glacier	1.1	0.5
2.	Forest	156.1	65.8
3.	Agriculture area	34.3	14.5
4.	Shrub land	4.2	1.8
5.	Grassland	33.9	14.3
6.	Barren area	7.6	3.2
	Total	237.0	100

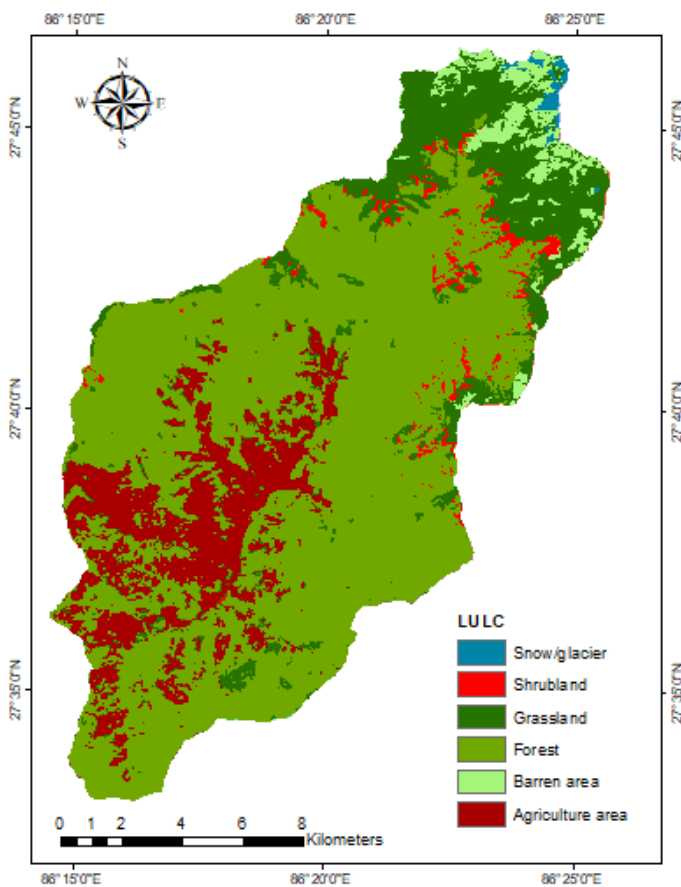


Figure 3-3: Land use/cover (LULC) in khimti watershed (source: prepared based on data from ICIMOD, 2010)

3.2 Identification of Hazards and Indicators

Three major types of hazards namely flood, landslide and seismic hazards are adopted for this study based on literature review and prevalence of such hazards in the study area. A landslide hazard map depicts the likelihood of landslides occurring in the study area. The chances of study area to become flooded is given by flood hazard map. Similarly, Seismic hazard maps represent areas that are in high risk to earthquake occurrences. To identify each hazards, a set

of indicators were identified through literature review (Devkota et al., 2013; Sarchani et al., 2020; Thapa and Guoxin, 2013) and data suitability and availability. Each individual hazard was mapped separately based on selected contributing factors and is described in the following sub-sections. Individual hazard maps were obtained, which were then aggregated using appropriate weights to create a multi-hazard map.

In Table 3-4, the indicators utilized for various hazard assessments are listed.

Table 3-4: Data layer source for different hazard assessment

Indicator	Landslide effective factor	Flood effective factor	Earthquake effective factor	Future climate projection
Precipitation	-	✓	-	✓
Temperature	-	-	-	✓
Inundation Depth	-	✓	-	-
Land Use/Cover	✓	✓	✓	-
Discharge	-	✓	-	-
Settlement	✓	✓	✓	-
Geology	✓	-	-	-
Distance From road	✓	-	-	-
Distance From stream	✓	-	-	-
Slope Aspect	✓	-	-	-
Lineament Density	✓	-	-	-
Slope Gradient	✓	-	-	-
Relative Relief	✓	-	-	-
Curvature	✓	-	-	-
Stream Power Index	✓	-	-	-
Topographic Wetness Index	✓	-	-	-
Earthquake Catalogue	-	-	✓	-
Historical and Projected Precipitation and Temperature	-	-	-	✓

The indicators for each hazard were quantified either using statistical method or using model simulation as indicated in Table 3-5.

Table 3-5: Hazard estimation approaches used in this study

Hazard Type	Indicator	Statistical Method	Simulation based evaluation
Landslide hazard	LULC, Geology, SPI, TWI, Lineament density, Slope gradient, Aspect, curvature,	✓	-

Hazard Type	Indicator	Statistical Method	Simulation based evaluation
	relative relief, Distance from stream and road		
Flood hazard	Inundation depth	-	✓
Seismic hazard	Ground acceleration	-	✓

3.3 Framework for Landslide Hazard Mapping

A customized indicator-based framework with 11 indicators, and an index was selected based on review of literature, suitability to the study area, and availability of data. The indicators and their logical link with the landslide hazard are shown in Table 3-6.

Table 3-6: Selected indicators for landslide hazard mapping

Indicators	Definition	Logical link to landslide hazard	References	Functional relationship
Slope Gradient	Inclination of land surface to horizontal plane	Shear stress in soil increases with increase in slope gradient making it susceptible to failure	(Javier et al., 2019; Khan et al., 2019; Lee et al., 2006; Nepal et al., 2019)	↑↓
Slope Aspect	It represents slope direction	Controls slope's meteorological and hydrological processes	(Javier et al., 2019; Khan et al., 2019; Lee et al., 2006; Nepal et al., 2019)	↑↓
Curvature	Shape of slope	Water storage depends upon shape of slope affecting landslide occurrence	(Javier et al., 2019; Lee et al., 2006; Sujatha et al., 2014)	↑(Concave)
				↑(Flat)
				↓(Convex)
Lineament Density	Ground features are known as lineaments	Features of rock mass contributes to its resistance to erosion	(Akgun et al., 2010; Mondal et al., 2019)	↑↓
Geology	Represents the study area's geological features	Determines nature and intensity of landslides	(Khan et al., 2019; Lee et al., 2006; Nepal et al., 2019; Yilmaz et al., 2009)	↑↓

Indicators	Definition	Logical link to landslide hazard	References	Functional relationship
Distance From Road	Represents road proximity to slope	Road construction causes destabilizing of slope	(Javier et al., 2019; Khan et al., 2019; Regmi et al., 2014a)	↓
Distance From Stream	Represented by river proximity in area	Rivers erode the slope's base and saturate the slope's underwater area, resulting in landslides	(Javier et al., 2019; Khan et al., 2019; Lee et al., 2006)	↓
Relative Relief	Within a particular area, the difference between the maximum and minimum elevations	High relative relief in an area indicates high slope making susceptible for landslide	(Basu et al., 2019; Pachauri et al., 1992; Acharya et al., 2019)	↑↓
Stream Power Index	Measure's erodibility of a stream	Affects the area's stability	(Yilmaz et al., 2009; Regmi et al., 2014b; Devkota et al., 2013)	↓
Topographic Wetness Index	Predicts where water will accumulate in an area with different altitudes	Decrease in soil strength due to water infiltration into slope	(Yilmaz et al., 2009; Regmi et al., 2014b; Devkota et al., 2013)	↑↓
Land Use/Cover	It describes the actual land surface as well as human land use	Landslide susceptibility is different for different land use types	(Javier et al., 2019; Khan et al., 2019; Lee et al., 2006; Nepal et al., 2019)	↑↓

Details of each layers/indicators, and methods to quantify them are elaborated in following sub-chapters and they are illustrated in Figure 3-4.

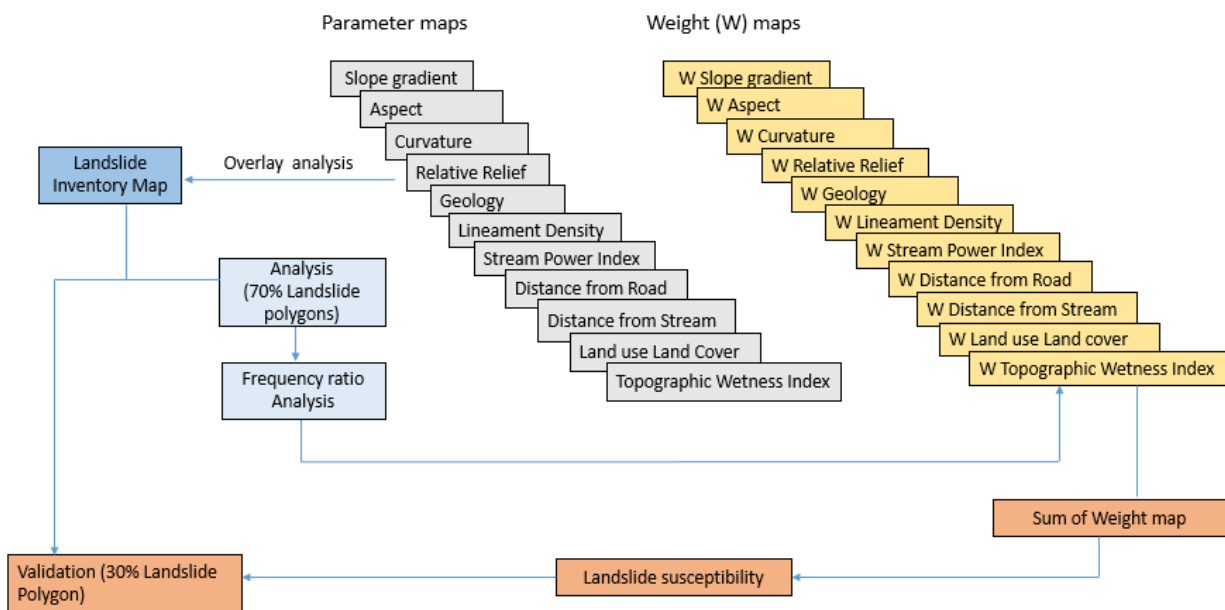


Figure 3-4: Process involved in preparing landslide hazard map

Based on a survey of the literature, a number of geological, topographic, and other important factors linked individually and in combination with the occurrence of landslides were chosen. As a result, eleven parameters were considered for this study: slope gradient, slope aspect, lineament density, distance from road, distance from stream, stream power index (SPI), topographic wetness index (TWI), curvature, relative relief, land use land cover, and geology. Because the majority of landslides occur near highways and river banks, distance from the road and the stream were included as conditioning factors. Because topography affects the spatial distribution of soil moisture, topographic indices such as SPI and TWI were considered. Type of land pattern and geology greatly influence landslides. The details regarding each factor are discussed in the succeeding sections. Series of factor maps were prepared along with landslide inventory map which represent past landslide and based on weight of individual factor map, landslide susceptibility map was prepared.

After quantifying each indicator and their spatial distribution are mapped, they are aggregated together in the form of index using weighted-overlay methods. Indicator values were reclassified appropriately before aggregating. Weights could also be differential, but we have adopted equal weights to each layer, as assigning more importance to one indicator to another was the most challenging thing.

Finally, a landslide hazard map was created by categorizing the landslide hazard index value into four categories: low, medium, high, and very high. By overlaying the hazard map with landslide inventory maps, the hazard map was validated.

3.3.1 **Landslide Inventory**

The landslide inventory map shows where previous landslides have occurred in the watershed. Gathering information on prior landslides is the first and most important phase in landslide susceptibility study (Chacón et al., 2006). Because historical and present landslide occurrences are critical to future spatial prediction, a landslide inventory map is required for such a study (Guzzetti et al., 1999). Furthermore, a landslide inventory map provides vital information for analyzing landslide hazards or risk on a regional scale for probabilistic landslide susceptibility analysis (Regmi et al., 2014a).

This landslide inventory map was created in Google Earth using a kml file of the study area generated by a GIS. Past landslides were mapped using polygons. The inventory map was then converted to raster format for processing in ArcGIS 10.2, with 70% of the recorded landslides being utilized for landslide susceptibility map development and the remaining 30% being used for map validation as used in other research (e.g., Acharya et al., 2019; Arabameri et al., 2019).

3.3.2 **Geology**

Geology describes the type of exposure that exists in a certain place. The physical, chemical, and engineering features of the rock types also influence landslide initiation and triggering. Based on their properties, different rock types have varying degrees of landslide risk.

From ICIMOD's Regional Database System, a geology map of Nepal prepared by the Department of Mines and Geology and digitized by ICIMOD was downloaded (<https://rds.icimod.org/Home/DataDetail?metadataId=2521&searchlist=True>). The acquired map was then processed in ArcGIS 10.2 using the DEM of the study area, and the geology map of the study area was clipped using the raster tool. Himal Group, Dware Kharka Schist, Himal Group, Himal Gneiss, Panglema Quartzite, Ghanapokhara Formation, Seti Formation, Ulleri Formation, and Kushma Formation were the nine geological groups studied.

3.3.3 Lineament Density

Lineaments are topographical or tonal linear features on the ground, as well as on photographs and maps, that may indicate a structural weakness region. Faults, cracks, and joints not only destabilize the area, but they also speed up weathering and reduce the strength of the rocks (Sujatha et al., 2014).

The lineament structures were generated using the hill shade tool in ArcGIS 10.2 from DEM of the study area. It operates by computing the azimuth values and determining the position of a hypothetical light source. Four hill shaded images were created for this study by merging 315 - 45, 200 - 50, 100 - 60, and 50 - 90. The spatial analyst tool in ArcGIS 10.2 was used to create the lineament density map from the lineament map. The density of lineaments was categorized into four categories: < 0.5, 0.5 - 1.0, 1.0 - 1.5, > 1.5.

3.3.4 Slope Gradient

Slope gradient refers to the angle of a land surface with respect to a horizontal plane, or its steepness. Increase in slope gradient induce an increase in shear stress in soil or other unconsolidated material, making it more prone to failure; thus, it is one of the most important parameter contributing to slope instability (Oh and Lee, 2011). Mass at a specific height will be more prone to falling or sliding as the slope angle increases. The slope largely determines the spatial distribution and intensity of landslides.

The slope gradient map was created using the spatial analyst tool in ArcGIS 10.2 from DEM of the study area. The slope value typically runs from 0 to 90. The slope was classified into five categories: < 15 °, 15 ° - 25 °, 25 ° - 35 °, 35 ° - 45 °, > 45 °.

3.3.5 Slope Aspect

The direction of maximum slope, or aspect, is related to the area's general physiographic tendency and/or the predominant precipitation direction (Duman et al., 2006). It has an impact on some hydrological processes including evapotranspiration, weathering, vegetation, and plant root growth, as well as meteorological events like rainfall and sunlight amounts, drying winds, and the morphological structure of the area (Yalcin, 2008; Galli et al., 2008). As a result, it has the potential to impact landslide initiation.

The slope aspect map was created using the spatial analyst tool in ArcGIS 10.2 from DEM of the study area. The slope aspect was divided into ten classes: Flat (-1), North (0 - 22.5), Northeast (22.5 - 67.5), East (67.5 - 112.5), Southeast (112.5 - 157.5), South (157.5 - 202.5), Southwest (202.5 - 247.5), West (247.5 - 292.5), Northwest (292.5 - 337.5), North (337.5 - 360).

3.3.6 Curvature

The geometry of a slope or curvature influences the direction and volume of surface runoff or lateral inflow that reaches a site. Because they concentrate water at the lowest point and contribute to the build-up of unfavorable hydrostatic pressure, concave slopes are potentially unstable. Since runoff is distributed more uniformly down the slope, convex slopes are more stable.

The curvature map was created using the spatial analyst tool in ArcGIS 10.2 using a DEM of the study area. The curvature was divided into three classes: Concave (< -0.05), Flat ($-0.05 - 0.05$), Convex (> 0.05).

3.3.7 Distance From Road

Modification of slopes in the course of road construction, such as uncontrolled or controlled blasting and widening of roadways, or loss of support owing to material removal from the toe, are the most common anthropogenic activities that cause slope instability problems (Sujatha et al., 2014). Road cuttings also expose joints and fractures in the rock, making it more vulnerable to landslides. In addition, depending on its location in the environment, a road section might act as a barrier, a net source, a net sink, or a corridor for water movement, and thus is usually a source of landslides (Pradhan and Lee, 2010).

The Nepal road network map was taken from (<https://data.humdata.org/dataset/nepal-road-network>), which was created by the Nepal Survey Department and combined by Humanitarian Data Exchange. The map was then processed in ArcGIS 10.2 with the DEM of the study area, and the road network map of the study area was clipped using the raster tool. The distance from the road map was created using the spatial analyst tool. The distance from road map was divided into three classes: 0 - 1000 m, 1000 - 2000 m, >2000 m.

3.3.8 Distance From Stream

In the study area, there are several landslides along riverbanks. The stability of a substance on a slope is determined by its saturation level, and proximity to streams is considered an aggravation factor because of its contribution to saturation. Streams gradually erode the banks in normal conditions, but this accelerates during floods, triggering landslides through toe cutting (TU-CDES, 2016).

The flow accumulation map obtained from the DEM of the study area and used to create the stream network map in ArcGIS 10.2. The distance from the stream map was created using the spatial analyst tool. The distance from stream was divided into three classes: 0 - 1500 m, 1000 - 2500 m, > 2500 m.

3.3.9 Relative Relief

Relative relief refers to the difference in elevation between a morphological feature and the features around it. Soil characterization and related geomorphological processes on land are influenced by the context of a feature within a landscape and its surroundings.

The relative relief map was created in ArcGIS using focal statistics and raster tools from DEM of the study area. The relative relief was divided into four classes: 0 - 30 m, 30 - 49 m, 49 - 74 m, 74 - 254 m.

3.3.10 Land Use/Cover

Land use patterns can be used to determine slope stability and instability. The land use land cover map demonstrates the various types of land use patterns that can be found in the study region, as well as whether the terrain is natural or has been altered by anthropogenic activity and other natural processes. The area covered by forest maintains continuous water flow and ensures that water infiltrates on a regular basis, whereas cultivated land has an impact on slope stability due to saturated soil (Devkota et al., 2013).

The ICIMOD Regional Database System (<https://rds.icimod.org/Home/DataDetail?metadataId=9224&searchlist=True>) was used to obtain a land use and land cover map of Nepal. The acquired map was then processed in ArcGIS 10.2 using the DEM of the study area, and the LULC map of the study area was clipped using the raster tool. The land use land cover was

divided into six classes: Grassland, Barren area, Snow/glacier, Forest, Shrub land, Agriculture area.

3.3.11 Stream Power Index (SPI)

Stream power index is the product of stream discharge, stream slope, and water weight that has a direct link with sediment transport. SPI is a factor that contributes to the stability of the study area since it measures the erosion power of a stream. The following relationship determines it (Moore et al., 1991).

$$SPI = A_s \tan \beta$$

where,

A_s represents specific catchment area,

β represents the specific catchment area and slope gradient measured in degrees

Using the raster tool in ArcGIS, the stream power index map was created from a DEM of the study area. The stream power index was divided into four classes: 0 - 100000, 100000 - 500000, 500000 - 1000000, > 1000000.

3.3.12 Topographic Wetness Index (TWI)

The topographic wetness index (TWI), which comprises the local upslope contributing zone and the total slope, is frequently used to measure topographic influence on hydrological processes. It describes the spatial patterns of soil moisture. The following relationship is used to express it (Beven et al., 1979).

$$TWI = \ln \left(\frac{a}{\tan \beta} \right)$$

where a = cumulative upslope area draining through a point (per unit contour length)

$\tan \beta$ = slope angle at the point

Using the raster tool in ArcGIS, the topographic wetness index map was created from DEM of the study area. The topographic wetness index was divided into four classes: < 6, 6 - 8, 8 - 12, > 12.

3.3.13 Landslide Susceptibility Analysis

The weighting of the selected conditioning factors is part of the landslide hazard mapping procedure. The weight calculation of landslide susceptibility analysis can be done using a variety of statistical methods. The frequency ratio approach is utilized in this study to identify the link between landslide location and factors in the study area. It is based on the observed relationships between landslide distribution and each landslide related factor (Lee et al., 2006). The frequency ratio was calculated using the equation below.

$$FR = \frac{N_i^p / N}{N_i^{lp} / N^l}$$

Where, N_i^p = Number of pixels in each factor class

N = Number of all pixels in the whole study area

N_i^{lp} = Number of landslide pixels in each factor class

N^l = Number of all landslide pixels in whole study area

Using the above equation, frequency ratio for each conditioning factor is calculated. After that relative frequency (RF) is calculated to normalize the FR and its value ranges between 0 to 1. The mathematical expression for RF calculation is

$$RF = \frac{FR_i}{\sum_i^n FR}$$

Where FR_i = Frequency ratio of each class in conditioning factor

$\sum FR$ = Total sum of Frequency ratio of each class in conditioning factor

Relative frequency has the drawback of weighing all conditioning factors equally (Acharya et al., 2019). To solve this flaw, the prediction rate (PR) is determined for all factors, taking into consideration their mutual interaction. For the calculation, the following equation was utilized.

$$PR = \frac{MaxRF - MinRF}{Min(MaxRF - MinRF)}$$

Finally, a landslide susceptibility map was created in ArcGIS 10.2 using the raster calculator by combining conditioning factors classed according to their RF values and multiplying each value by its appropriate PR value.

$$LSM = \sum(PR * RF)$$

3.4 Framework for Flood Hazard Mapping

The most crucial step in determining flood hazard is to identify the flood genesis factors (Stefanidis et al., 2013). Rainfall duration/ intensity affects soil saturation and infiltration which leads to flooding. Similarly, different land use affects interception and permeability which is also one of reasons for flooding. The factor influencing flood hazard is based on literature review (Chen et al., 2009; Thapa et al., 2020).

Table 3-7: Selected indicators for flood hazard mapping

Indicators	Definition	Logical link to flood hazard	References	Functional relationship
Precipitation	Any liquid or frozen water that develops in the atmosphere and falls back to Earth	Heavy rainfall exceeds the ability of the ground to absorb it.	(Sarchani et al., 2020; Thapa et al., 2020)	↑
Discharge	It is a measure of the quantity of any fluid flow over unit time	Increase in discharge causes flooding	(Sarchani et al., 2020; Thapa et al., 2020)	↑
Inundation Depth	As a result of a flood, the entire water level that occurs on typically dry ground.	Indicates intensity of flood	(Sarchani et al., 2020; Thapa et al., 2020)	↑
Land use land cover	It describes physical land surface and land use by humans	Flood hazard is different for different land use types	(Khatakho et al., 2021; Thapa et al., 2020)	↑↓

Hazard map is prepared with respect to hydraulic and hydrological parameters of the inundation. Inundation depth is an important factor for estimating flood damage in many riverine settings. Because the velocity of flooding in floodplains is sufficiently low (0.5 - 1.5 m/s) to cause any substantial damage, the risk of flooding can be ignored. Flood depth has been considered as a primary indication of flood hazard in numerous studies. Flood depth is considered the most important indicator of the severity of a flood hazard (Islam et. al, 2002). This indicates that a flood will impact a certain area with the same hydraulic parameters regardless of land use. The presence of flooding in any location is a hazard in and of itself, with

the severity of flooding being classified according to the depth of flooding. In this study, flood hazard is classified into three classes based on depth and description of it is presented below.

- High hazard: depth greater than 3 m (> 3 m)
- Moderate hazard: depth between 1 m to 3 m
- Low hazard: depth below 1 m (< 1 m)

Inundation depths of less than 1 m are considered low-risk. In most scenarios, this depth is inadequate to infiltrate residential buildings and inflict significant damage to life and property. Streets and business hubs, on the other hand, are heavily inundated and harmed as a result of this depth. Flood depth greater than 3m is considered a dangerous level as it can seriously damage human life, residential areas, and agricultural land, etc. (Bhattarai et al., 2019; Pandey & Dugar, 2019; Ward et al., 2013). A high score indicates a high level of danger, whereas a low ranking indicates a lower level of danger. Hazard maps for the study area was created by overlapping a terrain layer with a depth grid for a flood with a 100-year return period. The flood hazard mapping process is outlined in the flowchart shown in Figure 3-5 below.

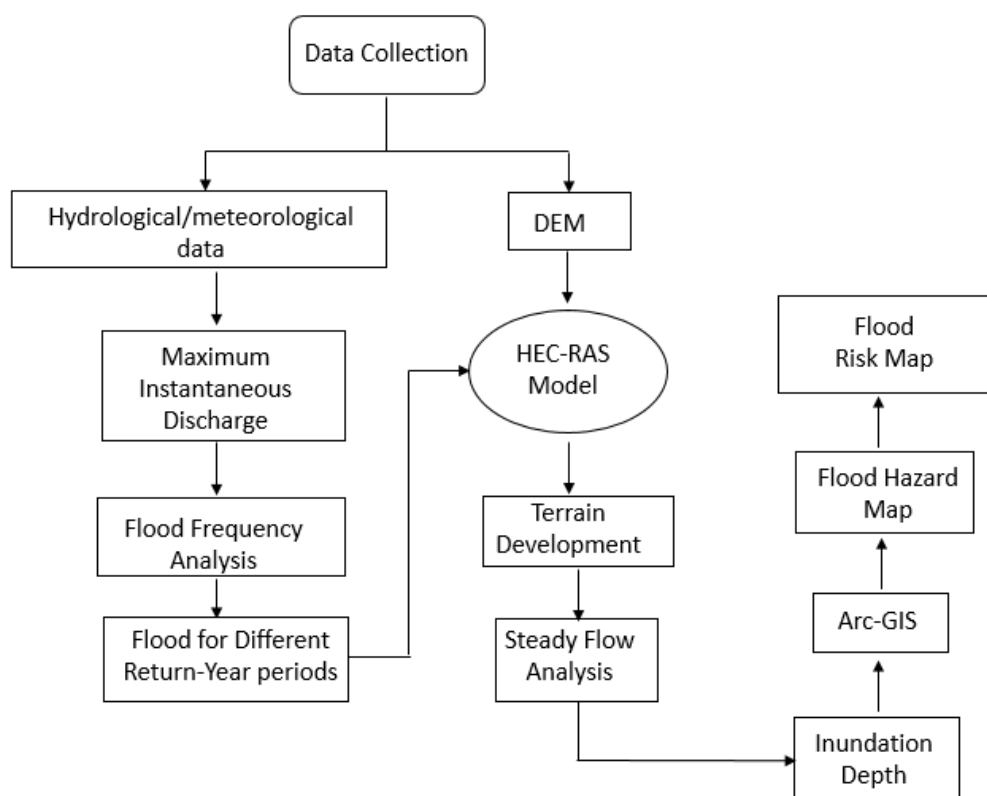


Figure 3-5: Process involved in preparing flood risk map

3.4.1 Average Precipitation Calculation

1. Thiessen Polygon Method

The rainfall at any rain gauge station gives point rainfall so it gives rainfall around the station and not all over the catchment area. For hydrological analysis, average rainfall is required. So to compute average rainfall in the catchment area, the Thiessen polygon method was used. Rainfall recorded at each station is given a weightage based on the area close to the station in the Thiessen polygon method.

Thiessen Polygon in ArcGIS 10.2 was used to obtain the average observed daily rainfall datasets for the basin and study catchment region. The average rainfall across a catchment region can be calculated using the Thiessen Polygon method using the equation below.

$$\bar{P} = \frac{P_1 A_1 + P_2 A_2 + \dots + P_n A_n}{A}$$

Where,

P_1, P_2, \dots, P_n = Precipitation recorded at respective stations.

A_1, A_2, \dots, A_n = Thiessen polygon areas

$A = A_1 + A_2 + A_3 + \dots + A_n$

3.4.2 Catchment Area Ratio Method

The catchment area ratio method is used to transpose the nearest flow data to the study area for ungauged stations. Considering long-term stream flow records at study area were unavailable, stream flow data at the study area was estimated via correlation of catchment with gauging station number 650.

Historically available daily flow data from year 1980-2006 were collected from DHM for gauging station number 650. Then, using the equations given below, daily flow data for the study area were generated from catchment correlation with gauging station number 650.

$$Q_2 = Q_1 \frac{A_2}{A_1} \frac{P_2}{P_1}$$

Where,

Q_2 = Flow at Khimti Khola at study area

Q_1 = Flow at Gauging Station No. 650

A_2 = Catchment area at study area of Khimti Khola

A_1 = Catchment area of Gauging Station No. 650

P_1 = Mean annual precipitation for the catchment of Gauging Station No. 650

P_2 = Mean annual precipitation for catchment of the study area

Similarly, using catchment area ratio method instantaneous discharge for study area was estimated from available historical data at gauging station number 650.

3.4.3 Flood Frequency Analysis

Flood flows are estimated using frequency analysis for various storm events using hydrologic data series and rainfall events using rainfall data series. Flood frequency analysis was performed using Extreme Value (EV) distributions since flooding is an extreme hydrological event. Statistical approaches were used to conduct a flood frequency analysis (Gumbel, Log Pearson type III, and Lognormal). Finally, Log-Pearson method was selected based upon the statistical indicators (Correlation coefficient, and Chi-square test).

3.4.4 Hydraulic Modelling

Hydraulic modelling required for this study was done using HEC-RAS 5.0.7. The DEM of the study area was imported into HEC-RAS using the RAS Mapper tool of HEC-RAS. The coordinate system used for the study is WGS 1984 UTM zone 45N. At first co-ordinate system was stored in HEC-RAS using RAS Mapper tool followed by DEM import. The terrain was created in HEC-RAS. The geometric data (Figure 3-6) used area created in RAS Mapper namely river profile, cross-sections. The HEC-RAS flow plan utilized hydraulic data, including flow data and associated boundary conditions (Figure 3-7), and the computed flood frequency for a 100-year return period flood was applied to the river cross-section. Due to the unavailability of hourly rainfall data within the catchment and neither in the vicinity of the catchment area, 2-D unsteady flood flow analysis was a great challenge. Hence, a steady-state 1-D flow simulation was performed to calculate the water surface profile. The depth for given value of Q_{100} was calculated in RAS Mapper (Figure 3-8) and saved as raster file.

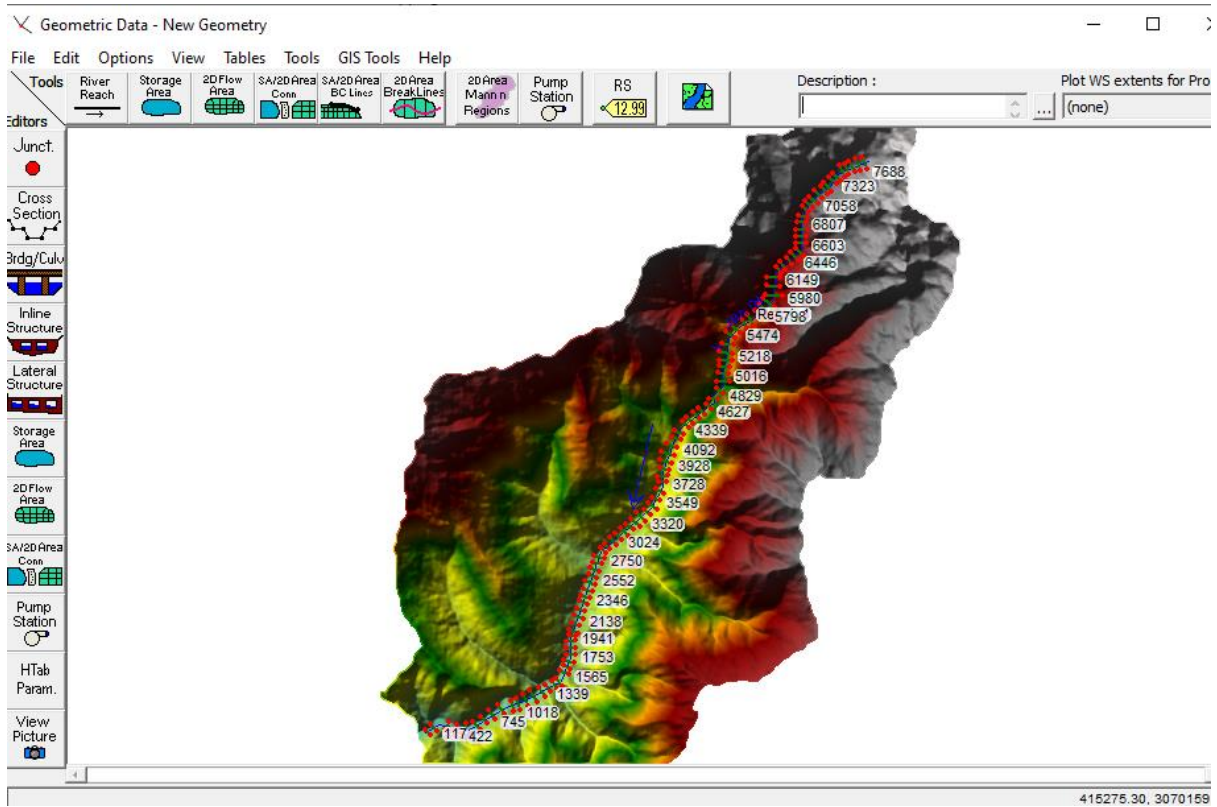


Figure 3-6: Geometric data of khimti watershed

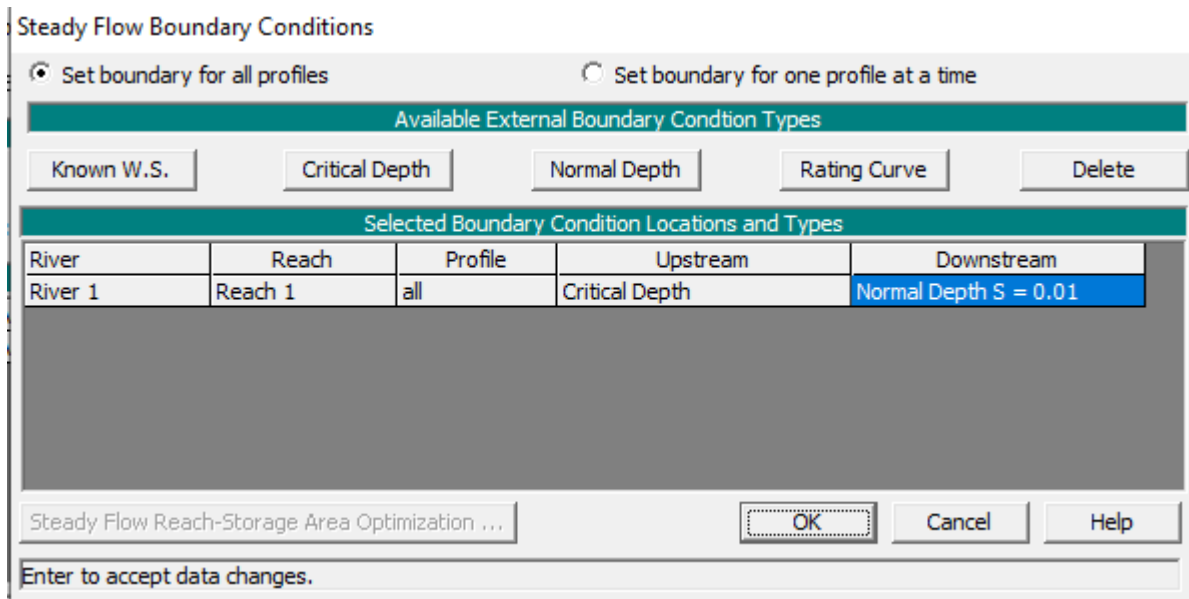


Figure 3-7: Steady flow boundary conditions

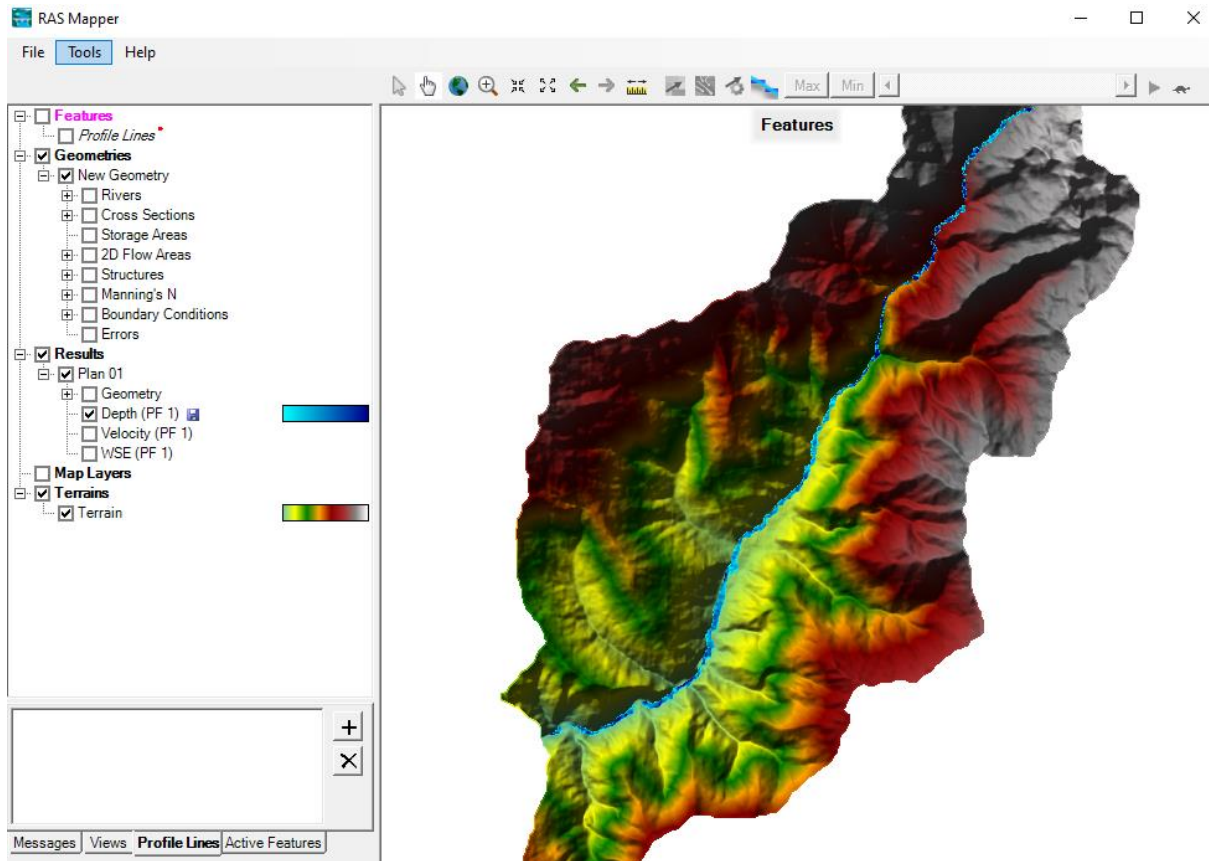


Figure 3-8: Khimti watershed inundation depth

3.5 Framework for Seismic Hazard Assessment

Since the majority of the damages are caused by significant ground shaking or structural collapse, seismic hazard assessment is the process of determining the design motion of the ground during earthquakes (Aksha et al., 2020). The variables needed to determine seismic hazard are based on a survey of the literature (Chaulagain et al, 2015; Thapa and Guoxin, 2013; Pourghasemi et al., 2019). For seismic hazard assessment, there are two approaches: scenario seismic hazard analysis and probabilistic seismic hazard analysis. A scenario hazard analysis is based on a specific seismic event, and the ground motion parameters acquired are usually at their maximum value, which is rarely used as a seismic input in structural analysis. Uncertainties in earthquake size, location, and time of occurrence can all be included in probabilistic seismic hazard assessments (Chaulagain et al., 2015). Probabilistic seismic hazard analysis (PSHA) is used in this study. The earthquake catalogue, probability density of earthquake magnitude, and peak horizontal acceleration (PHA) are all needed parameters. The parameters are described in greater detail in the following section.

The following flowchart given in Figure 3-9 represents methodology adopted for seismic hazard mapping.

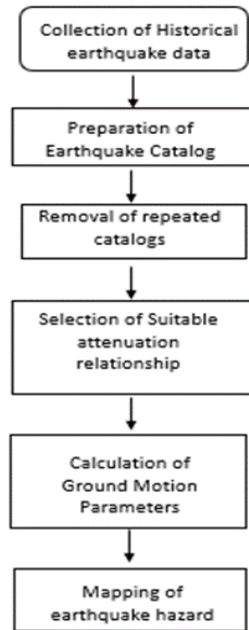


Figure 3-9: Process involved in preparing seismic hazard map

3.5.1 Steps Involved in Probabilistic Seismic Hazard Analysis

1. Earthquake Catalogue

Earthquake catalogue is an important parameter for earthquake hazard prone area determination. The earthquake catalogue is created based on earthquakes that have occurred in the past. Historical earthquake data higher than 4 M_w within circle of radius 350 kilometers from the study area was collected from 1255 to 2021 based on earlier research (Bhusal et al., 2019) and data from the National Seismological Center (NSC). Data on earthquakes has been recorded in a variety of magnitudes and intensity ratings. For declustering and completeness work, the obtained data, which were measured in several magnitudes such as Richter scale, Moment Magnitude, Surface Magnitude, and Body Wave Magnitude, were converted to Moment Magnitude. To convert the Richter magnitude and surface waves, (Ambraseys and Douglas, 2004) and to convert body waves, (Scordilis, 2006) were used. The surface wave magnitude (M_s) was converted to moment-magnitudes (M_w) combining the empirical relations $M_w = (2/3) \log M_0 - 10.63$ (Hanks and Kanamori, 1979), and $\log M_0 = 16.03 + 1.5 M_s$ (for $M_s > 5.94$) and $\log M_0 = 19.38 + 0.93 M_s$ (for $M_s \leq 5.94$) (Ambraseys and Douglas, 2004).

2. Declustering Earthquake Catalogue and Completeness

Declustering is a technique for filtering overlapping or related occurrences in a catalog. Because the presence of such occurrences can lead to an overestimation of earthquake rates, they must be removed. To remove the dependent events, this study employs (Gardner and Knopoff's, 1974) algorithm in the form of self-written python programs. A total of 817 earthquake of magnitude higher than 4 M_w after declustering was found from year 1255 to 2021.

It is quite difficult to determine the exact site of an earthquake, and even more difficult to determine which earthquakes are associated with which fault. Because of the difficulty in obtaining historical data, the recorded earthquake data contains a non-uniform number of events. As a result, for the optimum fit of the frequency formula, it is important to conduct a completeness analysis. Stepp, 1972 method is used to measure the completeness of various magnitude classes.

3. Earthquake Source Models

It is extremely difficult to characterize the source zone due to uncertainty in the location and nature (geometry) of the source. The study area's tectonic border has been separated into 20 quadratics and polygon-shaped areal sources (Figure 3-10). All of the sources are believed to be equally capable of causing an earthquake, with the epicenter occurring in the center of each areal cell.

4. Attenuation relationship

The attenuation relationship, also known as the prediction relationship, describes how ground shaking events affect ground motion characteristics such as peak ground acceleration, spectral displacement, and spectral acceleration. Because the ground motion attenuation model characterizes the propagation and alteration of seismic ground motion from source to site as a function of both earthquake magnitude and distance, selecting an appropriate attenuation relationship is crucial in a probabilistic seismic hazard assessment (Cornell, 1968; Li et al., 2011). The effect is determined using the magnitude and distance from the source to the site, as well as other factors. Researchers have identified four types of site-specific attenuation connections: stable continental regions, subduction zones, active shallow crustal regions, and

volcanic regions. The majority of earthquakes in Nepal are classified as interface events due to the subduction of the Indian plate beneath the Eurasian plate. As a result, the Young's et al., 1997 attenuation relationship for the subduction zone is used in this study.

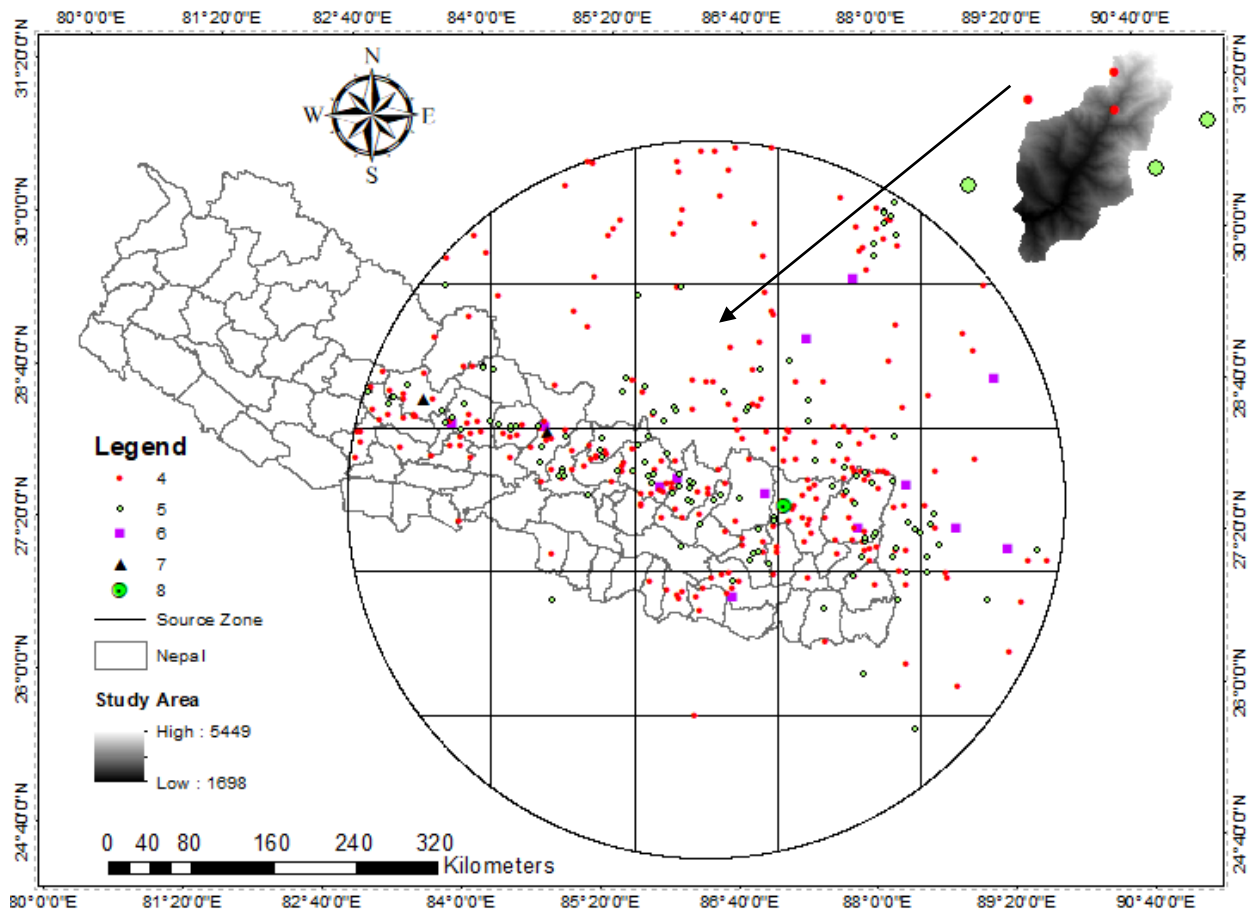


Figure 3-10: Seismic source zones

For rock it is expressed as

$$\ln(y) = 0.2418 + 1.414 M + C_1 + C_2 (10 - M)^3 + C_3 \ln (r_{rup} + 1.7818 e^{0.554M}) + 0.00607 H + 0.3846 Z_T$$

$$\text{Standard deviation} = C_4 + C_5 M$$

Where,

y: spectral acceleration in g,

M: moment magnitude,

r_{rup} : closest distance to rupture (km),

H: depth (km)

Z_T : coefficient for source type which is 0 for interface event and 1 for intra-slab event.

Table 3-8: Attenuation relation for horizontal response spectral acceleration (for rock)

Periods	C ₁	C ₂	C ₃	C ₄	C ₅
PGA	0	0	-2.552	1.45	-0.1
0.075	1.275	0	-2.707	1.45	-0.1
0.1	1.188	-0.0011	-2.655	1.45	-0.1
0.2	0.722	-0.0027	-2.528	1.45	-0.1
0.3	0.246	-0.0036	-2.454	1.45	-0.1
0.4	-0.115	-0.0043	-2.401	1.45	-0.1
0.5	-0.4	-0.0048	-2.36	1.45	-0.1
0.75	-1.149	-0.0057	-2.286	1.45	-0.1
1	-1.736	-0.0064	-2.234	1.45	-0.1
1.5	-2.634	-0.0073	-2.16	1.5	-0.1
2	-3.328	-0.008	-2.107	1.55	-0.1
3	-4.511	-0.0089	-2.033	1.65	-0.1

For Soil it is expressed as

$$\ln(y) = -0.6687 + 1.438 M + C_1 + C_2 (10 - M)^3 + C_3 \ln(r_{rup} + 1.097 e^{0.617M}) + 0.00648 H + 0.3643 Z_T$$

$$\text{Standard deviation} = C_4 + C_5 M$$

Table 3-9: Attenuation relation for horizontal response spectral acceleration (for soil)

Periods	C ₁	C ₂	C ₃	C ₄	C ₅
PGA	0	0	-2.329	1.45	-0.1
0.075	2.4	-0.0019	-2.697	1.45	-0.1
0.1	2.516	-0.0019	-2.697	1.45	-0.1
0.2	1.549	-0.0019	-2.464	1.45	-0.1
0.3	0.793	-0.002	-2.327	1.45	-0.1
0.4	0.144	-0.002	-2.23	1.45	-0.1
0.5	-0.438	-0.0035	-2.14	1.45	-0.1
0.75	-1.704	-0.0048	-1.952	1.45	-0.1
1	-2.87	-0.0066	-1.785	1.45	-0.1
1.5	-5.101	-0.0114	-1.47	1.5	-0.1
2	-6.433	-0.0164	-1.29	1.55	-0.1
3	-6.672	-0.0221	-1.347	1.65	-0.1
4	-7.618	-0.0235	-1.272	1.65	-0.1

5. Seismic hazard analysis

Plotting the mean annual rate of exceedance versus peak ground acceleration yields the seismic hazard curve. The Probabilistic Seismic Hazard Analysis (PSHA) is carried out using the software CRISIS 2007.

3.5.2 Modelling and Analysis

CRISIS 2007 is a Windows-based tool that uses a completely probabilistic method to perform Probabilistic Seismic Hazard Analysis (PSHA), allowing findings to be estimated in terms of outputs with various characteristics (i.e., exceedance probability plots, set of stochastic events). All of the information needed to conduct the hazard analysis is entered into the software.

The series of steps involved in modeling and analysis are described below:

1. Map of Nepal was given as initial input in the software.

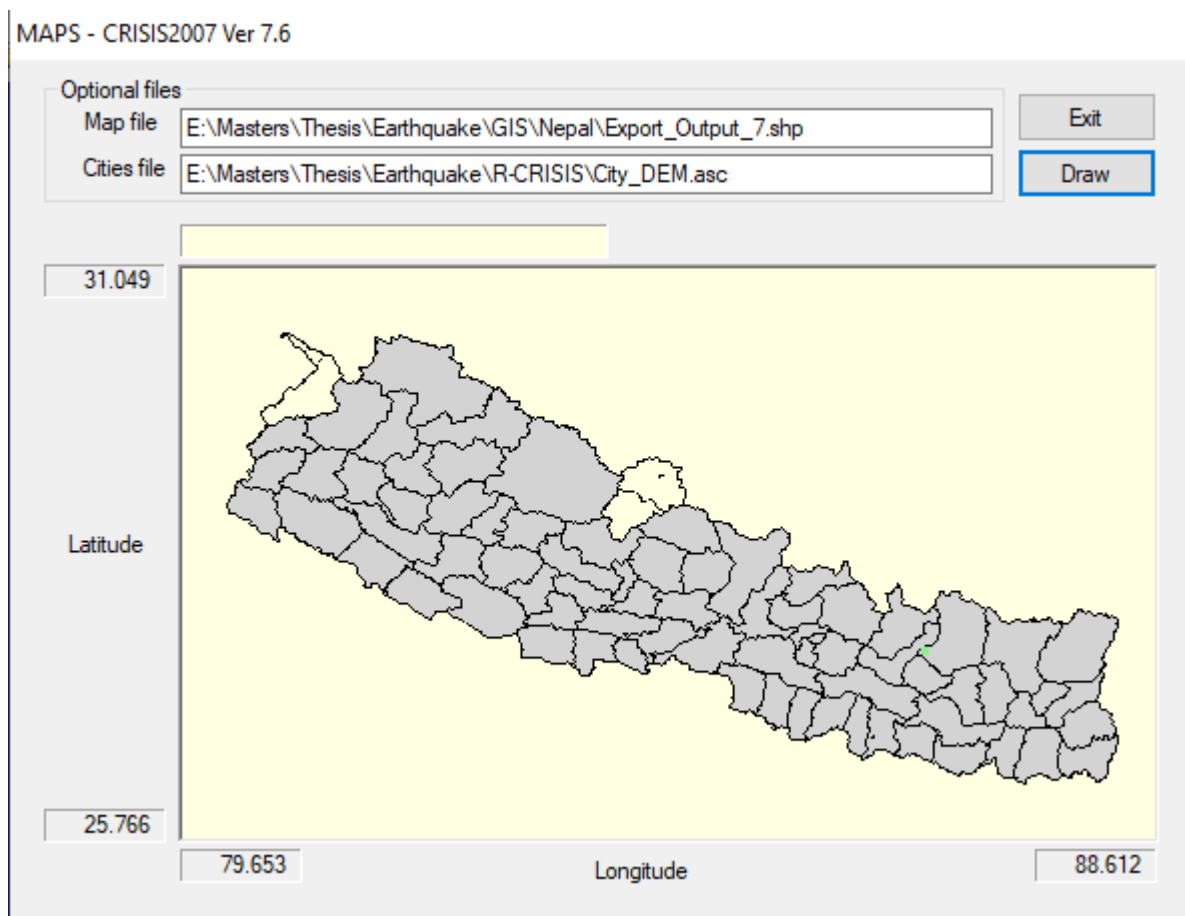


Figure 3-11: Map of Nepal inserted in software

- The region was divided into smaller grids of $0.32^\circ \times 0.32^\circ$, each representing a single site for determining hazard.

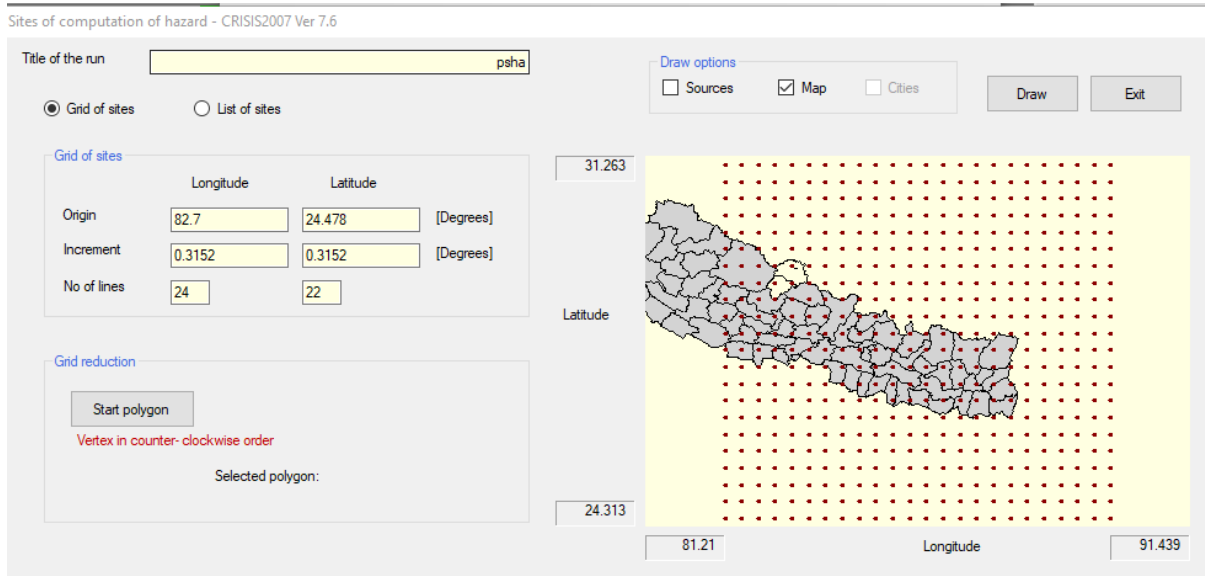


Figure 3-12: Division of area into grids of size $0.32^\circ \times 0.32^\circ$

- In geometry of seismic sources, 20 numbers of area sources were defined and drawn.

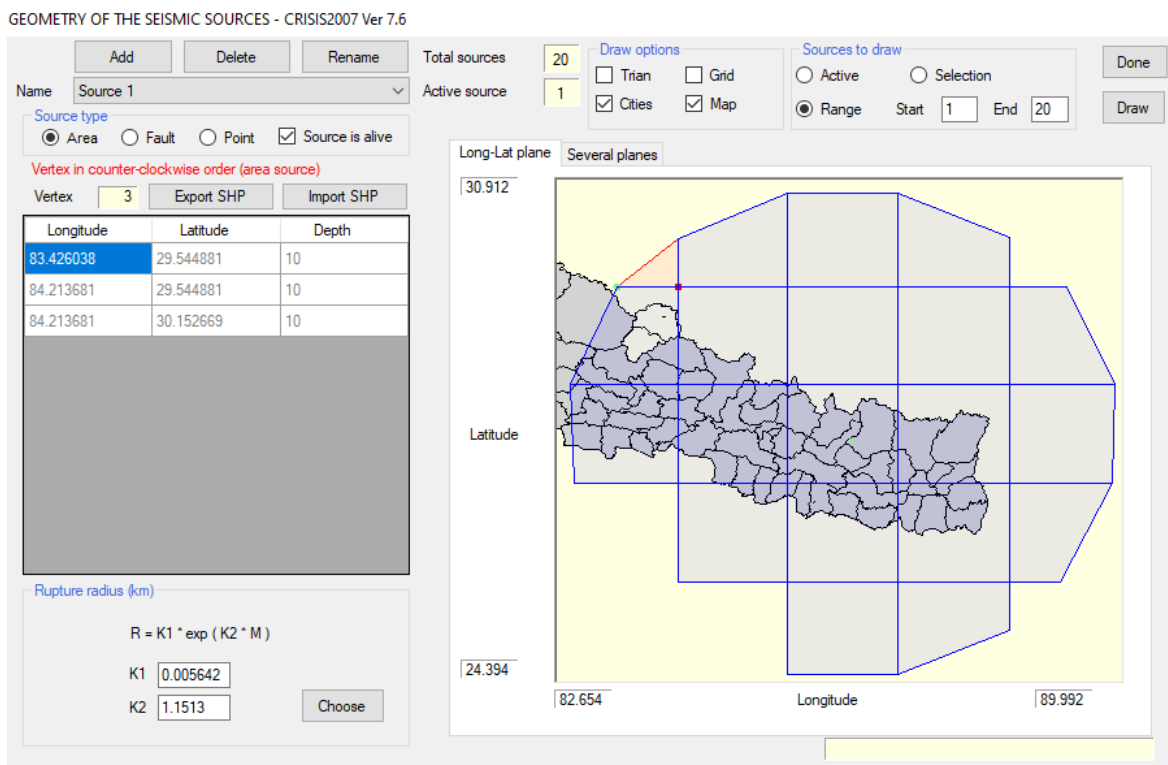


Figure 3-13: Modelling the area source zones in the software

- The G-R b value, threshold magnitude, maximum magnitude, and other inputs were used to define the source seismicity for each source.

SEISMICITY - CRISIS2007 Ver 7.6

Source number < > of total sources

Source name

Occurrence model
 G-R
 Characteristic

Draw options
 Active Map
 All

Longitude Latitude

G-R Characteristic

Threshold magnitude (M0)

Lambda(M0)

Expected value of Beta

Coefficient of variation of Beta

Parameters defining Mu:

Untruncated expected value

Untruncated standard deviation

Lower limit (M1)

Upper limit (M2)

Moment and slip rates
 Moment rate = 1.03E+21 dyne-cm/year
 Slip rate = 3.63E-03 mm/year

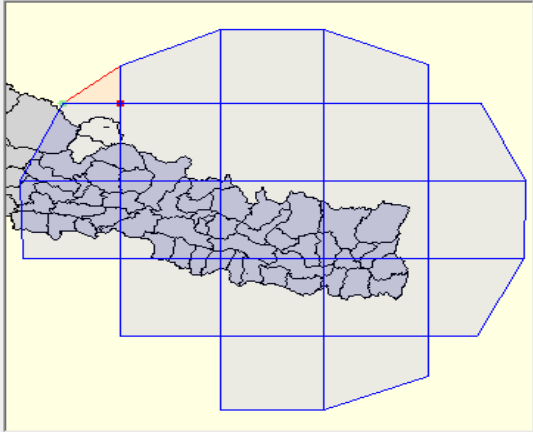


Figure 3-14: Providing seismicity values for each zone

- For time periods of 0 sec, the spectral ordinates parameters were established (i.e. PHA).

INTENSITIES FOR EACH SPECTRAL ORDINATE - CRISIS2007 Ver 7.6

Spectral ordinates

Total number of spectral ordinates

Actual spectral ordinate

Structural period of actual spectral ordinate

Lower limit of intensity level

Upper limit of intensity level

Units

Number of levels of intensity for which seismic hazard will be computed

Figure 3-15: Defining spectral ordinate parameters

- Young's et al., 1997 attenuation relationship for soil and rock was established and applied to each source zone.

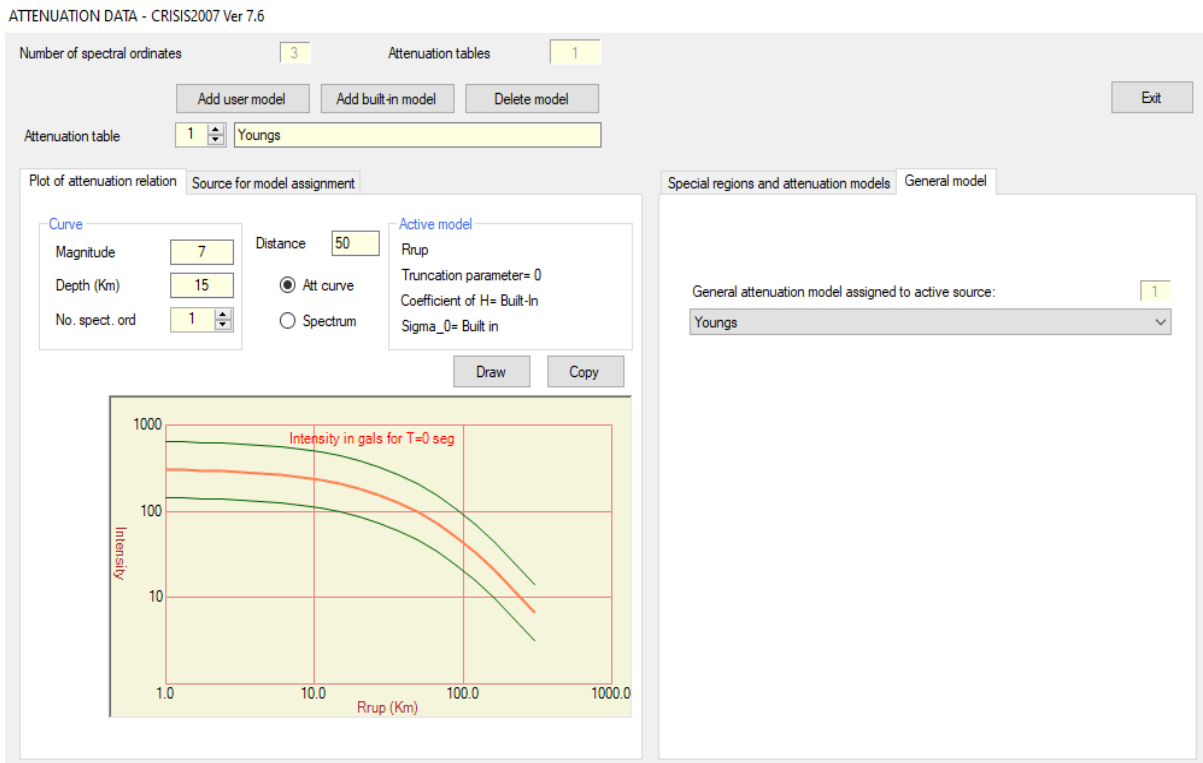


Figure 3-16: Defining attenuation relationship

- For the purpose of calculating the seismic hazard, return periods were defined.

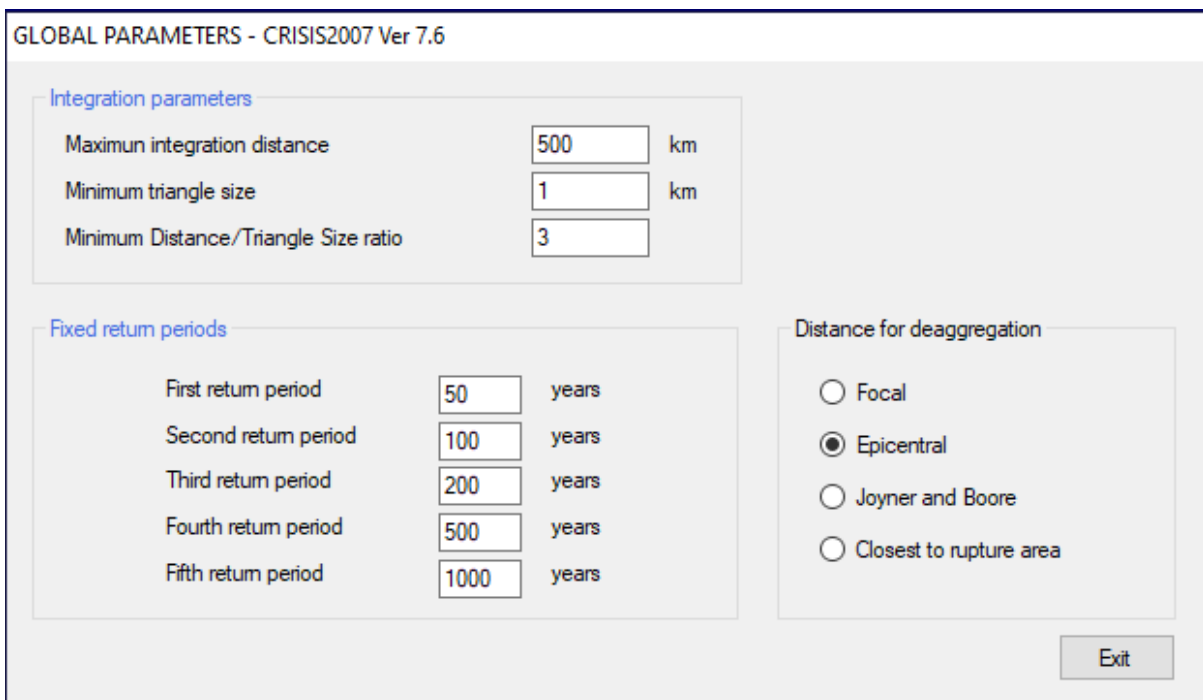


Figure 3-17: Defining return periods

8. Finally, the analysis was run and the outputs were obtained.

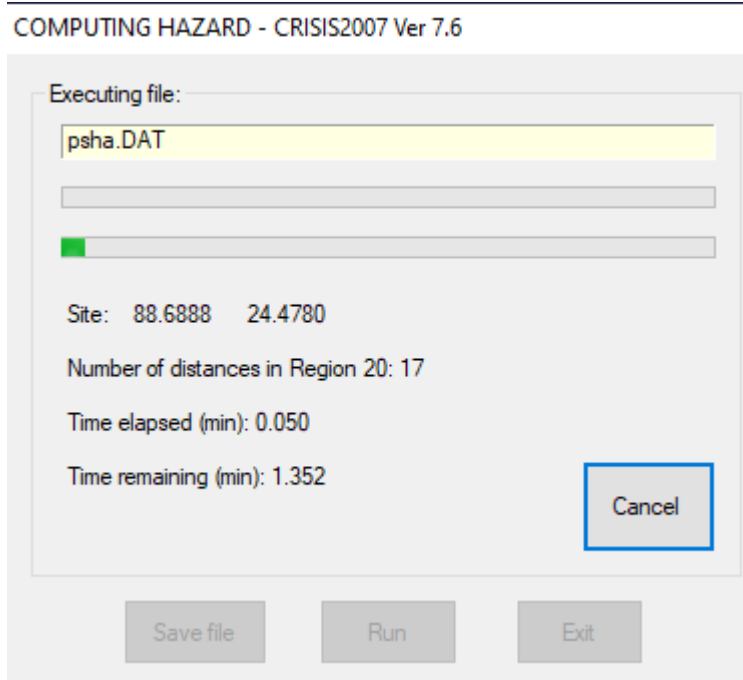


Figure 3-18: Running the analysis

3.6 Multi-Hazard Mapping

By simply overlaying the obtained individual hazard maps, we cannot achieve an accurate multi-hazard map. Weighting and ranking of factors for each particular hazard category (landslide, flood, and earthquake) is required to integrate various factors in a spatial decision-making process and evaluate their relative relevance (Bathrellos et al., 2012). So, in this study for integration of three individual hazard maps, Analytical Hierarchy Process in GIS was used. It's worth noting that the most important factor in determining the multi-hazard level on any scale is historical records of natural hazards (Barua et al., 2016). Natural disasters in Nepal's past have not been adequately documented in terms of losses. Only disasters that occurred after 2000 are recorded in terms of economic losses. The number of natural hazard events, as well as some relevant information on losses, are used to describe the relative hazard score. The study area seems to have suffered from numbers of landslides (Gautam et al., 2021). Thus, we assigned the larger relative significance to landslide hazard as the study area falls landslide risk zone. Earthquakes are one of the most significant risks in eastern Nepal, as evidenced by the 1934 Bihar-Nepal Earthquake (Mw 8.3), the 1988 Udaypur Earthquake (Mw 6.8), and the 2015 Gorkha Earthquake (Mw 7.8) (Chaulagain et al., 2015). Thus, second largest weight was

assigned to landslide hazard. Hence, the third and the last relative importance was given to flood hazard.

To assign different weights to the individual hazard maps used in this study, the analytical hierarchy process was applied. To calculate the weight in the AHP analysis, a 3 x 3 matrix was used for pairwise comparison. The maximum weight (0.49) was attributed to landslide hazard, while the lowest weight (0.2) was assigned to flood hazard (Table 3-10). The CR value was 0.046, which is less than 0.10, which is within the acceptable range for the analysis to be consistent, as suggested by (Saaty, 1990).

The multi-hazard map was prepared on the basis of following equation in Arc GIS 10.2.

$$MHI = \sum_{i=1}^n H_i W_i$$

Where,

MHI= Multi-hazard Index,

n = Number of hazards,

H_i = hazard,

W_i = Weightage of each hazard

Finally, a multi-hazard map was created by classifying and ranking multi-hazard index from 1 to 5 using Arc-GIS' Jenks Natural Break classification method (1= very low, 5= very high) (Devkota et al., 2013; Ebrahimi et al., 2020).

Table 3-10: Pair-wise comparisons and weighting coefficients of each adopted factor in multi-hazard evaluation

	H1	H2	H3	Weight Wi
H1(Landslide)	1	2	2	0.49
H2(Earthquake)	0.5	1	3	0.31
H3(Flood)	0.5	0.5	1	0.20
CR= 0.046				

3.6.1 Possible Combination of Two Different Hazard Maps

To assign different weights to the individual hazard maps used in this study, the analytical hierarchy process was used. A 2 x 2 matrix was used for pairwise comparison in the AHP analysis to calculate the weight.

As discussed in section 3.6, since maximum number of landslides had occurred in the past in Khimti region, it was given number 1 ranking followed by the earthquake for assessing combination of landslide and seismic hazard maps. The maximum weight (0.67) was attributed to landslide hazard, and weight (0.33) was assigned to seismic hazard (Table 3-11). The CR value cannot be evaluated since random index is zero in case of 2 x 2 matrix.

For assessing combination of landslide and flood hazard maps, rank 1 was given to landslide followed by flood because of higher number of past landslide events as compared to flooding event. The maximum weight (0.82) was attributed to landslide hazard, and weight (0.27) was assigned to flood hazard (Table 3-12).

For assessing combination of seismic and flood hazard maps, rank 1 was given to seismic hazard followed by flood because damage caused by earthquake events was greater as compared to flooding event. The maximum weight (0.82) was attributed to seismic hazard, and weight (0.27) was assigned to flood hazard (Table 3-13).

The possible combination hazard maps were prepared on the basis of following equation in Arc GIS 10.2.

$$SI = \sum_{i=1}^n H_i W_i$$

Where,

SI= Possible combination of two hazards Index,

n = Number of hazards,

H_i = hazard,

W_i = Weightage of each hazard

Finally, a combination of landslide seismic hazard, landslide flood hazard, and seismic flood hazard, maps were created by classifying and ranking SI between 1 to 5, using the Jenks Natural Break classification method provided in Arc-GIS (1=very low, 5=very high) (Devkota et al. 2013; Ebrahimi et al. 2020).

Table 3-11: Pair-wise comparisons and weighting coefficients of each adopted factor in combination of landslide and seismic hazard evaluation

	H1	H2	Weight Wi
H1(Landslide)	1	2	0.67
H2(Earthquake)	0.5	1	0.33

Table 3-12: Pair-wise comparisons and weighting coefficients of each adopted factor in combination of landslide and flood hazard evaluation

	H1	H2	Weight W_i
H1(Landslide)	1	3	0.82
H2(Flood)	0.5	1	0.27

Table 3-13: Pair-wise comparisons and weighting coefficients of each adopted factor in combination of seismic and flood hazard evaluation

	H1	H2	Weight W_i
H1(Earthquake)	1	3	0.82
H2(Flood)	0.5	1	0.27

3.7 Future Climate Projection

In this study, five (5) Coupled Model Inter-comparison Project Phase 6 (CMIP 6) GCMs for period (2015 – 2095) were used for the projection of the future climate. CMIP6 is used because it employs a new set of socioeconomic pathways that take into account radiative forcing, societal concerns, and land use scenarios. GCMs under two SSP scenarios, i.e. SSP 245 and SSP 585 were used to project future climate. In order to fit the GCMs of coarser resolution, GCM projections were bias adjusted using observed data from the study area. Among various methods available for bias correction, Quantile Mapping (QM) was implemented in this study due to its better technique in improving the performance of GCMs. The primary goal of QM is to align the quantiles of raw RCM data with the quantiles of observed data by generating a transfer function that shifts the quantiles of rainfall and temperature. Enayati et al., (2021) discovered that robust empirical quantiles (RQUANT) methods were excellent options for correcting the bias of rainfall data, while all bias correction methods performed relatively well for the temperature variable, with the notable exceptions of performed PTF: scale and SSPLIN. This is mostly due to the unique character of temperature and the GCM/RCM combinations' superior ability to model this climatic variable when compared to rainfall.

For multi-model ensembles, there is no logic for choosing number of GCMs. (Raju & Kumar, 2020). Multi-model ensembles, on the other hand, can minimize the overall uncertainty in model predictions (Scinocca et al., 2016). The use of a single GCM for climate change assessment was opposed by Hussain et al., (2017). For multi-model ensembles, Herger et al., (2018) presented three approaches: (a) random ensemble, (b) performance ranking ensemble, and (c) optimal ensemble.

Daily precipitation, daily maximum and minimum temperature data from 5 of the 13 CMIP6 GCMs proposed by Mishra et al. (2020) for South Asia are listed in Table 3-14. were downloaded from <https://esgf-node.llnl.gov/search/cmip6/> for two scenarios SSP245 & SSP585.

Table 3-14: List of CMIP6 GCMs used in this study

S.N.	Model Name	Country	Latitude Resolution (Deg)	Longitude Resolution (Deg)	Research Center
1.	ACCESS-CM2	Australia	1.25	1.875	Australian Community Climate and Earth System Simulator (ACCESS)
2.	EC-EARTH3	Europe	0.7018	0.703125	European Community Earth (EC Earth)
3.	INM-CM5-0	Russia	1.5	2	Institute for Numerical Mathematics (INM)
4.	MPI-ESM1-2-HR	Germany	0.9351	0.9375	Max Planck Institute for Meteorology (MPI)
5.	MRI-ESM2-0	Japan	1.1215	1.125	Meteorological Research Institute (MRI)

3.8 Data and Sources

For this study, different sets of data such as DEM, precipitation, land cover, lithology, relative relief, earthquake catalog are required which are obtained from various organizations. The quality and quantity of data used in this study are discussed in the following section. The available data and sources are shown in the Table 3-15 below.

Table 3-15 : List of data acquired from different sources

Dataset	Data Type	Data Description/ Processing	Resolution	Data Source
Terrain/DEM	Spatial grids	Digital Elevation Model	30 m x 30 m	USGS
Precipitation	Time series	Daily	-	DHM
Temperature	Time series	Daily	-	DHM
Discharge	Time series	Daily, Instantaneous	-	DHM
Land Use	Spatial grids	Land use classification	30 m x 30 m	ICIMOD(2010), DEM
Settlement	Socio-economic	Settlements built in vicinity of khimti watershed	-	Survey Department of Nepal (2015), HDX

Dataset	Data Type	Data Description/ Processing	Resolution	Data Source
Geology	Polygon	Geology map of Nepal	30 m x 30 m	Department of Mines and Geology (1994), DEM
Distance from road	Line	Derived from Road map of Nepal and DEM	30 m x 30 m	Survey Department of Nepal (2015), USGS
Distance from stream	Line	Derived from stream order using DEM	30 m x 30 m	USGS
Slope aspect	Spatial grids	Derived from DEM	30 m x 30 m	USGS, ArcGIS
Lineament Density	Spatial grids	Derived from DEM	30 m x 30 m	USGS, ArcGIS
Slope gradient	Spatial grids	Derived from DEM	30 m x 30 m	USGS, ArcGIS
Relative relief	Spatial grids	Derived from DEM	30 m x 30 m	USGS, ArcGIS
Curvature	Spatial grids	Derived from DEM	30 m x 30 m	USGS, ArcGIS
SPI	Spatial grids	Stream Power Index	30 m x 30 m	USGS, ArcGIS
TWI	Spatial grids	Topographic Wetness Index	30 m x 30 m	USGS, ArcGIS
Earthquake catalogue	Earthquake data	Historical events	-	Previous Studies, (NSC)
Future Precipitation [mm]	Time – series extracted from spatial grids	Daily projected values	-	5 GCMs detailed in Table 3-14
Future Temperature [Kelvin]	Time – series extracted from spatial grids	Daily projected values	-	5 GCMs detailed in Table 3-14

4 Results and Discussion

4.1 Landslide Hazard Assessment

4.1.1 Landslide Inventory Map

As shown in Figure 4-1, a landslide inventory map for the Khimti watershed was developed. The location of historical landslide events is represented by the blue dots in the figure. In the study area, a total of 70 landslides were discovered. The polygon sizes were created to cover as much of the landslide-affected area as possible. As in prior studies, 70% of the identified landslides were utilized for LSI computation and 30% for validation (e.g., Acharya et al., 2019). The training and validation datasets were chosen randomly using ArcGIS 10.2.2's geo-statistical analyst tool.

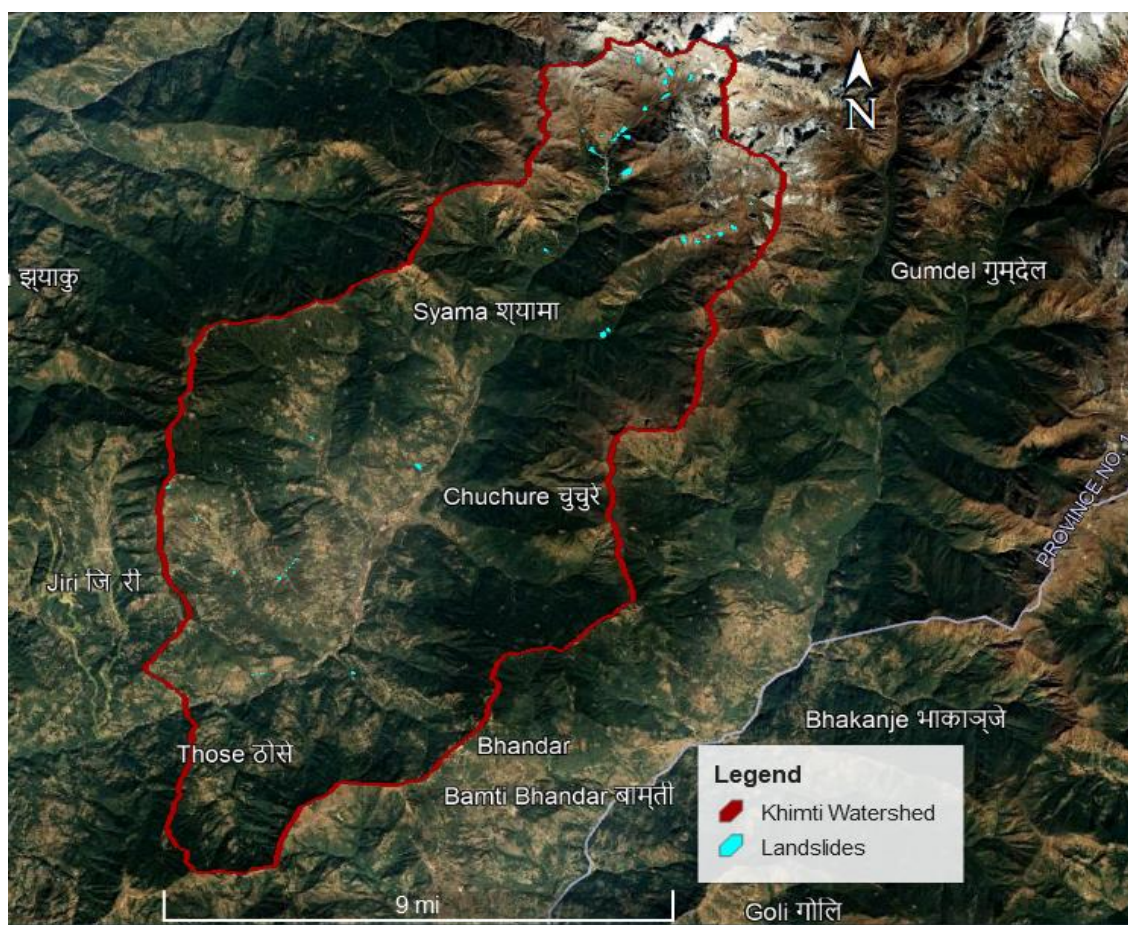


Figure 4-1 : Landslide inventory map

4.1.2 Spatial Distribution of Thematic Layers

A total of 11 factors Table 3-6 were used to identify areas with different degrees of susceptibility to landslide occurrences. The detail regarding spatial distribution for each indicator is given in sub-sections of 3.3. In this study, we can see that FR value for slope is 2.1 in 35° - 45° class range which is highest for slope gradient with 19.2% of slope area followed by > 45° class representing 4.8% area. It is evident from this that landslide susceptibility increases with increasing slope gradient up to a certain point, after which it begins to decline. In case of slope aspect, slope facing South consisting 13.8% of total aspect area, South east consisting 12.6% of total aspect area and South west consisting 15.5% of total aspect area direction has higher FR values 4.4, 1.4 and 0.8 respectively. Also, human interventions and river cutting works are more in South directions, making it more susceptible to landslides. Flat surface consists of 4.8% area of total curvature area and is prone to landslide since they support washing out of least resistive material aiding debris flow. This is also indicated by FR value of 1.2 for flat surface which is highest among other classes of curvature. In relative relief factor, class 49 - 74 m shows high FR value 1.9 and represents 25.0% area of total area followed by FR value of 0.9 in 30 - 49 class comprising of 39.7% area, among indicating past landslides have mostly occurred in these two classes as compared to rest class. For geology, Himal group comprising 4.8% area is more prone to landslide occurrences with 5.2 FR value which is highest amongst geology classes. In case of Land use land cover, barren land represents 3.2% area and has highest FR value 7.1 followed by grassland representing 14.3% area of total land use area with 3.3 FR value. For lineament density, class range 0.5 - 1.0 has highest FR value 1.2, which represents presence of faults is more in this class than other classes and represents 27.1% of total lineaments area. For distance from road factor, class ranging from 1000 - 2000 m with 94.3% area is more vulnerable towards landslide with highest FR value 2.2 for this factor. The most vulnerable class for stream network is 0 - 1500 m with 1.3 FR value and 75.7% of stream area. In case of TWI, 6 - 8 class is more susceptible towards landslide with 1.3 FR value which is among classified classes for TWI and consists of 25.9% area of total TWI area. SPI value class (0 - 1,00,000) consists of 99.6% of area and is the highest contributing landslide class factor for this study area with FR value 10.4. The area under different classes of thematic layers is given in Table 4-1. The thematic maps produced for selected factors is given in Figure 4-2 and Figure 4-3.

Table 4-1 : Thematic layers area under different classes

Parameters	Class	Area (Km ²)	Area (%)
Slope	< 15	26.8	11.3%
	15 - 25	71.9	30.3%
	25 - 35	81.6	34.4%
	35 - 45	45.4	19.2%
	> 45	11.4	4.8%
Aspect	Flat(-1)	0.002	0.001%
	North(0 - 22.5)	10.9	4.6%
	Northeast(22.5 - 67.5)	23.6	9.9%
	East(67.5 - 112.5)	26.6	11.2%
	Southeast(112.5 - 157.5)	29.9	12.6%
	South(157.5 - 202.5)	32.6	13.8%
	Southwest(202.5 - 247.5)	36.7	15.5%
	West(247.5 - 292.5)	35.2	14.9%
	Northwest(292.5 - 337.5)	29.1	12.3%
Curvature	North(337.5 - 360)	12.3	5.2%
	Concave(< -0.05)	112.1	47.3%
	Flat(-0.05 - 0.05)	11.4	4.8%
Relative Relief	Convex(> 0.05)	113.5	47.9%
	0 - 30	70.5	29.7%
	30 - 49	95.4	40.2%
	49 - 74	60.1	25.4%
Geology	74 - 254	14.0	5.9%
	Himal Group	11.4	4.8%
	Dware Kharka Schist	17.5	7.4%
	Himal Group	62.2	26.2%
	Himal Gneiss	20.2	8.5%
	Panglema Quartzite	88.4	37.3%
	Ghanapokhara Formation	13.7	5.8%
	Seti Formation	20.9	8.8%
	Ulleri Formation	0.8	0.3%
Land use land cover	Kushma Formation	2.0	0.8%
	Grassland	34.0	14.3%
	Barren area	7.6	3.2%
	Snow/glacier	1.1	0.4%
	Forest	156.1	65.8%
	Shrub land	4.2	1.8%
Lineament Density	Agriculture area	34.2	14.5%
	< 0.5	80.4	33.9%
	0.5 - 1.0	64.1	27.1%
	1.0 - 1.5	58.3	24.6%
Distance from road	> 1.5	34.1	14.4%
	0 - 1000	223.5	94.3%

Parameters	Class	Area (Km ²)	Area (%)
	1000 - 2000	11.6	4.9%
	> 2000	1.9	0.8%
Distance from stream	0 - 1500	179.3	75.6%
	1000 - 2500	53.6	22.6%
	> 2500	4.1	1.7%
TWI	< 6	152.4	64.3%
	6 - 8	61.4	25.9%
	8 - 12	20.1	8.5%
	> 12	3.1	1.3%
SPI	0 - 100000	236.2	99.6%
	100000 - 500000	0.7	0.3%
	500000 - 1000000	0.1	0.1%
	> 1000000	0.03	0.01%

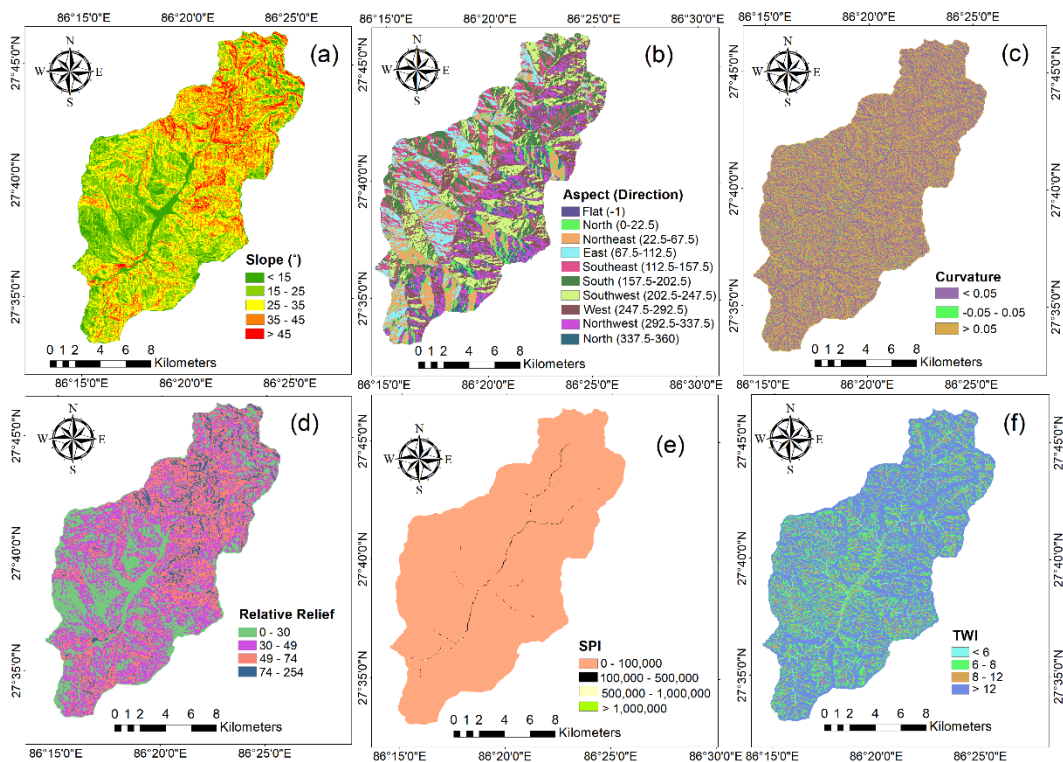


Figure 4-2: Thematic maps of factors used in landslide susceptibility mapping: (a) slope, (b) aspect, (c) curvature, (d) relative relief, (e) SPI, (f) TWI

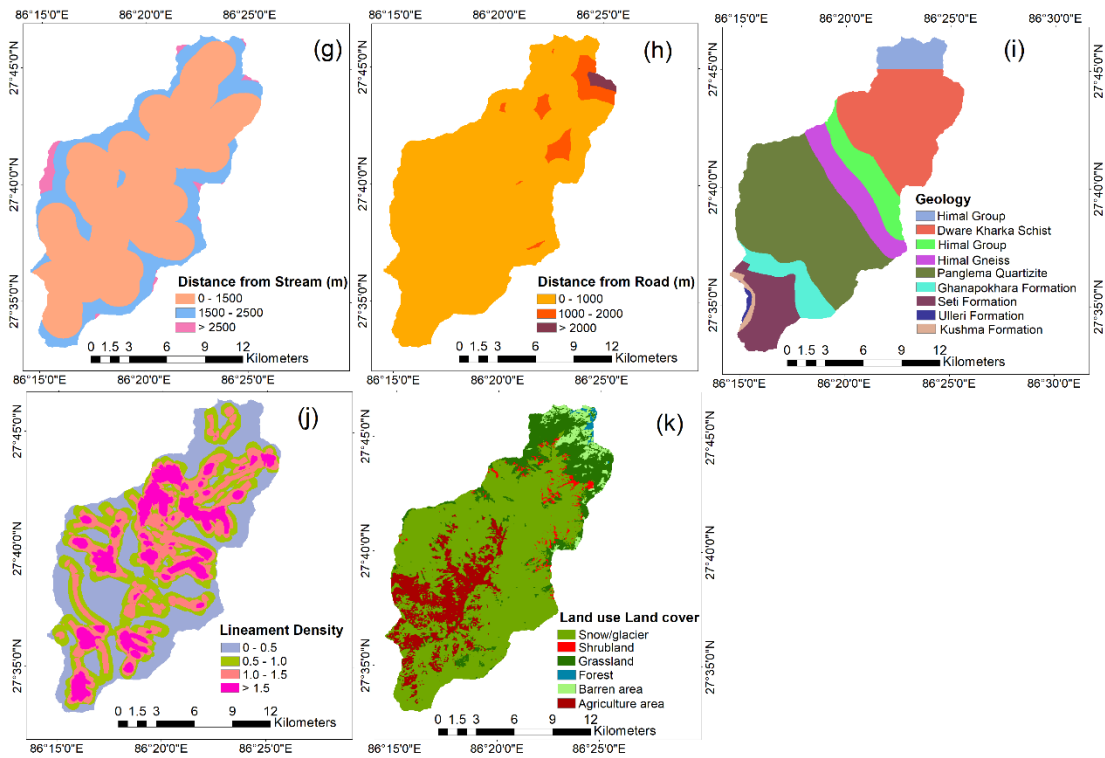


Figure 4-3: Thematic maps of factors used in landslide susceptibility mapping: (g) distance from stream, (h) distance from road, (i) geology, (j) lineament density, (k) land use/cover

4.1.3 Frequency Ratio Model

The implementation of the Frequency ratio model for landslide susceptibility analysis in the Khimti river basin is presented in this study. The parameters required for the analysis were prepared using ArcGIS 10.2 and Google earth. There were altogether eleven parameters selected for the study which were extracted from SRTM DEM of cell size 30m x 30m and relationship between previous occurred landslides and parameters was obtained using equations presented in section 3.3.13. The relationship between parameters and landslide occurrence is further explained by frequency ratio values, higher the value, more susceptible the parameter is susceptible to landslide. The FR values calculated for different classes of the parameters are presented in Table 4-2.

The FR and PR of each class were determined using the 70% training dataset after all of the conditioning factors had been prepared. Table 4-2 shows the percentage of landslides and domains, FR, RF, and PR, for each class and factor. In landslide susceptibility studies, FR is

used often. However, we have standardized between 0 and 1 for a better comparison and understanding of the influence in LSI computation. The PR value determines the weightage of each factor impacting landslide susceptibility.

Table 4-2: Frequency ratio (FR), relative frequency (RF), prediction rate (PR) of each factor for each considered class

Parameters	Class	Class Pixels	% Class Pixels	Landslide Pixel	% Landslide Pixel	FR	RF	Min(MaxRF-MinRF)	PR
Slope	< 15	29734.0	11.3	12.0	6.8	0.6	0.1		
	15 - 25	79842.0	30.3	20.0	11.3	0.4	0.1		
	25 - 35	90674.0	34.4	64.0	36.2	1.1	0.2		
	35 - 45	50463.0	19.2	70.0	39.6	2.1	0.4		
	> 45	12627.0	4.8	11.0	6.2	1.3	0.2		
Total		263340.0		177.0		5.4	1.0	0.1	3.3
Aspect	Flat(-1)	2.0	0.0	0.0	0.0	0.0	0.0		
	North(0 - 22.5)	12139.0	4.6	0.0	0.0	0.0	0.0		
	Northeast(22.5 - 67.5)	26187.0	9.9	2.0	1.1	0.1	0.0		
	East(67.5 - 112.5)	29609.0	11.2	7.0	3.9	0.4	0.1		
	Southeast(112.5 -	33169.0	12.6	32.0	18.1	1.4	0.2		
	South(157.5 - 202.5)	36275.0	13.8	108.0	61.0	4.4	0.6		
	Southwest(202.5 -	40800.0	15.5	23.0	13.0	0.8	0.1		
	West(247.5 - 292.5)	39132.0	14.9	5.0	2.8	0.2	0.0		
	Northwest(292.5 -	32360.0	12.3	0.0	0.0	0.0	0.0		
North(337.5 - 360)	13667.0	5.2	0.0	0.0	0.0	0.0			
Total		263340.0		177.0		7.4	1.0	0.1	6.3
Curvature	Concave(< -0.05)	124607.0	47.3	93.0	52.5	1.1	0.4		
	Flat(-0.05 - 0.05)	12653.0	4.8	10.0	5.7	1.2	0.4		
	Convex(> 0.05)	126080.0	47.9	74.0	41.8	0.9	0.3		
Total		263340.0		177.0		3.2	1.0	0.1	1.0
Relative Relief	0 - 30	78297.0	29.4	20.0	11.3	0.4	0.1		

Parameters	Class	Class Pixels	% Class Pixels	Landslide Pixel	% Landslide Pixel	FR	RF	Min(MaxRF-MinRF)	PR
	30 - 49	105957.0	39.7	64.0	36.2	0.9	0.2		
	49 - 74	66775.0	25.0	84.0	47.5	1.9	0.5		
	74 - 254	15597.0	5.9	9.0	5.1	0.9	0.2		
Total		266626.0		177.0		4.1	1.0	0.1	3.9
Geology	Himal Group	12667.0	4.8	44.0	24.9	5.2	0.7		
	Dware Kharka Schist	19400.0	7.4	0.0	0.0	0.0	0.0		
	Himal Group	69078.0	26.2	104.0	58.8	2.2	0.3		
	Himal Gneiss	22415.0	8.5	0.0	0.0	0.0	0.0		
	Panglema Quartzite	98235.0	37.3	28.0	15.8	0.4	0.1		
	Ghanapokhara	15262.0	5.8	1.0	0.6	0.1	0.0		
	Seti Formation	23200.0	8.8	0.0	0.0	0.0	0.0		
	Ulleri Formation	864.0	0.3	0.0	0.0	0.0	0.0		
Kushma Formation	2219.0	0.8	0.0	0.0	0.0	0.0			
Total		263340.0		177.0		7.9	1.0	0.1	6.8
Land use land cover	Grassland	37730.0	14.3	84.0	47.5	3.3	0.3		
	Barren area	8441.0	3.2	40.0	22.6	7.1	0.6		
	Snow/glacier	1185.0	0.5	0.0	0.0	0.0	0.0		
	Forest	173396.0	65.8	36.0	20.3	0.3	0.0		
	Shrub land	4624.0	1.8	3.0	1.7	1.0	0.1		
	Agriculture area	38054.0	14.5	14.0	7.9	0.6	0.0		
Total		263430.0		177.0		12.	1.0	0.1	6.0
Lineament Density	< 0.5	89322.0	33.9	63.0	35.6	1.1	0.3		
	0.5 - 1.0	71249.0	27.1	55.0	31.1	1.2	0.3		
	1.0 - 1.5	64758.0	24.6	31.0	17.5	0.7	0.2		
	> 1.5	37851.0	14.4	28.0	15.8	1.1	0.3		
Total		263180.0		177.0		4.0	1.0	0.1	1.1
	0 - 1000	248384.0	94.3	158.0	89.3	0.9	0.3		

Parameters	Class	Class Pixels	% Class Pixels	Landslide Pixel	% Landslide Pixel	FR	RF	Min(MaxRF-MinRF)	PR
Distance From Road	1000 - 2000	12867.0	4.9	19.0	10.7	2.2	0.7		
	> 2000	2089.0	0.8	0.0	0.0	0.0	0.0		
Total		263340.0		177.0		3.1	1.0	0.1	7.3
Distance From Stream	0 - 1500	199211.0	75.7	171.0	96.6	1.3	0.9		
	1000 - 2500	59529.0	22.6	6.0	3.4	0.2	0.1		
	> 2500	4600.0	1.8	0.0	0.0	0.0	0.0		
Total		263340.0		177.0		1.4	1.0	0.1	9.3
TWI	< 6	169317.0	64.3	104.0	58.8	0.9	0.2		
	6 - 8	68277.0	25.9	59.0	33.3	1.3	0.3		
	8 - 12	22301.0	8.5	12.0	6.8	0.8	0.2		
	> 12	3445.0	1.3	2.0	1.1	0.9	0.2		
Total		263340.0		177.0		3.9	1.0	0.1	1.3
SPI	0 - 100000	262398.0	99.6	177.0	100.0	1.0	1.0		
	100000 - 500000	756.0	0.3	0.0	0.0	0.0	0.0		
	500000 - 1000000	148.0	0.1	0.0	0.0	0.0	0.0		
	> 1000000	38.0	0.01	0.0	0.0	0.0	0.0		
Total		263340.0		177.0		1.0	1.0	0.1	10.

4.1.4 Landslide Susceptibility of the Watershed

Figure 4-4 shows the landslide susceptibility map created using PR values. Using the Jenks natural break classification method in GIS, the landslide susceptibility map is categorized into four classes: low (368 - 1067), moderate (1067 - 1701), high (1701 - 2055), and very high (2055 - 3108). Table 4-3 shows the area under various degrees of susceptibility. Around 70% of the total area in the study region is identified as low and moderate, and around 30% of the total area is classified as high and very high.

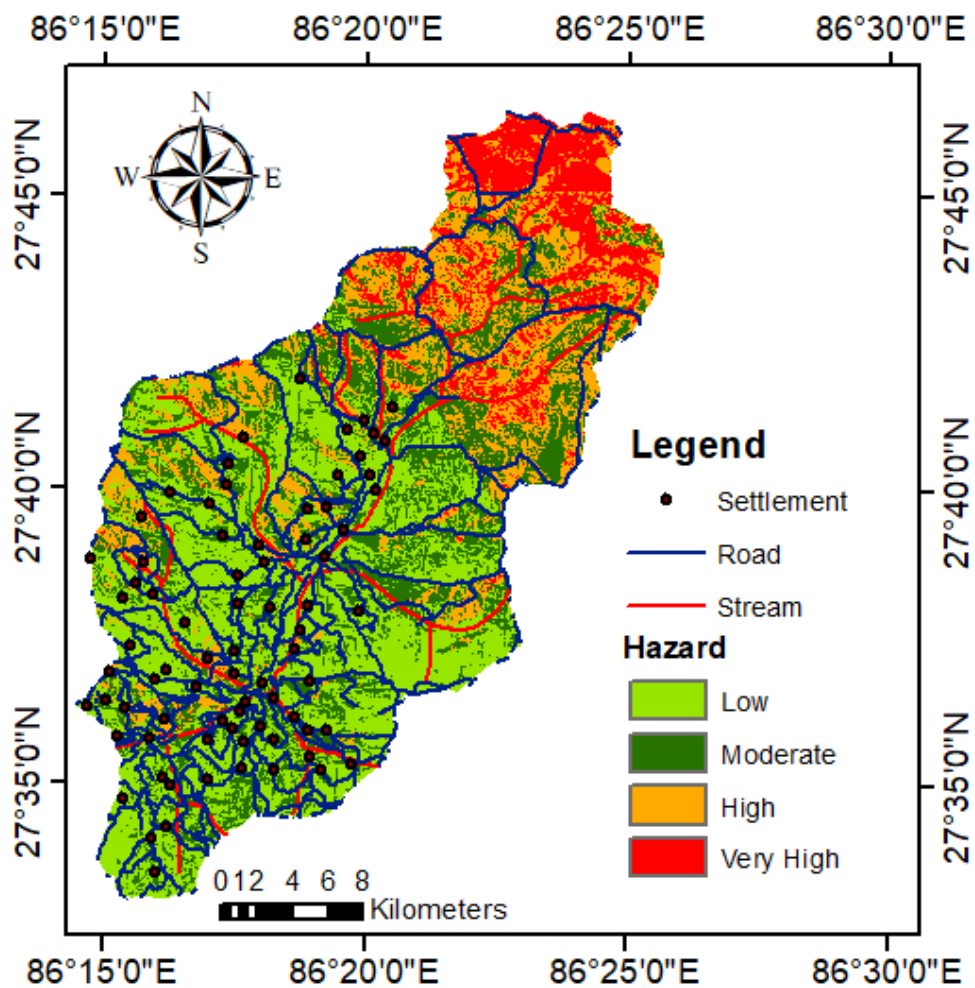


Figure 4-4: Landslide susceptibility map

Table 4-3: Landslide affected area for different hazard level

S.N.	Hazard	Area (km ²)	Landslide Number
1	Low	96.9	9
2	Moderate	66.5	15
3	High	49.7	20
4	Very High	23.2	26

4.1.5 Validation of the Map

The area under the curve (AUC) is utilized to validate the model in this study. The region between the horizontal axis and a specific curve that displays changes in classification result is known as the AUC curve. The landslide susceptibility map was reclassified into 100 classes using natural break in ArcGIS 10.2 to create the graph. For both the training and testing data sets, a graph was generated using a reclassified landslide susceptibility map, yielding success and prediction rate curves, respectively. 70% of the data from the landslide inventory map was used as training data, while the remaining 30% was used as testing data in this study. The model's ability to reliably categorize actual landslide occurrence is represented by the success rate, whereas the proposed landslide model's ability to forecast future landslides is represented by the prediction rate (Mersha et al., 2020). This study's success and prediction rates were found to be 71.4% and 65.8%, respectively. In this study, AUC value obtained is lower than that of AUC values obtained in other studies (Devkota et al., 2013; Regmi et al., 2014a; Regmi et al., 2014b). However, the AUC value spans from 0.5 to 1, and a model with an AUC value greater than 0.5 is considered acceptable (Swets et al., 1988). The lower value implies model limitations, as well as insufficient conditioning factor selection and unpredictability of training and testing dataset sampling. It could be linked to the longitudinal selection of the research region, as well as the complicated pattern of landslides caused by the great earthquakes of 2015. Consider the scenario in northern Pakistan after the 2005 Kashmir earthquake (Figure 4-5) (Kamp et al., 2008).



(a)



(b)



(c)

Figure 4-5: Landslides at khimti watershed: (a) siwalaya area (b) chyama landslide (c) pharpu dada area

The curve obtained for this study is given in Figure 4-6.

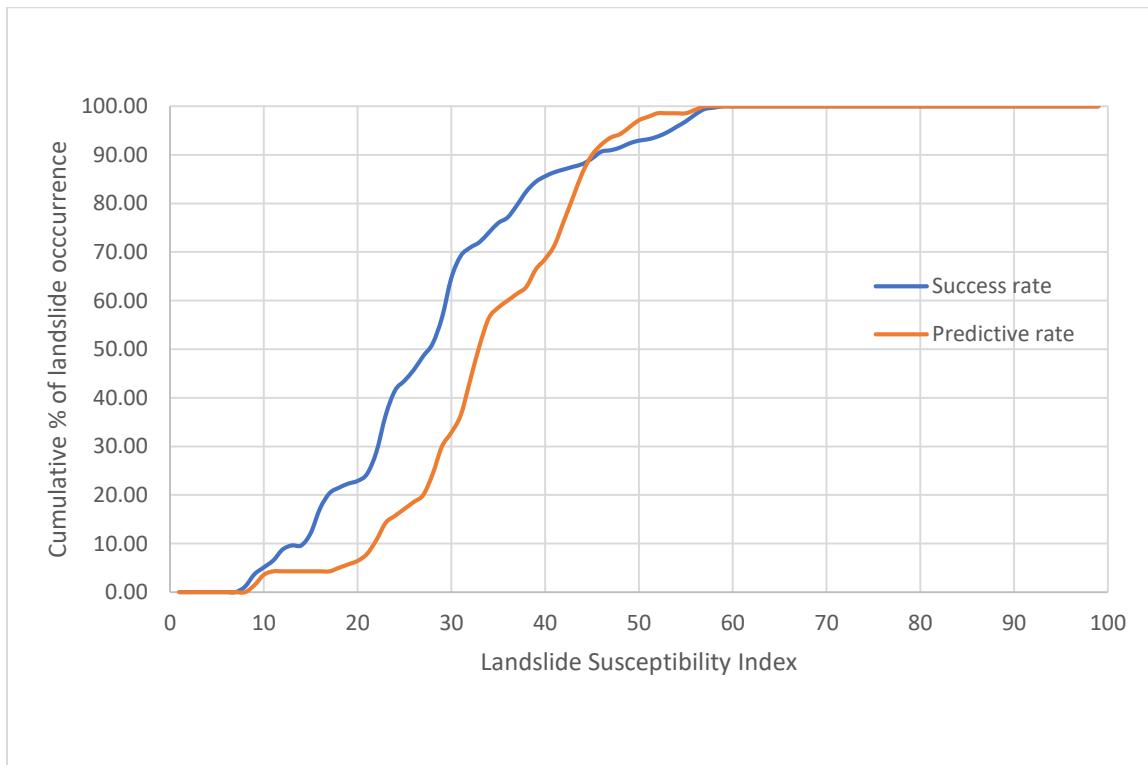


Figure 4-6: Area under curve

4.2 Flood Hazard Assessment

4.2.1 Floods of Different Return Periods

As Rasnalu Village (Station Index: 650) gauging station is situated at outside of the study area measures discharge of Khimti River, various statistical methods (Gumbel, Log Pearson Type III, Lognormal) were used in this study for comparative proposes. Statistical approaches apply techniques that involve calculating statistical information like mean values, standard deviations, skewness, and recurrence intervals utilizing observed yearly peak flow discharge data. These statistical data are then used to create frequency distributions, which are graphs and tables that show the probability of different discharges as a function of recurrence interval or exceedance probability. As a result, best-fit distribution analysis of floods derived from statistical approaches was undertaken to determine the applicability of a statistical method in flood estimation. The result obtained has been presented in Table 4-4 and comparison graph is illustrated in Figure 4-7. Figure 4-7 shows that log Pearson and log normal distribution forecasts higher flood values for different return periods whereas the Gumbel method underestimated the flood values.

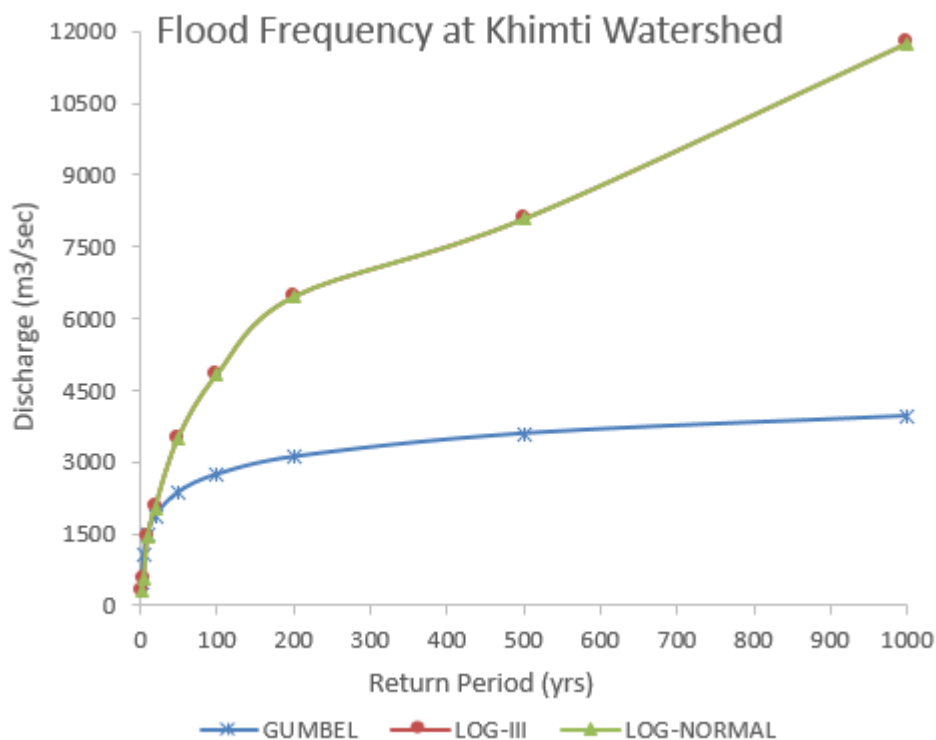


Figure 4-7: Flood frequency analysis using different methods at khimti watershed

Table 4-4: Comparison of flood discharge using various methods

Return period (yrs)	Flood frequency method			
	Gumbel's analitical	Gumbel's graphical	Log-Pearson Type III distribution	Log-normal distribution
2	482	402	317	317
5	1083	1024	556	556
10	1482	1494	1420	1419
20	1864	1965	2046	2046
50	2358	2586	3502	3501
100	2729	3057	4814	4811
200	3098	3527	6450	6445
500	3585	4149	8082	8074
1000	3954	4620	11769	11755

1. Best fit distribution

The best fit distributions were determined by comparing various statistical parameters among the observed and derived flood discharges as shown in Table 4-5.

Table 4-5: Statistical parameters for best fit distributions

Methods	Chi-Square	Co-relation Coefficient
Gumbel	0.59	0.63
Log-Pearson	1.74	0.86
Log-Normal	1.74	0.86

Based upon Correlation coefficient, and Chi-square test, Log-Pearson and Log-Normal both distribution represented a better approximation of observed discharge. Since, flood values obtained from Log-Pearson distribution are slightly higher than Log-Normal (Table 4-4), Log Pearson distribution was selected for flood inundation mapping.

4.2.2 Flood Hazard Map

The flood hazard map prepared using inundation depth obtained from HEC-RAS is given in Figure 4-8. Regarding the flow depth for the Q_{100} , it is divided into three categories. Less than 1 m, between 1 m to 3 m and greater than 3 m. 12.7% of inundated area has a depth of below 1 m, 28.3% of area has depth between 2 – 3m and 59% area has depth greater than 3m. The area affected for different types of hazards is given in table below. From the Table 4-6, it is concluded that area for inundation depth greater than 3m is highest which is 1.495 km². The detailed section of the flood hazard map is shown in Figure 4-9 and Figure 4-10 respectively.

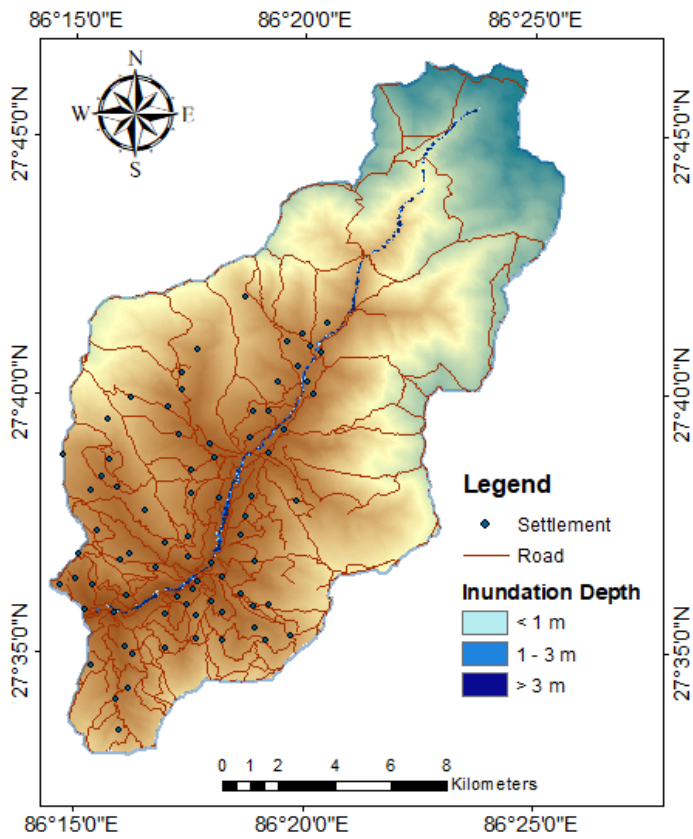


Figure 4-8: Flood hazard map

Table 4-6: Flood affected area for different hazard level

S.N.	Hazard	Depth(m)	Area(km ²)
1	Low	< 1	0.3
2	Moderate	1 - 3	0.6
3	High	> 3	1.3

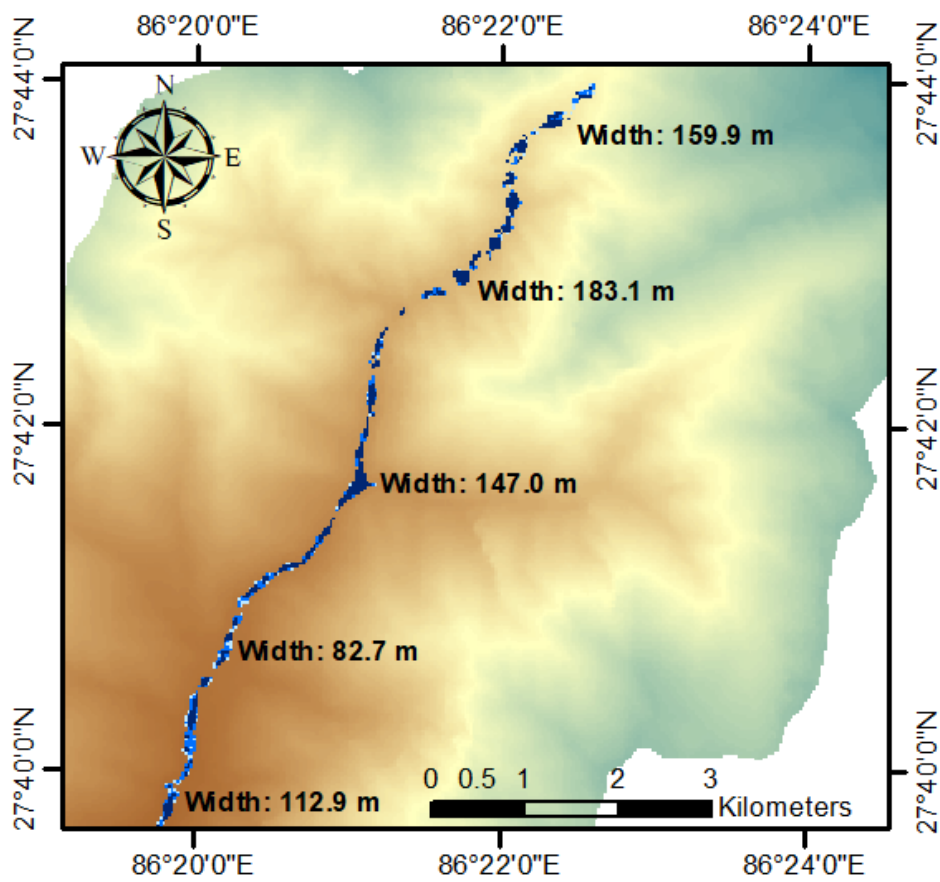
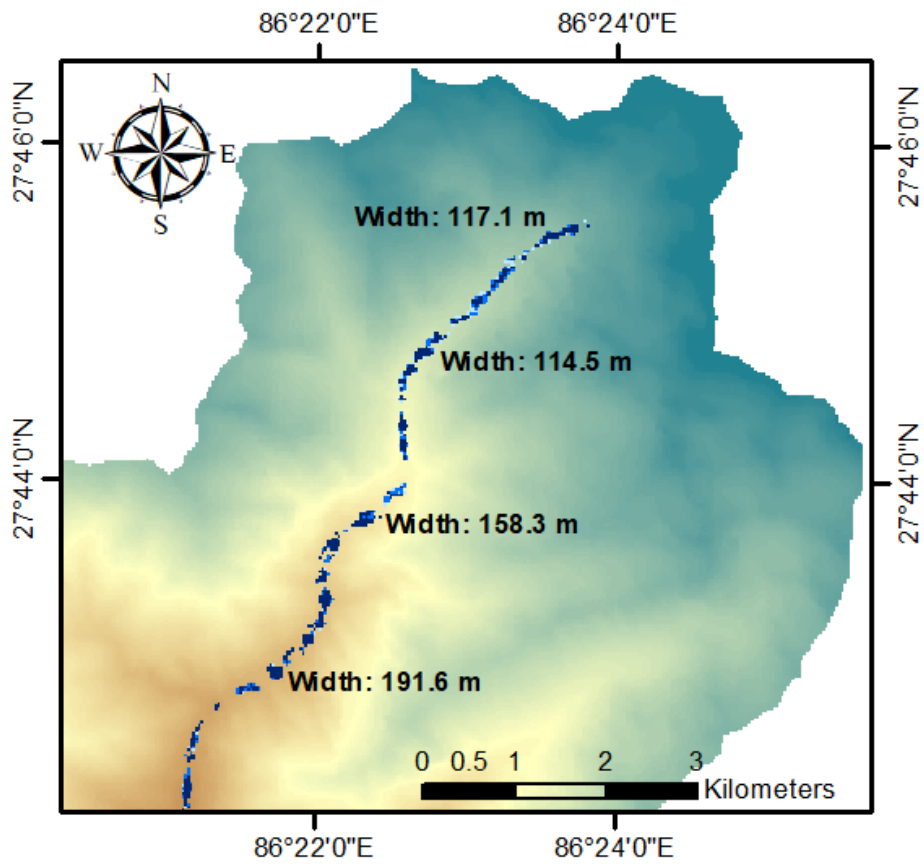


Figure 4-9: Detailed section of flood hazard map (a)

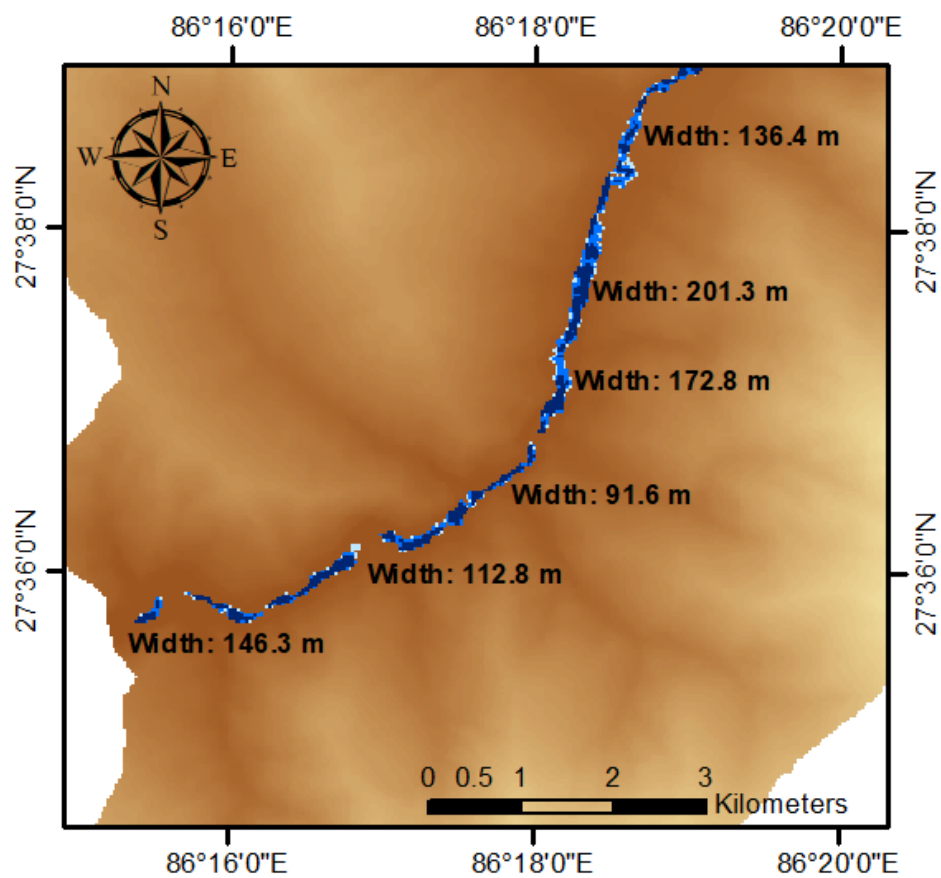
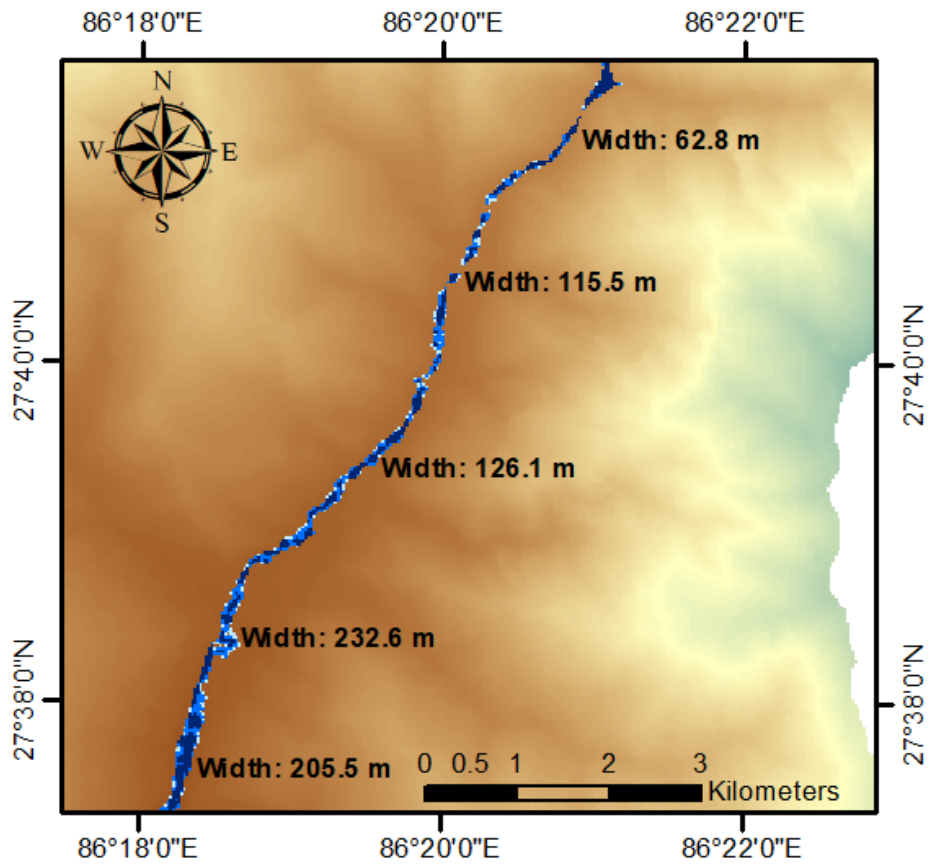


Figure 4-10: Detailed section of flood hazard map (b)

4.2.3 Flood Risk in the Watershed

For modelled flood event, the risky areas were estimated by clipping the land use/cover map of the study area. The low risk consists barren land, medium risk consists forest, shrub land and grass land, high risk consists agriculture area. It is computed that 1.1 % of the inundated area fall under low hazard, 46.2 % fall under medium hazard and 52.7 % fall under high hazard. The classification of flooded area according to land use risk is given in Table 4-7 below.

Table 4-7: Classification of flooded area according to land use risk

S.N.	Risk	Area(km²)
1	Low	0.02
2	Medium	0.9
3	High	1.1

Regarding LULC it is also seen that Agricultural areas are mostly affected by the flood which is accounted to be 51.6 % and barren land is least affected which is found to be 1.0 %.The flood affected area for different land use land cover is given in Table 4-8 below.

Table 4-8: Flood affected area of land use

S.N.	Land use	Area(km²)
1	Forest	0.7
2	Agriculture area	1.1
3	Shrub land	0.04
4	Grassland	0.3
5	Barren area	0.02

The flood risk map is given in Figure 4-11.

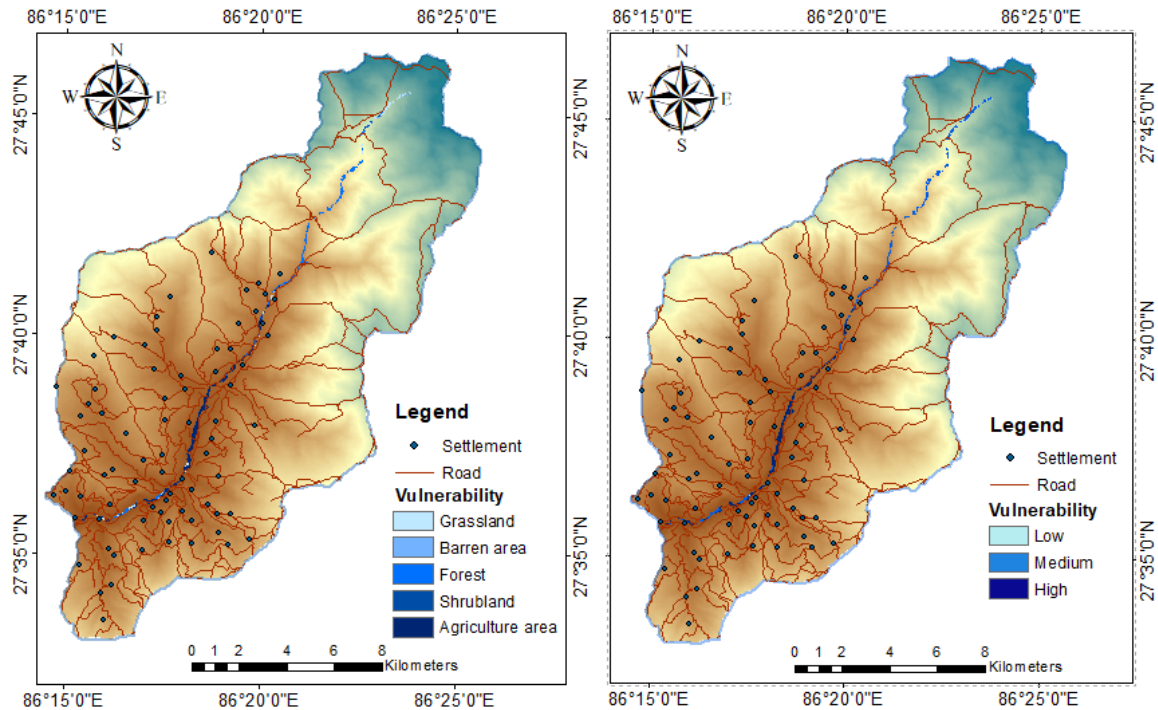


Figure 4-11: Flood risk map

4.3 Seismic Hazard Assessment

4.3.1 Completeness Test

All the declustered earthquake events were divided into a magnitude range with an interval of 1 starting from magnitude 4.0. It has been observed that 4.0 magnitude will be completed in 35 years' time interval, 5.0 in 46 years' time interval, 6.0 in 65 years' time interval, 7.0 in 90 years' time interval and 8.0 in 100 years' time interval. Earthquakes data for completeness test and Completeness test of Earthquakes data have been presented in Table 4-9 and Figure 4-12 respectively.

Table 4-9: Activity rate and interval of completeness

Magnitude (M_w)	No. of Events $\geq M_w$	Complete in Interval (year)	No. of Events per year $\geq M_w$
4	424	35	12.11
5	143	46	3.11
6	17	65	0.26
7	3	90	0.03
8	1	100	0.01

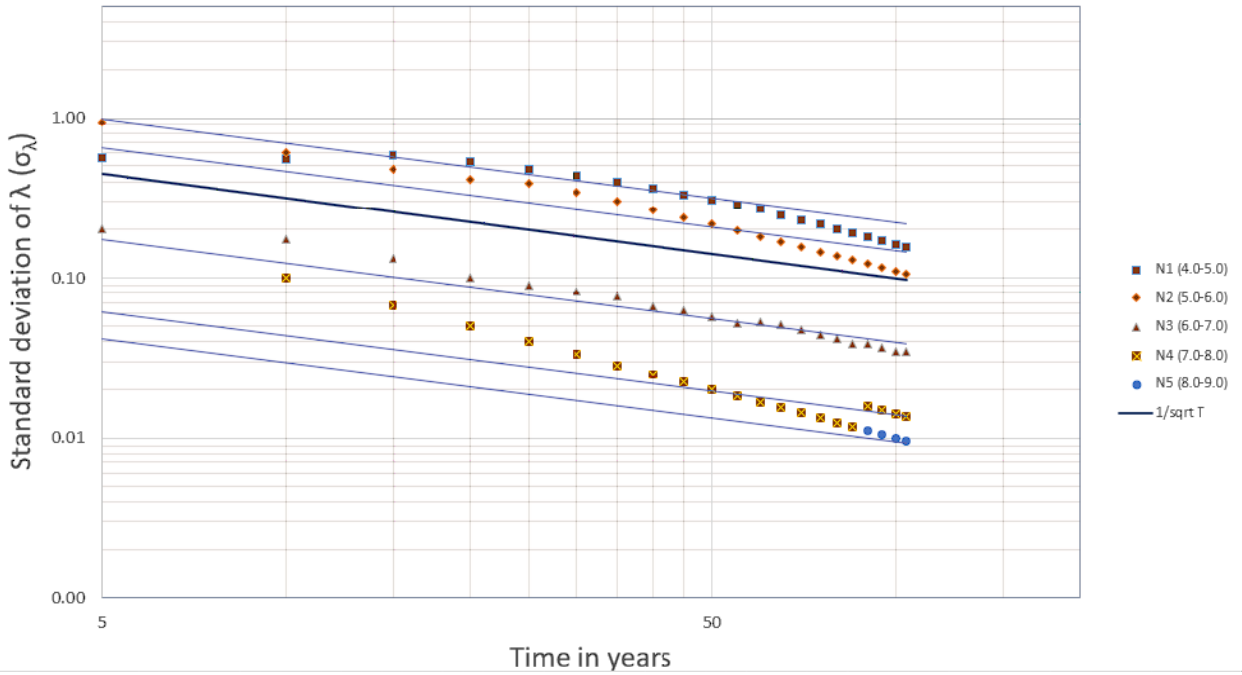


Figure 4-12: Completeness analysis of earthquake data

Using completeness analysis Regional Recurrence Relationship has been obtained as

$$\text{Log}_{10}(N) = 4.39 - 0.81 M_w$$

On comparing the regional recurrence relationship with the Gutenberg-Richter formula

$\text{Log}_{10}N = a - b M_w$, the essential parameter b is obtained as 0.81.

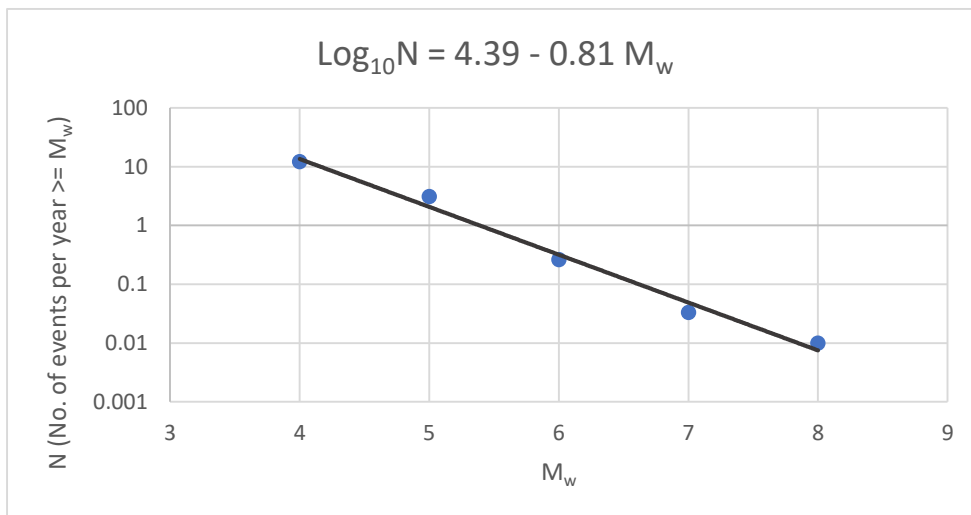


Figure 4-13: Regional recurrence relationship

4.3.2 Seismic Hazard in the Watershed

Following the procedure explained in Section 3.5.2 and after assigning the parameters for all the sources, the Seismic Hazard Map for various return periods is produced by CRISIS 2007. The hazard map for a 500-year return time was used in this investigation, since the design basis earthquake for Nepal is based on a 500-year return period, (i.e., 10% probability of exceedance in 50 years) is the only factor evaluated.

Figure 4-14 and Figure 4-16 shows the contour plot of PHA as obtained from different sources for rock site and soil site respectively. There is a concentration of higher PHA values in eastern region as comparison to other regions. In Khimti watershed area, it can be observed from Figure 4-15 and Figure 4-17 that the PHA value ranges from 0.51g to 0.52g and 0.76g to 0.764g for rock sites and soil sites respectively. The obtained results are consistent with the results from some recent literatures. For example, Thapa and Guoxin, (2013) obtained that in eastern part of Nepal for rock sites, PGA value varies from 0.57 g to 0.62 g at 10% probability of exceedance in 50 years. Subedi et al., (2016) obtained seismic hazard maps for 3 types of soil and showed that the PGA values is least for the hard soil, highest for soft soil and in between for medium type soil.

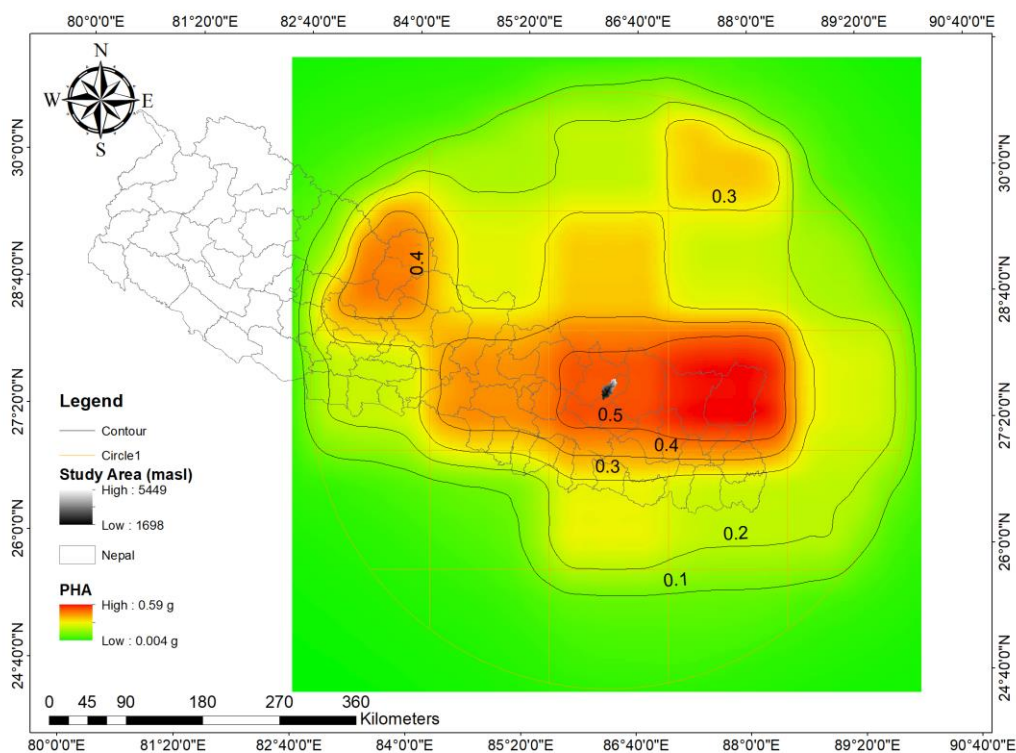


Figure 4-14: Seismic hazard map of source zone for PHA for rock sites (for 500 yrs. Return Period)

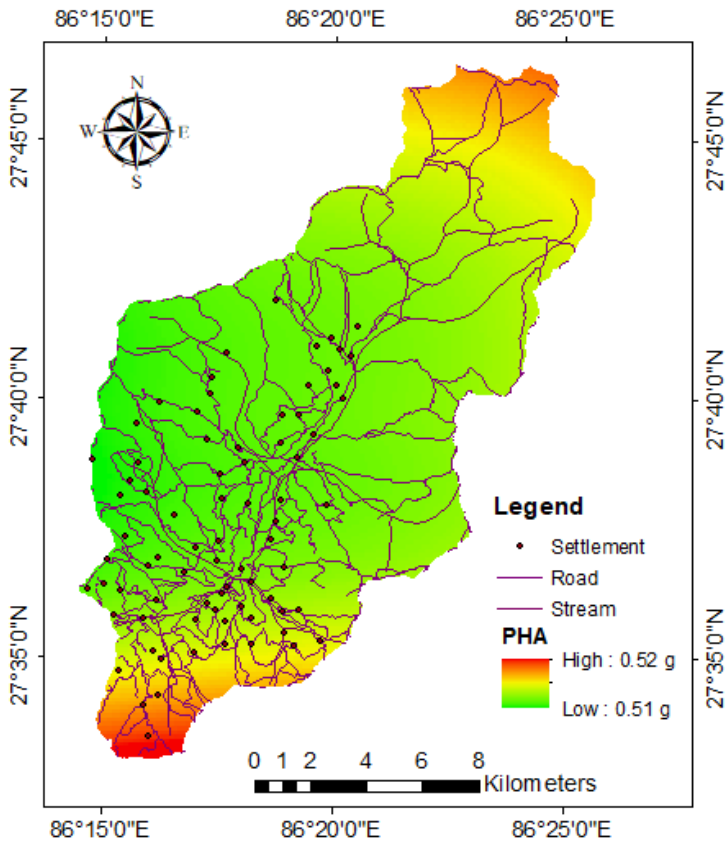


Figure 4-15: Seismic hazard map of khimti watershed for PHA for rock sites (for 500 yrs. return period)

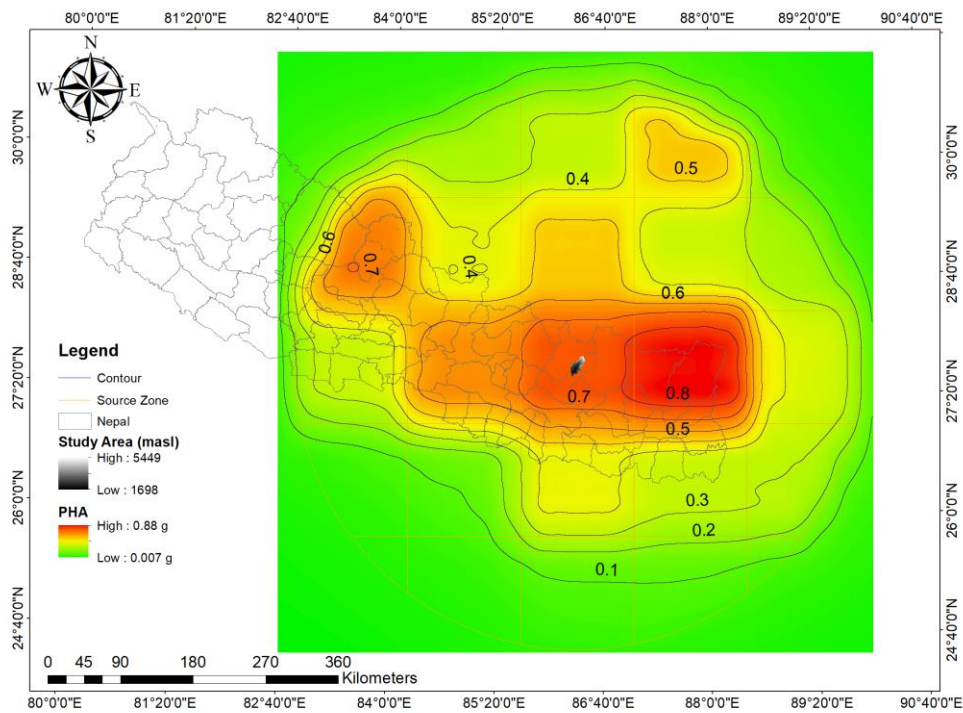


Figure 4-16: Seismic hazard map of source zone for PHA for soil sites (for 500 yrs. return period)

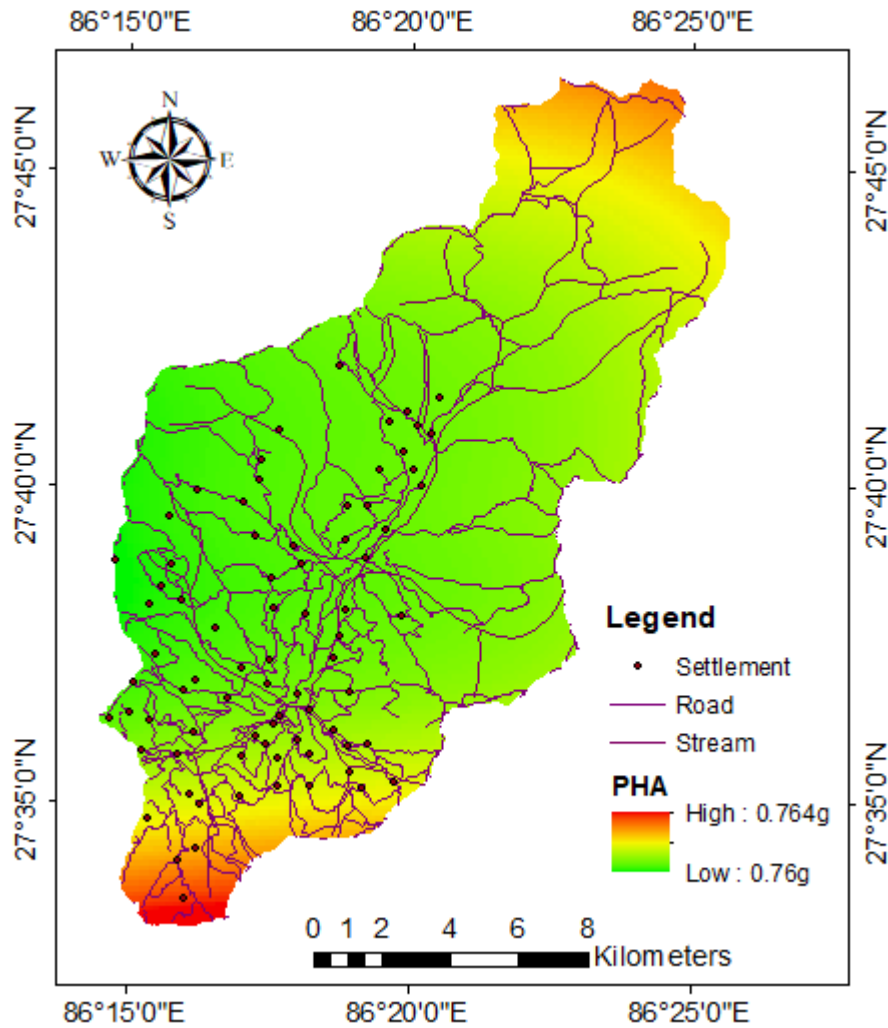


Figure 4-17: Seismic hazard map of khimti watershed for PHA for soil sites (for 500 yrs. return period)

4.4 Multi-Hazard Mapping

For assessing risk to multi-hazard, firstly two different hazard maps were integrated together to determine risks related to combination of any two hazards and then all hazards were integrated together to provide standardized information related to all hazards for khimti watershed.

Figure 4-18, Figure 4-19, Figure 4-20, Figure 4-21 and Figure 4-22 shows combination of two different hazard maps of Khimti watershed. These areas are characterized by a very low to very high level of landslides, flood and seismic hazard.

4.4.1 Combination of Landslide and Seismic Hazard Maps

As illustrated in Table 4-10 and Table 4-11, 0.3%, 47.5%, 28.7%, 15.7%, and 7.8% of the total area of the Khimti watershed represent very low, low, moderate, high and very high potential to combination of landslide and seismic hazard for both rock and soil sites.

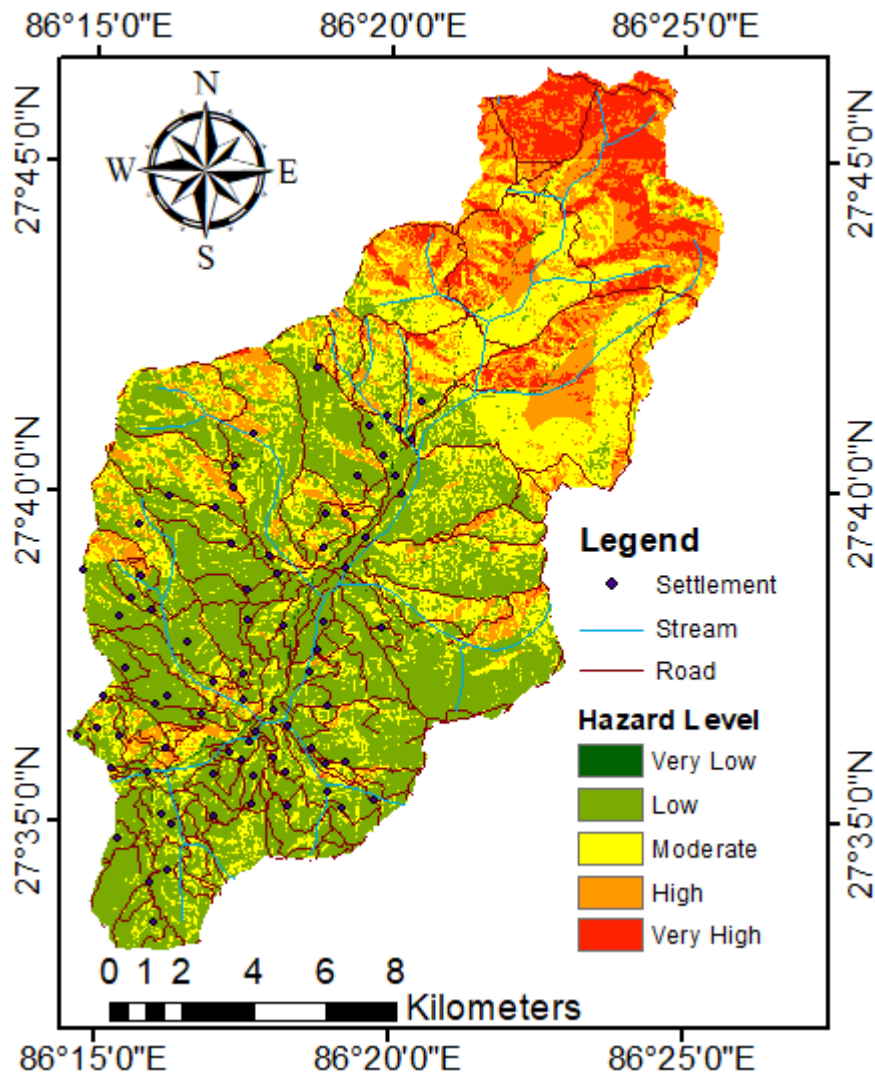


Figure 4-18: Combination of landslide and seismic hazard map of khimti watershed in case of rock site

Table 4-10: Combination of landslide and seismic hazard affected area for different hazard level for rock site

S.N.	Hazard	Area (km ²)	Area (%)
1	Very Low	0.8	0.3
2	Low	112.2	47.5
3	Moderate	67.7	28.7
4	High	37.2	15.7
5	Very High	18.3	7.8

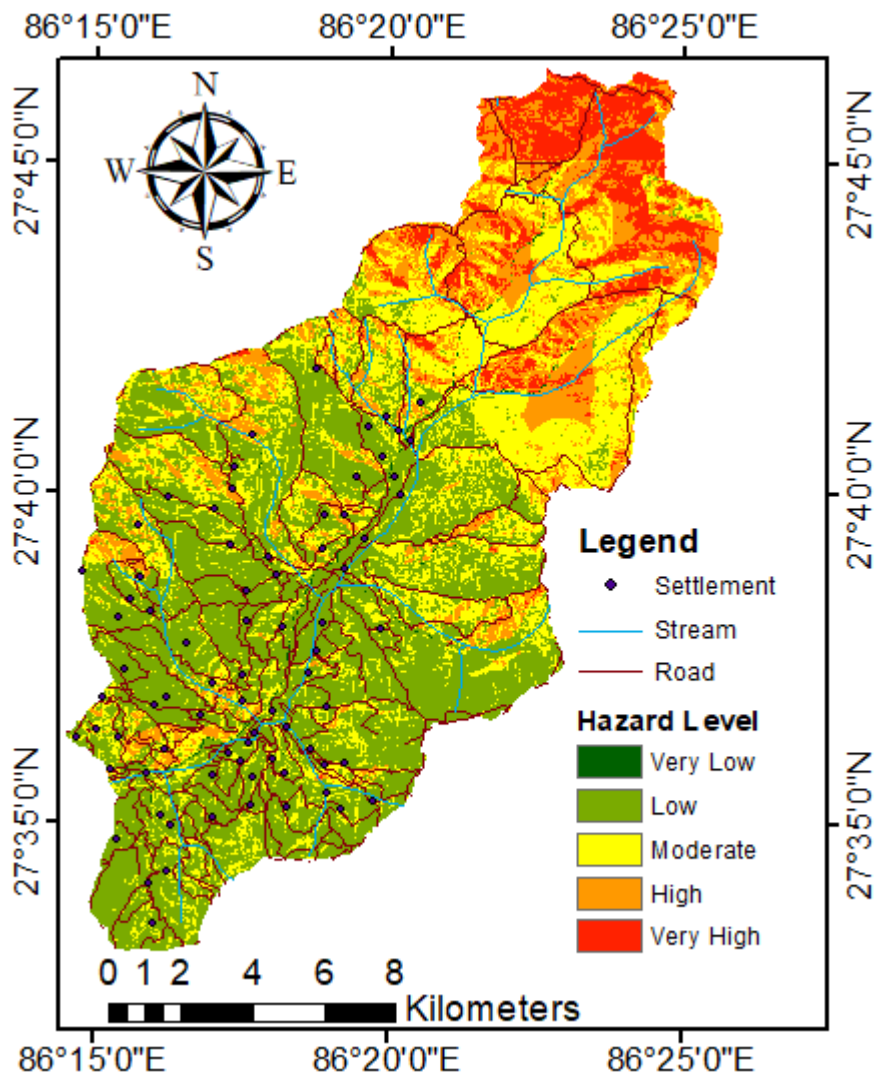


Figure 4-19: Combination of landslide and seismic hazard map of khimti watershed in case of soil site

Table 4-11: Combination of landslide and seismic hazard affected area for different hazard level for soil site

S.N.	Hazard	Area (km ²)	Area (%)
1	Very Low	0.8	0.3
2	Low	112.2	47.5
3	Moderate	67.7	28.7
4	High	37.2	15.7
5	Very High	18.3	7.8

4.4.2 Combination of Landslide and Flood Hazard Maps

From Table 4-12, it can be seen that 36.6%, 27.8%, 19.2%, 11.7% and 4.6% of the total area of the Khimti watershed represent very low, low, moderate, high and very high potential to combination of landslide and flood hazard.

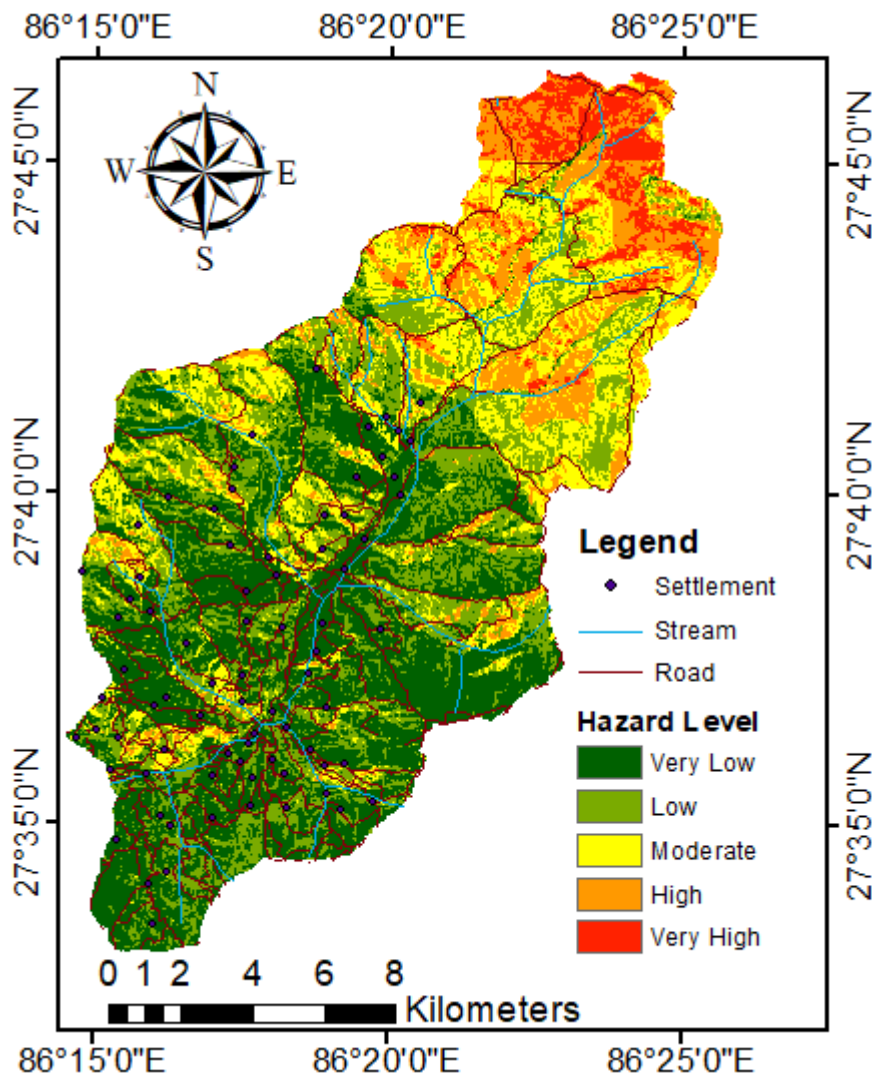


Figure 4-20: Combination of landslide and flood hazard map of khimti watershed

Table 4-12: Combination of landslide and flood hazard affected area for different hazard level

S.N.	Hazard	Area (km ²)	Area (%)
1	Very Low	86.5	36.6
2	Low	65.8	27.8
3	Moderate	45.4	19.2
4	High	27.6	11.7
5	Very High	10.9	4.6

4.4.3 Combination of Seismic and Flood Hazard Maps

From Table 4-13 and Table 4-14, it can be seen that, 33.3%, 35.2%, 16.0%, 11.6%, and 3.9% of the area of the Khimti watershed represent very low, low, moderate, high and very high potential to combination of seismic and flood hazard in rock site and 34.0%, 35.3%, 15.6%, 11.4%, and 3.6% of the area of the study area represent very low, low, moderate, high and very high potential to combination of seismic and flood hazard for soil site.

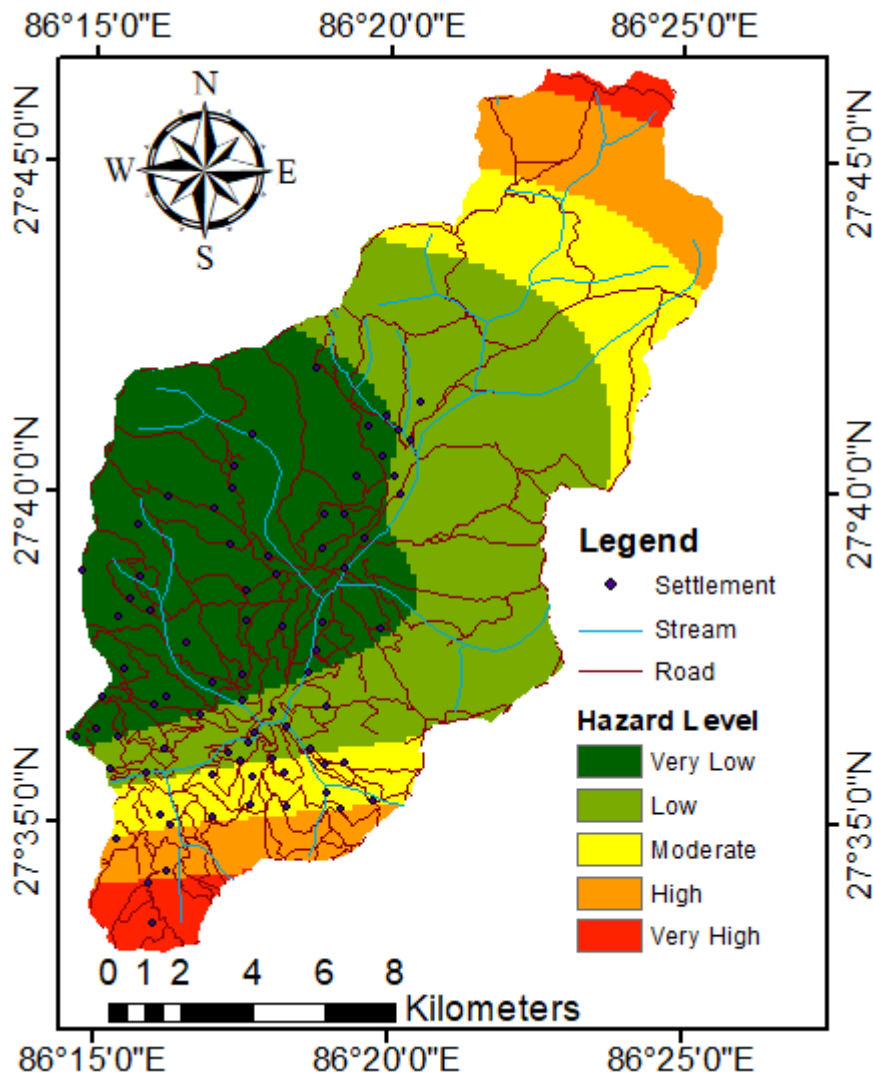


Figure 4-21: Combination of seismic and flood hazard map of khimti watershed in case of rock site

Table 4-13: Combination of seismic and flood hazard affected area for different hazard level for rock site

S.N.	Hazard	Area (km ²)	Area (%)
1	Very Low	79.0	33.3
2	Low	83.3	35.2
3	Moderate	37.9	16.0
4	High	27.5	11.6
5	Very High	9.3	3.9

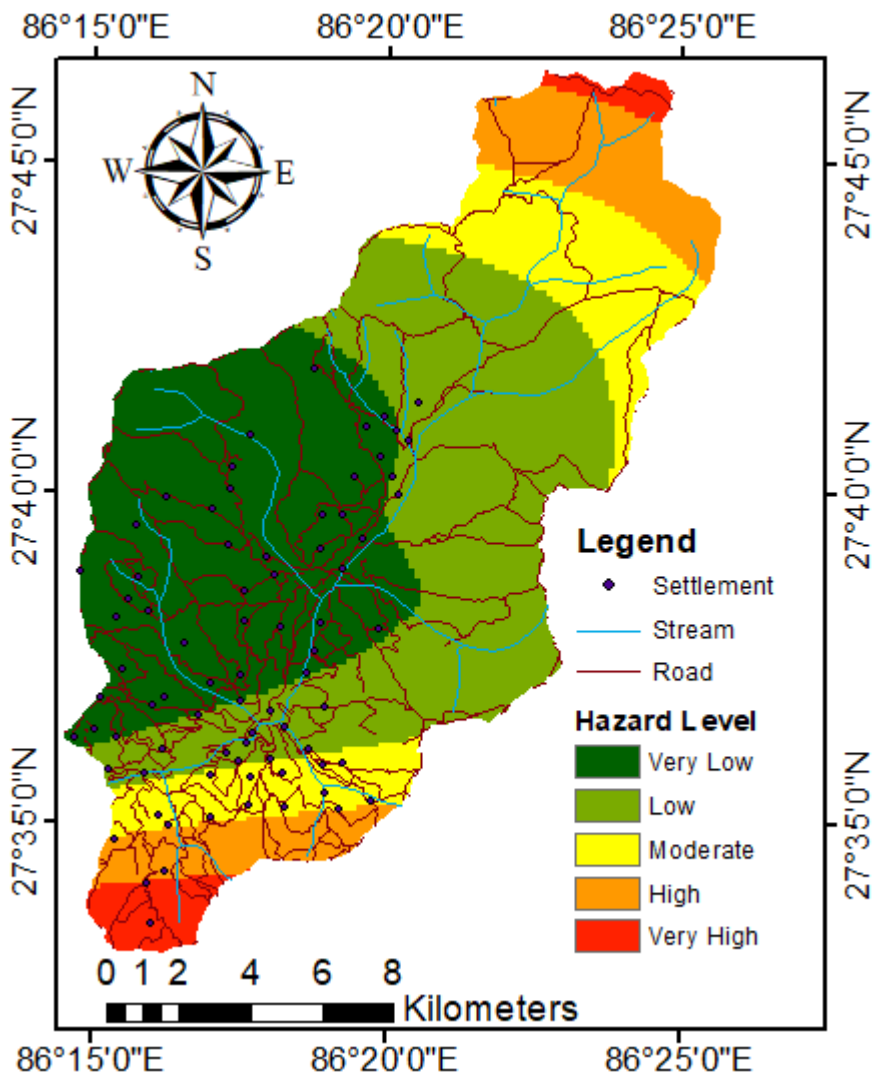


Figure 4-22: Combination of seismic and flood hazard map of khimti watershed in case of soil site

Table 4-14: Combination of seismic and flood hazard affected area for different hazard level for soil site

S.N.	Hazard	Area (km²)	Area (%)
1	Very Low	80.5	34
2	Low	83.7	35.3
3	Moderate	37.1	15.6
4	High	27.1	11.4
5	Very High	8.6	3.6

4.4.4 Multi-Hazard Map

Figure 4-23 and Figure 4-24 shows multi-hazard map of Khimti watershed for seismic hazard at rock and soil sites respectively. These areas characterized by very low to very high level of landslides, seismic, and flood hazard. As illustrated in Table 4-15 and Table 4-16, 41.3%, 23.0%, 4.8%, 21.1%, and 9.8% of the area of the Khimti watershed represent very low, low, moderate, high and very high potential to multi-hazard, respectively in rock site and 41.3%, 23.1%, 4.7%, 21.1%, and 9.8% of the area of the study area represent very low, low, moderate, high and very high potential to multi-hazard for soil site.

Some of the issues that cause major challenges in multi-hazard analysis include differences in hazard characteristics (Carpignano et al. 2009), inter-relationships of hazard that cause triggering and cascading effects (Kappes et al., 2010), natural processes that have heterogeneous impacts on elements at risk, and methods to describe vulnerability that differ between hazards (Kappes et al., 2012). The multi-hazard map is time-dependent and subject to change as a result of future events and unanticipated occurrences. To update the multi-hazard map, it is necessary to upgrade and improve the database.

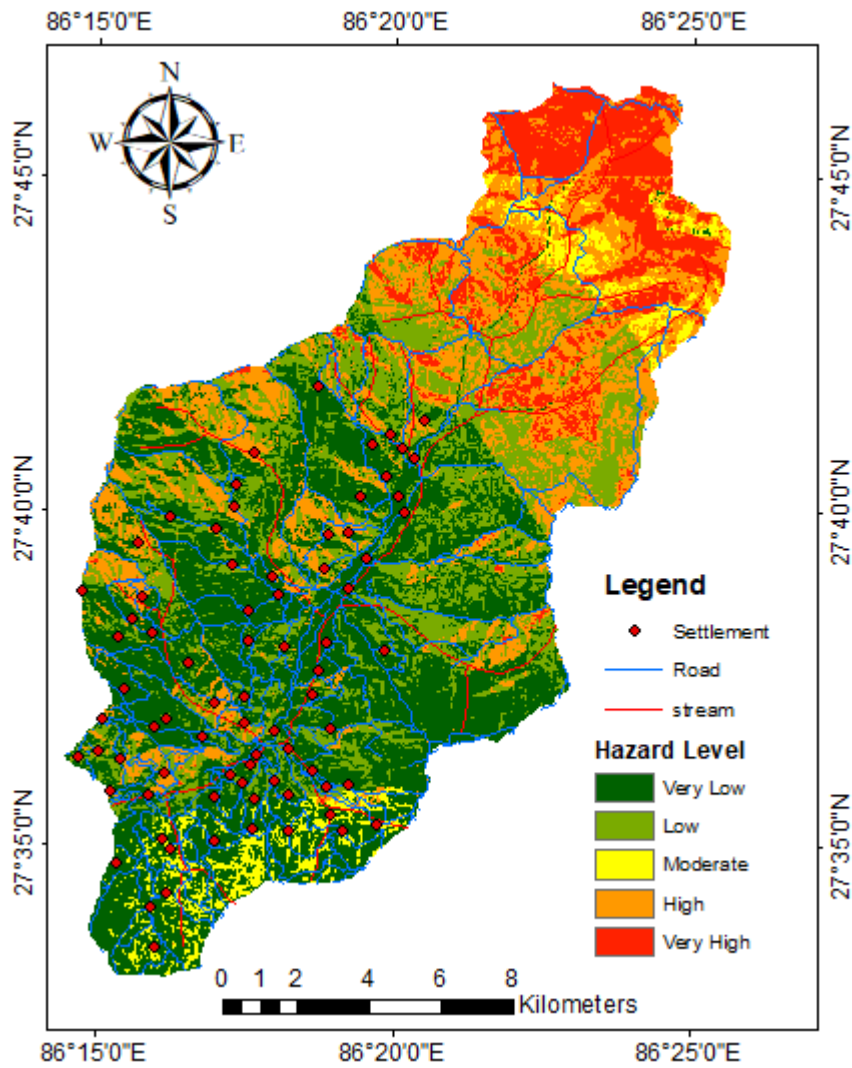


Figure 4-23: Multi-hazard map of khimti watershed in case of rock site

Table 4-15: Multi-hazard affected area for different hazard level for rock site

S.N.	Hazard	Area (km ²)	Area (%)
1	Very Low	97.5	41.3
2	Low	54.3	23.0
3	Moderate	11.4	4.8
4	High	49.7	21.1
5	Very High	23.2	9.8

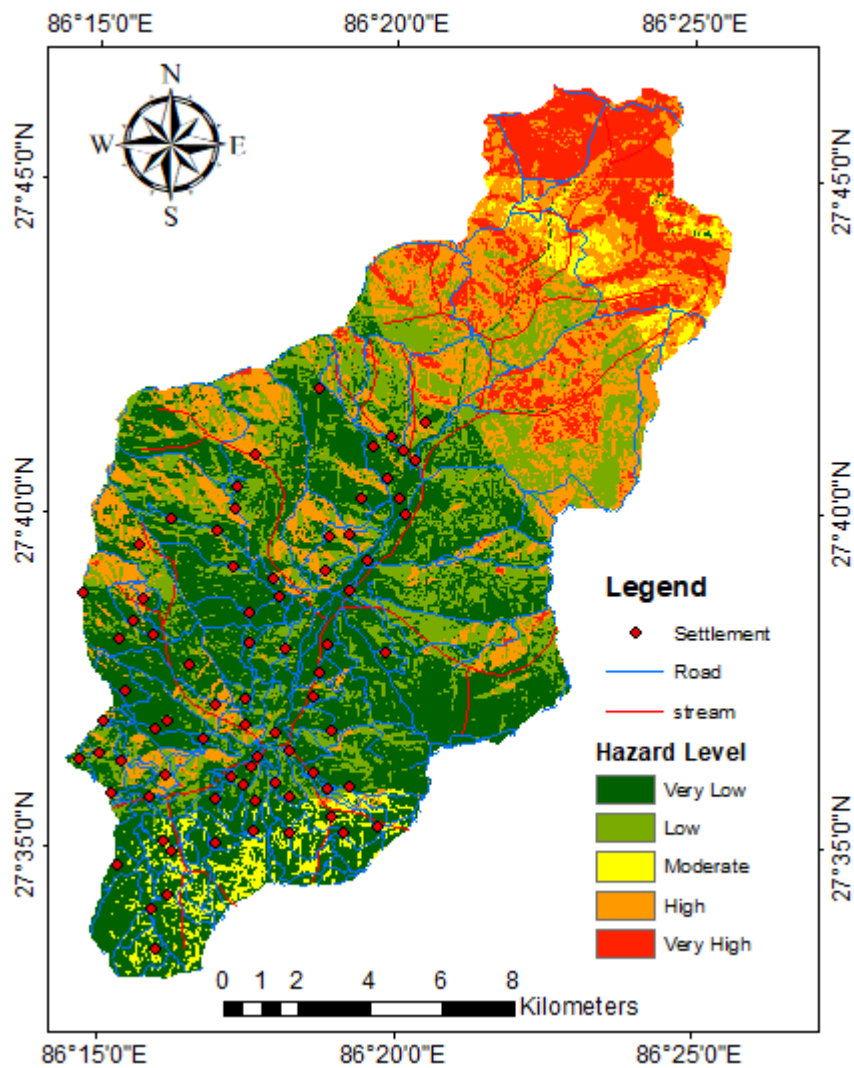


Figure 4-24: Multi-hazard map of khimti watershed in case of soil site

Table 4-16: Multi-hazard affected area for different hazard level for soil site

S.N.	Hazard	Area (km ²)	Area (%)
1	Very Low	97.6	41.3
2	Low	54.6	23.1
3	Moderate	11.1	4.7
4	High	49.7	21.1
5	Very High	23.2	9.8

The hazard potential to different levels (i.e. very low, low, moderate, high, and very high) varies from the multi-hazard map when two different hazard maps are integrated together. For landslide and seismic hazard combination, maximum area is under low hazard zone (112.2 Km²) followed by moderate zone (67.7 Km²), whereas for landslide and flood hazard combination, maximum area is under very low zone (86.5 Km²) followed by low zone (65.8

Km²) and for combination of seismic and flood hazard, maximum area lies under low zone (83.3 Km²) followed by very low zone (79.0 Km²) for rock sites and low zone area (83.7 Km²) and very low zone area (80.5 Km²) for soil sites. For multi-hazard map, maximum area is under very low zone (97.5 Km², 97.6 Km²) followed by low zone (54.3 Km², 54.6 Km²) for rock and soil sites respectively. The developed maps for different hazards will be useful to the researchers, planners for the well managed sustainable development of the study area.

4.5 Projected Future Climate

The Khimti watershed projected future climate, including precipitation, maximum temperature (T_{\max}) and minimum temperature (T_{\min}) were analyzed based on the data from representative 1103 meteorological station as this is the only station near the watershed providing both precipitation and temperature data representing the overall spatial heterogeneity existing in the projected future climate of the watershed. In this study long term average annual, monthly and seasonal trend of baseline and projected precipitation, T_{\max} and T_{\min} were analyzed. In this study ensemble of 5 bias corrected GCMs output were taken under SSP245 and SSP585 scenarios. Three future time frames were considered: near-future (NF, 2021 – 2045), mid-future (MF, 2046 – 2070) and far-future (FF, 2071 – 2095) to analyze climate change against the baseline period of 1980-2006. The detail description of projected future climate is described in the upcoming section.

4.5.1 Performance Evaluation of Bias Correction

CMIP6 model output was downloaded from <https://esgf-node.llnl.gov/search/cmip6/>. Raw GCMs output cannot be directly used for future prediction because of the differences observed between observed and GCMs output in historical time period as shown in Figure 4-25, Figure 4-26 and Figure 4-27 for ACCESS-CM2 model. As a result, bias correction of the GCM output is required. For hydrological applications, bias adjustment of raw GCM results is strongly suggested, especially for use at finer geographic scales (Teutschbein & Seibert, 2012). For improving the performance of GCMs, quantile mapping (QM) has emerged as a better technique for bias correction (Berg et al., 2012). Using a transfer function, QM corrects the quantiles of raw GCM data with those of observed data (Pandey et al., 2019).

i. Bias Correction for precipitation

Out of different QM methods, Enayati et al., (2021) found that robust empirical quantiles (RQUANT) methods proved to be excellent options to correct the bias of rainfall data. Thus, in this study, empirical robust quantile mapping was utilized, and the result is presented in Figure 4-25 was suitable for bias correcting future GCM output derived under SSP245 and SSP585 scenarios using the relation established.

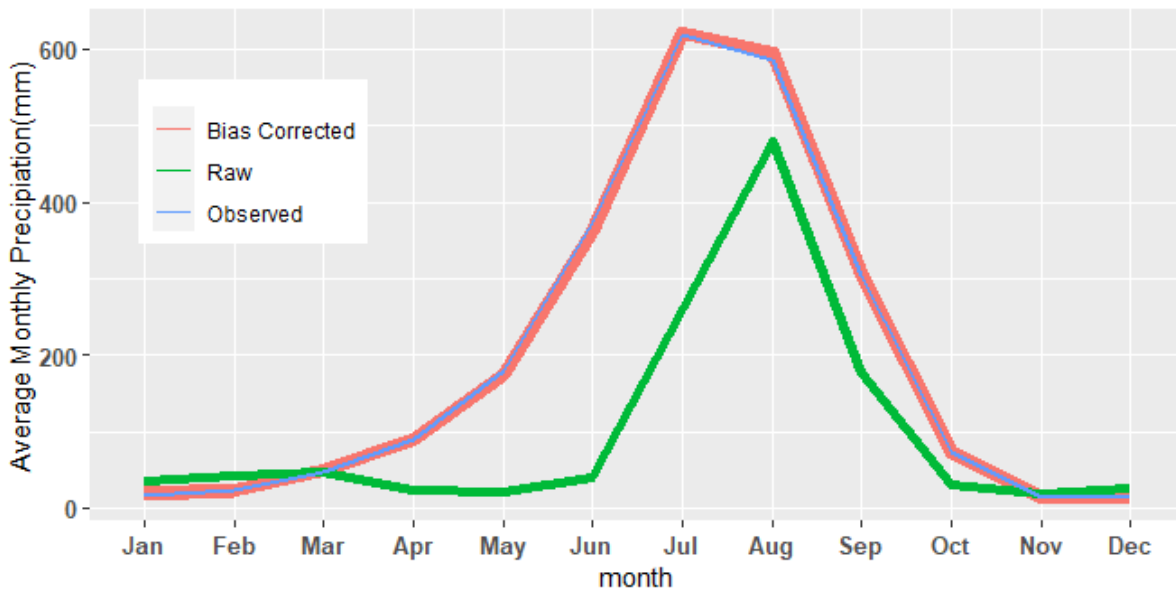


Figure 4-25: Comparison of raw and bias corrected data with observed data for precipitation of baseline period and for ACCESS- CM2 GCM used in this study for station 1103

i. Bias correction for temperature

Robust empirical quantiles (RQUANT) approaches were excellent options for correcting the bias of rainfall data, whereas all bias correction methods performed rather well for the temperature variable, with the significant exceptions of performed PTF: scale and SSPLIN. This is mostly due to the unique nature of temperature and the GCM/RCM combinations' superior ability to model this climatic variable when compared to rainfall (Enayati et al., 2021). Therefore, in this study, the PTF: linear transfer function was utilized, and the results produced as shown in Figure 4-26 and Figure 4-27 were satisfactory for bias correcting future GCM output obtained under the SSP245 and SSP585 scenarios using the relation formed.

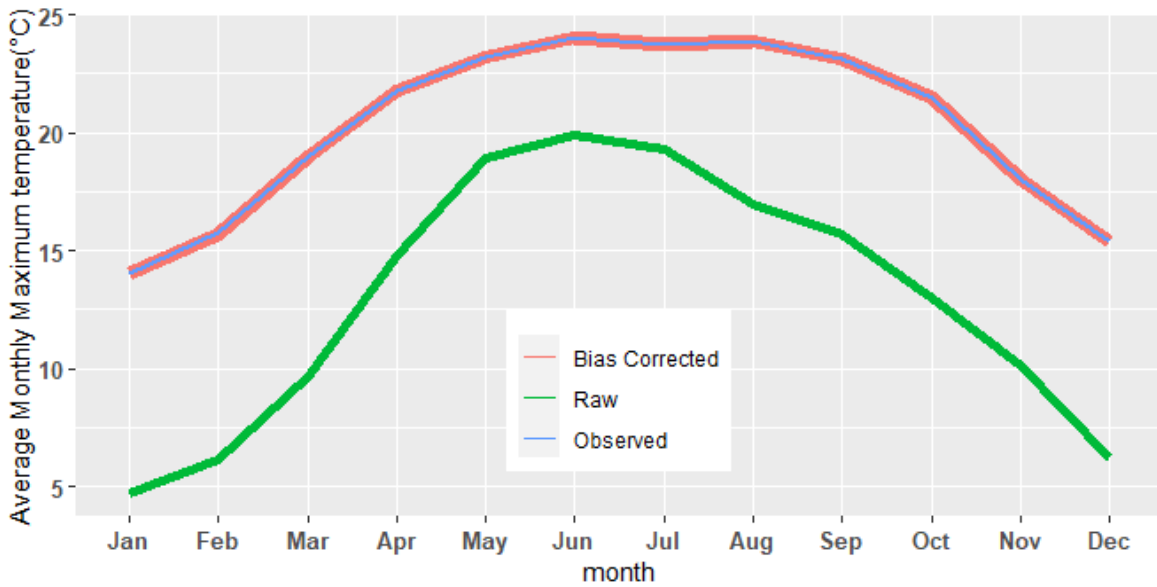


Figure 4-26: Comparison of raw and bias corrected data with observed data for maximum temperature of baseline period and for ACCESS- CM2 GCM used in this study for station 1103

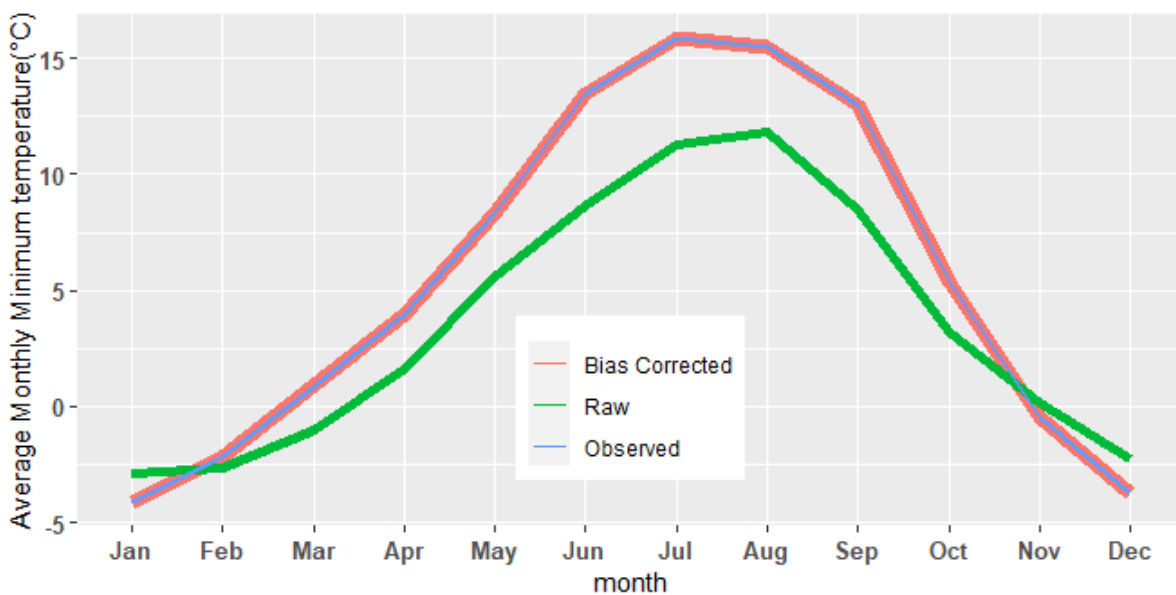


Figure 4-27: Comparison of raw and bias corrected data with observed data for minimum temperature of baseline period and for ACCESS- CM2 GCM used in this study for station 1103

4.5.2 Projected Future Precipitation

Annual total precipitation for the climate baseline and future periods shows no obvious trend as shown in Figure 4-28. Projected range of annual total precipitation for the three future periods are 2301.7 – 2465.4 mm (NF); 2496.2 – 2572.7 mm (MF); and 2739.7 – 2798.8 mm

(FF); respectively. It indicates an increase in the uncertainty range when we progress further in the future.

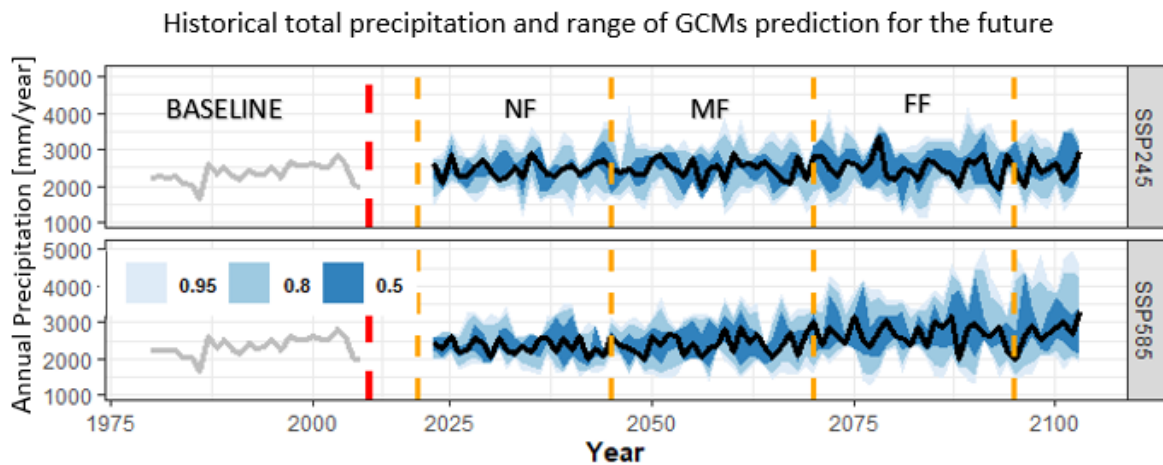


Figure 4-28: Trends in long-term annual average total precipitation at station 1103

From Figure 4-28, it can be seen that for both SSP scenarios, the baseline period shows observed data, while the future time frames show a range of bias corrected projections from different GCMs. Near-, mid-, and far- futures are denoted by the letters NF, MF, and FF, respectively. For each scenario, the dark line depicts an ensemble of five GCMs. The projections' range is indicated by shaded areas.

The range of changes in projected total precipitation by the five GCMs for annual time series is presented in Figure 4-28. The annual ranges are clearly not representative of seasonal changes because the negative and positive changes over the seasons are averaged out in the annual numbers (Pandey et al., 2019). The annual and monsoon (JJAS) precipitations have the least uncertainty when considering the range of projections as a measure of uncertainty. For all the scenarios and futures analyzed, post monsoon (ON) precipitation demonstrates a significant level of uncertainty. Even while the estimates from different GCMs are similar for the yearly and monsoon seasons, they differ significantly for other seasons.

In the Figure 4-29, each box represents a range in a single GCM, with whiskers indicating maximum and minimum values excluding outliers, line markers indicating the median, and x markers indicating the mean annual total precipitation change projected for each future time frame. DJF refers to the winter months of December, January, and February, MAM to the dry months of March, April, and May, JJAS to the monsoon months of June, July, August, and September, and ON to the autumn months of October and November (post monsoon season).

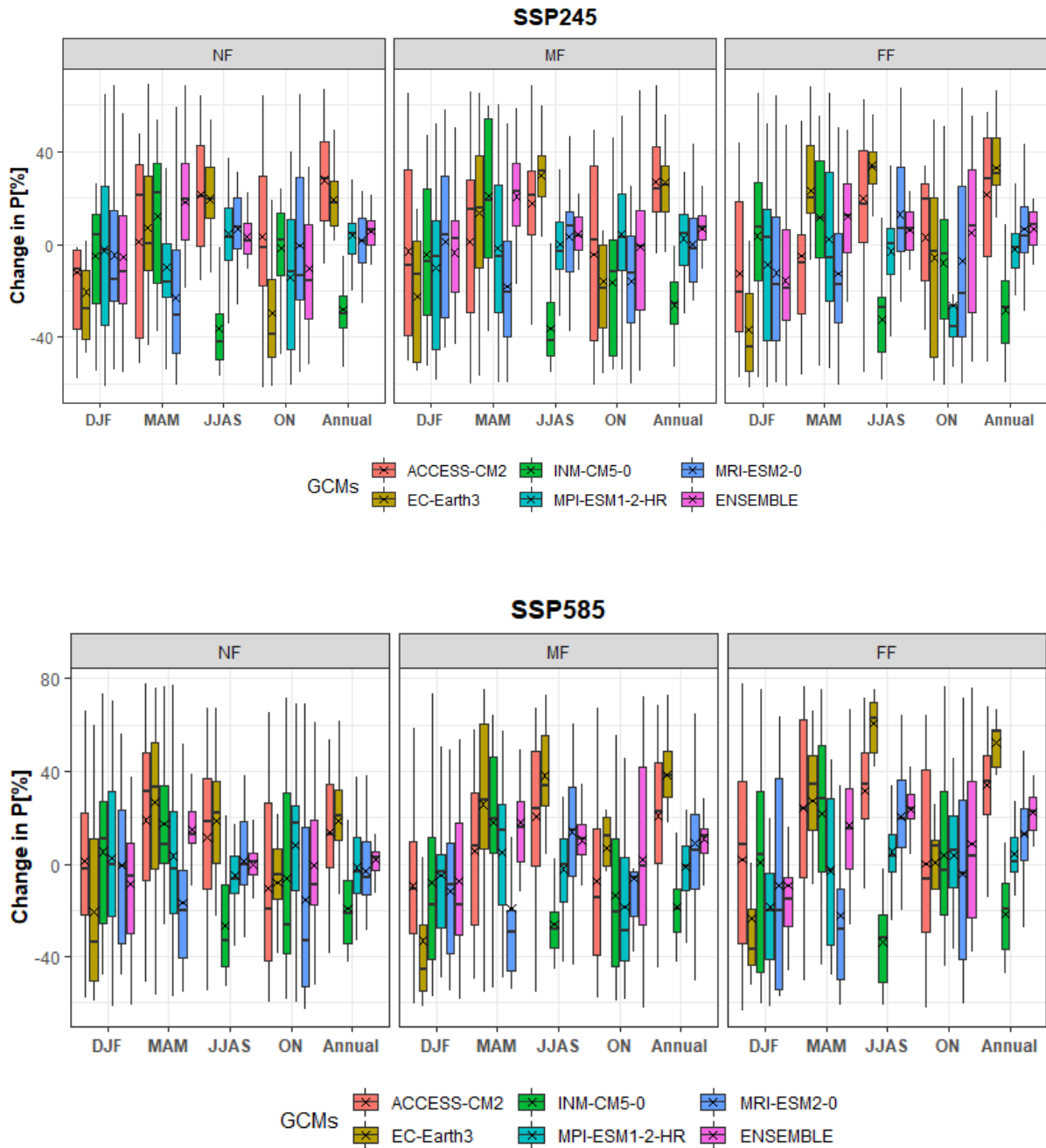


Figure 4-29: Range of projected change in annual total future precipitation for different futures, SSPs and GCMs at station 1103

Figure 4-29 summarizes the projected changes in average annual and seasonal precipitation values for SSP245 and SSP585 scenarios based on the ensemble of five GCMs. In the context of the SSP585 scenario, average yearly values are expected to increase throughout three future periods and are found to be constantly increasing, while rate of change varies over time (Figure 4-29). Taking an example of SSP245 scenarios, average annual precipitation is projected to increase by 5.3% in NF, 6.8% in MF and 6.7% in FF; however, it varies over the years from -8.8 – 21.4 % for NF, -10.5 – 24.8% for MF and -9 - 19.7% for FF. Table 4-17 shows that only

the MAM season has consistent increasing trends from NF to FF, as well as a faster rate of change than the other seasons. For the SSP245 scenario, the DJF season shows a consistent gradual decreasing trend from NF to FF; however, all other seasons shows an increasing trend from NF to MF. When we move from NF to MF, the range of projection brackets expands, indicating a higher degree of uncertainty in projection as we move further into the future. The above result clearly indicates that climate change is causing drier winter/dry season and wetter other seasons, which is a cause for concern because it will cause energy and water scarcity during the dry season and may exacerbate water-related disasters such as floods and landslides (Bajracharya et al., 2018) during the monsoon season.

Table 4-17: Projected changes in total precipitation (mm) at seasonal and annual scales at 1103 station based on ensemble of five GCMs under SSPs scenarios

Range from baseline [%]		DJF	MAM	JJAS	ON	Annual	
Baseline (mm)		55.54	318.18	1881.92	86.59	2342.23	
SSP 245	NF	mean[%]	-1.6	17.9	3.4	6.3	5.3
		Range[%]	-55 – 96.5	-19.2 – 68.3	-10.6 – 22.3	-51.6 – 122.8	-8.8 – 21.4
	MF	mean[%]	- 3	20.6	4.4	14.2	6.8
		Range[%]	-68.3 – 74.3	-17.5 – 58.5	-11.3 – 21.6	-54.6 – 154.2	-10.5 – 24.8
	FF	mean[%]	- 9.7	12.2	6	11.5	6.7
		Range[%]	-61.1 -132.8	-25.2 – 49.2	-11.1 – 22.8	-51 – 171.1	-9 - 19.7
SSP 585	NF	mean[%]	-4.2	15	-0.3	-0.4	1.7
		Range[%]	-60.9 – 106.4	-9.6 – 43.4	-15.4 – 18.8	-52 – 60.7	-12.5 – 12.7
	MF	mean[%]	1	17.8	10.2	7.3	10.9
		Range[%]	-58.3 - 113	-12.1 – 76.3	-9.4 – 34.1	-81.7 – 140.5	-9.4 – 28.3
	FF	mean[%]	-9.2	19.6	23.5	29.4	22.4
		Range[%]	-46.1 – 52.9	-26 – 87.3	4.2 - 41.8	-38 – 133.7	7 - 38.3

4.5.3 Projected Future Temperature

Unlike precipitation, the average annual time series of projected temperature, as shown in Figure 4-30 and Figure 4-31, shows a clear increasing trend until the end of the century for both maximum and minimum temperatures. Projected range of average annual maximum temperature within each future periods are 21.2 – 21.4 °C for NF, 21.9 – 22.5 °C for MF, and 22.4 – 24 °C for FF as shown in Figure 4-30, higher than the baseline value of 20.6 °C. In case of minimum temperature, the range is 7.2 – 7.3 °C for NF, 8.3 – 9.2 °C for MF, and 9 -11.7 °C for FF as shown in Figure 4-31. In both cases, the range widens as we get closer to the future, reflecting greater uncertainty in the distant future.

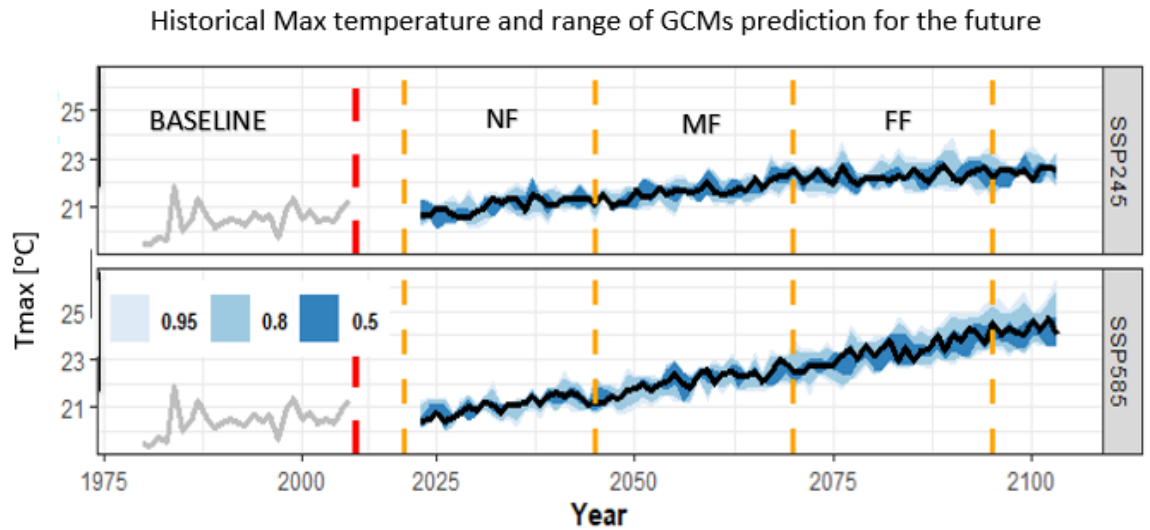


Figure 4-30: Trends in long-term annual average maximum temperature at station 1103

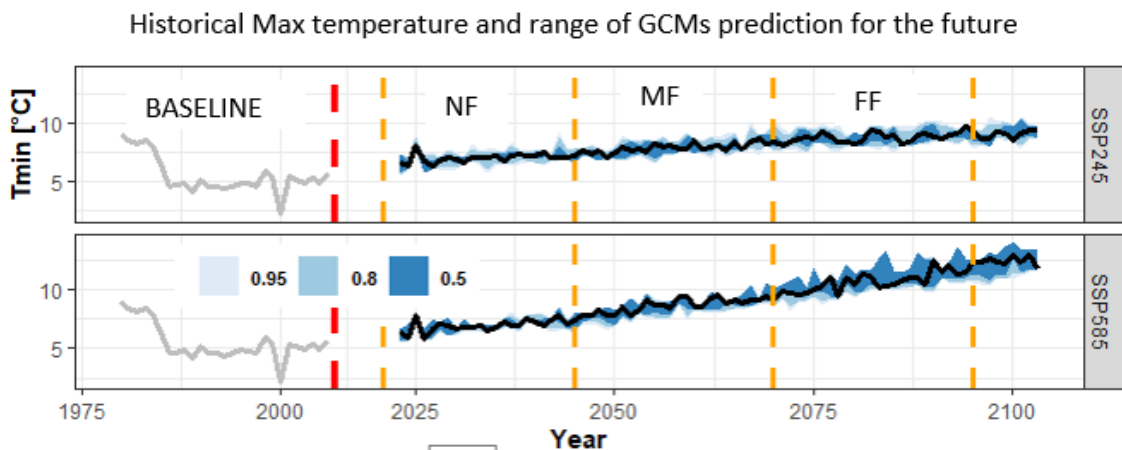


Figure 4-31: Trends in long-term annual average minimum temperature at station 1103

i. Maximum Temperature:

The range of maximum temperature predictions across the different GCMs is more consistent and predictable than the range of precipitation predictions. With both means and medians, all changes for all GCMs, SSPs, and futures imply a rise. As shown in Table 4-18, projected average annual maximum temperatures for SSp245 scenarios, based on an ensemble of five GCMs, are steadily increasing 0.9 °C (for NF), 1.6 °C (for MF), and 2.1 °C (for FF) during three future periods compared to the baseline. In case of SSP585, it is projected to increase by 1.1 °C (for NF), 2.2 °C (for MF), 3.5 °C (for FF). It is also increasing throughout the year, though the amount of increase varies. The range of the uncertainty in the projection is relatively high in winter (DJF) and pre-monsoon (MAM) seasons as shown in Figure 4-32.

Table 4-18: Projected future maximum temperature [$^{\circ}\text{C}$] at station 1103 based on ensemble of five GCMs under SSPs scenarios

Range from baseline [$^{\circ}\text{C}$]			DJF	MAM	JJAS	ON	Annual
Baseline ($^{\circ}\text{C}$)			48.23	21.32	23.70	19.75	28.25
SSP 245	NF	mean [$^{\circ}\text{C}$]	1.3	1	0.7	0.8	0.9
		Range [$^{\circ}\text{C}$]	0.6 - 1.9	-2.1	0.2 - 1	0.1 - 1.2	0.4 - 1.4
	MF	mean [$^{\circ}\text{C}$]	2.2	1.8	1.3	1.4	1.6
		Range [$^{\circ}\text{C}$]	1.4 - 3.2	0.9 - 3.1	0.7 - 1.6	2-1	1.2 - 2.3
	FF	mean [$^{\circ}\text{C}$]	2.7	2.4	1.6	1.8	2.1
		Range [$^{\circ}\text{C}$]	2.3 - 3.1	1.7 - 3.1	1.3 - 2	0.8 - 2.5	1.9 - 2.5
SSP 585	NF	mean [$^{\circ}\text{C}$]	1.5	1.1	0.8	0.9	1.1
		Range [$^{\circ}\text{C}$]	0.6 - 2.3	-2.1	0.4 - 1.7	0 - 1.8	0.5 - 1.6
	MF	mean [$^{\circ}\text{C}$]	2.8	2.4	1.7	2	2.2
		Range [$^{\circ}\text{C}$]	1.8 - 3.7	1.3 - 3.2	1.3 - 2.5	1.1 - 2.6	1.5 - 2.9
	FF	mean [$^{\circ}\text{C}$]	4.3	3.9	2.8	3.3	3.5
		Range [$^{\circ}\text{C}$]	3 - 5.3	2.8 - 4.5	2.2 - 3.4	2.4 - 4.2	2.7 - 4.2

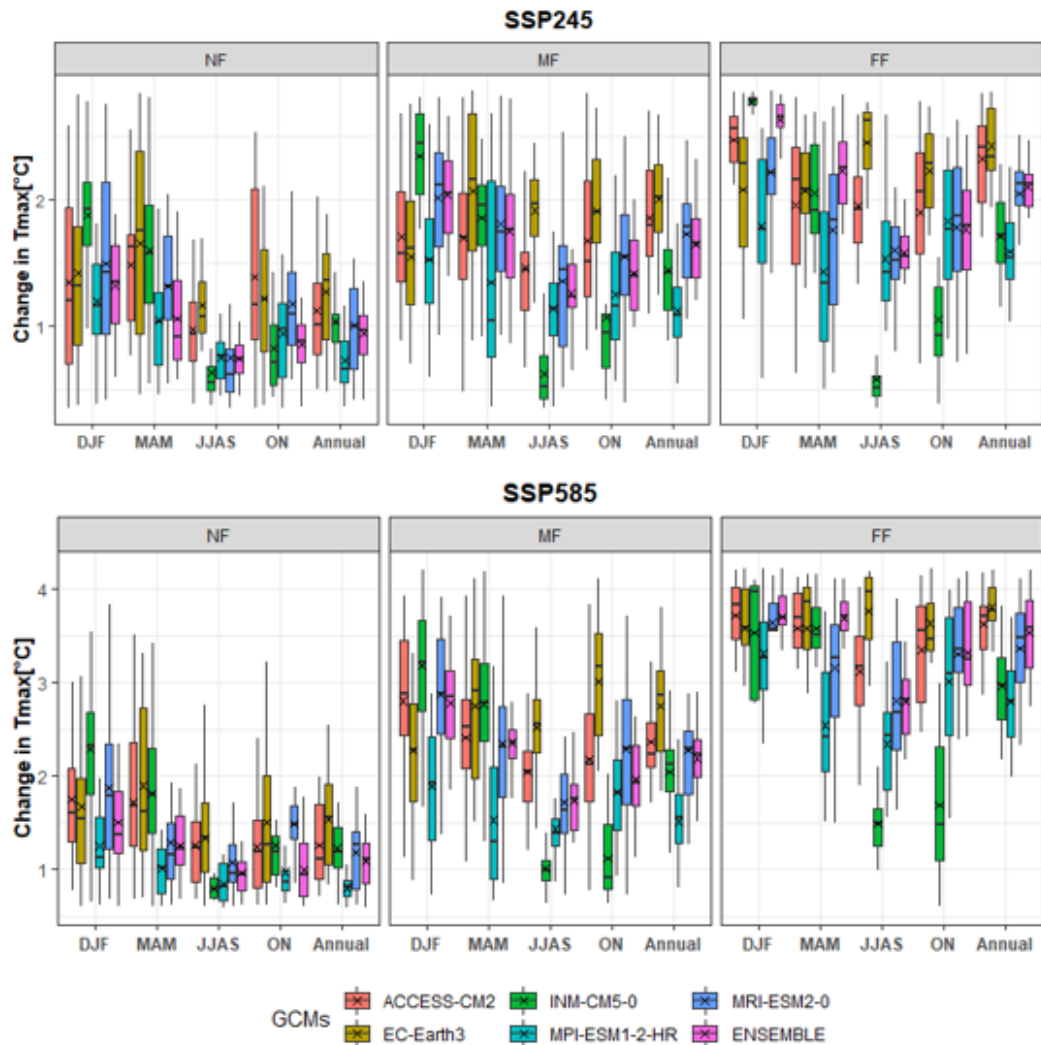


Figure 4-32: Range of projected change in future maximum temperature for different futures, SSPs and GCMs at station 1103

ii. Minimum Temperature:

The range of minimum temperature projections across different GCMs is more consistent and certain than the range of precipitation predictions. With both means and medians, all changes for all GCMs, SSPs, and futures imply a rise.

Projected average annual minimum temperature for SSP245 scenarios, based on ensemble of five GCMs, are gradually increasing compared to the baseline over three future periods by 1.7 °C (for NF), 2.7 °C (for MF) and 3.4 °C (for FF) (Table 4-19). In case of SSP585, it is projected to increase by 1.8 °C (for NF), 3.7 °C (for MF) and 5.9 °C (for FF). The increasing trend is consistent throughout all the seasons and for both the scenarios; although the rate of increase varies with the season (Figure 4-33).

Table 4-19: Projected future minimum temperature [°C] at station 1103 based on ensemble of five GCMs under SSPs scenarios

Range from baseline [°C]			DJF	MAM	JJAS	ON	Annual
Baseline (°C)			-11.45	4.39	14.49	2.51	2.49
SSP 245	NF	mean[°C]	1.6	2.1	1.5	1.6	1.7
		Range[°C]	0.9 - 2.2	0.8 - 3.1	1 - 2.1	0.5 - 2.9	1.2 - 2.3
	MF	mean[°C]	2.5	3.3	2.4	3	2.7
		Range[°C]	1.5 - 3.4	2.4 - 4.5	1.7 - 3	2.1 - 3.9	2.1 - 3.4
	FF	mean[°C]	3.1	4.2	2.9	3.6	3.4
		Range[°C]	2.4 - 3.6	3.2 - 5.1	2.4 - 3.2	1.7 - 5.2	2.9 - 3.8
SSP 585	NF	mean[°C]	1.7	2.2	1.7	1.6	1.8
		Range[°C]	0.8 - 2.7	0.9 - 3.3	1 - 2.6	0 - 3.1	1 - 2.6
	MF	mean[°C]	3.2	4.1	3.4	4.2	3.7
		Range[°C]	2.1 - 4	2.8 - 5.4	2.3 - 4.5	2.5 - 6.3	2.8 - 4.8
	FF	mean[°C]	5.1	6.7	5.3	7.3	5.9
		Range[°C]	3.9 - 6.5	5.2 - 8.1	4.4 - 6.5	5.2 - 9.4	4.7 - 7.1

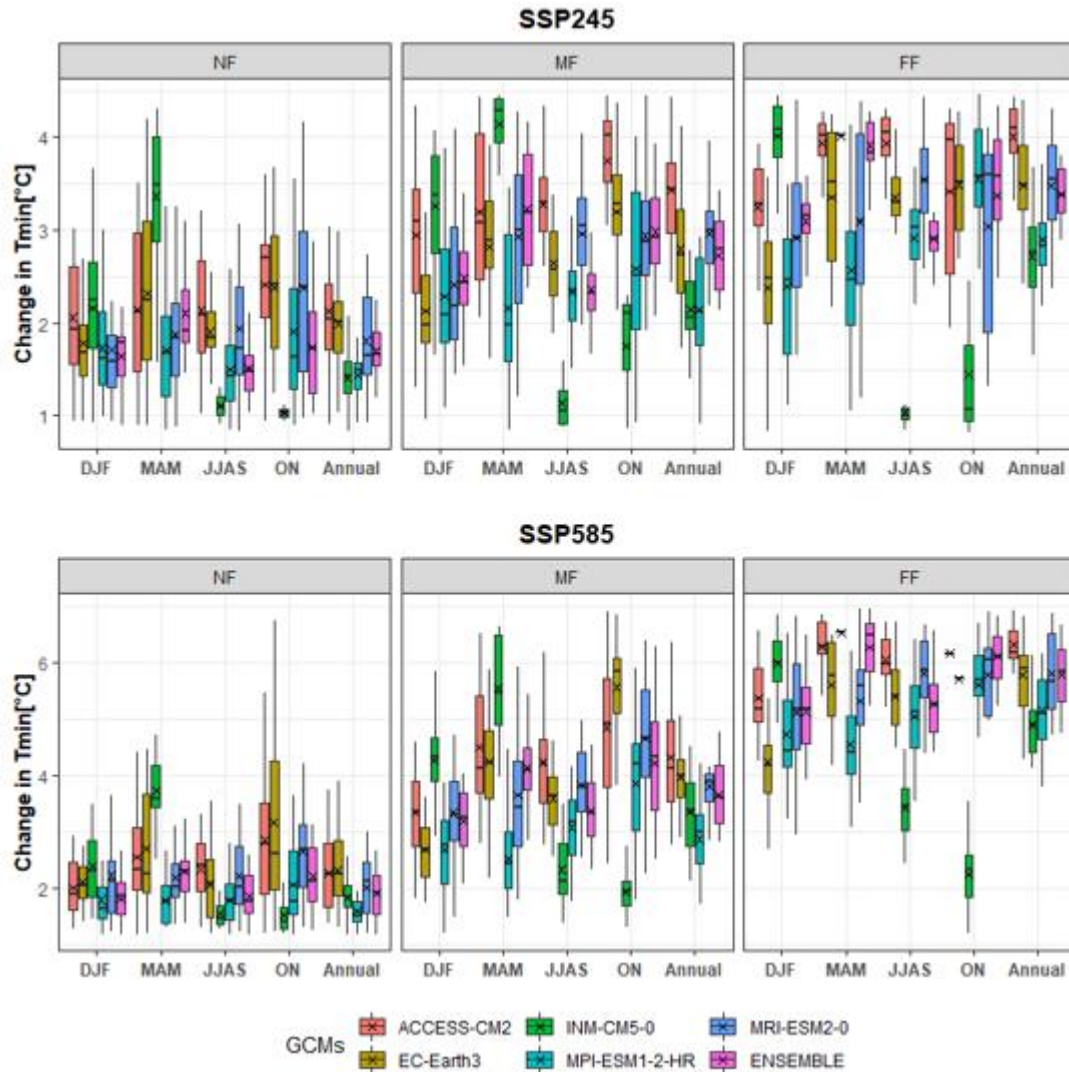


Figure 4-33: Range of projected change in future minimum temperature for different futures, SSPs and GCMs at station 1103

4.5.4 Scope for Flood Inundation Mapping using Climate Change Projections

Due to time constraints, only projections for maximum, minimum temperature and precipitation of the study area was done using CMIP6 GCM's under SSP245 and SSP585 scenarios. Climate change projections obtained in this study can be used to map flood inundation map of the Khimti watershed to access climate change impact on flooding.

5 Conclusions and Recommendations

5.1 Conclusions

Like many hilly areas of Nepal, Khimti watershed in the eastern Nepal is also vulnerable towards natural hazards. Multi-hazard was mapped in the Khimti watershed using analytical hierarchy process with the goal of providing evidence for informed decision-making for climate-resilient development planning and implementation in the Khimti watershed. This was accomplished by analyzing and integrating the hazard maps of three natural hazards (landslides, floods, and earthquakes), and then creating a multi-hazard map that included all three hazards.

Some of the major conclusions drawn from this study are:

- Landslide susceptibility map of the study area is prepared using predictive rate values of the 11 selected factors. From the analysis, it can be concluded that 23.2 Km² and 49.7 Km² area within the Khimti watershed is found to be at very high risk, whereas 66.5 Km² area is found to be at moderate risk and 96.9 Km² is at minimal risk.
- The success and prediction rate for this study are found to be 71.4% and 65.8% respectively, frequency ratio approach used for landslide susceptibility estimation is found to be justifiable.
- Flood frequency analysis using Log Pearson method was found as appropriate one to determine maximum flood in the Khimti watershed based on higher value of chi square test.
- Flood hazard map of the study area is prepared accordingly by overlapping terrain layer with depth grid for 100-year return period. From the analysis, it can be concluded that 1.3 Km² area within the Khimti watershed is found to be at very high risk during high flood whose water depths exceeded more than 3 m, whereas 0.6 Km² area is found to be at moderate risk with water depth 1 to 3 m and 0.3 Km² is at minimal risk with water depths less than 1m.
- Seismic hazard maps using software r-crisis are found to be consistent with some recent studies.
- The seismic hazard maps are generated for a 500-year return period, which is used as the earthquake design basis in Nepal. The maximum PHA in the study area was found to be 0.52g and 0.764g for rock site and soil site respectively. It can be seen that the study area is more hazardous to earthquake.

- The multi-hazard map is prepared for rock and soil sites since seismic hazard is different for rock and soil sites respectively.
- The combination of different hazard maps (landslide seismic hazard, landslide flood hazard and seismic flood hazard) is prepared using analytical hierarchy process giving certain weightage to individual hazard. The obtained results show that 0.8 Km² (112.2 Km²), area lies in very low (low) hazard zone for landslide seismic hazard combination for both rock and soil sites, 86.5 Km² (65.8 Km²), 79 Km² (83.3Km²), 80.5 Km² (83.7 Km²) lies in very low (low) hazard zones respectively for landslide flood and seismic flood hazard combination for rock and soil sites, for moderate category (67.7 Km²) area for landslide and seismic hazard combination for both rock and soil sites, 45.4 Km², 37.9 Km², 37.1 Km² area lies in moderate zone for landslide flood and seismic flood hazard combination for rock and soil sites respectively. Finally, for high (very high) category, 37.2 Km² (18.3 Km²) area falls for combination of landslide seismic hazard for both rock and soil sites, 27.6 Km² (10.9 Km²), 27.5 Km² (9.3 Km²), 27.1 Km² (8.6 Km²) area falls in high (very high) zone for combination of landslide flood and seismic flood hazard for rock and soil sites respectively.
- The multi-hazard map is prepared using analytical hierarchy process giving certain weight to each individual hazard map. The obtained results show that 97.5 Km² and 97.6 Km² area of the Khimti watershed fall under very low hazard category respectively, for rock and soil sites, whereas for low and moderate category, 54.3 Km² and 11.4 Km² area fall in rock site and 54.6 Km² and 11.1 Km² area fall in soil sites and 49.7 Km² and 23.2 Km² area are at high and very high risk respectively, for both sites.
- Annual rainfall across the Khimti watershed is projected to increase from baseline by 5.3% (1.7%), 6% (10.9%), 6.7% (22.4%) for near, mid and far futures under SSP245 (SSP585) scenarios. Annual maximum temperature is projected to increase from baseline by 0.9 °C (1.1 °C), 1.6 °C (2.2 °C), 2.1 °C (3.5 °C) for near, mid and far futures under SSP245 (SSP585) scenarios. Annual minimum temperature is projected to increase from baseline by 1.7 °C (1.8 °C), 2.7 °C (3.7 °C), 3.4 °C (5.9 °C) for near, mid and far futures under SSP245 (SSP585) scenarios.
- The hydro-climatic projections under SSP 245 and SSP585 scenarios for the future period (2020-2100) can be used by decision-makers on how climate change impact on flooding.

5.2 Recommendations

From the present study following recommendations has been made for all three hazards (landslide, flood and earthquake) control and mitigation at policy level:

- Hazard mapping using 30 m DEM which was readily available through open source. Future studies may consider using finer resolution DEM and evaluate the extent to which results are affected due to resolution of DEM.
- The settlement and cultivated land areas falling under high risk and very high risk zones need counter measures to reduce the damages and losses due to multi hazard.
- Slope stabilization and protection work can be carried out using geometry modification and bioengineering.
- The hazard maps will assist civil and structural engineers in designing and analyzing the seismic performance of key facilities such as hospitals, schools, pipelines, bridges, power plants, tunnels, and dams that are built on bedrock and soil foundations.
- Construction of levees and flood wall, improvement of river channels, river bank stabilization are some of the flood control measures that can be adopted.
- Watershed management, afforestation of Khimti watershed helps to reduce peak landslide and flood. Hence, this should be encouraged at local level.
- All the infrastructure development planning should be carried out by considering the multi-hazard in the area.

References

Acharya, T.D. and Lee, D.H., 2019. Landslide susceptibility mapping using relative frequency and predictor rate along Araniko Highway. *KSCE Journal of Civil Engineering*, 23(2), pp.763-776.

Akgun, A. and Türk, N., 2010. Landslide susceptibility mapping for Ayvalik (Western Turkey) and its vicinity by multicriteria decision analysis. *Environmental Earth Sciences*, 61(3), pp.595-611. Alkhasawneh,

Aksha, S.K., Resler, L.M., Juran, L. and Carstensen Jr, L.W., 2020. A geospatial analysis of multi-hazard risk in Dharan, Nepal. *Geomatics, Natural Hazards and Risk*, 11(1), pp.88-111.

Ambraseys, N.N. and Douglas, J., 2004. Magnitude calibration of north Indian earthquakes. *Geophysical Journal International*, 159(1), pp.165-206.

Arabameri, A., Pradhan, B., Rezaei, K. and Lee, C.W., 2019. Assessment of landslide susceptibility using statistical-and artificial intelligence-based FR–RF integrated model and multiresolution DEMs. *Remote Sensing*, 11(9), p.999.

Aryal, D., Wang, L., Adhikari, T.R., Zhou, J., Li, X., Shrestha, M., Wang, Y. and Chen, D., 2020. A model-based flood hazard mapping on the southern slope of Himalaya. *Water*, 12(2), p.540.

Aryal, K.R., 2012. The history of disaster incidents and impacts in Nepal 1900–2005. *International Journal of Disaster Risk Science*, 3(3), pp.147-154.

Ayalew, L., Yamagishi, H. and Ugawa, N., 2004. Landslide susceptibility mapping using GIS-based weighted linear combination, the case in Tsugawa area of Agano River, Niigata Prefecture, Japan. *Landslides*, 1(1), pp.73-81.

Baeza, C. and Corominas, J., 2001. Assessment of shallow landslide susceptibility by means of multivariate statistical techniques. *Earth Surface Processes and Landforms: The Journal of the British Geomorphological Research Group*, 26(12), pp.1251-1263.

- Baidya, S.K., Shrestha, M.L. and Sheikh, M.M., 2008. Trends in daily climatic extremes of temperature and precipitation in Nepal. *Journal of Hydrology and Meteorology*, 5(1), pp.38-51.
- Bajracharya, A.R., Bajracharya, S.R., Shrestha, A.B. and Maharjan, S.B., 2018. Climate change impact assessment on the hydrological regime of the Kaligandaki Basin, Nepal. *Science of the Total Environment*, 625, pp.837-848.
- Barua, U., Akhter, M.S. and Ansary, M.A., 2016. District-wise multi-hazard zoning of Bangladesh. *Natural Hazards*, 82(3), pp.1895-1918.
- Basu, T., Das, A. and Pal, S., 2020. Application of geographically weighted principal component analysis and fuzzy approach for unsupervised landslide susceptibility mapping on Gish River Basin, India. *Geocarto International*, pp.1-24.
- Bathrellos, G.D., Gaki-Papanastassiou, K., Skilodimou, H.D., Papanastassiou, D. and Chousianitis, K.G., 2012. Potential suitability for urban planning and industry development using natural hazard maps and geological–geomorphological parameters. *Environmental earth sciences*, 66(2), pp.537-548.
- Berg, P., Feldmann, H. and Panitz, H.J., 2012. Bias correction of high resolution regional climate model data. *Journal of Hydrology*, 448, pp.80-92.
- Beven, KJ and Kirkby, MJ, 1979. A physically based, variable contributing area model of basin hydrology. *Hydrological Sciences Journal*, 24 (1), pp. 43-69.
- Bhattarai, P., Khanal, P., Tiwari, P., Lamichhane, N., Dhakal, P., Lamichhane, P., Panta, N.R. and Dahal, P., 2019. Flood Inundation Mapping of Babai Basin using HEC-RAS & GIS. *Journal of the Institute of Engineering*, 15(2), pp.32-44.
- Bhusal, B. and Parajuli, H.R., 2019. Probabilistic Seismic Hazard Analysis for Nepal Using Areal and Longitudinal Faults Source. In *Proceedings of IOE Graduate Conference*.
- Bouwer, L.M., 2011. Have disaster losses increased due to anthropogenic climate change? *Bulletin of the American Meteorological Society*, 92(1), pp.39-46.
- Caffrey, P. and Farmer, A., 2014. A review of Downscaling methods for climate change projections. *Tetra Tech ARD*.

Cardona, O.D., 2013. The need for rethinking the concepts of vulnerability and risk from a holistic perspective: a necessary review and criticism for effective risk management. In *Mapping vulnerability* (pp. 56-70). Routledge.

Cardona, O.D., Ordaz Schroder, M.G., Reinoso, E., Yamín Lacouture, L.E. and Barbat Barbat, H.A., 2010. Comprehensive approach for probabilistic risk assessment (CAPRA): international initiative for disaster risk management effectiveness. In *14th European Conference on Earthquake Engineering* (pp. 1-10).

Carpignano, A., Golia, E., Di Mauro, C., Bouchon, S. and Nordvik, J.P., 2009. A methodological approach for the definition of multi-risk maps at regional level: first application. *Journal of risk research*, 12(3-4), pp.513-534.

Carrara, A., Cardinali, M., Detti, R., Guzzetti, F., Pasqui, V. and Reichenbach, P., 1991. GIS techniques and statistical models in evaluating landslide hazard. *Earth surface processes and landforms*, 16(5), pp.427-445.

Carrara, A., Guzzetti, F., Cardinali, M. and Reichenbach, P., 1999. Use of GIS technology in the prediction and monitoring of landslide hazard. *Natural hazards*, 20(2), pp.117-135.

Chacón, J., Irigaray, C., Fernandez, T. and El Hamdouni, R., 2006. Engineering geology maps: landslides and geographical information systems. *Bulletin of Engineering Geology and the Environment*, 65(4), pp.341-411.

Chaulagain, H., Rodrigues, H., Silva, V., Spacone, E. and Varum, H., 2015. Seismic risk assessment and hazard mapping in Nepal. *Natural Hazards*, 78(1), pp.583-602.

Chaumont, D., 2014. A guidebook on climate scenarios: Using climate information to guide adaptation research and decisions. *Ouranos: Montréal, QC, Canada*.

Chen, J., Brissette, F.P., Chaumont, D. and Braun, M., 2013. Finding appropriate bias correction methods in downscaling precipitation for hydrologic impact studies over North America. *Water Resources Research*, 49(7), pp.4187-4205.

Chen, J., Hill, A.A. and Urbano, L.D., 2009. A GIS-based model for urban flood inundation. *Journal of Hydrology*, 373(1-2), pp.184-192.

- Chow, V.T., 1951. A general formula for hydrologic frequency analysis. *Eos, Transactions American Geophysical Union*, 32(2), pp.231-237.
- Cornell, C.A., 1968. Engineering seismic risk analysis. *Bulletin of the seismological society of America*, 58(5), pp.1583-1606.
- Cornell, C.A., Banon, H. and Shakal, A.F., 1979. Seismic motion and response prediction alternatives. *Earthquake Engineering & Structural Dynamics*, 7(4), pp.295-315.
- Crowley, H., Bommer, J.J., Pinho, R. and Bird, J., 2005. The impact of epistemic uncertainty on an earthquake loss model. *Earthquake engineering & structural dynamics*, 34(14), pp.1653-1685.
- Dai, F.C., Lee, C.F. and Ngai, Y.Y., 2002. Landslide risk assessment and management: an overview. *Engineering geology*, 64(1), pp.65-87.
- Dangol, S. and Bormudoi, A., 2015. Flood hazard mapping and vulnerability analysis of Bishnumati River, Nepal. *Nepalese Journal of Geoinformatics*, 14, pp.20-24.
- Demir, V. and Kisi, O., 2016. Flood hazard mapping by using geographic information system and hydraulic model: Mert River, Samsun, Turkey. *Advances in Meteorology*, 2016.
- Department of Mines and Geology. 1994 Geology Map of Nepal. *ICIMOD Regional Database System*. Available at: <https://rds.icimod.org/DatasetMasters/Download/2521>
- Devkota, K.C., Regmi, A.D., Pourghasemi, H.R., Yoshida, K., Pradhan, B., Ryu, I.C., Dhital, M.R. and Althuwaynee, O.F., 2013. Landslide susceptibility mapping using certainty factor, index of entropy and logistic regression models in GIS and their comparison at Mugling–Narayanghat road section in Nepal Himalaya. *Natural hazards*, 65(1), pp.135-165.
- Dhakal, S., 2012. Fundamentals of geology, A reference book for students of Geology. *Civil Engineering, Environmental Science and Forestry*, Kalyani Subedi Publishers, 167p.
- Dixit, A., 2009. Kosi embankment breach in Nepal: Need for a paradigm shift in responding to floods. *Economic and political weekly*, pp.70-78.
- Donovan, N.C., 1973. *A statistical evaluation of strong motion data: Including the February 9, 1971 San Fernando earthquake* (pp. 1252-1261). Dames & Moore.

Duman, T.Y., Can, T., Gokceoglu, C., Nefeslioglu, H.A. and Sonmez, H., 2006. Application of logistic regression for landslide susceptibility zoning of Cekmece Area, Istanbul, Turkey. *Environmental Geology*, 51(2), pp.241-256.

Ebrahimi, H., Feizizadeh, B., Salmani, S. and Azadi, H., 2020. A comparative study of land subsidence susceptibility mapping of Tasuj plane, Iran, using boosted regression tree, random forest and classification and regression tree methods. *Environmental Earth Sciences*, 79, pp.1-12.

Enayati, M., Bozorg-Haddad, O., Bazrafshan, J., Hejabi, S. and Chu, X., 2021. Bias correction capabilities of quantile mapping methods for rainfall and temperature variables. *Journal of Water and Climate Change*, 12(2), pp.401-419.

Galli, M., Ardizzone, F., Cardinali, M., Guzzetti, F. and Reichenbach, P., 2008. Comparing landslide inventory maps. *Geomorphology*, 94(3-4), pp.268-289.

Gardner, J.K. and Knopoff, L., 1974. Is the sequence of earthquakes in Southern California, with aftershocks removed, Poissonian?. *Bulletin of the seismological society of America*, 64(5), pp.1363-1367.

Gautam, D., Thapa, S., Pokhrel, S. and Lamichhane, S., 2021. Local level multi-hazard zonation of Nepal. *Geomatics, Natural Hazards and Risk*, 12(1), pp.405-423.

Ghimire, S., 2019. Probabilistic seismic hazard analysis of Nepal. *Journal of Innovations in Engineering Education*, 2(1).

Gökceoglu, C. and Aksoy, H.Ü.S.E.Y.İ.N., 1996. Landslide susceptibility mapping of the slopes in the residual soils of the Mengen region (Turkey) by deterministic stability analyses and image processing techniques. *Engineering Geology*, 44(1-4), pp.147-161.

Granger, K., Jones, T.G., Leiba, M. and Scott, G., 1999. Community risk in Cairns: a multi-hazard risk assessment. *Australian Journal of Emergency Management, The*, 14(2), pp.25-26.

Guha-Sapir, D., Hargitt, D. and Hoyois, P., 2004. *Thirty years of natural disasters 1974-2003: The numbers*. Presses univ. de Louvain.

Gutenberg, B. and Richter, C.F., 1944. Frequency of earthquakes in California. *Bulletin of the Seismological society of America*, 34(4), pp.185-188.

Guzzetti, F., Carrara, A., Cardinali, M. and Reichenbach, P., 1999. Landslide hazard evaluation: a review of current techniques and their application in a multi-scale study, Central Italy. *Geomorphology*, 31(1-4), pp.181-216.

Guzzetti, F., Reichenbach, P., Ardizzone, F., Cardinali, M. and Galli, M., 2006. Estimating the quality of landslide susceptibility models. *Geomorphology*, 81(1-2), pp.166-184.

Hanks, T.C. and Kanamori, H., 1979. A moment magnitude scale. *Journal of Geophysical Research: Solid Earth*, 84(B5), pp.2348-2350.

Hasalanka, H.H.H., Kularatne, W.D.M., Siriwardana, C.S.A., Wijesekara, N.W.A.N.Y. and Kodituwakku, K.A.L.C., 2019, July. A framework to develop multi-hazard maps to identify the natural hazards which affect the safety of Sri Lankan hospitals. In *2019 Moratuwa Engineering Research Conference (MERCon)* (pp. 418-423). IEEE.

HEC-RAS, U.S.A.C.E., 2016. River Analysis System. *Hydraulic Reference Manual; US Army Corps of Engineers, Hydrologic Engineering Center: Davis, CA, USA*, p.547.

Herger, N., Abramowitz, G., Knutti, R., Angélil, O., Lehmann, K. and Sanderson, B.M., 2018. Selecting a climate model subset to optimise key ensemble properties. *Earth System Dynamics*, 9(1), pp.135-151.

Hicks, FE and Peacock, T., 2005. Suitability of HEC-RAS for flood forecasting. *Canadian water resources journal*, 30 (2), pp. 159-174.

Hussain, M., Yusof, K.W., Mustafa, M.R.U., Mahmood, R. and Jia, S., 2018. Evaluation of CMIP5 models for projection of future precipitation change in Bornean tropical rainforests. *Theoretical and Applied Climatology*, 134(1), pp.423-440.

ICIMOD. 2010 Land Cover of Nepal. *ICIMOD Regional Database System*. Available at: <https://rds.icimod.org/DatasetMasters/Download/9224>

International Panel on Climate Change, 2007. Climate change 2007: Synthesis report. *Contribution of Working Groups I, II and III to the Fourth Assessment Report of the Intergovernmental Panel on Climate Change*, p.104.

IPCC (Intergovernmental Panel on Climate Change), 2012. Managing the risks of extreme events and disasters to advance climate change adaptation. *A special report of working groups I and II of the intergovernmental panel on climate change*, p.582.

IPCC, 2014. AR 5 Climate Change 2014: *Impacts, Adaptation, and Vulnerability*, Cambridge: Cambridge University Press.

Islam, M.M. and Sado, K., 2002. Development priority map for flood countermeasures by remote sensing data with geographic information system. *Journal of hydrologic engineering*, 7(5), pp.346-355.

Javier, D.N. and Kumar, L., 2019. FREQUENCY RATIO LANDSLIDE SUSCEPTIBILITY ESTIMATION IN A TROPICAL MOUNTAIN REGION. *International Archives of the Photogrammetry, Remote Sensing & Spatial Information Sciences*.

Kafle, M.R. and Shakya, N.M., 2018. Two-Dimensional Hydrodynamic Modelling of Koshi River and Prediction of Inundation Parameters. *Hydrology: Current Research*, 9, p.30.

Kamp, U., Growley, B.J., Khattak, G.A. and Owen, L.A., 2008. GIS-based landslide susceptibility mapping for the 2005 Kashmir earthquake region. *Geomorphology*, 101(4), pp.631-642.

Kanamori, H., 1977. The energy release in great earthquakes. *Journal of geophysical research*, 82(20), pp.2981-2987.

Kappes, M., Keiler, M. and Glade, T., 2010. Mountain risks: bringing science to society. In *Proceedings of the international conference, Florence, chapter from single-to multi-hazard risk analyses: a concept addressing emerging challenges*, CERIG Editions, Strasbourg (pp. 351-356).

Kappes, M.S., Papathoma-Koehle, M. and Keiler, M., 2012. Assessing physical vulnerability for multi-hazards using an indicator-based methodology. *Applied Geography*, 32(2), pp.577-590.

Kaur, H., Gupta, S., Parkash, S. and Thapa, R., 2018. Application of geospatial technologies for multi-hazard mapping and characterization of associated risk at local scale. *Annals of GIS*, 24(1), pp.33-46.

- Kavzoglu, T., Sahin, E.K. and Colkesen, I., 2015. An assessment of multivariate and bivariate approaches in landslide susceptibility mapping: a case study of Duzkoy district. *Natural Hazards*, 76(1), pp.471-496.
- Khan, H., Shafique, M., Khan, M.A., Bacha, M.A., Shah, S.U. and Calligaris, C., 2019. Landslide susceptibility assessment using Frequency Ratio, a case study of northern Pakistan. *The Egyptian Journal of Remote Sensing and Space Science*, 22(1), pp.11-24.
- Khanal, N.R., Shrestha, M. and Ghimire, M., 2007. *Preparing for flood disaster: mapping and assessing hazard in the Ratu Watershed, Nepal*. International Centre for Integrated Mountain Development (ICIMOD).
- Khatakho, R., Gautam, D., Aryal, K.R., Pandey, V.P., Rupakhety, R., Lamichhane, S., Liu, Y.C., Abdouli, K., Talchabhadel, R., Thapa, B.R. and Adhikari, R., 2021. Multi-Hazard Risk Assessment of Kathmandu Valley, Nepal. *Sustainability*, 13(10), p.5369.
- Lamichhane, S., Aryal, K.R., Talchabhadel, R., Thapa, B.R., Adhikari, R., Khanal, A., Pandey, V.P. and Gautam, D., 2021. Assessing the Prospects of Transboundary Multihazard Dynamics: The Case of Bhotekoshi—Sunkoshi Watershed in Sino—Nepal Border Region. *Sustainability*, 13(7), p.3670.
- Lee, S. and Choi, J., 2004. Landslide susceptibility mapping using GIS and the weight-of-evidence model. *International Journal of Geographical Information Science*, 18(8), pp.789-814.
- Lee, S. and Pradhan, B., 2006. Probabilistic landslide hazards and risk mapping on Penang Island, Malaysia. *Journal of Earth System Science*, 115(6), pp.661-672.
- Li, W., Li, S.Y., Lu, J.Q. and Zhao, Z., 2011. An Improved Method for Fitting Ground Motion Attenuation Relationship. In *Applied Mechanics and Materials* (Vol. 90, pp. 1639-1643). Trans Tech Publications Ltd.
- Mahendra, R.S., Mohanty, P.C., Bisoyi, H., Kumar, T.S. and Nayak, S., 2011. Assessment and management of coastal multi-hazard vulnerability along the Cuddalore–Villupuram, east coast of India using geospatial techniques. *Ocean & Coastal Management*, 54(4), pp.302-311.
- Malczewski, J., 1999. *GIS and multicriteria decision analysis*. John Wiley & Sons.

- Manandhar, S., Vogt, D.S., Perret, S.R. and Kazama, F., 2011. Adapting cropping systems to climate change in Nepal: a cross-regional study of farmers' perception and practices. *Regional Environmental Change*, 11(2), pp.335-348.
- Marahatta, S., Dangol, B.S. and Gurung, G.B., 2009. *Temporal and spatial variability of climate change over Nepal, 1976-2005*. Practical Action Nepal Office.
- Marzocchi, W., Garcia-Aristizabal, A., Gasparini, P., Mastellone, M.L. and Di Ruocco, A., 2012. Basic principles of multi-risk assessment: a case study in Italy. *Natural hazards*, 62(2), pp.551-573.
- Maskey, P.N. and Dutta, T.K., 2004, August. Risk consistent response spectrum and hazard curve for a typical location of Kathmandu valley. In *13th World Conference on Earthquake Engineering paper no* (Vol. 3124).
- Mersha, T. and Meten, M., 2020. GIS-based landslide susceptibility mapping and assessment using bivariate statistical methods in Simada area, northwestern Ethiopia. *Geoenvironmental Disasters*, 7(1), pp.1-22.
- Mishra, V., Bhatia, U. and Tiwari, A.D., 2020. Bias-corrected climate projections from Coupled Model Intercomparison Project-6 (CMIP6) for South Asia. *arXiv preprint arXiv:2006.12976*.
- MoHA, 2009. Nepal disaster report: The hazard scale and vulnerability, Kathmandu: Ministry of Home Affairs.
- MoHA, 2017. Loss of lives and properties from Disaster 2073, Kathmandu: Ministry of Home Affairs.
- MoHA, 2019. Nepal Disaster Report 2019, Kathmandu: Ministry of Home Affairs.
- Mondal, S. and Mandal, S., 2019. Landslide susceptibility mapping of Darjeeling Himalaya, India using index of entropy (IOE) model. *Applied Geomatics*, 11(2), pp.129-146.
- Moore, I.D. and Grayson, R.B., 1991. Terrain-based catchment partitioning and runoff prediction using vector elevation data. *Water Resources Research*, 27(6), pp.1177-1191.

MoSTE, 2014. Nepal second national communication to United Nations framework convention on climate change, Kathmandu: MoSTE.

Nepal, N., Chen, J., Chen, H. and Sharma, T.P.P., 2019. Assessment of landslide susceptibility along the araniko highway in poiqu/bhote koshi/sun koshi watershed, Nepal himalaya. *Progress in Disaster Science*, 3, p.100037.

Nyimbili, P.H., Erden, T. and Karaman, H., 2018. Integration of GIS, AHP and TOPSIS for earthquake hazard analysis. *Natural hazards*, 92(3), pp.1523-1546.

Ogras, S. and Onen, F., 2020. Flood Analysis with HEC-RAS: A Case Study of Tigris River. *Advances in Civil Engineering*, 2020.

Oh, H.J. and Lee, S., 2011. Cross-application used to validate landslide susceptibility maps using a probabilistic model from Korea. *Environmental Earth Sciences*, 64(2), pp.395-409.

Ordaz, M., Aguilar, A. and Arboleda, J., 2007. CRISIS2007. Program for computing seismic hazard. *Instituto de Ingenieria, Universidad Nacional Autónoma de México, UNAM, México*.

O'Sullivan, J.N., 2018. Synergy between population policy, climate adaptation and mitigation. In *Pathways to a Sustainable Economy* (pp. 103-125). Springer, Cham.

Pachauri, A.K. and Pant, M., 1992. Landslide hazard mapping based on geological attributes. *Engineering geology*, 32(1-2), pp.81-100.

Pandey, M.R., Chitrakar, G.R., Kafle, B., Sapkota, S.N., Rajaure, S.N. and Gautam, U.P., 2002. Seismic hazard map of Nepal. *Kathmandu: Department of Mines and Geology*.

Pandey, P. and Dugar, S., 2019. Flood Hazard Mapping in an Urban Context: A Case Study of Hanumante Stream, Bhaktapur (Nepal). In *Proceedings of IOE Graduate Conference*.

Pandey, V.P., Dhaubanjari, S., Bharati, L. and Thapa, B.R., 2019. Hydrological response of Chamelia watershed in Mahakali Basin to climate change. *Science of the Total Environment*, 650, pp.365-383.

Parajuli, H.R., 2009. Dynamic analyses of low strength masonry houses based on site specific earthquake ground motions.

Parajuli, H.R., 2015. Seismic Hazard Assessment of Kavre Valley Municipalities. In *Proceedings of IOE Graduate Conference* (pp. 193-201).

Parashar, A.K., Atmapoojya, S. and Rathore, S.S., Seismic Hazard Analysis of District Headquarters Dhamtari and Kanker of Chhattisgarh State, India: Deterministic Method.

Pistocchi, A., Luzi, L. and Napolitano, P., 2002. The use of predictive modeling techniques for optimal exploitation of spatial databases: a case study in landslide hazard mapping with expert system-like methods. *Environmental geology*, 41(7), pp.765-775.

Pourghasemi, H.R., Gayen, A., Panahi, M., Rezaie, F. and Blaschke, T., 2019. Multi-hazard probability assessment and mapping in Iran. *Science of the total environment*, 692, pp.556-571.

Pradhan, B., 2013. A comparative study on the predictive ability of the decision tree, support vector machine and neuro-fuzzy models in landslide susceptibility mapping using GIS. *Computers & Geosciences*, 51, pp.350-365.

Pradhan, B. and Lee, S., 2010. Landslide susceptibility assessment and factor effect analysis: backpropagation artificial neural networks and their comparison with frequency ratio and bivariate logistic regression modelling. *Environmental Modelling & Software*, 25(6), pp.747-759.

Pradhan, P.M., Timalisina, S.P. and Bhatt, M.R., 2020. Probabilistic Seismic Hazard Analysis for Nepal. *Lowland Technology International*, 22(1, June), pp.75-80.

Raju, K.S. and Kumar, D.N., 2020. Review of approaches for selection and ensembling of GCMs. *Journal of Water and Climate Change*, 11(3), pp.577-599.

Ram, T.D. and Wang, G., 2013. Probabilistic seismic hazard analysis in Nepal. *Earthquake Engineering and Engineering Vibration*, 12(4), pp.577-586.

Rastogi, A.K., Thakur, P.K., Rao, G.S., Aggarwal, S.P., Dadhwal, V.K. and Chauhan, P., 2018. Integrated flood study of Bagmati river basin with hydro processing, flood inundation mapping & 1-d hydrodynamic modeling using remote sensing and GIS. *ISPRS Annals of the Photogrammetry, Remote Sensing and Spatial Information Sciences*, 4, pp.165-172.

Regmi, A.D., Devkota, K.C., Yoshida, K., Pradhan, B., Pourghasemi, H.R., Kumamoto, T. and Akgun, A., 2014a. Application of frequency ratio, statistical index, and weights-of-evidence

models and their comparison in landslide susceptibility mapping in Central Nepal Himalaya. *Arabian Journal of Geosciences*, 7(2), pp.725-742.

Regmi, A.D., Yoshida, K., Pourghasemi, H.R., Dhital, M.R. and Pradhan, B., 2014b. Landslide susceptibility mapping along Bhalubang—Shiwapur area of mid-Western Nepal using frequency ratio and conditional probability models. *Journal of Mountain Science*, 11(5), pp.1266-1285.

Riahi, K., Van Vuuren, D.P., Kriegler, E., Edmonds, J., O’neill, B.C., Fujimori, S., Bauer, N., Calvin, K., Dellink, R., Fricko, O. and Lutz, W., 2017. The Shared Socioeconomic Pathways and their energy, land use, and greenhouse gas emissions implications: *An overview. Global environmental change*, 42, pp.153-168.

Ristya, Y. and Afdhalia, F., 2020, August. Application GIS (Geographic Information System) for multi-hazard mapping in Cisolok Village, Indonesia. In IOP Conference Series: *Earth and Environmental Science* (Vol. 561, No. 1, p. 012050). IOP Publishing.

Rupke, J., Cammeraat, E., Seijmonsbergen, A.C. and van Westen, C.J., 1988. Engineering geomorphology of the widentobel catchment, appenzell and sankt gallen, switzerland. A geomorphological inventory system applied to geotechnical appraisal of slope stability. *Engineering geology*, 26(1), pp.33-68.

Saaty, T.L., 1980. *The Analytic Hierarchy Process* McGraw Hill, New York. *Agricultural Economics Review*, 70.

Saaty, T.L., 1990. How to make a decision: the analytic hierarchy process. *European journal of operational research*, 48(1), pp.9-26.

Saaty, T.L., 1994. How to make a decision: the analytic hierarchy process. *Interfaces*, 24(6), pp.19-43.

Saaty, T.L., 2000. *Fundamentals of decision making and priority theory with the analytic hierarchy process* (Vol. 6). RWS publications.

Saaty, T.L. and Vargas, L.G., 2001. How to make a decision. In *Models, methods, concepts & applications of the analytic hierarchy process* (pp. 1-25). Springer, Boston, MA.

- Salzmann, N., Frei, C., Vidale, P.L. and Hoelzle, M., 2007. The application of Regional Climate Model output for the simulation of high-mountain permafrost scenarios. *Global and Planetary Change*, 56(1-2), pp.188-202.
- Sarchani, S., Seiradakis, K., Coulibaly, P. and Tsanis, I., 2020. Flood inundation mapping in an ungauged basin. *Water*, 12(6), p.1532.
- Schmidt, J., Matcham, I., Reese, S., King, A., Bell, R., Henderson, R., Smart, G., Cousins, J., Smith, W. and Heron, D., 2011. Quantitative multi-risk analysis for natural hazards: a framework for multi-risk modelling. *Natural hazards*, 58(3), pp.1169-1192.
- Schneider, P.J. and Schauer, B.A., 2006. HAZUS—its development and its future. *Natural Hazards Review*, 7(2), pp.40-44.
- Scinocca, J.F., Kharin, V.V., Jiao, Y., Qian, M.W., Lazare, M., Solheim, L., Flato, G.M., Biner, S., Desgagne, M. and Dugas, B., 2016. Coordinated global and regional climate modeling. *Journal of Climate*, 29(1), pp.17-35.
- Scordilis, E.M., 2006. Empirical global relations converting MS and mb to moment magnitude. *Journal of seismology*, 10(2), pp.225-236.
- Skilodimou, H.D., Bathrellos, G.D., Chousianitis, K., Youssef, A.M. and Pradhan, B., 2019. Multi-hazard assessment modeling via multi-criteria analysis and GIS: a case study. *Environmental Earth Sciences*, 78(2), p.47.
- Soriano, E., Mediero, L. and Garijo, C., 2019. Selection of bias correction methods to assess the impact of climate change on flood frequency curves. *Water*, 11(11), p.2266.
- Stefanidis, S. and Stathis, D., 2013. Assessment of flood hazard based on natural and anthropogenic factors using analytic hierarchy process (AHP). *Natural hazards*, 68(2), pp.569-585.
- Stepp, J.C., 1972, October. Analysis of completeness of the earthquake sample in the Puget Sound area and its effect on statistical estimates of earthquake hazard. In *Proc. of the 1st Int. Conf. on Microzonation, Seattle* (Vol. 2, pp. 897-910).
- Subedi, B. and Parajuli, H.R., 2016. Probabilistic seismic hazard analysis of Nepal. In *Proceedings of IOE Graduate Conference* (pp. 265-270).

Subramanya, K., 2008. Engineering Hydrology. Third ed. New Delhi: The McGraw-Hill companies.

Sujatha, E.R., Kumaravel, P. and Rajamanickam, G.V., 2014. Assessing landslide susceptibility using Bayesian probability-based weight of evidence model. *Bulletin of Engineering Geology and the Environment*, 73(1), pp.147-161.

Survey Department of Nepal. 2015 Nepal Road Network. Humanitarian Data Exchange. Available at: <https://data.humdata.org/dataset/675d4343-b21a-4033-89b1-9ba386429c03/resource/622249ae-fb42-44ea-8208-1bb32928ff01/download/npl-rdsl-trans-25k-50k-sdn-wgs84.zip>

Survey Department of Nepal. 2015 Nepal Settlement Data. Humanitarian Data Exchange. Available at: https://data.humdata.org/dataset/85c83e1c-80d1-4136-b9cc-a90b853e7d6c/resource/39db8258-b11d-40e2-954b-0b53044058a7/download/nplsettlements_pcode.zip

Swets, J.A., 1988. Measuring the accuracy of diagnostic systems. *Science*, 240(4857), pp.1285-1293.

Talchabhadel, R., Shakya, N.M., Dahal, V. and Eslamian, S., 2015. Rainfall runoff modelling for flood forecasting (a case study on west rapti watershed). *Journal of Flood Engineering*, 6(1), pp.53-61.

Talukdar, P., 2014. Preparation of a comprehensive earthquake catalog for Northeast India and its completeness analysis. *IOSR Journal of Applied Geology and Geophysics (IOSR-JAGG)*, pp.22-26.

Tate, E., Cutter, S.L. and Berry, M., 2010. Integrated multihazard mapping. *Environment and Planning B: Planning and Design*, 37(4), pp.646-663.

Teutschbein, C. and Seibert, J., 2012. Bias correction of regional climate model simulations for hydrological climate-change impact studies: Review and evaluation of different methods. *Journal of hydrology*, 456, pp.12-29.

Thapa, S., Shrestha, A., Lamichhane, S., Adhikari, R. and Gautam, D., 2020. Catchment-scale flood hazard mapping and flood vulnerability analysis of residential buildings: The case of Khando River in eastern Nepal. *Journal of Hydrology: Regional Studies*, 30, p.100704.

TU-CDES (2016). Landslide Inventory Characterization and Engineering Design for Mitigation Works of Chure Area in Ten Districts. Central Department of Environmental Science, Tribhuvan University and Government of Nepal, President Chure-Tarai Madhesh Conservation Development Board, Kathmandu.

United Nations Development Programme. Bureau for Crisis Prevention, 2004. *Reducing Disaster Risk: A Challenge for Development-a Global Report*. United Nations.

UNISDR, U., 2009. Making Disaster Risk Reduction Gender Sensitive: Policy and Practical Guidelines.

UNISDR (United Nations International Strategy for Disaster Reduction), 2009. Terminology: Basic Terms of Disaster Risk Reduction.

United Nations Framework Convention on Climate Change, 2007. Climate change: impacts, vulnerabilities and adaptation in developing countries. Bonn, Germany: United Nations Framework Convention on Climate Change.

USGS 1990. Earth explorer data available on the World Wide Web, United State Geological Survey (USGS). Available online: <https://earthexplorer.usgs.gov/>

van Vuuren, D.P., Edmonds, J., Kainuma, M., Riahi, K., Thomson, A., Hibbard, K., Hurtt, G.C., Kram, T., Krey, V., Lamarque, J.F. and Masui, T., 2011. The representative concentration pathways: an overview. *Climatic change*, 109(1), pp.5-31.

van Westen, C.J., 1993. Application of geographic information systems to landslide hazard zonation, ITC Publication No 15. *International Institute for Aerospace and Earth Resources Survey, Enschede, The Netherlands*, 245.

van Westen, C.J., Montoya, L., Boerboom, L. and Badilla Coto, E., 2002. September. Multi-hazard risk assessment using GIS in urban areas: a case study for the city of Turrialba, Costa Rica. In *Proc. Regional workshop on Best Practise in Disaster Mitigation, Bali* (pp. 120-136).

van Westen, C.J., Soeters, R. and Sijmons, K., 2000. Digital geomorphological landslide hazard mapping of the Alpago area, Italy. *International Journal of Applied Earth Observation and Geoinformation*, 2(1), pp.51-60.

Varnes, D.J., 1984. *Landslide hazard zonation: a review of principles and practice* (No. 3).

Viner, D., 2012. *Spatial Downscaling*. East Anglia: University of East Anglia.

Ward, P. J., Winsemius, H., Bouwman, A. & Jongman, B., 2013. A Framework for Global Flood Risk Assessments. *Hydrology and Earth System Sciences*, Volume 17, pp. 1871-1892.

Wiles, J.J. and Levine, N.S., 2002. A combined GIS and HEC model for the analysis of the effect of urbanization on flooding; the Swan Creek watershed, Ohio. *Environmental & Engineering Geoscience*, 8(1), pp.47-61.

Yalcin, A., 2008. GIS-based landslide susceptibility mapping using analytical hierarchy process and bivariate statistics in Ardesen (Turkey): comparisons of results and confirmations. *catena*, 72(1), pp.1-12.

Yilmaz, I., 2009. Landslide susceptibility mapping using frequency ratio, logistic regression, artificial neural networks and their comparison: a case study from Kat landslides (Tokat—Turkey). *Computers & Geosciences*, 35(6), pp.1125-1138.

Youngs, R.R., Chiou, S.J., Silva, W.J. and Humphrey, J.R., 1997. Strong ground motion attenuation relationships for subduction zone earthquakes. *Seismological Research Letters*, 68(1), pp.58-73.

Annexes

Declustered Earthquake Catalogue

Mag	Yr	Mo	day	hr	min	sec	depth	long	lat
7.6	1254	12	31	0	0	0	0	85.3	27.7
6.7	1259	12	31	0	0	0	0	86.8	27.1
7.2	1343	12	31	0	0	0	0	86.8	27.5
7.6	1407	12	31	0	0	0	0	85.3	27.7
8.1	1505	1	6	0	0	0	0	83	29.5
7	1680	12	31	0	0	0	0	85.3	27.7
7	1809	12	31	0	0	0	0	85.3	27.7
6.3	1816	5	26	0	0	0	0	79	30.9
4.3	1819	8	3	0	0	0	0	85.5	26.5
5.7	1826	10	29	0	0	0	0	85	28
5	1832	2	7	0	0	0	0	79.6	29.4
7.6	1833	8	26	0	0	0	0	85.7	27.7
7	1833	4	10	0	0	0	0	85	27
6.3	1833	10	18	0	0	0	0	84	27
5	1833	5	30	0	0	0	0	79.6	29.4
5.7	1835	1	14	0	0	0	0	79.6	29.4
5	1842	1	16	0	0	0	0	83	26
5.6	1843	8	10	0	0	0	0	88.3	27
6.3	1849	2	27	0	0	0	0	88.3	27
5	1849	2	28	0	0	0	0	88.5	26.5
4.3	1851	2	14	0	0	0	0	79.4	29.4
7	1852	4	30	0	0	0	0	88.3	27
5.6	1863	3	29	0	0	0	0	88.3	27
4.3	1864	8	30	0	0	0	0	80.9	26.8
5	1865	12	16	0	0	0	0	88.3	27
6.3	1866	5	23	0	0	0	0	85.3	27.7
7	1869	7	7	0	0	0	0	85	28
6.3	1869	1	10	0	0	0	0	90	26
5.6	1869	8	9	0	0	0	0	88.3	27
4.3	1869	3	23	0	0	0	0	88.3	27
4.3	1869	7	25	0	0	0	0	79.4	29.4
4.3	1875	4	26	0	0	0	0	88.3	27
6.3	1899	9	25	0	0	0	0	88.3	27
5.5	1909	2	17	0	0	0	0	87	27
5.7	1910	8	13	0	0	0	0	90	28
6.7	1911	10	14	0	0	0	0	80.5	31
6.2	1913	3	6	0	0	0	0	83	30
7.3	1916	8	28	0	0	0	0	81	30
6	1918	2	4	0	0	0	0	87.8	29.6

Mag	Yr	Mo	day	hr	min	sec	depth	long	lat
5.5	1925	11	6	0	0	0	0	81.5	26.5
6	1926	7	27	0	0	0	0	80.5	30.5
5.6	1931	6	18	0	0	0	0	84	30.5
8.3	1934	1	15	0	0	0	0	87.1	27.6
6.2	1935	5	21	0	0	0	0	89.2	28.7
6	1935	3	5	0	0	0	0	80.2	29.7
7	1936	5	27	0	0	0	0	83.5	28.5
5.6	1936	2	11	0	0	0	0	87	27.5
5.5	1937	4	30	0	0	0	0	81.5	30
5.5	1938	1	29	0	0	0	0	87	27.5
5.5	1940	4	10	0	0	0	0	81.5	30
6.7	1944	10	17	0	0	0	0	83.3	31.4
6.5	1945	6	4	0	0	0	0	80	30
5.5	1947	8	19	0	0	0	0	79.9	31.2
6	1953	2	23	0	0	0	0	81.3	29.5
6.5	1954	9	4	0	0	0	0	83.8	28.3
5.6	1955	9	20	0	0	0	0	90	27.5
5	1955	11	23	0	0	0	0	90	26.5
4.5	1955	4	17	0	0	0	0	90	26.5
6.5	1957	4	14	0	0	0	0	84.3	30.6
6.2	1957	4	14	0	0	0	0	84.5	31
6.3	1958	12	28	0	0	0	0	80	29.5
5.5	1960	8	21	0	0	0	0	88.5	27
5.7	1961	12	24	0	0	0	0	80.8	29.5
5.5	1962	7	13	0	0	0	0	79.6	30.5
5	1962	1	11	0	0	0	0	84.9	27.9
5.5	1963	1	30	0	0	0	0	80.6	29.7
4.8	1963	11	27	0	0	0	0	79.1	30.8
6.1	1964	3	27	0	0	0	0	89.3	27.2
6	1964	9	26	0	0	0	0	80.5	30
5	1964	10	6	0	0	0	0	80.98	29.4
4.9	1964	8	30	0	0	0	0	88.3	27.6
4.8	1964	5	24	0	0	0	0	82.1	30.1
4.8	1964	11	9	0	0	0	0	86.04	29.53
4.5	1964	2	1	0	0	0	0	87.78	27.3
4.5	1964	2	1	0	0	0	0	87.8	27.4
4.5	1964	10	25	0	0	0	0	88.6	27.9
4.1	1964	1	25	0	0	0	0	86.64	28.27
4.1	1964	1	25	0	0	0	0	86.8	28.5
4.1	1964	12	3	0	0	0	0	89.4	31.49
6.1	1965	1	12	0	0	0	0	87.84	27.4
5.1	1965	6	1	0	0	0	0	83.2	28.5
6.5	1966	3	6	0	0	0	0	80.5	31.5

Mag	Yr	Mo	day	hr	min	sec	depth	long	lat
6	1966	6	27	0	0	0	0	80.8	29.6
4.9	1966	12	28	0	0	0	0	89	28
4.8	1966	6	25	0	0	0	0	82.3	30.5
4.8	1966	11	5	0	0	0	0	84	28.2
4.6	1966	3	17	0	0	0	0	82.9	31.6
4.1	1966	1	11	0	0	0	0	85.8	27.8
4.9	1967	1	5	0	0	0	0	86	30
4.9	1967	8	14	0	0	0	0	80	28
4.9	1967	9	13	0	0	0	0	87	27
4.9	1967	12	18	0	0	0	0	81.9	29.1
4.6	1967	7	16	0	0	0	0	82	28
4.6	1967	11	21	0	0	0	0	79	28
4.5	1967	1	2	0	0	0	0	79.3	30.6
4.5	1967	3	2	0	0	0	0	86.4	28.7
4.5	1967	3	11	0	0	0	0	81.4	29.3
5.1	1968	1	5	0	0	0	0	79.1	30.4
4.8	1968	5	27	0	0	0	0	80.4	29.7
4.8	1968	5	31	0	0	0	0	80	29.9
4.6	1968	10	28	0	0	0	0	86.03	27.57
4.3	1968	2	7	0	0	0	0	80.3	30.9
6.2	1969	2	11	0	0	0	0	82.7	28.1
5.7	1969	8	9	0	0	0	0	88.3	27
5	1969	2	13	0	0	0	0	81.8	28.2
5	1969	3	3	0	0	0	0	79.9	30.2
5	1969	6	22	0	0	0	0	79.4	30.6
4.9	1969	2	24	0	0	0	0	85.6	27.9
4.9	1969	3	5	0	0	0	0	81.1	29.2
4.8	1969	2	4	0	0	0	0	81.4	28.3
4.6	1969	12	5	0	0	0	0	80.8	29.7
4.5	1969	3	7	0	0	0	0	83.8	28.1
5	1970	2	12	0	0	0	0	81.6	29.2
4.9	1970	2	26	0	0	0	0	85.7	27.62
4.3	1970	7	21	0	0	0	0	84.8	27.9
5	1971	5	3	0	0	0	0	84.3	30.8
4.8	1971	10	24	0	0	0	0	87.16	28.25
4.7	1971	12	4	0	0	0	0	87.87	27.9
4.6	1971	6	6	0	0	0	0	85.6	28.1
4.2	1971	1	30	0	0	0	0	79.1	30.5
4	1971	6	25	0	0	0	0	83.6	28
5	1972	3	15	0	0	0	0	84.5	30.4
4.8	1972	4	28	0	0	0	0	84.9	31.3
4.8	1972	8	21	0	0	0	0	88.02	27.23
4.5	1972	4	8	0	0	0	0	89.42	29.67

Mag	Yr	Mo	day	hr	min	sec	depth	long	lat
4.5	1972	11	6	0	0	0	0	88.71	26.96
4.5	1972	11	6	0	0	0	0	88.7	27
4.9	1973	3	22	0	0	0	0	87	28.1
4.9	1973	10	16	0	0	0	0	82.9	28.2
4.6	1973	8	1	0	0	0	0	89.17	29.59
4.5	1973	4	4	0	0	0	0	83.7	30.5
4.2	1973	2	10	0	0	0	0	80.3	30.5
5.3	1974	9	27	0	0	0	0	85.5	28.6
5.1	1974	3	24	0	0	0	0	86	27.7
5	1974	3	3	0	0	0	0	86.29	30.83
4.9	1974	12	23	0	0	0	0	81.4	29.4
4.1	1974	3	13	0	0	0	0	81.6	29.3
4.1	1974	5	6	0	0	0	0	81.7	29.3
5.1	1975	1	31	0	0	0	0	84.7	28.1
4.9	1975	6	24	0	0	0	0	87.3	27.5
4.8	1975	4	24	0	0	0	0	86.9	27.2
4.8	1975	9	6	0	0	0	0	82.2	29.3
4.8	1975	11	26	0	0	0	0	87.6	28.3
4.6	1975	4	9	0	0	0	0	84.89	30.41
4.6	1975	9	8	0	0	0	0	84.9	31.5
4.6	1975	11	21	0	0	0	0	86.5	27
4.3	1975	2	6	0	0	0	0	87.8	27.9
5.9	1976	5	10	0	0	0	0	81.5	29.3
5.2	1976	9	14	0	0	0	0	89.57	29.81
4.8	1976	10	23	0	0	0	0	86.2	28.7
4.7	1976	9	29	0	0	0	0	81.4	29.8
4.5	1976	7	23	0	0	0	0	83.9	31.7
4.5	1976	9	12	0	0	0	0	85.8	27.7
4.7	1977	9	20	0	0	0	0	81.1	29.5
4.5	1977	4	20	0	0	0	0	79.4	30.5
4.5	1977	6	5	0	0	0	0	88.3	26.2
4.3	1977	1	7	0	0	0	0	79.4	30.6
4.9	1978	2	10	0	0	0	0	84.6	28.1
4.9	1978	10	4	0	0	0	0	86	27.8
4.5	1978	8	15	0	0	0	0	84.6	31.3
4.5	1978	10	14	0	0	0	0	87.3	27.7
4.3	1978	2	19	0	0	0	0	85	29.3
4.3	1978	2	28	0	0	0	0	80.7	29.3
4.1	1978	12	25	0	0	0	0	83.9	28.1
4	1978	1	1	0	0	0	0	81.14	30.02
4	1978	2	10	0	0	0	0	85	27.9
4	1978	8	13	0	0	0	0	85.2	28
4	1978	10	23	0	0	0	0	86.8	28.8

Mag	Yr	Mo	day	hr	min	sec	depth	long	lat
5.9	1979	5	20	0	0	0	0	80.3	29.9
5	1979	6	19	0	0	0	0	87.5	26.7
4.5	1979	4	11	0	0	0	0	88.8	26
4.2	1979	10	17	0	0	0	0	87.6	28
4.2	1979	11	16	0	0	0	0	88.2	27.2
6.6	1980	7	29	0	0	0	0	81.1	29.6
6.2	1980	2	22	0	0	0	0	88.58	30.51
6.1	1980	11	19	0	0	0	0	88.8	27.4
4.8	1980	6	22	0	0	0	0	81.8	30.1
4.5	1980	11	20	0	0	0	0	85.2	29.6
4.1	1980	9	8	0	0	0	0	80.4	30
4.1	1980	12	22	0	0	0	0	89.3	26.3
4.1	1980	12	26	0	0	0	0	88.9	29.1
4.8	1981	2	9	0	0	0	0	89.8	27
4.8	1981	5	15	0	0	0	0	81.9	29.5
4.5	1981	11	21	0	0	0	0	89.12	29.53
4.2	1981	7	1	0	0	0	0	80.31	30.77
4.1	1981	4	9	0	0	0	0	84.4	28
4	1981	6	19	0	0	0	0	79.2	30.5
6.5	1982	1	23	0	0	0	0	82.2	31.7
5.7	1982	1	22	0	0	0	0	89.87	30.89
4.5	1982	12	29	0	0	0	0	79.8	30.3
4.3	1982	9	9	0	0	0	0	81.99	28.68
4.2	1982	3	24	0	0	0	0	88.74	30.57
4.2	1982	8	3	0	0	0	0	85.5	27.9
4.2	1982	8	18	0	0	0	0	89.5	27.1
4.1	1982	2	20	0	0	0	0	85.7	27.7
4.1	1982	5	2	0	0	0	0	81.7	29.2
4.1	1982	6	20	0	0	0	0	90	26.2
4.1	1982	9	9	0	0	0	0	82	28.7
4.1	1982	10	16	0	0	0	0	79.1	30.3
4	1982	5	29	0	0	0	0	83.6	28.5
4.5	1983	1	27	0	0	0	0	81.4	29.1
4.2	1983	7	5	0	0	0	0	80.7	29.5
4.2	1983	11	23	0	0	0	0	83.1	30.4
4.1	1983	5	20	0	0	0	0	79.77	30.36
5.3	1984	5	18	0	0	0	0	81.9	29.6
5	1984	11	18	0	0	0	0	84.1	28.8
4.7	1984	2	19	0	0	0	0	80.5	29.9
4.7	1984	4	15	0	0	0	0	82.3	31.7
4.6	1984	3	14	0	0	0	0	81.1	29.1
4.5	1984	4	22	0	0	0	0	84.2	30.6
4.3	1984	12	5	0	0	0	0	81.7	27.2

Mag	Yr	Mo	day	hr	min	sec	depth	long	lat
4.3	1984	12	18	0	0	0	0	80.9	29.4
4.2	1984	1	25	0	0	0	0	86.1	27.5
4.2	1984	9	15	0	0	0	0	81.5	29.2
4.1	1984	1	6	0	0	0	0	84.7	27.8
4.1	1984	5	30	0	0	0	0	83.9	28.8
4.1	1984	11	26	0	0	0	0	79.3	30.5
4	1984	10	2	0	0	0	0	88.76	30.98
4.6	1985	12	8	0	0	0	0	86.62	30.75
4.5	1985	1	30	0	0	0	0	85.44	30.92
4.3	1985	7	12	0	0	0	0	82.4	31.7
4.2	1985	5	25	0	0	0	0	88.5	27.6
4.2	1985	10	30	0	0	0	0	82.9	31.6
4.2	1985	12	23	0	0	0	0	85.7	27.6
4.1	1985	5	6	0	0	0	0	82.3	28.3
4.1	1985	7	28	0	0	0	0	88.8	30.36
4.1	1985	9	13	0	0	0	0	84.1	29.8
4.1	1985	10	21	0	0	0	0	84	28.8
4	1985	2	15	0	0	0	0	81.6	30.1
4	1985	10	2	0	0	0	0	89.7	27.1
5.4	1986	1	10	0	0	0	0	86.5	28.6
4.7	1986	1	7	0	0	0	0	88.3	26.9
4.6	1986	2	2	0	0	0	0	86.45	27.92
4.3	1986	2	10	0	0	0	0	87.86	28.15
4.2	1986	2	28	0	0	0	0	81.9	29.1
4.1	1986	1	6	0	0	0	0	85.4	27.8
4.1	1986	4	4	0	0	0	0	88.26	30.86
4.1	1986	9	16	0	0	0	0	86.61	30.99
5.3	1987	8	9	0	0	0	0	83.7	29.5
5.2	1987	1	19	0	0	0	0	83.7	28.4
4.3	1987	4	23	0	0	0	0	87.1	28
4.3	1987	6	6	0	0	0	0	79.3	30.6
4.3	1987	8	21	0	0	0	0	80.2	31.7
4.2	1987	5	10	0	0	0	0	86.7	28.2
4.2	1987	11	25	0	0	0	0	85.9	28
4.1	1987	4	30	0	0	0	0	85.8	28.4
4	1987	2	24	0	0	0	0	81.9	29.1
6.8	1988	8	20	0	0	0	0	86.6	26.8
5.1	1988	10	29	0	0	0	0	85.6	27.9
4.7	1988	9	27	0	0	0	0	88.3	27.2
4.6	1988	4	11	0	0	0	0	85.9	27.5
4.5	1988	5	15	0	0	0	0	80.5	29.9
4.5	1988	6	9	0	0	0	0	79.2	30.7
4.5	1988	6	12	0	0	0	0	82.4	28.5

Mag	Yr	Mo	day	hr	min	sec	depth	long	lat
4.3	1988	1	23	0	0	0	0	81.6	29.5
4.3	1988	5	26	0	0	0	0	88.6	27.4
4.3	1988	9	21	0	0	0	0	85.6	28.7
4.2	1988	2	12	0	0	0	0	82.9	30.5
4.2	1988	12	7	0	0	0	0	83.1	31.6
4.2	1988	12	27	0	0	0	0	87.8	27.9
4.1	1988	4	9	0	0	0	0	86.9	29.8
4.1	1988	8	29	0	0	0	0	87.5	26.4
4.1	1988	11	14	0	0	0	0	82.1	30.2
4.1	1988	12	2	0	0	0	0	81.2	29.6
4.1	1988	12	15	0	0	0	0	81.6	29.1
4	1988	12	24	0	0	0	0	88	26.9
5.4	1989	2	3	0	0	0	0	89.94	30.19
4.7	1989	5	22	0	0	0	0	87.9	27.2
4.2	1989	10	10	0	0	0	0	87.5	28.7
4.1	1989	3	8	0	0	0	0	84	28
4	1989	11	19	0	0	0	0	89.7	29
5.2	1990	1	9	0	0	0	0	88.2	28.2
4.8	1990	9	21	0	0	0	0	79.8	29.7
4.6	1990	5	20	0	0	0	0	83.16	28.35
4.6	1990	10	14	0	0	0	0	86.39	30.82
4.6	1990	12	18	0	0	0	0	79.1	30.3
4.5	1990	2	21	0	0	0	0	82.4	28.1
4.5	1990	12	20	0	0	0	0	82.9	28.1
4.2	1990	2	9	0	0	0	0	80.7	29.9
4.1	1990	1	30	0	0	0	0	85.7	28.6
4.1	1990	2	18	0	0	0	0	89.95	29.39
4.1	1990	5	6	0	0	0	0	89.98	29.99
4.1	1990	7	13	0	0	0	0	86.93	28.25
4.1	1990	10	28	0	0	0	0	81.6	30.7
5.6	1991	12	9	0	0	0	0	81.6	29.5
4.6	1991	12	21	0	0	0	0	88.1	27.9
4.3	1991	9	14	0	0	0	0	80.92	30.7
4.2	1991	3	15	0	0	0	0	87.7	28.3
4.2	1991	4	22	0	0	0	0	79.7	30.1
4.2	1991	5	18	0	0	0	0	80.1	31.7
4.2	1991	5	20	0	0	0	0	86.77	30.99
4.2	1991	5	27	0	0	0	0	80.3	29.3
4.1	1991	2	15	0	0	0	0	84.24	29.43
4.1	1991	10	15	0	0	0	0	79.3	30.6
5.2	1992	6	2	0	0	0	0	81.91	28.98
4.8	1992	4	1	0	0	0	0	87.2	27.6
4.7	1992	6	13	0	0	0	0	82.93	28.94

Mag	Yr	Mo	day	hr	min	sec	depth	long	lat
4.6	1992	3	14	0	0	0	0	79	30.4
4.6	1992	3	24	0	0	0	0	81.6	31.4
4.6	1992	4	4	0	0	0	0	88	28.2
4.5	1992	3	7	0	0	0	0	89.31	29.68
4.1	1992	1	30	0	0	0	0	81.2	29.2
6.4	1993	3	20	0	0	0	0	87.33	29.08
4.9	1993	1	2	0	0	0	0	81.12	29.15
4.7	1993	10	20	0	0	0	0	82.26	28.78
4.5	1993	9	13	0	0	0	0	83.67	30.98
4.3	1993	4	12	0	0	0	0	82.8	28.31
4.3	1993	7	3	0	0	0	0	86.63	28.36
4.3	1993	7	5	0	0	0	0	85.12	27.94
4.2	1993	3	4	0	0	0	0	86.91	29.48
4.2	1993	3	25	0	0	0	0	80.55	29.62
4.2	1993	7	9	0	0	0	0	86.06	26.81
4.2	1993	12	14	0	0	0	0	86.84	28.49
4.1	1993	1	13	0	0	0	0	86.56	28.5
4.1	1993	9	5	0	0	0	0	87.31	27.29
4	1993	8	19	0	0	0	0	80.04	30.08
4	1993	11	14	0	0	0	0	80.36	30.66
4	1993	11	22	0	0	0	0	82.86	28.2
5.9	1994	8	31	0	0	0	0	79.51	26.09
5.6	1994	7	17	0	0	0	0	81.52	29.37
5.4	1994	7	23	0	0	0	0	86.55	31.07
5.3	1994	6	25	0	0	0	0	86.16	27.75
5.2	1994	12	8	0	0	0	0	79.69	30.44
5.1	1994	9	25	0	0	0	0	87.35	28.34
5.03	1994	1	31	0	0	0	0	81.79	29.55
5	1994	10	24	0	0	0	0	82	28.92
4.94	1994	5	25	0	0	0	0	87.79	27.65
4.9	1994	12	12	0	0	0	0	80.69	29.84
4.9	1994	12	13	0	0	0	0	82.88	28.7
4.77	1994	5	10	0	0	0	0	83.94	29.23
4.68	1994	12	30	0	0	0	0	88.26	30.35
4.51	1994	3	29	0	0	0	0	79.5	30.61
5.9	1995	6	21	0	0	0	0	85.27	21.81
5.2	1995	1	1	0	0	0	0	87.59	27.77
5.2	1995	8	7	0	0	0	0	81.63	29.88
5.2	1995	10	21	0	0	0	0	78.96	31.43
5.11	1995	7	30	0	0	0	0	88.23	30.27
5.03	1995	3	29	0	0	0	0	84.2	28.77
5.03	1995	11	25	0	0	0	0	86.8	31.11
5	1995	10	4	0	0	0	0	84.44	28.27

Mag	Yr	Mo	day	hr	min	sec	depth	long	lat
4.94	1995	4	24	0	0	0	0	88.25	29.89
4.9	1995	1	29	0	0	0	0	86.11	26.85
4.9	1995	2	18	0	0	0	0	85.88	27.74
4.9	1995	8	7	0	0	0	0	86.24	25.75
4.85	1995	6	28	0	0	0	0	86.83	31.13
4.77	1995	2	2	0	0	0	0	87.84	30.05
4.7	1995	1	19	0	0	0	0	83.44	28.35
4.7	1995	1	30	0	0	0	0	82.3	29.38
4.7	1995	6	11	0	0	0	0	87.95	27.22
4.68	1995	7	28	0	0	0	0	86.41	30.73
4.68	1995	10	27	0	0	0	0	83.52	28.73
4.6	1995	2	4	0	0	0	0	81.71	31.11
4.6	1995	12	24	0	0	0	0	86.27	27.53
4.6	1995	12	25	0	0	0	0	89.38	31.15
5.7	1996	7	3	0	0	0	0	88.19	30.15
5.6	1996	7	3	0	0	0	0	88.23	29.98
5.4	1996	4	26	0	0	0	0	87.705	27.935
5.4	1996	12	3	0	0	0	0	86.842	27.39
5.4	1996	12	29	0	0	0	0	81.828	29.75
5.28	1996	9	25	0	0	0	0	88.55	27.43
5.11	1996	3	26	0	0	0	0	79.1	30.65
5.1	1996	2	28	0	0	0	0	86.766	27.122
4.94	1996	7	17	0	0	0	0	78.55	31.39
4.94	1996	9	25	0	0	0	0	78.58	30.44
4.85	1996	9	13	0	0	0	0	88.23	27.03
4.8	1996	10	16	0	0	0	0	79.951	28.778
4.8	1996	12	22	0	0	0	0	81.726	29.012
4.77	1996	1	25	0	0	0	0	87.22	28.7
4.6	1996	1	19	0	0	0	0	86.58	28.99
4.6	1996	2	7	0	0	0	0	80.49	29.6
4.6	1996	2	12	0	0	0	0	88.28	28.46
4.6	1996	2	18	0	0	0	0	83.97	29.95
4.6	1996	2	22	0	0	0	0	87.23	28.01
4.6	1996	7	24	0	0	0	0	87.61	31.32
4.51	1996	2	26	0	0	0	0	84.1	30.28
4.51	1996	5	14	0	0	0	0	87.94	29.68
5.9	1997	5	21	0	0	0	0	80.47	23.71
5.8	1997	1	31	0	0	0	0	85.286	28.078
5.6	1997	1	5	0	0	0	0	80.588	29.785
5.4	1997	10	24	0	0	0	0	82.54	28.66
5.2	1997	1	31	0	0	0	0	85.301	28.015
5.2	1997	12	8	0	0	0	0	86.85	27.19
5.11	1997	7	5	0	0	0	0	86.86	28.8

Mag	Yr	Mo	day	hr	min	sec	depth	long	lat
5.1	1997	10	11	0	0	0	0	86.41	27.65
5.03	1997	3	3	0	0	0	0	86.08	27.24
4.94	1997	9	18	0	0	0	0	88.15	28.87
4.9	1997	1	1	0	0	0	0	86.561	27.005
4.9	1997	4	7	0	0	0	0	87.746	27.5
4.9	1997	5	28	0	0	0	0	82.58	28.68
4.85	1997	4	5	0	0	0	0	86.06	30.09
4.7	1997	11	26	0	0	0	0	86	27.75
4.68	1997	9	13	0	0	0	0	88.19	30.12
4.68	1997	9	17	0	0	0	0	83.7	29.74
6.2	1998	9	3	0	0	0	0	86.92	27.71
5.9	1998	8	25	0	0	0	0	88.11	30.08
5.6	1998	2	22	0	0	0	0	85.52	28.72
5.5	1998	11	26	0	0	0	0	87.814	27.859
5.3	1998	7	15	0	0	0	0	81.247	29.551
5.2	1998	2	28	0	0	0	0	87.86	27.15
5.2	1998	6	27	0	0	0	0	85.812	27.866
5.2	1998	9	10	0	0	0	0	88.33	27.444
5.11	1998	6	6	0	0	0	0	89.22	30.37
5.11	1998	6	6	0	0	0	0	89.29	30.38
5.1	1998	5	16	0	0	0	0	84.817	26.76
5	1998	5	10	0	0	0	0	82.38	29.41
4.94	1998	2	22	0	0	0	0	88.05	30.22
4.9	1998	2	12	0	0	0	0	88.19	27.59
4.85	1998	2	1	0	0	0	0	87.12	28.19
4.77	1998	3	15	0	0	0	0	86.89	28.55
4.77	1998	5	1	0	0	0	0	79.54	30.04
4.77	1998	12	25	0	0	0	0	86.47	30.33
4.6	1998	10	2	0	0	0	0	85.14	29.17
4.6	1998	11	14	0	0	0	0	86.51	31.08
4.51	1998	2	22	0	0	0	0	88.16	30.12
4.51	1998	7	31	0	0	0	0	87.73	28.01
6.6	1999	3	28	0	0	0	0	79.4	30.51
6.5	1999	3	28	0	0	0	0	79.38	30.38
6.3	1999	3	28	0	0	0	0	79.257	30.498
5.7	1999	8	10	0	0	0	0	86.208	27.795
5.45	1999	8	1	0	0	0	0	86.73	28.44
5.03	1999	3	28	0	0	0	0	79.31	30.34
5	1999	2	11	0	0	0	0	83.348	28.61
4.94	1999	11	16	0	0	0	0	82.77	30.39
4.9	1999	2	19	0	0	0	0	80.618	29.867
4.9	1999	8	25	0	0	0	0	84.742	28.157
4.9	1999	9	20	0	0	0	0	87.897	27.38

Mag	Yr	Mo	day	hr	min	sec	depth	long	lat
4.9	1999	12	11	0	0	0	0	81.563	30.159
4.85	1999	9	5	0	0	0	0	87.41	28.16
4.8	1999	4	7	0	0	0	0	81.226	29.596
4.68	1999	4	24	0	0	0	0	81.16	28.38
4.51	1999	12	25	0	0	0	0	87.69	30.31
5.3	2000	2	26	0	0	0	0	82.314	28.617
5.3	2000	3	13	0	0	0	0	87.71	27.73
5.2	2000	3	13	0	0	0	0	87.42	27.99
5.11	2000	10	26	0	0	0	0	81.88	29.21
5.03	2000	10	8	0	0	0	0	88.12	30.19
4.9	2000	9	2	0	0	0	0	85.334	28.071
4.85	2000	6	3	0	0	0	0	87.19	31.19
4.85	2000	7	3	0	0	0	0	84.71	31.47
4.77	2000	5	5	0	0	0	0	81.57	29.4
4.77	2000	5	29	0	0	0	0	86.98	30.76
4.7	2000	6	2	0	0	0	0	83.29	28.07
4.6	2000	12	31	0	0	0	0	87.71	27.84
4.51	2000	10	9	0	0	0	0	81.48	29.33
6.6	2001	1	26	0	0	0	0	69.853	24.173
5.8	2001	7	16	0	0	0	0	84.68	27.97
5.8	2001	11	27	0	0	0	0	81.81	29.53
5.7	2001	11	27	0	0	0	0	81.79	29.63
5.45	2001	4	28	0	0	0	0	87.16	28.87
5.4	2001	11	27	0	0	0	0	81.99	29.52
5.37	2001	12	2	0	0	0	0	88.17	27.15
5.2	2001	9	13	0	0	0	0	80.644	29.821
5.1	2001	4	4	0	0	0	0	86.171	27.806
5.1	2001	7	16	0	0	0	0	84.27	28.29
5.1	2001	9	27	0	0	0	0	87.78	26.98
5.1	2001	12	19	0	0	0	0	89.88	23.83
4.94	2001	4	12	0	0	0	0	88.11	29.94
4.85	2001	6	13	0	0	0	0	85.76	31.38
4.85	2001	7	2	0	0	0	0	86.54	30.55
4.8	2001	4	15	0	0	0	0	81.4	29.458
4.77	2001	8	6	0	0	0	0	87.43	27.66
4.77	2001	12	2	0	0	0	0	86.4	31.43
4.68	2001	8	9	0	0	0	0	79.17	30.49
4.51	2001	11	7	0	0	0	0	85.45	30.11
4.51	2001	11	23	0	0	0	0	87.41	31.29
5.9	2002	6	4	0	0	0	0	81.34	30.71
5.6	2002	6	20	0	0	0	0	88.38	25.63
5.4	2002	5	2	0	0	0	0	86.67	27.67
5.11	2002	11	5	0	0	0	0	86.58	31.01

Mag	Yr	Mo	day	hr	min	sec	depth	long	lat
4.94	2002	3	9	0	0	0	0	79.97	29.96
4.94	2002	4	2	0	0	0	0	87.01	29.29
4.7	2002	7	16	0	0	0	0	87.36	27.75
4.6	2002	2	6	0	0	0	0	88.07	31.31
4.6	2002	4	2	0	0	0	0	86.87	29.04
4.6	2002	7	2	0	0	0	0	84.82	27.17
4.6	2002	8	11	0	0	0	0	86.4	26.97
4.6	2002	10	9	0	0	0	0	83.9	28.18
4.6	2002	11	4	0	0	0	0	82.21	28.86
4.6	2002	12	30	0	0	0	0	86.27	30.72
4.51	2002	5	3	0	0	0	0	86.39	30.88
4.51	2002	11	13	0	0	0	0	84.15	30.74
4.5	2002	4	15	0	0	0	0	86.31	26.87
4.5	2002	6	4	0	0	0	0	80.53	28.79
4.5	2002	6	7	0	0	0	0	81.12	28.77
5.7	2003	3	25	0	0	0	0	89.59	27.18
5.37	2003	1	16	0	0	0	0	88.01	29.8
5.2	2003	2	26	0	0	0	0	86.01	28.47
5.2	2003	4	4	0	0	0	0	80.39	30.1
5.2	2003	5	27	0	0	0	0	79.29	30.55
5.2	2003	11	22	0	0	0	0	83.91	28.47
5.11	2003	9	3	0	0	0	0	80.43	30.58
5.1	2003	6	23	0	0	0	0	87.97	27.79
4.94	2003	8	20	0	0	0	0	82.22	30.17
4.9	2003	7	28	0	0	0	0	82.52	28.75
4.85	2003	12	10	0	0	0	0	83.28	30.47
4.8	2003	8	2	0	0	0	0	82.1	29.51
4.77	2003	6	3	0	0	0	0	86.03	30.63
4.7	2003	8	5	0	0	0	0	86.03	27.99
4.7	2003	9	24	0	0	0	0	81.96	28.99
4.68	2003	1	18	0	0	0	0	81.95	28.62
4.68	2003	7	1	0	0	0	0	86.38	30.92
4.6	2003	3	21	0	0	0	0	80.57	29.75
4.6	2003	12	11	0	0	0	0	80.54	29.85
4.51	2003	5	27	0	0	0	0	79.09	30.38
4.5	2003	3	29	0	0	0	0	86.63	27.46
4.5	2003	10	29	0	0	0	0	86.69	27.26
5.6	2004	1	3	0	0	0	0	86.06	27.87
5.6	2004	10	26	0	0	0	0	81.15	31.02
5.6	2004	10	26	0	0	0	0	81.09	30.91
5.2	2004	5	29	0	0	0	0	82.96	28.55
5.2	2004	7	11	0	0	0	0	83.64	30.71
5.11	2004	2	27	0	0	0	0	87.66	28.13

Mag	Yr	Mo	day	hr	min	sec	depth	long	lat
5.11	2004	7	23	0	0	0	0	88.12	30.18
5.11	2004	10	26	0	0	0	0	81.23	31.03
5	2004	2	18	0	0	0	0	87.8	27.61
4.94	2004	1	6	0	0	0	0	86.04	30.54
4.94	2004	4	3	0	0	0	0	81.12	29.85
4.9	2004	1	3	0	0	0	0	86.07	27.76
4.9	2004	3	31	0	0	0	0	87.63	27.18
4.9	2004	7	16	0	0	0	0	84.06	28.32
4.85	2004	7	11	0	0	0	0	83.67	30.82
4.8	2004	9	12	0	0	0	0	81.84	29.51
4.77	2004	8	25	0	0	0	0	86.07	30.21
4.77	2004	9	9	0	0	0	0	80.28	29.47
4.7	2004	5	29	0	0	0	0	82.98	28.59
4.7	2004	5	29	0	0	0	0	89.97	28.58
4.7	2004	12	26	0	0	0	0	81.63	29.9
4.68	2004	6	24	0	0	0	0	87.91	29.87
4.6	2004	2	2	0	0	0	0	81.53	29.32
4.6	2004	5	21	0	0	0	0	85.12	30.62
4.6	2004	8	22	0	0	0	0	85.24	28.03
4.6	2004	10	5	0	0	0	0	86.55	26.83
4.6	2004	11	10	0	0	0	0	87.78	27.93
4.6	2004	11	17	0	0	0	0	84.67	28.26
4.6	2004	12	5	0	0	0	0	81.24	30.48
4.5	2004	1	7	0	0	0	0	85	28.07
6.3	2005	4	7	0	0	0	0	83.66	30.49
6.3	2005	4	7	0	0	0	0	83.64	30.45
5.5	2005	3	19	0	0	0	0	84.39	28.25
5.3	2005	10	29	0	0	0	0	81.88	29.5
5.2	2005	1	16	0	0	0	0	81.14	29.68
5.2	2005	2	8	0	0	0	0	86.07	27.76
5.2	2005	10	25	0	0	0	0	81.21	30.15
5.1	2005	12	14	0	0	0	0	79.26	30.48
4.94	2005	5	11	0	0	0	0	85.17	30.6
4.9	2005	1	16	0	0	0	0	81.04	29.81
4.9	2005	6	14	0	0	0	0	87.89	27.28
4.9	2005	8	20	0	0	0	0	88.17	31.22
4.9	2005	10	31	0	0	0	0	84.83	28.65
4.77	2005	8	16	0	0	0	0	78.56	30.92
4.77	2005	8	20	0	0	0	0	88.21	31.14
4.7	2005	3	26	0	0	0	0	87.93	28.26
4.7	2005	4	7	0	0	0	0	81.88	29.35
4.7	2005	7	27	0	0	0	0	68.88	27.47
4.7	2005	8	8	0	0	0	0	85.51	27.98

Mag	Yr	Mo	day	hr	min	sec	depth	long	lat
4.6	2005	4	4	0	0	0	0	83.31	28.54
4.6	2005	4	4	0	0	0	0	83.18	28.56
4.6	2005	5	5	0	0	0	0	87.7	27.69
4.51	2005	4	7	0	0	0	0	81.45	29.3
4.51	2005	4	8	0	0	0	0	82.71	29.87
5.5	2006	2	3	0	0	0	0	86.8	27.18
5.3	2006	2	14	0	0	0	0	88.39	27.38
5.2	2006	9	19	0	0	0	0	81.54	29.62
5	2006	2	19	0	0	0	0	83.89	28.24
4.94	2006	1	20	0	0	0	0	85.01	31.44
4.9	2006	4	4	0	0	0	0	85.83	27.91
4.9	2006	9	26	0	0	0	0	80.83	30.1
4.85	2006	2	14	0	0	0	0	80.53	30.27
4.85	2006	8	5	0	0	0	0	80.1	29.89
4.7	2006	8	30	0	0	0	0	83.6	29.05
4.7	2006	9	17	0	0	0	0	87.8	26.98
4.51	2006	7	17	0	0	0	0	89.43	26.74
5.4	2007	8	11	0	0	0	0	87.9	27.28
5.2	2007	10	29	0	0	0	0	85.45	27.9
5.11	2007	8	26	0	0	0	0	89.21	30.03
4.94	2007	1	20	0	0	0	0	82.73	31.04
4.9	2007	8	1	0	0	0	0	81.91	29.49
4.9	2007	8	3	0	0	0	0	87.03	27.24
4.9	2007	11	5	0	0	0	0	84.45	28.2
4.85	2007	8	9	0	0	0	0	80.16	31.34
4.7	2007	2	6	0	0	0	0	83.43	28.36
4.7	2007	6	4	0	0	0	0	83.89	27.44
4.7	2007	6	17	0	0	0	0	84.91	27.83
4.7	2007	8	3	0	0	0	0	87.04	27.2
4.6	2007	2	6	0	0	0	0	83.43	28.35
4.6	2007	9	7	0	0	0	0	86.26	27.72
4.6	2007	10	18	0	0	0	0	82.07	29.83
4.6	2007	11	13	0	0	0	0	83.27	30.08
4.51	2007	4	17	0	0	0	0	87.76	28.26
6.7	2008	8	25	0	0	0	0	83.52	30.9
6.7	2008	8	25	0	0	0	0	83.59	30.98
5.9	2008	8	25	0	0	0	0	83.33	30.85
5.9	2008	12	8	0	0	0	0	81.86	30.15
5.5	2008	12	2	0	0	0	0	87.99	27.32
5.45	2008	8	25	0	0	0	0	83.52	30.83
5.45	2008	8	25	0	0	0	0	83.38	30.8
5.28	2008	8	25	0	0	0	0	83.38	30.71
5.28	2008	9	4	0	0	0	0	80.35	30.28

Mag	Yr	Mo	day	hr	min	sec	depth	long	lat
5.2	2008	6	15	0	0	0	0	80.96	29.73
5.11	2008	12	25	0	0	0	0	88.63	27.24
5.1	2008	6	20	0	0	0	0	85.73	27.98
5.1	2008	8	25	0	0	0	0	83.29	30.63
5.1	2008	12	1	0	0	0	0	85.29	28.18
5	2008	8	25	0	0	0	0	83.47	30.93
4.94	2008	8	25	0	0	0	0	83.27	30.51
4.94	2008	8	25	0	0	0	0	83.51	30.98
4.94	2008	11	17	0	0	0	0	88.23	29.19
4.9	2008	3	17	0	0	0	0	81.53	29.76
4.85	2008	8	25	0	0	0	0	83.33	30.69
4.85	2008	11	18	0	0	0	0	83.77	30.25
4.8	2008	12	23	0	0	0	0	84.39	28.19
4.77	2008	5	25	0	0	0	0	89	28.96
4.77	2008	8	25	0	0	0	0	83.29	30.78
4.7	2008	2	16	0	0	0	0	86.25	26.8
4.7	2008	5	8	0	0	0	0	87.52	27.5
4.7	2008	5	20	0	0	0	0	83.33	28.33
4.68	2008	8	25	0	0	0	0	83.36	30.75
4.6	2008	1	15	0	0	0	0	86.53	27.37
4.6	2008	2	14	0	0	0	0	86.53	27.8
4.6	2008	8	19	0	0	0	0	80.01	30.08
4.6	2008	8	25	0	0	0	0	83.47	30.71
4.6	2008	8	25	0	0	0	0	83.45	30.68
4.6	2008	9	10	0	0	0	0	83.01	28.4
4.51	2008	8	25	0	0	0	0	83.38	30.73
5.8	2009	7	24	0	0	0	0	85.9	31.16
5.5	2009	11	7	0	0	0	0	86.06	29.52
4.9	2009	5	14	0	0	0	0	87.36	27.48
4.9	2009	6	6	0	0	0	0	86.31	31
4.9	2009	11	22	0	0	0	0	82.15	29.02
4.9	2009	12	16	0	0	0	0	81.51	29.6
4.7	2009	1	10	0	0	0	0	88.04	27.9
4.7	2009	1	23	0	0	0	0	81.4	29.05
4.7	2009	5	14	0	0	0	0	87.35	27.43
4.7	2009	7	12	0	0	0	0	86.36	27.71
4.6	2009	10	29	0	0	0	0	83.11	28.73
4.6	2009	12	15	0	0	0	0	84.4	28.28
4.51	2009	7	24	0	0	0	0	85.81	30.95
4.5	2009	8	2	0	0	0	0	85.18	28.12
4.5	2009	11	2	0	0	0	0	87.94	27.87
5.45	2010	6	22	0	0	0	0	80.43	29.87
5.2	2010	3	15	0	0	0	0	81.95	30.64

Mag	Yr	Mo	day	hr	min	sec	depth	long	lat
5.2	2010	10	17	0	0	0	0	85.71	28.64
5.11	2010	7	5	0	0	0	0	80.54	31.06
5.1	2010	2	26	0	0	0	0	86.75	28.47
5.1	2010	6	13	0	0	0	0	81.65	29.6
5.1	2010	12	29	0	0	0	0	86.51	30.94
5	2010	11	25	0	0	0	0	83.17	28.44
4.94	2010	7	10	0	0	0	0	86.98	29.32
4.94	2010	7	10	0	0	0	0	79.61	30.08
4.9	2010	11	25	0	0	0	0	82.32	28.38
4.8	2010	11	30	0	0	0	0	85.79	26.93
4.7	2010	3	1	0	0	0	0	83.11	29.76
4.7	2010	4	14	0	0	0	0	83.09	28.31
4.7	2010	5	13	0	0	0	0	84.51	28.3
4.6	2010	1	18	0	0	0	0	83.97	28.37
4.6	2010	2	17	0	0	0	0	86.08	26.79
4.6	2010	2	28	0	0	0	0	81.52	28.4
4.6	2010	12	18	0	0	0	0	84.79	28.18
4.5	2010	4	30	0	0	0	0	86.36	27.75
4.5	2010	6	13	0	0	0	0	86.77	28.01
6.5	2011	9	18	0	0	0	0	88.32	27.78
5.7	2011	4	4	0	0	0	0	80.54	29.92
5.2	2011	6	20	0	0	0	0	79.34	30.61
5.2	2011	8	15	0	0	0	0	86.27	27.44
5.2	2011	8	19	0	0	0	0	81.34	29.7
5.2	2011	8	27	0	0	0	0	86.6	26.94
5.2	2011	11	13	0	0	0	0	84.93	28.2
5.11	2011	9	18	0	0	0	0	88.58	27.52
5.03	2011	9	18	0	0	0	0	88.45	27.35
5	2011	2	13	0	0	0	0	87.01	27.47
5	2011	10	1	0	0	0	0	81.81	30.16
4.85	2011	5	24	0	0	0	0	85.39	30.04
4.8	2011	3	12	0	0	0	0	83.78	28.31
4.8	2011	8	25	0	0	0	0	82.53	28.15
4.7	2011	1	18	0	0	0	0	85.94	27.8
4.7	2011	3	10	0	0	0	0	85.24	28.02
4.7	2011	3	22	0	0	0	0	82.74	28.11
4.7	2011	6	18	0	0	0	0	87.35	27.83
4.7	2011	11	23	0	0	0	0	81.68	28.91
4.7	2011	12	2	0	0	0	0	85.34	28.05
4.6	2011	1	18	0	0	0	0	81.97	30.03
4.6	2011	4	4	0	0	0	0	80.81	30
4.6	2011	7	12	0	0	0	0	83.73	30.34
4.6	2011	8	11	0	0	0	0	86.81	30.09

Mag	Yr	Mo	day	hr	min	sec	depth	long	lat
4.5	2011	8	18	0	0	0	0	84.31	28.21
4.5	2011	8	22	0	0	0	0	83.96	28.29
4.5	2011	12	8	0	0	0	0	82.86	27.97
5.6	2012	8	23	0	0	0	0	82.84	28.38
5.6	2012	11	11	0	0	0	0	81.13	29.51
5.4	2012	3	27	0	0	0	0	87.87	26.12
5.3	2012	6	9	0	0	0	0	84.17	28.32
5.2	2012	7	3	0	0	0	0	88.01	29.91
5.2	2012	7	28	0	0	0	0	80.54	30.12
5.11	2012	5	27	0	0	0	0	83.47	30.82
5.03	2012	8	9	0	0	0	0	86.74	28.46
5.03	2012	11	30	0	0	0	0	88.2	27.22
5	2012	3	19	0	0	0	0	82.02	28.7
4.9	2012	1	19	0	0	0	0	81.91	29.73
4.85	2012	8	1	0	0	0	0	85.34	29.97
4.85	2012	11	5	0	0	0	0	86.19	28.45
4.8	2012	8	28	0	0	0	0	81.81	28.73
4.6	2012	9	24	0	0	0	0	84.44	30.99
4.6	2012	12	21	0	0	0	0	88.54	28.57
5.9	2013	8	30	0	0	0	0	86.03	28.43
5.7	2013	10	3	0	0	0	0	88.51	27.14
5.6	2013	1	9	0	0	0	0	81.7	29.82
5.6	2013	6	28	0	0	0	0	82.4	28.76
5.45	2013	5	16	0	0	0	0	86.6	31.5
4.94	2013	4	6	0	0	0	0	88.05	30.04
4.9	2013	9	12	0	0	0	0	87.34	26.96
4.8	2013	6	26	0	0	0	0	85.96	26.85
4.8	2013	6	27	0	0	0	0	80.8	30.05
4.77	2013	9	15	0	0	0	0	83.22	30.92
4.7	2013	5	26	0	0	0	0	85.91	27.72
4.7	2013	6	9	0	0	0	0	86.7	27.31
4.7	2013	10	28	0	0	0	0	87.37	27.36
4.68	2013	8	4	0	0	0	0	87.14	28.27
5.8	2014	8	3	0	0	0	0	85.64	29.45
5.2	2014	12	26	0	0	0	0	87.35	28.53
4.9	2014	7	4	0	0	0	0	87.91	27.83
4.9	2014	11	25	0	0	0	0	84.94	28.25
4.85	2014	6	7	0	0	0	0	81.6	30.27
4.77	2014	8	24	0	0	0	0	79.96	30.04
4.7	2014	4	11	0	0	0	0	81.26	29.29
4.7	2014	5	20	0	0	0	0	84.73	28.32
4.7	2014	7	7	0	0	0	0	80.93	29.73
4.68	2014	10	29	0	0	0	0	86.54	31.1

Mag	Yr	Mo	day	hr	min	sec	depth	long	lat
4.6	2014	5	25	0	0	0	0	84.09	28.23
4.6	2014	8	29	0	0	0	0	87.88	29.84
4.6	2014	10	1	0	0	0	0	82.11	30.43
4.51	2014	7	6	0	0	0	0	80.34	30.32
4.51	2014	7	11	0	0	0	0	86.39	30.94
4.51	2014	12	6	0	0	0	0	80.03	30.67
4.5	2014	4	23	0	0	0	0	87.62	27.3
7	2015	4	25	0	0	0	0	84.75	28.24
6.5	2015	4	26	0	0	0	0	86.05	27.84
6.3	2015	4	25	0	0	0	0	84.72	28.28
5.7	2015	4	25	0	0	0	0	85.65	28.13
5.6	2015	1	31	0	0	0	0	83.73	28.29
5.6	2015	4	25	0	0	0	0	85.91	28.34
5.6	2015	4	25	0	0	0	0	85.8	28.41
5.6	2015	12	18	0	0	0	0	81.69	29.44
5.5	2015	6	20	0	0	0	0	82.76	28.65
5.4	2015	4	25	0	0	0	0	85.75	28.2
5.3	2015	4	21	0	0	0	0	82.18	28.85
5.2	2015	4	1	0	0	0	0	79.51	30.35
5.1	2015	5	22	0	0	0	0	81.47	30.31
5	2015	6	2	0	0	0	0	81.75	30
4.94	2015	4	2	0	0	0	0	86.33	28.7
4.9	2015	1	6	0	0	0	0	81.51	29.07
4.9	2015	2	14	0	0	0	0	87.01	27.42
4.9	2015	9	29	0	0	0	0	80.6	29.83
4.9	2015	11	27	0	0	0	0	87.95	27.11
4.8	2015	1	22	0	0	0	0	81.03	29.36
4.51	2015	2	13	0	0	0	0	80.39	31.22
4.5	2015	5	10	0	0	0	0	86.67	26.94
4.9	2016	2	23	0	0	0	0	87.15	27.47
4.8	2016	3	7	0	0	0	0	81.7	30.22
4.7	2016	1	27	0	0	0	0	86.27	26.68
4.6	2016	3	24	0	0	0	0	88.04	27.75
5.4	2017	12	8	0	0	0	0	86.19	27.63
5.2	2017	8	22	0	0	0	0	81.1	29.41
5.1	2017	8	24	0	0	0	0	85.94	28.06
4.9	2017	11	6	0	0	0	0	81.28	29.78
4.9	2017	12	28	0	0	0	0	80.76	29.82
4.7	2017	10	15	0	0	0	0	83.32	28.5
4.6	2017	2	10	0	0	0	0	80.61	29.88
4.6	2017	3	10	0	0	0	0	81.57	30.37
4.6	2017	4	24	0	0	0	0	81.31	29.75
4.6	2017	6	14	0	0	0	0	88.13	27.88

Mag	Yr	Mo	day	hr	min	sec	depth	long	lat
4.6	2017	10	2	0	0	0	0	82.55	28.83
4.5	2017	7	15	0	0	0	0	81.75	28.94
4.5	2017	10	26	0	0	0	0	81.45	29.08
5.2	2018	6	5	0	0	0	0	81.65	29.68
5.2	2018	6	28	0	0	0	0	84.91	27.87
5.1	2018	6	20	0	0	0	0	88.01	27.36
5	2018	6	20	0	0	0	0	87.9	27.31
4.9	2018	5	24	0	0	0	0	80.54	29.98
4.7	2018	5	31	0	0	0	0	81.77	28.9
4.7	2018	7	24	0	0	0	0	85.51	27.94
4.7	2018	8	29	0	0	0	0	87.41	27.79
4.5	2018	9	19	0	0	0	0	82.88	28.57
4.9	2018	10	6	5	7	0	0	81.72	28.94
5.2	2018	12	22	23	21	0	0	85.76	27.85
5.0	2019	1	22	16	45	0	0	86.96	27.09
5.1	2019	2	14	11	26	0	0	88.18	27.81
5.2	2019	4	14	22	42	0	0	81.24	29.49
5.5	2019	4	24	0	44	0	0	85.17	27.69
5.4	2019	5	11	18	51	0	0	81.78	28.98
5.3	2019	5	17	8	23	0	0	84.87	27.85
5.3	2019	5	25	5	17	0	0	86.47	27.7
5.1	2019	5	30	4	16	0	0	82.11	29.62
5.2	2019	8	9	12	41	0	0	83.22	28.5
5.3	2019	9	15	5	9	0	0	81.74	30.3
5.0	2019	9	16	14	33	0	0	80.48	29.8
5.2	2019	9	26	13	4	0	0	84.65	28.28
4.9	2019	10	20	19	24	0	0	87.98	27.82
4.8	2019	10	22	5	21	0	0	86.59	26.88
5.1	2019	11	12	2	0	0	0	80.1	30.2
5.8	2019	11	19	13	30	0	0	81.1	29.42
5.3	2019	11	27	16	23	0	0	85.79	27.79
5.0	2020	1	12	14	34	0	0	81.71	29.58
5.3	2020	3	15	15	0	0	0	83.8	28.34
5.5	2020	5	12	18	8	0	0	86.15	27.65
4.9	2020	5	26	10	15	0	0	82.01	29.73
5.2	2020	5	30	15	51	0	0	84.93	27.85
5.2	2020	8	25	15	24	0	0	80.89	29.59
4.7	2020	9	4	1	35	0	0	87.19	27.58
5.3	2020	9	11	3	45	0	0	88.21	26.76
6.0	2020	9	15	23	34	0	0	85.88	27.77
5.5	2021	2	2	16	14	0	0	84.1	28.78
5.6	2021	2	9	1	50	0	0	87.91	27.89
5.8	2021	4	5	15	19	0	0	89.09	26.75

Mag	Yr	Mo	day	hr	min	sec	depth	long	lat
5.8	2021	5	18	23	57	0	0	84.39	28.28
4.8	2021	7	2	16	17	0	0	81.59	29.79
4.9	2021	7	18	15	14	0	0	81.47	28.98
4.9	2021	7	23	13	12	0	0	86.9	27.28

Complete Analysis Table

Time	T Years	4 - 4.9			5 - 5.9			6 - 6.9			7 - 7.9			> 8			1/√T
		N	N/T(λ)	σ _λ	N	N/T(λ)	σ _λ	N	N/T(λ)	σ _λ	N	N/T(λ)	σ _λ	N	N/T(λ)	σ _λ	
2017-2021	5	8.0	1.6	0.6	22.0	4.4	0.9	1.0	0.2	0.2	0.0	0.0	0.0	0.0	0.00	0.00	0.4
2012-2021	10	31.0	3.1	0.6	36.0	3.6	0.6	3.0	0.3	0.2	1.0	0.10	0.1	0.0	0.00	0.00	0.3
2007-2021	15	76.0	5.1	0.6	52.0	3.5	0.5	4.0	0.3	0.1	1.0	0.07	0.1	0.0	0.00	0.00	0.3
2002-2021	20	113.0	5.7	0.5	69.0	3.5	0.4	4.0	0.2	0.1	1.0	0.05	0.1	0.0	0.00	0.00	0.2
1997-2021	25	140.0	5.6	0.5	94.0	3.8	0.4	5.0	0.2	0.1	1.0	0.04	0.0	0.0	0.00	0.00	0.2
1992-2021	30	169.0	5.6	0.4	106.0	3.5	0.3	6.0	0.2	0.1	1.0	0.03	0.0	0.0	0.00	0.00	0.2
1987-2021	35	191.0	5.5	0.4	110.0	3.1	0.3	7.0	0.2	0.1	1.0	0.03	0.0	0.0	0.00	0.00	0.2
1982-2021	40	208.0	5.2	0.4	112.0	2.8	0.3	7.0	0.2	0.1	1.0	0.03	0.0	0.0	0.00	0.00	0.2
1977-2021	45	225.0	5.0	0.3	113.0	2.5	0.2	8.0	0.2	0.1	1.0	0.02	0.0	0.0	0.00	0.00	0.1
1972-2021	50	238.0	4.8	0.3	116.0	2.3	0.2	8.0	0.2	0.1	1.0	0.02	0.0	0.0	0.00	0.00	0.1
1967-2021	55	250.0	4.5	0.3	117.0	2.1	0.2	8.0	0.1	0.1	1.0	0.02	0.0	0.0	0.00	0.00	0.1
1962-2021	60	260.0	4.3	0.3	119.0	2.0	0.2	10.0	0.2	0.1	1.0	0.02	0.0	0.0	0.00	0.00	0.1
1957-2021	65	260.0	4.0	0.2	121.0	1.9	0.2	11.0	0.2	0.1	1.0	0.02	0.0	0.0	0.00	0.00	0.1
1952-2021	70	260.0	3.7	0.2	120.0	1.7	0.2	11.0	0.2	0.0	1.0	0.01	0.0	0.0	0.00	0.00	0.1
1947-2021	75	260.0	3.5	0.2	120.0	1.6	0.1	11.0	0.1	0.0	1.0	0.01	0.0	0.0	0.00	0.00	0.1
1942-2021	80	260.0	3.3	0.2	120.0	1.5	0.1	11.0	0.1	0.0	1.0	0.01	0.0	0.0	0.00	0.00	0.1
1937-2021	85	260.0	3.1	0.2	121.0	1.4	0.1	11.0	0.1	0.0	1.0	0.01	0.0	0.0	0.00	0.00	0.1
1932-2021	90	260.0	2.9	0.2	122.0	1.4	0.1	12.0	0.1	0.0	2.0	0.02	0.0	1.0	0.01	0.01	0.1
1927-2021	95	260.0	2.7	0.2	122.0	1.3	0.1	12.0	0.1	0.0	2.0	0.02	0.0	1.0	0.01	0.01	0.1
1922-2021	100	260.0	2.6	0.2	122.0	1.2	0.1	12.0	0.1	0.0	2.0	0.02	0.0	1.0	0.01	0.01	0.1
1918-2021	104	260.0	2.5	0.2	122.0	1.2	0.1	13.0	0.1	0.0	2.0	0.02	0.0	1.0	0.01	0.01	0.1

Gumbel method calculation

Return period (T)	$Y_T = -\left[\ln \cdot \ln \frac{T}{T-1}\right]$	$K = \frac{Y_T - \bar{Y}_n}{S_n}$	Flood discharge $X_T = \bar{x} + K\sigma_{n-1}$
2	0.4	-0.2	482
5	1.5	0.9	1083
10	2.3	1.6	1482
20	3.0	2.2	1864
50	3.9	3.1	2358
100	4.6	3.7	2729
200	5.3	4.3	3098
500	6.2	5.2	3585
1000	6.9	5.8	3954

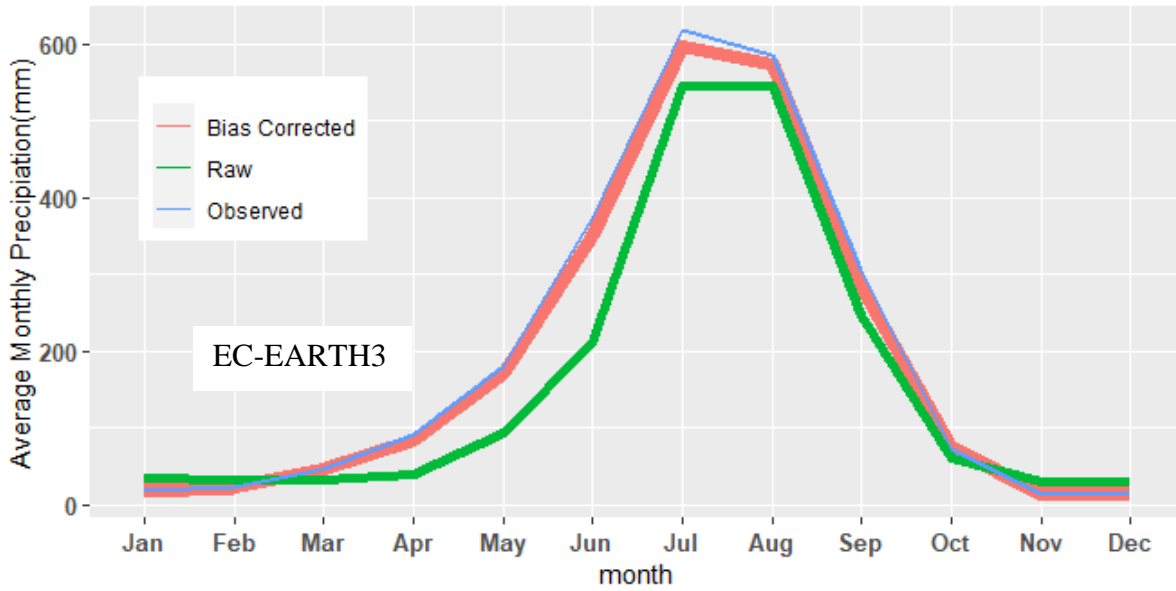
Log-Pearson method calculation

Return period (T)	K_z	$K_z\sigma_z$	$Z_T = \bar{z} + K_z\sigma_z$	$X_T = \text{Antilog } Z_T$
2	0.0	0.0	2.5	317
5	0.5	0.2	2.7	556
10	1.3	0.7	3.2	1420
20	1.6	0.8	3.3	2046
50	2.1	1.0	3.5	3502
100	2.3	1.2	3.7	4814
200	2.6	1.3	3.8	6450
500	2.8	1.4	3.9	8082
1000	3.1	1.6	4.1	11769

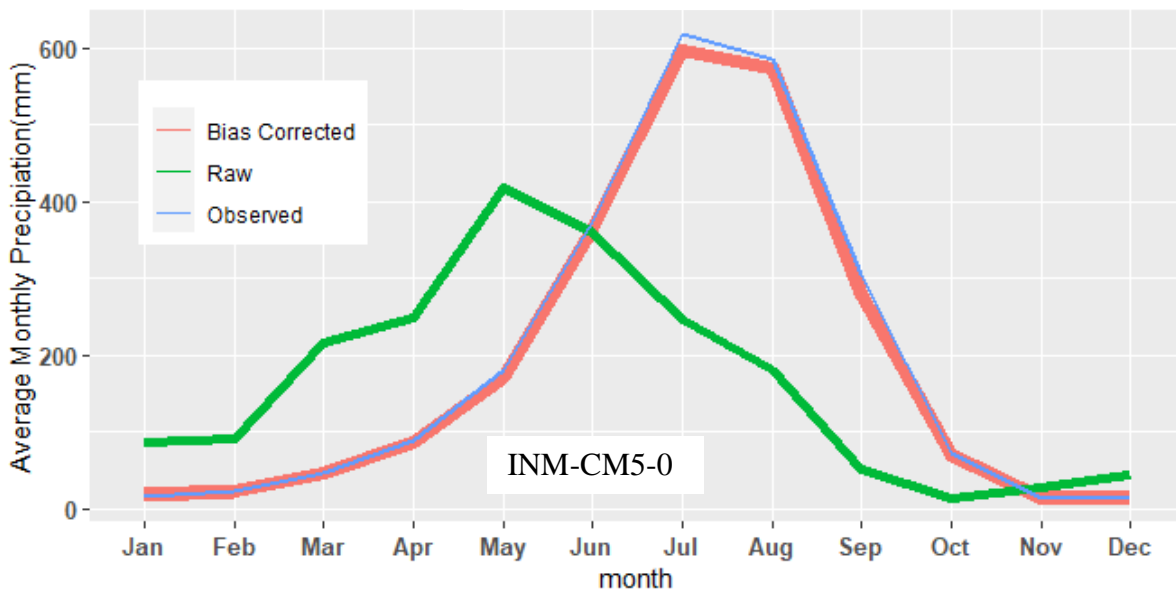
Log-Normal method calculation

Return period	K_z	$K_z\sigma_z$	$Z_T = \bar{z} + K_z\sigma_z$	$X_T = \text{Antilog } Z_T$
2	0.0	0.0	2.5	317
5	0.5	0.2	2.7	556
10	1.3	0.7	3.2	1419
20	1.6	0.8	3.3	2046
50	2.1	1.0	3.5	3501
100	2.3	1.2	3.7	4811
200	2.6	1.3	3.8	6445
500	2.8	1.4	3.9	8074
1000	3.1	1.6	4.1	11755

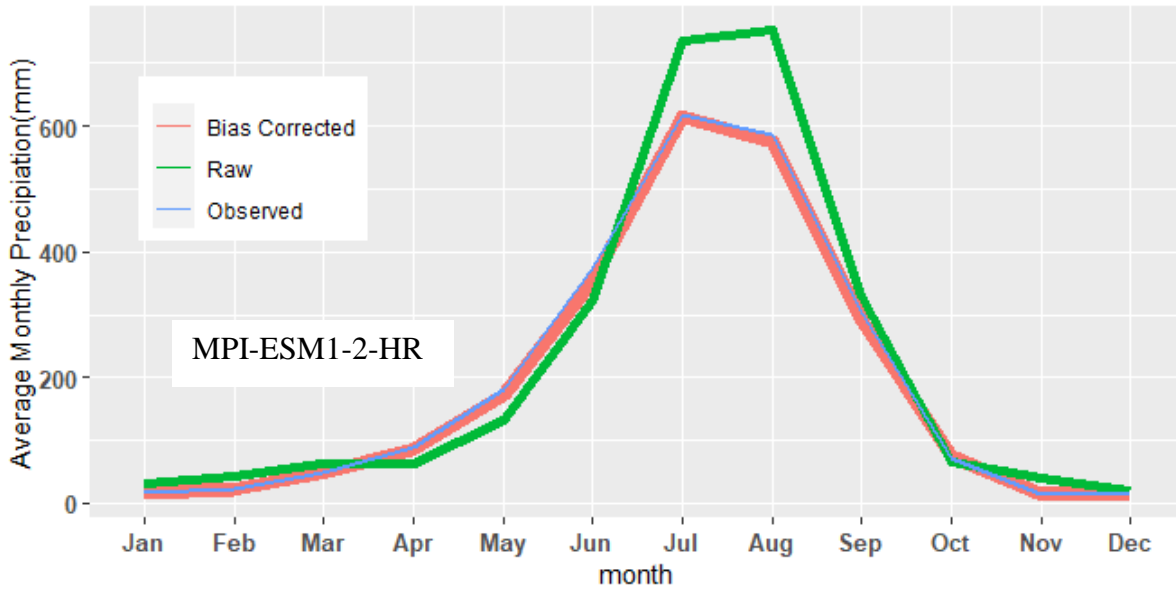
Comparison of raw and bias corrected data with observed data for precipitation of baseline period and for EC-EARTH3 GCM used in this study for station 1103



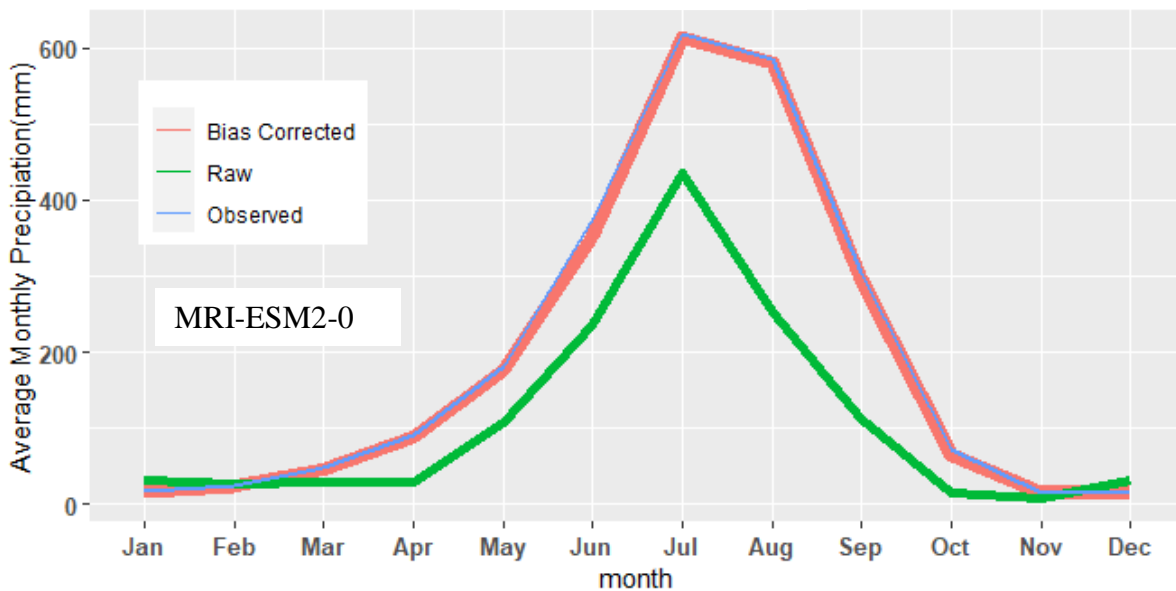
Comparison of raw and bias corrected data with observed data for precipitation of baseline period and for INM-CM5-0 GCM used in this study for station 1103



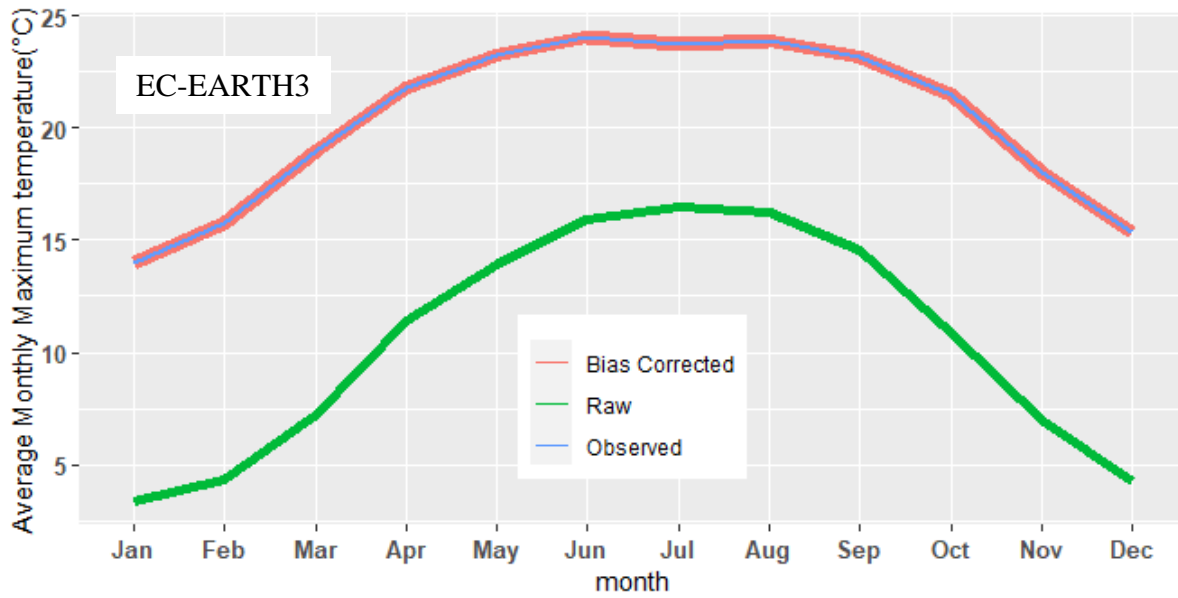
Comparison of raw and bias corrected data with observed data for precipitation of baseline period and for MPI-ESM1-2-HR GCM used in this study for station 1103



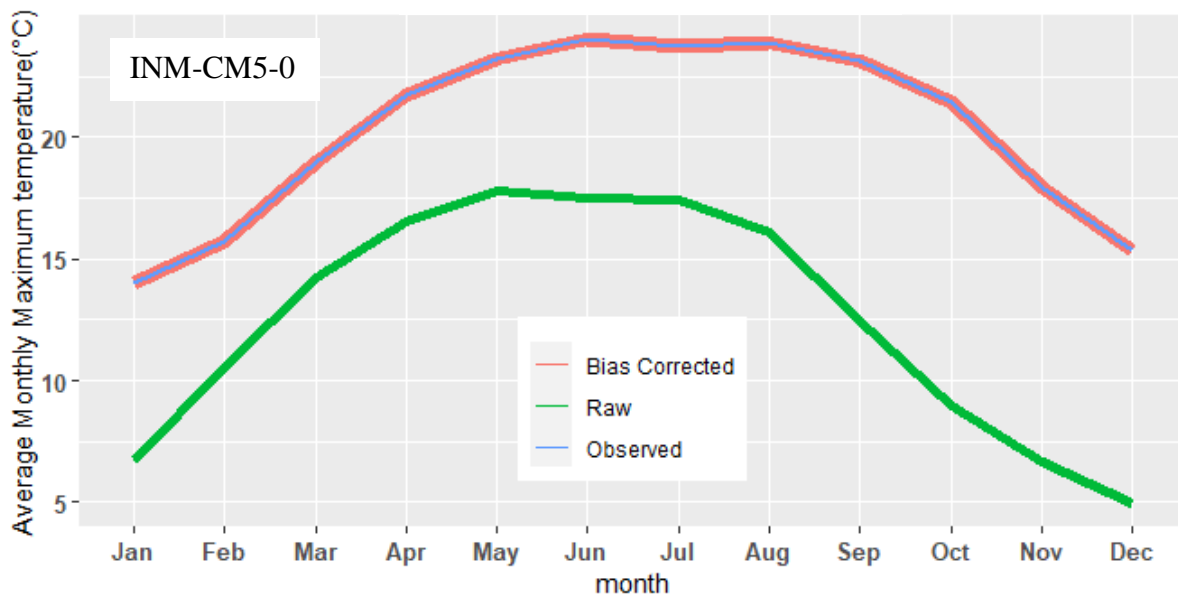
Comparison of raw and bias corrected data with observed data for precipitation of baseline period and for MRI-ESM2-0 GCM used in this study for station 1103



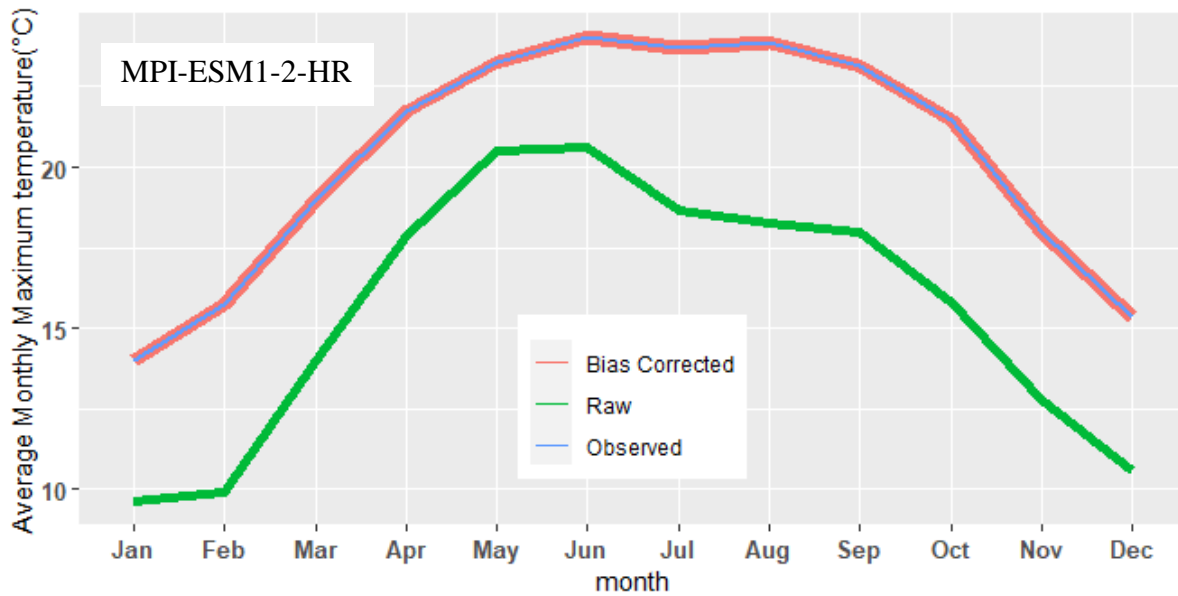
Comparison of raw and bias corrected data with observed data for maximum temperature of baseline period and for EC-EARTH3 GCM used in this study for station 1103



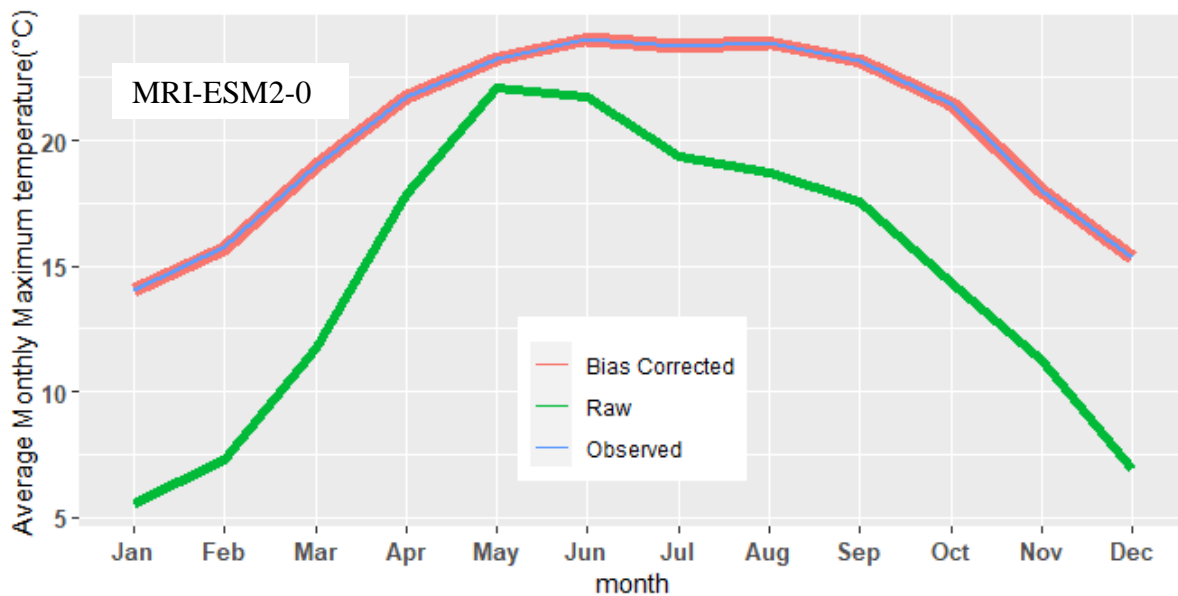
Comparison of raw and bias corrected data with observed data for maximum temperature of baseline period and for INM-CM5-0 GCM used in this study for station 1103



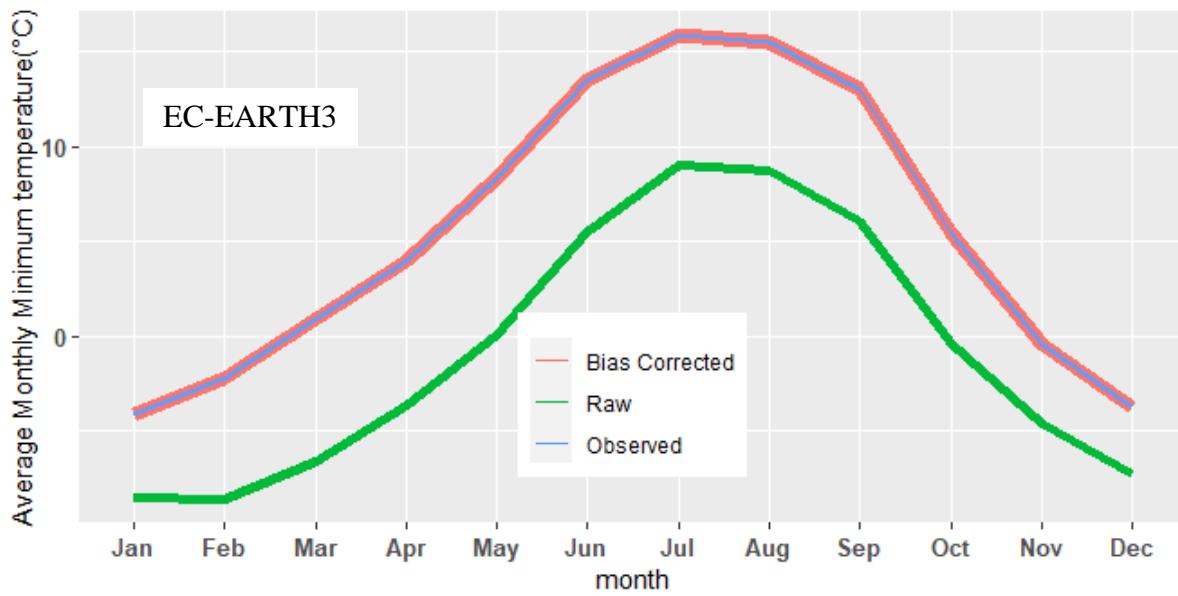
Comparison of raw and bias corrected data with observed data for maximum temperature of baseline period and for MPI-ESM1-2-HR GCM used in this study for station 1103



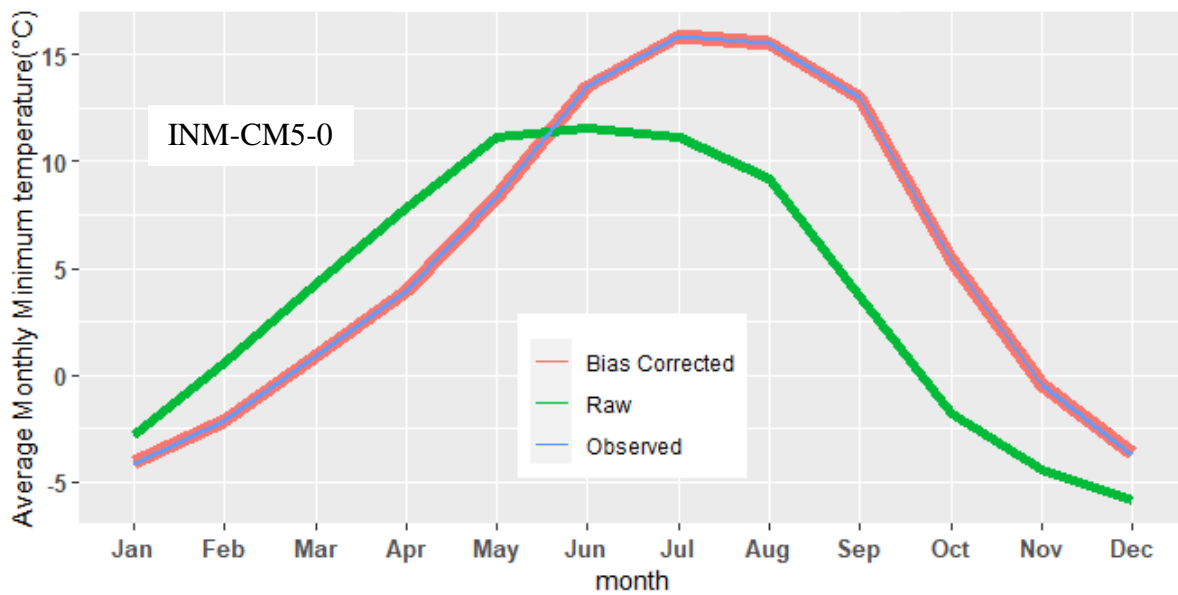
Comparison of raw and bias corrected data with observed data for maximum temperature of baseline period and for MRI-ESM2-0 GCM used in this study for station 1103



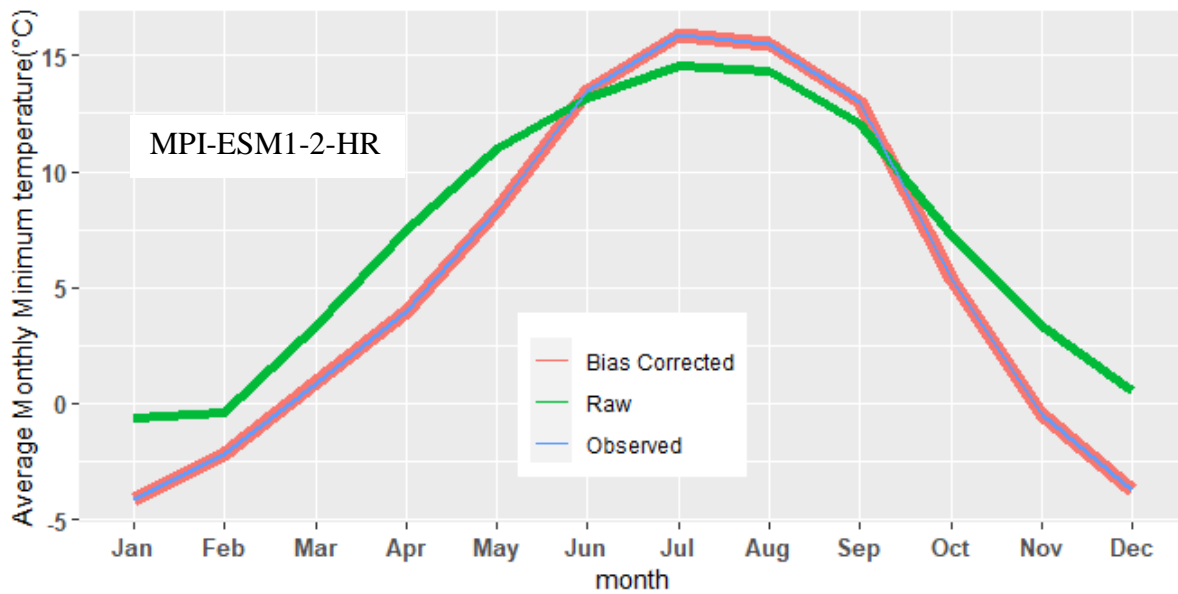
Comparison of raw and bias corrected data with observed data for minimum temperature of baseline period and for EC-EARTH3 GCM used in this study for station 1103



Comparison of raw and bias corrected data with observed data for minimum temperature of baseline period and for INM-CM5-0 GCM used in this study for station 1103



Comparison of raw and bias corrected data with observed data for minimum temperature of baseline period and for MPI-ESM1-2-HR GCM used in this study for station 1103



Comparison of raw and bias corrected data with observed data for minimum temperature of baseline period and for MRI-ESM2-0 GCM used in this study for station 1103

